

Nondestructive interaction of powerful electromagnetic waves with Bragg reflectors

Dissertation
zur Erlangung des Doktorgrades
an der Fakultät für Mathematik, Informatik und
Naturwissenschaften
Fachbereich Physik
der Universität Hamburg

vorgelegt von

Immo Bahns

Hamburg
2021

Gutachter/innen der Dissertation:

Prof. Dr. Jörg Rossbach
Dr. Harald Sinn

Zusammensetzung der Prüfungskommission:

Prof. Dr. Jörg Rossbach
Dr. Harald Sinn
Dr. Maurizio Vannoni
Prof. Dr. Roman Schnabel
Prof. Dr. Robin Santra

Vorsitzende/r der Prüfungskommission:

Prof. Dr. Roman Schnabel

Datum der Disputation:

02.09.2021

Vorsitzender Fach-Promotionsausschusses PHYSIK:

Prof. Dr. Wolfgang Hansen

Leiter des Fachbereichs PHYSIK:

Prof. Dr. Michael Potthoff

Dekan der Fakultät MIN:

Prof. Dr. Heinrich Graener

"What does it matter? Science has achieved some wonderful things of course, but I'd far rather be happy than right any day."

"And are you?"

"No. That's where it all falls down, of course."

"Pity", said Arthur. "It sounded like rather a good lifestyle otherwise."

– *Douglas Adams, The Hitchhiker's Guide to the Galaxy*

Contents

1. Introduction	3
2. Propagation of electromagnetic radiation	8
2.1. Monochromatic electromagnetic waves in dielectric media	10
2.1.1. Transverse electromagnetic (TEM) plane wave	11
2.1.2. Gaussian beam	12
2.1.3. Polarization of a TEM wave	17
2.2. Reflectance and absorption of electromagnetic radiation	20
2.3. Pulsed laser	22
2.4. Radiation pressure and remarks on quantum optics	24
3. Thermoelastic interaction of electromagnetic radiation with matter	27
3.1. Linear elasticity considering continuum mechanics	27
3.2. Thermodynamics of a solid crystal	34
3.3. Heat conduction	40
3.4. Equation of motion	42
3.5. Thermoelastic axisymmetric assumption for isotropic material	43
3.6. From classical thermodynamic theory to modern solid state physics	45
4. Material properties of diamond	47
4.1. Thermomechanical properties	49
4.2. Optical properties	66
5. Experimental setup and measurements	67
5.1. Michelson interferometer	72
5.2. Pump-probe measurement	79
5.2.1. Investigation of the connection between measured signal and the displacement of the crystal surface	82
5.2.2. Development of displacement after photon-matter interaction	84
6. Calculation of thermoelastic problems considering a diamond Bragg reflector	90
6.1. Analytical solutions	94
6.1.1. Initial temperature profile created by absorption of a laser pulse	94
6.1.2. One-dimensional thermoelastic models for pump-probe experiments	96

6.2. Solving thermoelastic equations with the finite element method	107
6.2.1. Thermoelastic axisymmetric simulations considering a time independent temperature profile	110
6.2.2. Time dependent temperature profile	119
6.2.3. Temperature dependent material parameters	123
6.2.4. Thermal conductivity	126
6.2.5. Excitation of eigenfrequencies	131
6.3. Simulation of the pump-probe experiment	134
6.4. Simulations of the thermoelastic effects for a diamond Bragg reflector in a CBXFEL at the European XFEL	144
7. Discussion and Outlook	153
8. Conclusion	160
A. Appendix	162
A.1. Cartesian coordinates and Cylindrical coordinates	162
A.2. Equation of motion	164
A.3. Anisotropic elasticity of cubic crystal	165
A.4. Input file for ab initio calculation	168
A.5. Temperature dependent thermal expansion coefficient	168
A.6. Finite element method (FEM)	170
Bibliography	179
Eidesstattliche Versicherung	186

Abstract

The thermoelastic interaction of an X-ray free electron laser (XFEL) with a Bragg reflector can cause a change of the local lattice constant of the Bragg reflector, which has a direct influence on the X-ray scattering conditions. Also, thermoelastic effects can excite macroscopic modes of vibrations, which can effect the angular stability of a reflection. For very demanding X-ray optical applications, like a cavity based X-ray free electron laser (CBXFEL), these effects must not exceed a critical amount, which would prohibit stable reflection conditions. Suitable theoretical models have to be determined to describe the thermoelastic interaction and must hold the comparison with the results of experimental data. Therefore, an in-house developed pump-probe setup has been set up, which gives the possibility to benchmark theoretical simulations with experimental data. A pulsed UV laser (pump) deposits an energy similar to the heatload expected from a powerful XFEL photon pulse into a single crystal diamond. A continuous wave (CW) laser (probe) in combination with an ultrafast photodiode (bandwidth 4.5 GHz) is used to measure the displacement of the crystal surface with a Michelson interferometer. With a cryogenic cooler in combination with a heater the initial crystal temperature can be adjusted in the range of 60 K to 300 K. In this work the dynamical thermoelastic effects caused by a photon-matter interaction are simulated with a finite element method (FEM) using the assumptions of continuum mechanics and a local thermodynamic equilibrium. The results of this work demonstrate that the measured data correspond well to the numerical solutions carried out with the FEM.

Zusammenfassung

Die thermoelastische Wechselwirkung eines Freie-Elektronen-Röntgenlasers mit einem Bragg-Spiegel kann die Gitterkonstante des Bragg-Spiegels ändern. Dies hat einen direkten Einfluss auf die Bedingung für Röntgenbeugung. Des Weiteren können durch thermoelastische Wechselwirkung makroskopische Schwingungsmoden angeregt werden. Dies kann die Winkelstabilität für die Reflexion beeinflussen. Für einen kavitätsbasierten Freie-Elektronen-Röntgenlasers gelten anspruchsvolle Stabilitätskriterien, welche durch thermoelastische Effekte nicht überschritten werden dürfen. Passende theoretische Formulierungen müssen gefunden werden, um die thermoelastische Wechselwirkung zu beschreiben und diese theoretischen Formulierungen müssen dem Vergleich mit experimentellen Beobachtungen standhalten. Deshalb wurde im Rahmen dieser Arbeit ein Anregungs-Abfrage (engl. Pump-probe) Experiment durchgeführt, um die Simulationsergebnisse, welche auf theoretischen Modellen basieren, mit experimentellen Messsignalen zu verifizieren. Im experimentellen Aufbau deponiert ein gepulster UV Laser (Anregung) eine Energiemenge in einen einkristallinen Diamanten, welche vergleichbar zur Wärmelast ist, die für einen Freie-Elektronen-Röntgenlaser mit hoher Leistung erwartet wird. Ein Dauerstrichlaser (Abfrage) in Kombination mit einer ultraschnellen Fotodiode (Bandbreite 4.5 GHz) wird

verwendet, um die Verschiebung der Kristalloberfläche mit einem Michelson-Interferometer zu messen. Mit kryogener Kühlung in Kombination mit einem Heizer kann die Ausgangstemperatur des Kristalls auf einen beliebigen Wert im Bereich von 60 K bis 300 K festgelegt werden. In dieser Arbeit wurden die dynamischen thermoelastischen Effekte, welche durch eine Photonen-Materie Wechselwirkung hervorgerufen wurden, durch Nutzung der Finite-Elemente-Methode simuliert. Dies geschieht unter der Annahme der Kontinuumsmechanik und eines lokalen thermodynamischen Gleichgewichts. Die Ergebnisse dieser Arbeit zeigen, dass die gemessenen Daten gut mit den numerischen Simulationsdaten übereinstimmen.

1. Introduction

Fourth generation X-ray free electron lasers are capable to deliver photon pulses with energies of a few millijoule and repetition rates in the MHz range [SZG⁺20] [DAA⁺20]. In this context Bragg reflectors with stable reflection conditions are needed for X-ray optical applications, like an XFEL-oscillator (XFELO) [Zem13], self-seeding setups [ABB⁺12] and spectrometers [SBC⁺19]. Under such conditions the question arises how the thermoelastic interaction of a high-energy photon pulse can deform the crystal structure of a Bragg reflector and on which timescales these deformations are reduced to a value that it does not disturb the reflection conditions of the following photon pulse.

The founding of this PhD project is connected to the development of an XFEL-oscillator (XFELO). The prior PhD projects of J. Zemella [Zem13] completed in 2013 and C. Maag [Maa18] completed in 2018 have investigated the possibilities and challenges of constructing an XFELO at the European XFEL facility. To allow a stable operation of an XFELO the angular misalignment shouldn't exceed values of about 100 nrad [Zem13] and the strain in propagation direction of the beam considering backscattering should not exceed values of about 1×10^{-6} [Maa18]. To continue the work of these projects a collaboration of two PhD projects with separated areas of responsibility were originated. One part is the simulation of a cavity based X-ray oscillator (CBXFEL) including the calculations of dynamical X-ray diffraction at thermally strained crystals, which is investigated in the PhD project of P. Rauer and will be complete probably in 2021 [Rau21]. The other part is the experimental investigation of the thermoelastic stability of Bragg reflectors under pulsed heat load and is the content of this work.

To avoid to be redundant with the prior PhD projects and the collaborating project of P. Rauer theoretical concepts regarding free electron lasers and dynamical X-ray diffraction will not be covered in this work. However, to given more detailed information about the motivation for the experimental investigations of this work a short overview about the concept of an XFELO will be presented in this introduction. For further information the interested reader is referred to the work of J. Zemella, C. Maag and P. Rauer [Zem13][Maa18][Rau21].

Facilities like the European XFEL can produce electron bunches of several GeV with a MHz repetition rate. These electron bunches can emit photons in the X-ray wavelength range when traveling through a periodically changing magnetic field of an undulator. Choosing suitable spacing and strength of the magnetic field in the undulator a particular photon energy distribution around a central wavelength will be emitted. Using a long undulator section radiation generated by spontaneous undulator radiation can be ampli-

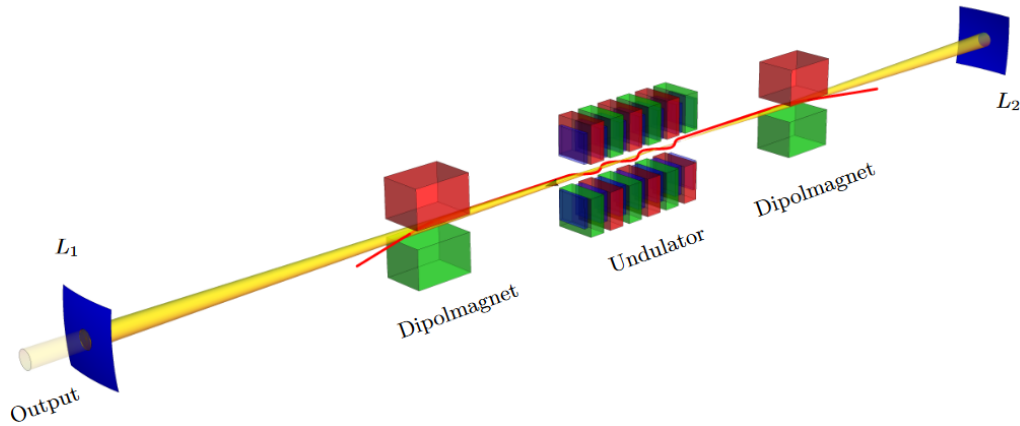


Figure 1.1.: Schematic illustration of an XFELO using Bragg reflectors (L_1 and L_2) in backscattering orientation [Zem13].

fied. This kind of free electron laser (FEL) is called a SASE (self-amplified spontaneous emission) FEL. A SASE FEL can achieve excellent transverse coherence. However, due to the amplification of spontaneous emission, various kinds of modes can be randomly amplified. The longitudinal coherence compared to a SASE FEL could be greatly improved by an XFELO. The basic concept of an XFELO is illustrated in Fig. 1.1. In this case the first electron bunch (the schematic path of the electrons is marked red in Fig. 1.1) will also generate photons by spontaneous undulator radiation. However, only a very narrow bandwidth of the photon radiation will be reflected by the Bragg reflector. With a suitable alignment of the lattice orientation of the Bragg reflectors a cavity for photons in the X-ray range can be constructed. If the round trip time of the generated photon pulses inside the cavity matches the repetition rate of the electron bunches the reflected photons can dominate the initiation of the FEL process for the next electron bunch. Over multiply round trips this causes a strong pulse energy increase of the photon pulses with a very narrow bandwidth and leads to photon pulses with stable pulse-to-pulse energies of a few millijoule in saturation. The particular design of an XFELO may vary from the simple concept illustrated in Fig. 1.1 by containing additional focusing elements and additional grazing incident mirrors to improve the stability of the XFELO regarding tolerances for vibrations and change of lattice spacing due to thermal expansion. Also the outcoupling process may vary which is in Fig. 1.1 proposed by using a sufficiently thin crystal (L_1) so that a part of the electromagnetic radiation is transmitted. Different concepts for an XFELO have been proposed in the past decades [KSR08] [LD18] [LKSF11], but so far none of them has been constructed. The concept of an XFELO introduced by Kim et al. [KSR08] proposed a low gain oscillator. This causes that the initial pulse energy inside the cavity is in the range of a few nanojoule and is increasing continuously over a few hundreds of pulses until saturation is reached with pulse energies of a few millijoule, which possess stable pulse-to-pulse energies [Zem13, p. 62]. A strongly related concept to an XFELO is a cavity based XFEL where a much higher gain is considered, which causes that the

initial pulse energy is in the range of one microjoule and saturation with pulse energies of a few millijoule are reached after just a few round trips. Such concept will be denoted as a cavity based XFEL (CBXFEL) in the following part of this work. The benefit of a CBXFEL compared to an XFEL is that the stability tolerance is less demanding. A detailed comparison of both concepts is given in the work of P. Rauer [Rau21]. A recently funded R&D project at the European XFEL facility is a promising candidate to be the first commissioned CBXFEL. Simulations carried out by P. Rauer for this R&D project proposes an initial crystal temperature of 77 K, a repetition rate of 2.25 MHz and photon pulse energies of a few mJ inside the cavity. It is assumed that at each reflection at a Bragg reflector, an amount of a few tens of μJ is absorbed and converted into heat inside the crystal. The beam radius in this context is about $50\ \mu\text{m}$ and the corresponding penetration depth is mostly in the range from a few μm to a few tens of μm . Because of its outstanding physical properties single crystalline diamond is a common choice for a Bragg reflector under such extraordinary conditions [SBT17]. In the simulations of P. Rauer the heat load effects have already been considered by calculating the temperature profile and corresponding local lattice expansion. However, due to simplicity in this simulation the mechanical dynamics caused by the rapid thermal expansion have not been included.

The conversion of the absorbed energy into heat may be assumed to take place on the picosecond time scale [YWW18]. The heating causes a dynamic thermal expansion of the material and can create mechanical displacement waves which propagate through the crystal. The dynamical thermal expansion for a diamond Bragg reflector under the assumptions of a three dimensional continuum theory have already been simulated with numerical methods considering a temperature range of about 300 K to about 2300 K [YWW18]. Also, a one-dimensional heat conduction and related strain wave propagation has been investigated experimentally by using a large pump spot size compared to the crystal thickness. In this experiment an optical pump, X-ray probe experiment has been used to measure the strain wave propagation in a nitrogen-doped diamond crystal at room temperature [SMW⁺12].

To the best knowledge of the author the present work is the first study which covers an experimental and theoretical investigation of a three-dimensional displacement/strain wave propagation, cause by pulsed heat load, for a diamond Bragg reflector. Another novel experimental investigation carried out in this work is the investigation of the impact of cryogenic cooling on the thermoelastic interaction and connected displacement/strain wave propagation.

For the experimental setup an optical pump, optical interferometer probe experiment in a temperature range of 60 K to 300 K has been used. The pump laser is a pulsed UV laser with a wavelength of 213 nm. The penetration depth for diamond at this wavelength is about $5\ \mu\text{m}$, which is on the same order of magnitude as the extinction length for X-rays reflecting at a diamond Bragg reflector considered for an XFEL concept by J. Zemella [p. 32][Zem13]. The absorbed energy per pulse of the UV laser is about $35\ \mu\text{J}$ and the

beam radius considered for the pump-probe experiment is about $300\ \mu\text{m}$. The heat load given for a saturated CBXFEL simulated by P. Rauer [Rau21] is about $45\ \mu\text{J}$, the beam radius is about $50\ \mu\text{m}$ and most of the absorbed energy can be connected to a penetration depth of roughly $20\ \mu\text{m}$. Since, the absorbed energy is similar in both cases the pump-probe experiment gives useful information to understand thermoelastic effects cause by the absorption of a saturated CBXFEL pulse. Nevertheless, due to the different shape of the heat load profile given by the penetration depth and beam radius there are also some important differences, which have been discussed in this work, regarding the reached maximum temperature value and kind of heat transfer process which may dominate the thermoelastic interaction.

The dynamic thermal expansion has been simulated in this work under the assumption of continuum mechanics and a local thermodynamic equilibrium for a radial symmetric heat load centered in a cylindrical crystal. The propagation of the mechanical waves, which are introduced by thermal expansion, are described in detail in Section 6 by comparing numerical results with simplified analytical solutions. These investigations give a phenomenological explanation of the development of the three dimensional wave propagation from the nanosecond to microsecond range. The results are in good agreement with experimental data obtained from the displacement measurement with a Michelson interferometer.

The experimental setup which has been built up in this work is a promising device to investigate photon-material interaction and could be used for an X-ray pump optical probe experiment and/or as a diagnostic tool to observe the stability of Bragg reflectors regarding fourth generation XFEL facilities. The underlying theory for the interferometer is presented in Section 2 by considering the propagation of electromagnetic waves in the context of a continuum theory based on Maxwell's equations. In this section also the absorption of the pulsed laser is explained by a phenomenological description using Beer's law.

In Section 3 the assumptions of continuum mechanics are discussed using the approximation of small deformations and describing the equation of motion which can be referred to Newton's laws. In this section also properties based on the law of thermodynamics and the empirical Fourier law are introduced. In Section 4 the temperature dependence of the thermodynamic properties of a single crystal diamond and the validity of the Fourier law are discussed in the context of solid state physics. In Section 5 the experimental setup is described in detail and the results of the pump-probe experiment are presented. The mentioned numerical simulations in Section 6 have been calculated with the finite element method. The assumptions for these simulations regarding temperature dependent material parameters are that a local thermodynamic equilibrium can be assumed at each time step carried out in the simulation. Further, it is assumed that the heat transport can be described by the Fourier law.

In Section 6.4 the same theoretical framework as considered for the pump-probe ex-

periment is used to predict the thermoelastic effects due to the heat load of a saturated CBXFEL for a diamond Bragg reflector. For the heat load the simulation results carried out by P. Rauer [Rau21] are used. Under the described assumptions for the thermoelastic interaction, the FEM simulations predicts a significant impact of these effect on the stability criteria of a CBXFEL. However, it should be mentioned that the prediction of the calculated displacement field might possess significant systematic errors because the initial temperature considered by the simulation of P. Rauer is 77 K and in this temperature region the assumption of the heat transport by the Fourier law of heat conduction may already not be valid anymore. In the last two sections the assumed range of validity and limits of the simulation results under the used assumptions are discussed in detail and an outlook for further experimental and theoretical work regarding thermoelastic interaction effects is given.

2. Propagation of electromagnetic radiation

The fundamentals of propagation of electromagnetic radiation is explained in detail in various textbooks [Hec16] [ST19]. Here only the parts which are important for the needs of this work are briefly summarized.

The propagation of electromagnetic radiation can be described in form of two mutually coupled vector waves, an electric-field wave and a magnetic-field wave (electromagnetic optics). Considering a solid material as a continuum, Maxwell's equations can be used to calculate the propagation of monochromatic electromagnetic waves in the UV-VIS light range. It is important to note that though the classical electromagnetic optics describes a lot of optical phenomena correctly, it does not cover quantum mechanical effects.

Maxwell's equations In a source free medium where no free electric charges or currents are present Maxwell's equations, in differential form can be written as [ST19, p. 153]

$$\begin{aligned}\nabla \times \mathfrak{H}(\mathbf{r}, t) &= \frac{\partial \mathfrak{D}(\mathbf{r}, t)}{\partial t} \\ \nabla \times \mathfrak{E}(\mathbf{r}, t) &= -\frac{\partial \mathfrak{B}(\mathbf{r}, t)}{\partial t} \\ \nabla \cdot \mathfrak{D}(\mathbf{r}, t) &= 0 \\ \nabla \cdot \mathfrak{B}(\mathbf{r}, t) &= 0,\end{aligned}\tag{2.1}$$

where the electric field \mathfrak{E} , the magnetic field \mathfrak{H} , the electric flux density \mathfrak{D} and the magnetic flux density \mathfrak{B} are vector fields which can be defined in every point of space \mathbf{r} and time t . For the sake of convenience the space \mathbf{r} and time t dependency will not be written out in the following part of this section. The connection of \mathfrak{D} and \mathfrak{E} depends on the electric properties of the medium and is given by

$$\mathfrak{D} = \epsilon_0 \mathfrak{E} + \mathfrak{P},\tag{2.2}$$

where \mathfrak{P} is the polarization density and ϵ_0 the electric permittivity of free space. In a dielectric medium the polarization density is given by the macroscopic sum of the electric dipole moments induced by \mathfrak{E} . The relation between \mathfrak{B} and \mathfrak{H} is given by

$$\mathfrak{B} = \mu_0 \mathfrak{H} + \mu_0 \mathfrak{M},\tag{2.3}$$

where \mathfrak{M} is the magnetization density and μ_0 is the magnetic permeability in free space. In an approximately linear, nondispersive, homogeneous and isotropic dielectric material the vectors fields \mathfrak{P} and \mathfrak{E} can be assumed to be everywhere in time and space parallel and proportional, so that

$$\mathfrak{P} = \epsilon_0 \chi \mathfrak{E}, \quad (2.4)$$

where χ is the electrical susceptibility. Inserting Eq. 2.4 into Eq. 2.2 gives

$$\mathfrak{D} = \epsilon \mathfrak{E}, \quad \text{where } \epsilon = \epsilon_0(1 + \chi). \quad (2.5)$$

Here, ϵ is the electric permittivity of the material. Equivalent considerations for the magnetic relation gives $\mathfrak{B} = \mu \mathfrak{H}$, where μ is the magnetic permeability of the material. However, considering a material like diamond which is transparent for visible light the ratio μ/μ_0 has a value of about 1.5×10^{-5} [Hec16, p. 143] and thus the approximation $\mu = \mu_0$ may be used. With these assumptions Eq. 2.1 can be rewritten as

$$\begin{aligned} \nabla \times \mathfrak{B} &= \mu_0 \epsilon \frac{\partial \mathfrak{E}}{\partial t} \\ \nabla \times \mathfrak{E} &= -\frac{\partial \mathfrak{B}}{\partial t} \\ \nabla \cdot \mathfrak{E} &= 0 \\ \nabla \cdot \mathfrak{B} &= 0. \end{aligned} \quad (2.6)$$

It can be derived that \mathfrak{E} and \mathfrak{H} satisfy the wave equation [Hec16, p. 98]

$$\begin{aligned} \nabla^2 \mathfrak{E} - \frac{1}{c^2} \frac{\partial^2 \mathfrak{E}}{\partial t^2} &= 0 \\ \nabla^2 \mathfrak{B} - \frac{1}{c^2} \frac{\partial^2 \mathfrak{B}}{\partial t^2} &= 0, \end{aligned} \quad (2.7)$$

where the Laplace operator ∇^2 is acting on each component of \mathfrak{E} and \mathfrak{B} so that both vector equations Eq. 2.7 are each represented by three scalar equations. In Cartesian coordinates this yields for the electric field¹ $\mathfrak{E} = \mathfrak{E}_x \hat{\mathbf{x}} + \mathfrak{E}_y \hat{\mathbf{y}} + \mathfrak{E}_z \hat{\mathbf{z}}$, with the unit vectors $\hat{\mathbf{x}}, \hat{\mathbf{y}}, \hat{\mathbf{z}}$ in $x - y - z$ direction, the following equations [Hec16, p. 99]:

$$\begin{aligned} \frac{\partial^2 \mathfrak{E}_x}{\partial x^2} + \frac{\partial^2 \mathfrak{E}_x}{\partial y^2} + \frac{\partial^2 \mathfrak{E}_x}{\partial z^2} - \frac{1}{c^2} \frac{\partial^2 \mathfrak{E}_x}{\partial t^2} &= 0 \\ \frac{\partial^2 \mathfrak{E}_y}{\partial x^2} + \frac{\partial^2 \mathfrak{E}_y}{\partial y^2} + \frac{\partial^2 \mathfrak{E}_y}{\partial z^2} - \frac{1}{c^2} \frac{\partial^2 \mathfrak{E}_y}{\partial t^2} &= 0 \\ \frac{\partial^2 \mathfrak{E}_z}{\partial x^2} + \frac{\partial^2 \mathfrak{E}_z}{\partial y^2} + \frac{\partial^2 \mathfrak{E}_z}{\partial z^2} - \frac{1}{c^2} \frac{\partial^2 \mathfrak{E}_z}{\partial t^2} &= 0. \end{aligned} \quad (2.8)$$

¹For \mathfrak{B} these equations have the same form.

The speed c of the electromagnetic wave in the material is given by

$$c = \frac{1}{\sqrt{\epsilon\mu_0}}. \quad (2.9)$$

The ratio of the speed of the wave in free space c_0 to that in the nonmagnetic material is defined as the refractive index:

$$n = \frac{c_0}{c} = \sqrt{\frac{\epsilon}{\epsilon_0}} = \sqrt{1 + \chi}, \quad \text{where } c_0 = \frac{1}{\sqrt{\epsilon_0\mu_0}}. \quad (2.10)$$

The quantities $\frac{\epsilon}{\epsilon_0}$ and $1 + \chi$ are called the relative permittivity and the dielectric constant, respectively.

2.1. Monochromatic electromagnetic waves in dielectric media

For the special case of a monochromatic electromagnetic wave in an optical medium all field components are harmonic function of time t with the same frequency ν_f . The function for the electric field $\mathfrak{E}(\mathbf{r}, t)$ and the magnetic flux density $\mathfrak{B}(\mathbf{r}, t)$ of a monochromatic electromagnetic wave with a complex amplitude propagating in an optical medium in this case can be written as [ST19, p. 162]

$$\begin{aligned} \mathfrak{E}(\mathbf{r}, t) &= \Re[\mathbf{E}(\mathbf{r}) \exp(j\omega t)], \quad \text{where } \omega = 2\pi\nu_f \\ \mathfrak{B}(\mathbf{r}, t) &= \Re[\mathbf{B}(\mathbf{r}) \exp(j\omega t)], \end{aligned} \quad (2.11)$$

where $\mathbf{E}(\mathbf{r})$ and $\mathbf{B}(\mathbf{r})$ define the complex amplitude vectors for the electric field and magnetic flux density, respectively. Inserting Eq. 2.11 into Eq. 2.6 gives

$$\begin{aligned} \nabla \times \mathbf{B}(\mathbf{r}) &= j\omega\mu_0\epsilon\mathbf{E}(\mathbf{r}) \\ \nabla \times \mathbf{E}(\mathbf{r}) &= -j\omega\mathbf{B}(\mathbf{r}) \\ \nabla \cdot \mathbf{E}(\mathbf{r}) &= 0 \\ \nabla \cdot \mathbf{B}(\mathbf{r}) &= 0. \end{aligned} \quad (2.12)$$

Further, substituting Eq. 2.11 into the wave equation Eq. 2.7 yields the Helmholtz equations

$$\begin{aligned} \nabla^2 \mathbf{E}(\mathbf{r}) + k^2 \mathbf{E}(\mathbf{r}) &= 0 \\ \nabla^2 \mathbf{B}(\mathbf{r}) + k^2 \mathbf{B}(\mathbf{r}) &= 0, \end{aligned} \quad (2.13)$$

where k is given by

$$k = \frac{\omega}{c} = \omega\sqrt{\epsilon\mu_0} = nk_0, \quad \text{where } k_0 = \frac{\omega}{c_0}. \quad (2.14)$$

In Cartesian coordinates considering the complex amplitude of an electric field $\mathbf{E}(\mathbf{r}) = E_x(\mathbf{r})\hat{\mathbf{x}} + E_y(\mathbf{r})\hat{\mathbf{y}} + E_z(\mathbf{r})\hat{\mathbf{z}}$, Eq. 2.13 can be written out as

$$\begin{aligned}\frac{\partial^2 E_x(\mathbf{r})}{\partial x^2} + \frac{\partial^2 E_x(\mathbf{r})}{\partial y^2} + \frac{\partial^2 E_x(\mathbf{r})}{\partial z^2} + k^2 E_x(\mathbf{r}) &= 0 \\ \frac{\partial^2 E_y(\mathbf{r})}{\partial x^2} + \frac{\partial^2 E_y(\mathbf{r})}{\partial y^2} + \frac{\partial^2 E_y(\mathbf{r})}{\partial z^2} + k^2 E_y(\mathbf{r}) &= 0 \\ \frac{\partial^2 E_z(\mathbf{r})}{\partial x^2} + \frac{\partial^2 E_z(\mathbf{r})}{\partial y^2} + \frac{\partial^2 E_z(\mathbf{r})}{\partial z^2} + k^2 E_z(\mathbf{r}) &= 0.\end{aligned}\tag{2.15}$$

2.1.1. Transverse electromagnetic (TEM) plane wave

A monochromatic plane wave can be defined with a wave vector \mathbf{k} where the complex amplitude vectors of Eq. 2.11 are given by [ST19, p. 165]

$$\mathbf{E}(\mathbf{r}) = \mathbf{E}_0 \exp(-j\mathbf{k} \cdot \mathbf{r})\tag{2.16}$$

$$\mathbf{B}(\mathbf{r}) = \mathbf{B}_0 \exp(-j\mathbf{k} \cdot \mathbf{r}),$$

where the complex envelopes \mathbf{E}_0 and \mathbf{B}_0 are constant vectors. Provided that the magnitude of \mathbf{k} is $k = nk_0$ the Helmholtz equation Eq. 2.13 is satisfied. Inserting² Eq. 2.16 into Eq. 2.12 it can be derived that the following conditions for \mathbf{B}_0 and \mathbf{E}_0 must hold to satisfy Maxwell's equations [ST19, p. 165]:

$$\mathbf{k} \times \mathbf{B}_0 = -\omega\mu_0\epsilon\mathbf{E}_0\tag{2.17}$$

$$\mathbf{k} \times \mathbf{E}_0 = \omega\mathbf{B}_0.\tag{2.18}$$

From Eq. 2.17 it follows that \mathbf{E} is perpendicular to \mathbf{k} and also to \mathbf{B} and Eq. 2.18 shows that \mathbf{B} is perpendicular to \mathbf{k} and \mathbf{E} . Thus, the electric field $\mathbf{E}(\mathbf{r})$, the magnetic flux density $\mathbf{B}(\mathbf{r})$ and the wave vector \mathbf{k} are mutually orthogonal, thus the vectors of \mathbf{E} and \mathbf{B} lie in a plane normal to the propagation direction \mathbf{k} . This defines the propagation of a transverse electromagnetic (TEM) wave [ST19, p. 165].

The flow of electromagnetic power is defined by the Poynting vector which in this case can be written as [ST19, p. 155]

$$\mathfrak{S} = \frac{1}{\mu_0} \mathfrak{E} \times \mathfrak{B}.\tag{2.19}$$

Inserting Eq. 2.11 into Eq. 2.19 it can be derived that the time averaged Poynting vector $\langle \mathfrak{S} \rangle$ is

$$\langle \mathfrak{S} \rangle = \Re[\mathbf{S}], \text{ where } \mathbf{S} = \frac{1}{2\mu_0} \mathbf{E} \times \mathbf{B}^*.\tag{2.20}$$

The average in Eq. 2.20 is taken over times, which are long in comparison of an optical

²For a general plane wave $\mathbf{X} = \mathbf{X}_0 e^{j(\mathbf{k} \cdot \mathbf{r} - \omega t)}$ the relation for the divergence $\nabla \cdot \mathbf{X} = j\mathbf{k} \cdot \mathbf{X}$ and for the curl $\nabla \times \mathbf{X} = j\mathbf{k} \times \mathbf{X}$ can be derived in this case.

cycle. For example, for a laser with wavelength³ of $\lambda = 532$ nm this would be⁴ about 1.8 fs. Further, another constraint for the time averaging is that it should be short to other times of interest⁵. The vector \mathbf{S} may be defined as the complex pointing vector and the optical intensity I is the magnitude of the vector $\Re[\mathbf{S}]$. By inserting Eq. 2.16 into Eq. 2.20 and using the relation of Eq. 2.17 the intensity in this case is calculated by

$$I = \frac{k}{2\mu_0\omega}|E_0|^2 = \frac{c\epsilon}{2}|E_0|^2 = \frac{1}{2\eta}|E_0|^2. \quad (2.21)$$

Here for the relations on the right hand side Eq. 2.14 has been used and $\eta = \sqrt{\frac{\mu_0}{\epsilon}}$ is the impedance for a nonmagnetic material [ST19, p. 165]. It should be mentioned that the introduced plane wave is an idealization which cannot really exist in this form. It is defined everywhere in space and at all times and has a constant intensity everywhere in space. These assumptions corresponds to an indefinite power. However, the derived formulae are useful for the approximations of real laser beams, which are going to be discussed in the following section.

2.1.2. Gaussian beam

Using the previously defined assumptions for the medium and considering further a plane wave given as by Eq. 2.16 propagating in z -direction, which is modulated by a scalar complex envelope $A(\mathbf{r})$ yields

$$\mathbf{E}(\mathbf{r}) = \mathbf{E}_0 A(\mathbf{r}) \exp(-jkz), \quad \text{where } \mathbf{E}_0 = E_{0x}\hat{\mathbf{x}} + E_{0y}\hat{\mathbf{y}} + E_{0z}\hat{\mathbf{z}}, \quad (2.22)$$

where the components of \mathbf{E}_0 are defined in Cartesian coordinates. Assuming that $A(\mathbf{r})$ varies slowly with respect to z , which causes a change of

$$\Delta A(\mathbf{r}) = \frac{\partial A(\mathbf{r})}{\partial z} \Delta z$$

and considering a distance of a wavelength $\Delta z = \lambda$ it is assumed that

$$\Delta A(\mathbf{r}) \ll A(\mathbf{r}).$$

This inequality considering complex values applies to the magnitudes for the real and the imaginary part separately [ST19, p. 48]. Further, this assumption gives the approximation

$$\frac{\partial A(\mathbf{r})}{\partial z} \ll kA(\mathbf{r}), \quad \text{where } k = \frac{2\pi}{\lambda}. \quad (2.23)$$

Also the derivative $\frac{\partial A(\mathbf{r})}{\partial z}$ must vary slowly within the distance of one wavelength

³The wavelength λ is connected to the magnitude of the wave vector by $\lambda = 2\pi/k$.

⁴The calculation done in this case is $T = \lambda/c_0$ where c_0 is the speed of light in free space.

⁵The rise and fall time of a fast photodiode should be short enough to detect the temporal change of a time varying signal.

$\frac{\partial^2 A(\mathbf{r})}{\partial z^2} \ll k \frac{\partial A(\mathbf{r})}{\partial z}$ which causes the inequation

$$\frac{\partial^2 A(\mathbf{r})}{\partial z^2} \lll k^2 A(\mathbf{r}) . \quad (2.24)$$

Inserting Eq. 2.22 into Eq. 2.13 gives the conditions for a paraxial Helmholtz equation. Neglecting terms with $\frac{\partial^2 A(\mathbf{r})}{\partial z^2}$ this equation becomes:

$$\begin{aligned} \frac{\partial^2 E_{0x} A(\mathbf{r})}{\partial x^2} + \frac{\partial^2 E_{0x} A(\mathbf{r})}{\partial y^2} - j2k \frac{\partial E_{0x} A(\mathbf{r})}{\partial z} &= 0 \\ \frac{\partial^2 E_{0y} A(\mathbf{r})}{\partial x^2} + \frac{\partial^2 E_{0y} A(\mathbf{r})}{\partial y^2} - j2k \frac{\partial E_{0y} A(\mathbf{r})}{\partial z} &= 0 \\ \frac{\partial^2 E_{0z} A(\mathbf{r})}{\partial x^2} + \frac{\partial^2 E_{0z} A(\mathbf{r})}{\partial y^2} - j2k \frac{\partial E_{0z} A(\mathbf{r})}{\partial z} &= 0. \end{aligned} \quad (2.25)$$

A Gaussian beam with the following solution satisfies the paraxial Helmholtz equation of Eq. 2.25:

$$\mathbf{E}(\mathbf{r}) = \mathbf{E}_0 A(\mathbf{r}) \exp(-jkz) \quad (2.26)$$

$$\mathbf{E}_0 = E_0 \left(-\hat{\mathbf{x}} + \frac{x}{z + jz_R} \hat{\mathbf{z}} \right)$$

$$A(\mathbf{r}) = \frac{jz_R}{q(z)} \exp \left(-jk \frac{\rho_r^2}{2q(z)} \right), \text{ where } \rho_r^2 = x^2 + y^2 \text{ and } q(z) = z + jz_R. \quad (2.27)$$

Here z_R has been chosen to be a constant with a positive real value.

The amplitude and phase of the complex envelope can be separated, by defining the complex function $1/q(z)$ in terms of two new real functions $R(z)$ and $W(z)$, such that:

$$\frac{1}{q(z)} = \frac{1}{z + jz_R} = \frac{z - jz_R}{z^2 + z_R^2} = \frac{1}{z + \frac{z_R^2}{z}} - \frac{j}{z_R + \frac{z_R^2}{z}} = \frac{1}{R(z)} - \frac{j\lambda}{\pi W^2(z)}. \quad (2.28)$$

which gives the following relation:

$$\begin{aligned} W(z) &= W_0 \sqrt{1 + \left(\frac{z}{z_R} \right)^2}, \text{ where } W_0 = \sqrt{\frac{\lambda z_R}{\pi}} \text{ and } \lambda = \frac{2\pi}{k} \\ R(z) &= z \left(1 + \left(\frac{z_R}{z} \right)^2 \right). \end{aligned} \quad (2.29)$$

Using the following relation

$$g = \frac{j}{z + jz_R} = \frac{z_R}{z^2 + z_R^2} + j \frac{z}{z^2 + z_R^2} \quad (2.30)$$

$$|g| = \frac{1}{\sqrt{z^2 + z_R^2}} = \frac{1}{z_R} \frac{W_0}{W(z)}$$

$$\zeta_g(z) = \arg(g) = \text{atan2} \left(\frac{z}{z^2 + z_R^2}, \frac{z_R}{z^2 + z_R^2} \right) = \arctan \left(\frac{z}{z_R} \right), \text{ where } z_R > 0,$$

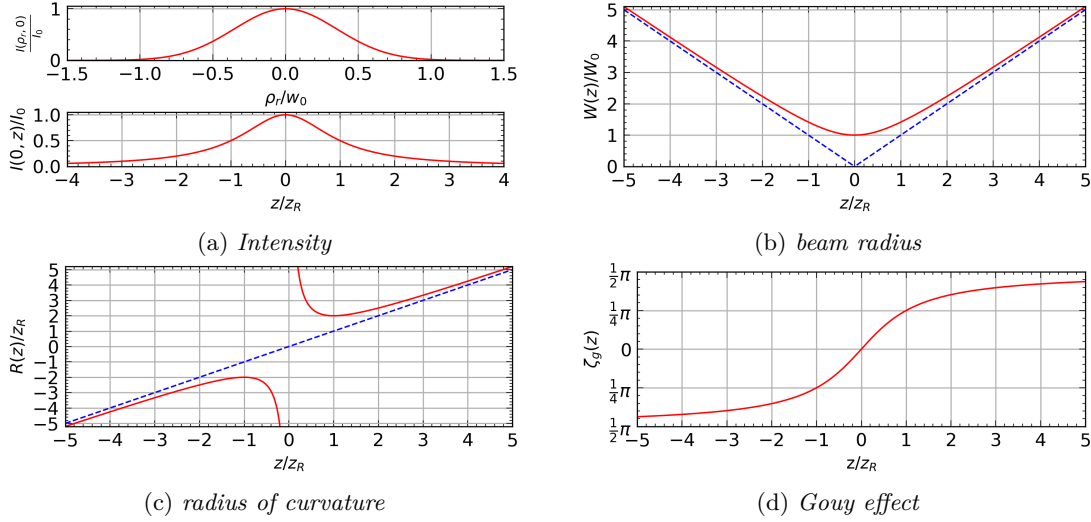


Figure 2.1.: Illustration of properties which describe the shape of a Gaussian beam given by Eq. 2.32. The Intensity profile in (a) has been calculated with Eq. 2.33. With the formulae in Eq. 2.29 the beam radius shown in (b) and the radius of curvature in (c) have been calculated. The function for the Gouy effect illustrated in (e) is given by Eq. 2.30.

the prefactor $\frac{jz_R}{q(z)}$ of $A(\mathbf{r})$ in Eq. 2.26 can be expressed by

$$\frac{jz_R}{z + jz_R} = \frac{W_0}{W(z)} \exp(j\zeta_g(z)). \quad (2.31)$$

With these definitions the complex envelope $A(r)$ becomes, using cylindrical coordinates (Appendix A.1)

$$A(\mathbf{r}) = \frac{W_0}{W(z)} \exp\left(-\frac{\rho_r^2}{W^2(z)}\right) \exp\left(-jk\frac{\rho_r^2}{2R(z)} + j\zeta_g(z)\right). \quad (2.32)$$

It can be shown that a monochromatic electromagnetic wave (Eq. 2.11) with a complex amplitude vector for the electric field $\mathbf{E}(r)$ of Eq. 2.26 satisfies the Maxwell's equations Eq. 2.12 by considering the paraxial approximation of a spherical wave [ST19, p. 166]. Further, due to the assumptions that $A(r)$ varies only slowly with respect to z , this paraxial electromagnetic wave can be locally approximated by a TEM plane wave [ST19, p. 169]. With this assumptions similar to the calculation of Eq. 2.21 the intensity of a Gaussian beam may be calculated by:

$$I(\rho_r, z) = I_0 \left(\frac{W_0}{W(z)}\right)^2 \exp\left(-\frac{2\rho_r^2}{W(z)^2}\right), \quad \text{where } I_0 = \frac{c\epsilon|E_0|^2}{2}. \quad (2.33)$$

To summarize the previous results, the electric field for a monochromatic Gaussian beam given by Eq. 2.11, Eq. 2.22, Eq. 2.26 and Eq. 2.32 can be expressed by

$$\mathfrak{E}(\mathbf{r}, t) = \Re \left[\mathbf{E}_0 \frac{W_0}{W(z)} \exp\left(-\frac{\rho_r^2}{W^2(z)}\right) \exp\left(-jk\frac{\rho_r^2}{2R(z)} + j\zeta_g(z)\right) \exp(j(\omega t - kz)) \right]. \quad (2.34)$$

The derived functions in Eq. 2.32 describes particular properties of a Gaussian beam [ST19, p.79]. The intensity profile given by Eq. 2.33 yields a Gaussian function in the transverse plane at any constant z value as illustrated for $z = 0$ in the first plot of Fig. 2.1a. In this context it should be mentioned that a normalized⁶ Gaussian function centered around the zero position can be defined by $f(\rho_r) = \exp\left(-\frac{\rho_r^2}{2\sigma_r^2}\right)$, where σ_r is known as the standard deviation or RMS width. Comparing this definition with Eq. 2.33 shows that $W(z)$ which in context of laser physics is known as the beam radius (or beam width) is twice the standard derivation. By considering Eq. 2.29 it is seen that $W(z)$ as illustrated in Fig. 2.1b has a minimum value at $W(0) = W_0$. This location is called the beam waist, the value W_0 is called the waist radius and $2W_0$ is named the spot size. The second plot of Fig. 2.1a shows the normalized intensity on the beam axis $\rho_r = 0$. The illustrated intensity is maximum at the position of the beam waist $z = 0$ and is reduced to half of the maximum intensity at a position $\pm z_R$ which is called the Rayleigh range. Given by Eq. 2.29 the beam radius at this position is $W(z_R) = \sqrt{2}W_0$, this radius correspond to an area which is doubled at z_R compared to the area at the beam waist. In this context the range $-z_R < z < z_R$ is known as the depth-of-focus, which has a value⁷ of $2z_R = 2\pi W_0^2/\lambda$ and therefore is directly proportional to the area πW_0^2 and inversely proportional to the wavelength. As indicated in Fig. 2.1b for large values of z , $W(z)$ increases linear with z represented by the function $W(z) \approx \frac{W_0}{z_R}z$ which is illustrated by the blue dashed line. The value⁸ $\theta_d = \frac{W_0}{z_R} = \frac{\lambda}{\pi W_0}$ describes that the beam diverges as a cone with half angle θ_d . The angular divergence of the beam is $2\theta_d$ and thus proportional to the wavelength and inversely proportional to the spot size. Given by Eq. 2.34 the phase of the Gaussian beam φ_{gauss} is represented by

$$\varphi_{gauss} = kz + \frac{k\rho_r^2}{2R(z)} - \zeta_g(z). \quad (2.35)$$

The phase shift $\zeta_g(z)$ is called the Gouy effect. This phase retardation is given by Eq. 2.30 and ranges from $-\pi/2$ at $z = -\infty$ to $\pi/2$ at $z = \infty$ as illustrated in Fig. 2.1d. An intuitive explanation for this effect can be derived by considering the transverse spatial confinement of a Gaussian beam, which due to the uncertainty principle causes a spread in the transverse momenta and hence a shift in the expectation value of the axial propagation constant [FW01]. The term $\frac{k\rho_r^2}{2R(z)}$ in Eq. 2.35 expresses the wavefront bending. Since $\zeta_z(z)$ and $R(z)$ are slowly varying functions, they can be approximated as constant at points within the beam radius on each wave front, which gives $z + \rho_r^2/2R = n\lambda + \zeta\lambda/2\pi$ where n is an integer. This equation yields a paraboloidal surface with radius of curvature R . Therefore, $R(z)$ given by Eq. 2.29 and illustrated in Fig. 2.1c determines the radius of curvature of the wavefront at position z along the beam axis. At $z = 0$, $R(z)$ becomes infinite which represents planar wave front. The minimum value is reached at $z = z_R$ to a value of $R(z) = 2z_R$. For $z > z_R$ the radius subsequently increases and for $z \gg z_R$,

⁶Such that the maximum value is one.

⁷Using the relation of Eq. 2.29.

⁸Using the relation of Eq. 2.29.

where $R(z) \approx z$ the wavefronts are approximately the same as those of spherical waves.

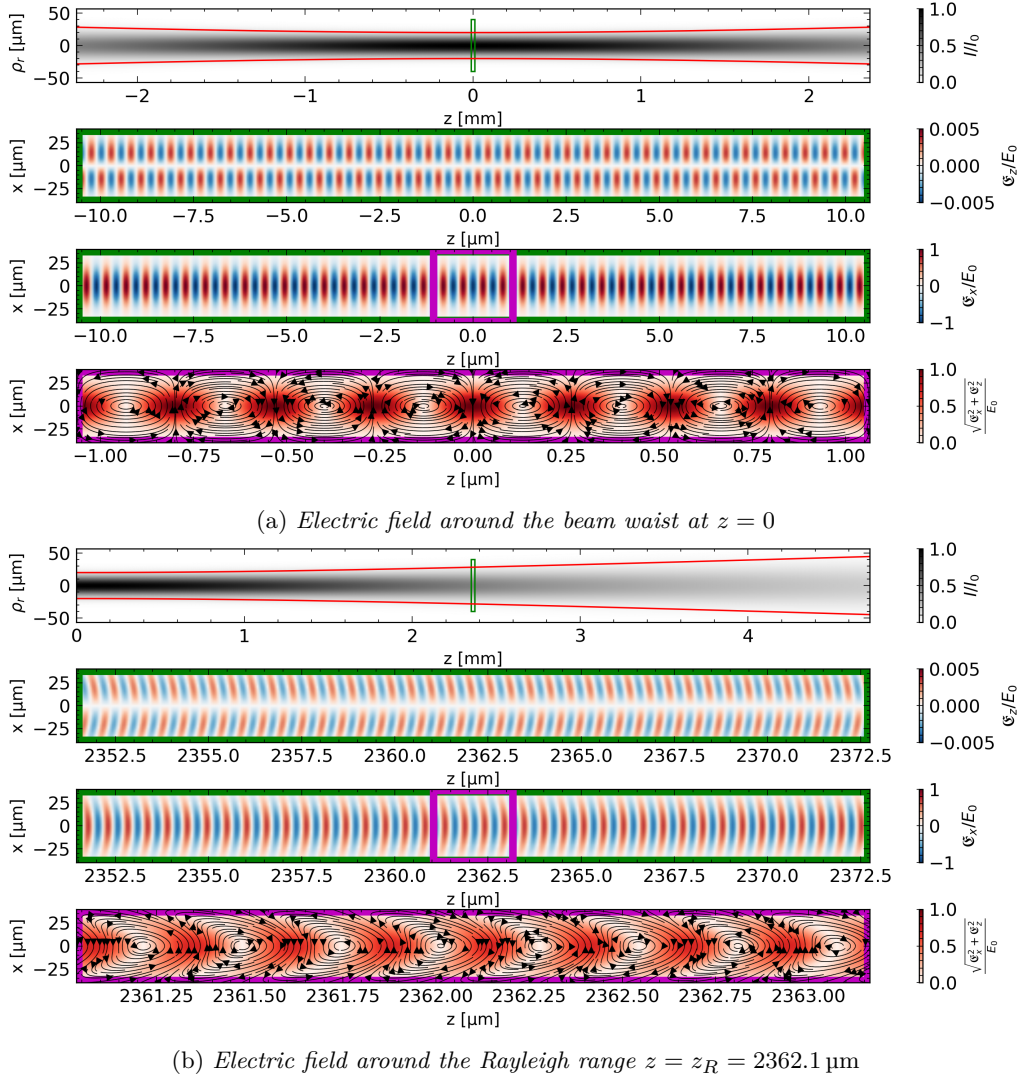


Figure 2.2.: Intensity calculated with Eq. 2.33 and electric field (at $y = 0$, $t = 0$) calculated with Eq. 2.36 and Eq. 2.34 of a monochromatic Gaussian beam with a wavelength of $\lambda = 532 \text{ nm}$ and a waist radius of $W_0 = 20 \mu\text{m}$ at (a) in the range of beam waist and in (b) around the Rayleigh range $z = z_R = 2362.1 \mu\text{m}$. The arrows indicated the direction of the electric field vectors. Since the electric field in y -direction is zero in this case the magnitude of the normalized electric field vector is given by $\frac{\sqrt{e_x^2 + e_z^2}}{E_0}$.

It should be mentioned that the validity of the paraxial approximation for a Gaussian beam depends on the beam waist W_0 and wavelength λ under consideration, the assumption is justified down to beam waists 5–10 times the wavelength [VT98]. To give an illustrative description of this approximation a Gaussian beam with a wavelength of $\lambda = 532 \text{ nm}$ and a waist radius of $W_0 = 20 \mu\text{m}$ will now be discussed. Assuming that the electric field only varies in x and z as discussed before by Eq. 2.26 the complex envelope \mathbf{E}_0 is given by

$$\mathbf{E}_0 = E_0 \left(-\hat{\mathbf{x}} + \frac{x}{z + jz_R} \hat{\mathbf{z}} \right). \quad (2.36)$$

Inserting Eq. 2.36 into Eq. 2.34 the electric field can be calculated. Considering the field at a time $t = 0$ and at $y = 0$ a two-dimensional vector plot of the three dimensional time dependent field as illustrated in Fig. 2.2 can be visualized. It can be seen from this plots that the z component of the electric field is much smaller than the x component. And therefore the approximation used for the intensity calculation of Eq. 2.33 introduces only a small error by neglecting the \mathcal{E}_z component in the calculation.

Power of a CW laser The power of a continuous wave (CW) laser can easily be measured with technical devices like a photodiode or a thermal sensor. Considering a power measurement⁹ of a laser with a Gaussian beam profile and a sensor area with the radius $\rho_{r,sen}$ in the transverse plane of the beam, the integral of the right hand side of Eq. 2.33 in cylinder coordinates gives [ST19, p. 78]

$$\begin{aligned} P(z) &= \int_0^{2\pi} \int_0^{\rho_{r,sen}} I_0 \left(\frac{W_0}{W(z)} \right)^2 \exp\left(-\frac{2\rho_r^2}{W(z)^2}\right) \rho_r d\rho_r d\theta \\ &= \frac{I_0 \pi W_0^2}{2} \left(1 - \exp\left(-\frac{2\rho_{r,sen}^2}{W(z)^2}\right) \right). \end{aligned} \quad (2.37)$$

For a sensor size of 1.5 $W(z)$ about 99 % of the power from the laser beam are collected. Therefore if the sensor area is bigger than this value the power is approximately $P = \frac{I_0 \pi W_0^2}{2}$. By knowing the value of P the intensity of Eq. 2.33 may be written as:

$$I(\rho_r, z) = \frac{2P}{\pi W(z)^2} \exp\left(-\frac{2\rho_r^2}{W(z)^2}\right). \quad (2.38)$$

2.1.3. Polarization of a TEM wave

The previously discussed TEM wave solution for Maxwell's equation allows also that the electromagnetic field is polarized in various states [ST19, p. 199]. In the following discussion it will be assumed that the TEM propagates in z -direction. The electric field vector of the illustrated Gaussian beam illustrated in Fig. 2.2 has a zero value component in the y -direction and therefore the three-dimensional vector field can be illustrated in a two-dimensional plot (Fig. 2.2). Such a polarization state of a TEM wave is called linearly polarized in x -direction [ST19, p. 200]. However, this is just a special case of a polarized TEM wave. In general the electric field of a monochromatic TEM wave propagating in z -direction can have various types of polarization lying in the x - y plane. This may be expressed by the complex values E_{0x} and E_{0y} of the complex envelope \mathbf{E}_0 and the definition of the Jones vector [ST19, p. 203]

$$\mathbf{J} = \begin{bmatrix} E_{0x} \\ E_{0y} \end{bmatrix} = \begin{bmatrix} |E_{0x}| e^{j\varphi_x} \\ |E_{0y}| e^{j\varphi_y} \end{bmatrix}, \text{ where } \varphi_x = \arg(E_{0x}), \varphi_y = \arg(E_{0y}). \quad (2.39)$$

⁹Assuming the laser is aligned in the center of a round shaped sensor

The amplitudes are defined by the total magnitude of the monochromatic wave $|E_0|^2 = |E_{0x}|^2 + |E_{0y}|^2$ and the total intensity of the wave considering Eq. 2.21 is

$$I = \frac{c\epsilon}{2}|E_0|^2 = \frac{c\epsilon}{2}(|E_{0x}|^2 + |E_{0y}|^2). \quad (2.40)$$

Interference of Gaussian beams To investigate the interference of Gaussian beams in the context of this work, the superposition principle for two monochromatic Gaussian beams, which both propagate in z -direction and have a beam waist with equal waist radii, at almost same position \mathbf{r} in space are considered. However, using the approximation of the Gaussian beam as a TEM both beams can have arbitrary Jones vectors \mathbf{J}_1 and \mathbf{J}_2 . Further, a small difference of the beam waist position in z -direction is allowed, this distance should be such small that the value of the beam radius at each position of the beams is still nearly the same. Under such conditions the intensity of the superimposed beams may be calculated with Eq. 2.33 and the maximum intensity is given by:

$$I_0 = \frac{c\epsilon}{2}(|E_{0x_1} \pm E_{0x_2}|^2 + |E_{0y_1} \pm E_{0y_2}|^2). \quad (2.41)$$

Using polar form the terms of Eq. 2.41 can be written as

$$\begin{aligned} |E_{0x_1} \pm E_{0x_2}|^2 &= (|E_{0x_1}|e^{j\varphi_{x_1}} \pm |E_{0x_2}|e^{j\varphi_{x_2}})(|E_{0x_1}|e^{-j\varphi_{x_1}} \pm |E_{0x_2}|e^{-j\varphi_{x_2}}) \\ |E_{0y_1} \pm E_{0y_2}|^2 &= (|E_{0y_1}|e^{j\varphi_{y_1}} \pm |E_{0y_2}|e^{j\varphi_{y_2}})(|E_{0y_1}|e^{-j\varphi_{y_1}} \pm |E_{0y_2}|e^{-j\varphi_{y_2}}) \end{aligned} \quad (2.42)$$

and writing out the terms on the right hand side of Eq. 2.42 gives¹⁰

$$\begin{aligned} |E_{0x_1} \pm E_{0x_2}|^2 &= |E_{0x_1}|^2 + |E_{0x_2}|^2 \pm 2|E_{0x_1}||E_{0x_2}|\cos\phi_x, \text{ where } \phi_x = \varphi_{x_1} - \varphi_{x_2} \\ |E_{0y_1} \pm E_{0y_2}|^2 &= |E_{0y_1}|^2 + |E_{0y_2}|^2 \pm 2|E_{0y_1}||E_{0y_2}|\cos\phi_y, \text{ where } \phi_y = \varphi_{y_1} - \varphi_{y_2}. \end{aligned} \quad (2.43)$$

If $|E_{0x_1}| = |E_{0x_2}| = |E_0|$ and $|E_{0y_1}| = |E_{0y_2}| = 0$ the equation for the intensity is reduced to

$$I = c\epsilon|E_0|^2(1 \pm \cos\phi_x). \quad (2.44)$$

It should be noted that the intensity for a single wave with $|E_{0x_1}| = E_0$ would be $I = \frac{c\epsilon}{2}|E_0|^2$. Thus the intensity can vary between a value of zero and four times the intensity of a single beam, depending on the value of phase difference ϕ_x . In the approximation for the calculation of the interference it is also assumed that the effect of the Gouy phase shift can be neglected. Considering the first terms of a Taylor series the Gouy phase in Eq. 2.30 is $\zeta_g(z) \approx z/z_r$. Considering the example of a Gaussian beam with waist radius $W_0 = 20 \mu\text{m}$ and Rayleigh range $z_R = 2.36 \text{ mm}$ as illustrated in Fig. 2.2 the shift in the range of one wavelength $\lambda = 532 \text{ nm}$ is just $\zeta_g(\lambda) = 0.00022$. This is corresponding to a distance of $\frac{\lambda\zeta_g(\lambda)}{2\pi} = 12 \text{ pm}$. This value is much smaller than λ and therefore the Gouy phase may be neglected and the phase varies in good approximation with $\phi = \frac{2\pi\Delta z}{\lambda}$.

¹⁰Using the relation $\cos x = \frac{1}{2}(e^{jx} + e^{-jx})$.

Matrix representation of polarization devices Considering a linear system under the assumption that superposition is valid, optical elements, which modify the polarization state of a Jones vector \mathbf{J}_{in} to a state \mathbf{J}_{out} can be expressed by a 2×2 Jones matrix \mathbf{T} , which can be used to describe many different optical elements. The formulae for the optical elements which are used in the experimental setup of this work will be introduced in the following sections. The action of cascaded optical systems can be determined by using matrix multiplication. In this work the convention is used that the positive z -direction is pointing in the propagation direction of the beam which is given by the wave vector \mathbf{k} of a TEM wave and further the convention is used that the $x - y - z$ axis form a right handed coordinate system. An illustration of this convention is illustrated in Fig. 2.3a.

Linear polarizers and polarizing beamsplitter Eq. 2.45 gives the Jones matrix of a linear polarizer (LP), which is eliminating the y component and transmits a wave polarized along the x -direction [ST19, p. 205]. The same matrix can be used to describe a polarizing beamsplitter (PBS), which is oriented in a way that it is transmitting light polarized in x -direction and a similar matrix for the PBS describes the part of light, which is reflected and polarized in y -direction:

$$\mathbf{T}_{LP,PBS_T} = \begin{bmatrix} 1 & 0 \\ 0 & 0 \end{bmatrix} \quad \mathbf{T}_{PBS_R} = \begin{bmatrix} 0 & 0 \\ 0 & 1 \end{bmatrix}. \quad (2.45)$$

Wave retarders The Jones matrix \mathbf{T}_R leaves the x component of the incoming Jones vector unchanged and is delaying the y component by the phase Γ :

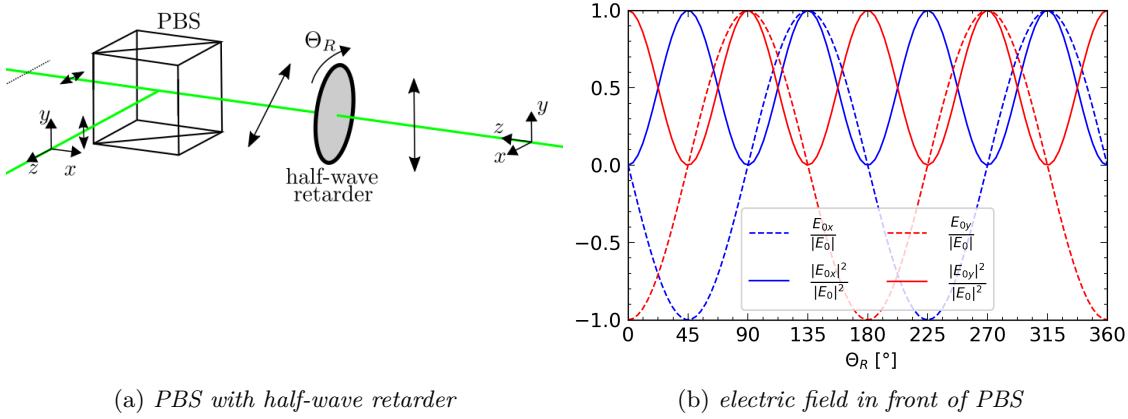
$$\mathbf{T}_{RET} = \begin{bmatrix} 1 & 0 \\ 0 & e^{-i\Gamma} \end{bmatrix}. \quad (2.46)$$

The axes which does not retard the wave is called the fast axes (which is in this case in x -direction). When $\Gamma = \pi/2$ the retarder is called a quarter-wave retarder which can convert a linear polarized state into circular and vice versa. When $\Gamma = \pi$ the retarder is called a half-wave retarder which can be used to change the plane of linear polarized light while remaining linear polarization [ST19, p. 206].

Rotation of a Jones matrix For a rotation in the x - y plane around the z -axes the following rotation matrix can be used [ST19, p. 206]:

$$\mathbf{R}(\Theta_R) = \begin{bmatrix} \cos \Theta_R & \sin \Theta_R \\ -\sin \Theta_R & \cos \Theta_R \end{bmatrix} \quad (2.47)$$

Considering the convention used in this work as (illustrated in Fig. 2.3a) the rotation of an optical element which is described by a Jones matrix can be carried out by using $\mathbf{R}(\Theta_R)\mathbf{T}\mathbf{R}(-\Theta_R)$. In this context a rotated half-wave retarder in combination with a



(a) PBS with half-wave retarder

(b) electric field in front of PBS

Figure 2.3.: (a) Sketch of a half-wave retarder in combination with a PBS. (b) Electric field components after the half-wave retarder for the case of a linear incoming wave which is linear polarized in x -direction (in this particular case E_{0x} and E_{0y} have only real values).

PBS can be used to control the amount of an electromagnetic wave which is transmitted/reflected at a PBS. To explain this with an example a Gaussian beam which can be approximated as a TEM wave and has a sufficient smaller beam diameter than the size of the PBS is considered. Using the setup illustrated in Fig. 2.3a and considering a TEM wave linear polarized in x -direction with the Jones vector \mathbf{J}_{in} , which is propagating through a half-wave plate, the wave after the wave retarder will still be linear polarized. However, the wave can now also have non-zero field components in y -direction and the amount will depend on the angle Θ_R about which the half-wave retarder is rotated. The resulting values for this case are shown in Fig. 2.3b and are calculated with $\mathbf{R}(\Theta_R)\mathbf{T}_{RET_{half}}\mathbf{R}(-\Theta_R)\mathbf{J}_{in}$, where $\mathbf{T}_{RET_{half}}$ is the Jones matrix of the half-plate retarder Eq. 2.46. Considering the Jones matrix of a PBS (Eq. 2.45) the TEM wave will be separated into a transmitted (x -direction) and a reflected part (y -direction). Since the intensity of the TEM wave is proportional to the square of the electric field, the PBS in combination with a rotatable half-wave retarder can be used to reduce the intensity/power of a Gaussian beam to a desired value by adjusting the angle Θ_R .

2.2. Reflectance and absorption of electromagnetic radiation

The previously discussed propagation of an electromagnetic wave did not cover the reflection of a wave which may occur when the wave meets the boundary of a new material. Also, it has not been considered that light may be partly absorbed by propagation through a solid. These topics will now be discussed by assuming that the wavelength λ of a TEM wave is much bigger than the range of the microscopic structures of a single crystalline material. For example, this is a valid assumption for a laser with a wavelength of $\lambda = 532$ nm in comparison to the microscopic dimensions of a single crystal diamond which ranges over

a few Å.

A phenomenological approach to describe the absorption of light in a linear media can be carried out by considering the electric susceptibility Eq. 2.4 to be a complex value [ST19, p.170]

$$\chi = \chi' + j\chi'' \quad (2.48)$$

For a monochromatic wave as discussed in Section 2.1 the same equation can be used considering the Eq. 2.48. However, now the wavenumber k (Eq. 2.14) has a complex value

$$k = \omega\sqrt{\epsilon\mu_0} = k_0\sqrt{1 + \chi} = k_0\sqrt{1 + \chi' + j\chi''} \quad (2.49)$$

Expressing $k = \beta_k - j\frac{1}{2}\alpha_k$ in terms of a real and imaginary part yield

$$k = \beta_k - j\frac{1}{2}\alpha_k = k_0\sqrt{1 + \chi' + j\chi''} \quad (2.50)$$

Considering the propagation of the wave in z -direction it can be seen by considering Eq. 2.16 and Eq. 2.34 that the electric field now contains the factor

$$\exp(-jkz) = \exp(-j\beta_k z) \exp(-\frac{1}{2}\alpha_k z),$$

which indicates that for $\alpha_k > 0$ the amplitude of the electric field will decrease while the wave propagates in z -direction. The intensity of a TEM wave Eq. 2.21 is proportional to $|E_0|^2$ and thus the intensity will decrease by a factor $\exp(-\alpha_k z)$ while propagating in z -direction. The value of α_k is known as the absorption coefficient¹¹ [ST19, p. 171] and the related value $\zeta = 1/\alpha_k$ is called the penetration depth. The exponential decay of the intensity described by these values can also be connected to Beer's law, which will be discussed in the next section. The value of β_k may be connected to the refractive index $\beta_k = nk_0$, which defines the phase velocity $c = c_0/n$. Inserting into Eq. 2.50 gives

$$n - j\frac{1}{2}\frac{\alpha_k}{k_0} = \sqrt{\frac{\epsilon}{\epsilon_0}} = \sqrt{1 + \chi' + j\chi''} \quad (2.51)$$

This equation relates the complex value of the electric susceptibility to the refractive index and the absorption coefficient. The impedance Eq. 2.21 can also be connected with the complex susceptibility

$$\eta = \sqrt{\frac{\mu_0}{\epsilon}} = \frac{\eta_0}{\sqrt{1 + \chi}} \quad (2.52)$$

It should be noted that χ , k , ϵ and η are complex quantities, whereas α_k , β_k and n have real values.

Considering boundary conditions given by Maxwell's equation it can be derived that

¹¹Also called the attenuation coefficient or extinction coefficient

the reflection of a TEM wave can be described by the Jones matrix [ST19, p. 210]:

$$\mathbf{T}_r = \begin{bmatrix} r_x & 0 \\ 0 & r_y \end{bmatrix}. \quad (2.53)$$

For the special case of a TEM wave reflected¹² at normal incident it can be derived that:

$$r_y = -r_x = \frac{\eta_2 - \eta_1}{\eta_2 + \eta_1}. \quad (2.54)$$

where η_1 is the complex impedance of the medium from which the incident wave is coming and η_2 is the complex impedance of the medium at which boundary the incident wave is reflected. The reflectance R which describes the ratio between the incoming and the reflected wave intensity is given in this case by [ST19, p. 210]

$$R = \left(\frac{\eta_2 - \eta_1}{\eta_2 + \eta_1} \right)^2. \quad (2.55)$$

For materials where the absorption coefficient is nearly zero Eq. 2.55 can be written as

$$R = \left(\frac{n_2 - n_1}{n_2 + n_1} \right)^2. \quad (2.56)$$

It should be mentioned that for the case of an arbitrary incident angle the polarization state is important for the value of the reflectance/transmission and can be calculated for dielectric materials by considering Fresnel's equation. With this knowledge by choosing materials with suitable impedance optical devices like a PBS (Eq. 2.45) can be designed for a particular wavelength range. However, the reflectance of an incident wave with an arbitrary angle will not be discussed further in this work. Addition information to this topic can be found in textbooks [ST19, chapter 6.2] [Hec16, chapter 4.6].

2.3. Pulsed laser

When electromagnetic radiation is absorbed by a material it can be thought of as an energy source inside the material. However, although driven by the incident radiation, this source can develop an own dynamics depending on the electronics and lattice response [Sch10, p.23]. Considering quantum mechanics, electromagnetic radiation interacts with matter only in portions of whole quanta. Here the angular frequency ω and intensity I corresponds to the flux $\frac{I}{\hbar\omega}$ of photons of energy $\hbar\omega$, where \hbar is the reduced Planck's constant. However, the photon numbers of pulsed lasers are enormous and classical concepts are generally adequate to describe beam-solid interaction phenomena [AB13, p. 6].

If the repetition rate $f_R = 1/T_p$, with T_p the period time of one pulse to the next one, of a pulsed laser is known¹³, the energy per pulse E_p can be computed by measuring the

¹²Considering the convention for the coordinate system used in this work (as illustrated in Fig. 2.3a)

¹³This can be measured for example with an oscilloscope in combination with a sufficiently fast photodiode.

average power P_{avg} with a thermal sensor and dividing the result by f_R . The pulse energy E_p is the optical power $P(t)$ integrated over time:

$$E_p = \int_0^{T_p} P(t) dt. \quad (2.57)$$

The temporal shape of a laser pulse with a pulse length of about 1 ns can be measured with a sufficiently fast photo diode in combination with an oscilloscope:

$$P(t) = E_p \frac{U(t)}{\int_0^{T_m} U(t') dt'}. \quad (2.58)$$

where $U(t)$ is the temporal signal measured in Volt and T_m is the time span measured with the oscilloscope. The time span T_m should be sufficiently long to cover the full rise and fall of the signal in relation to a constant initial value. The division by the integral in Eq. 2.58 is carried out to normalize the function in a way that the formulation of Eq. 2.57 holds. A laser with a narrow central optical bandwidth and pulse lengths in the nanosecond range may be considered to be a quasi-CW case. Further, considering a Gaussian beam profile with intensity I described by Eq. 2.38 is meeting the surface of an absorbing material under normal incident at position $z = 0$ and using Beer's law gives [Sch10, p. 30]

$$\frac{\partial I_z(\rho_r, z, t)}{\partial z} = -\frac{1}{\zeta} I_z(\rho_r, z, t). \quad (2.59)$$

Assuming that the Rayleigh range z_R of a Gaussian beam is much larger than the penetration depth ζ or the dimension of the medium in propagation direction, the value of the beam radius may be approximated as a constant value $W(z) = W$. Considering Eq. 2.38 and Eq. 2.59 the z dependent intensity inside the medium in this case may be written as

$$I_z(\rho_r, z, t) = I_0(t, \rho_r)(1 - R) \exp(-z/\zeta) \Theta_H(z), \quad (2.60)$$

$$\text{where } I_0(\rho_r, t) = \frac{2P(t)}{\pi W^2} \exp\left(-\frac{2\rho_r^2}{W^2}\right).$$

Here R is the reflectance of the surface and it is assumed that no reflection inside the material occurs. It should be noted that the Heaviside step function $\Theta_H(z)$ has been used here because $I_z(\rho_r, z, t)$ has no physical meaning for $z < 0$. The z depending fluence considering a single laser pulse (units J/m²) is the time integration of Eq. 2.60:

$$\mathfrak{F}_z(\rho_r, z) = \int_0^{T_R} I_z(\rho_r, z, t) dt = \frac{(1 - R)2E_p}{\pi W^2} \exp\left(-\frac{2\rho_r^2}{W^2}\right) \exp(-z/\zeta) \quad (2.61)$$

Considering a material with a cylindrical shape of thickness d and radius R_0 and regarding $\frac{\partial I_z(\rho_r, z, t)}{\partial z}$ and $\frac{\partial \mathfrak{F}_z(\rho_r, z)}{\partial z}$ as the power density $\Phi_P(\rho_r, z, t)$ and the energy density $\Phi_E(\rho_r, z)$, respectively, the absorbed energy per pulse in the material can be calculated

by the following spatial and temporal integration:

$$\begin{aligned}
E_{abs} &= \int_0^{T_R} \int_0^d \int_0^{2\pi} \int_0^{R_0} \Phi_P(\rho_r, z, t) \rho_r d\rho_r d\theta dz dt \\
&= \int_0^d \int_0^{2\pi} \int_0^{R_0} \Phi_E(\rho_r, z) \rho_r d\rho_r d\theta dz \\
&= \frac{(1-R)2E_p}{\zeta\pi W^2} \int_0^d \int_0^{2\pi} \int_0^{R_0} \exp\left(-\frac{2\rho_r^2}{W^2}\right) \exp(-z/\zeta) \rho_r d\rho_r d\theta dz.
\end{aligned} \tag{2.62}$$

What is neglected in this formula is that the penetrating radiation can also be reflected at the back side of the material $z = d$ and then at the front $z = 0$ again and so on. However, this may be considered to be a valid assumption if $\zeta \ll d$ or when the reflectance inside the material at the boundaries is small.

Solving the integrals in Eq. 2.62 gives:

$$\begin{aligned}
\int_0^{2\pi} \int_0^{R_0} \exp\left(-\frac{2\rho_r^2}{W^2}\right) \rho_r d\rho_r d\theta &= \frac{W^2\pi}{2} \left(1 - \exp\left(-\frac{2R_0^2}{W^2}\right)\right), \\
\int_0^d \exp(-z/\zeta) dz &= \zeta(1 - \exp(-d/\zeta)).
\end{aligned} \tag{2.63}$$

2.4. Radiation pressure and remarks on quantum optics

The linear momentum, which is carried by an electromagnetic wave causes a radiation pressure on objects from which the wave is reflected or absorbed. This can be described in the context of considering a continuous wave described by Maxwell's equations [Hec16, p. 125], as well as considering quantum effects where the electromagnetic wave consist of photons with discrete energies [Hec16, p. 127]. However, describing the radiation pressure by classical electromagnetic theory is a quite extensive task and would give no additional insights for the needs of this work. Also, the quantum theory is in accordance with the experimental observation of the Compton effect, which cannot be described by the classical theory of electromagnetism [Hec16, p. 127]. Therefore, in this work an explanation for the radiation pressure will only be discussed considering a quantum mechanical effect. In this context special relativity theory describes the relation between mass m , energy E and momentum p of a particle by [Hec16, p. 127]:

$$E = \sqrt{(cp)^2 + (mc^2)^2}. \tag{2.64}$$

A photon has the properties:

$$m = 0, \quad E = cp = \hbar\omega \quad \text{and} \quad c = \lambda\nu_f \quad \text{where} \quad \omega = 2\pi\nu_f. \tag{2.65}$$

Here \hbar is the reduced Planck's constant. The linear momentum associated with a photon in a plane wave with wave vector \mathbf{k} can be described by $\mathbf{p} = \hbar\mathbf{k}$, where the magnitude $|\mathbf{p}| = p$ is given in Eq. 2.65 [ST19, p. 452]. It should be mentioned that a photon can also

possess an angular momentum. However, this property is not investigated in this work and will not be discussed further.

Considering time spans which are sufficiently longer than an optical circle the intensity of a linearly polarized TEM wave can be described by Eq. 2.21. For a TEM wave with a wave vector direction perpendicular to a plain crystal surface the radiation pressure may be expressed by:

$$P_a = \frac{I_a}{c} \quad \text{and} \quad P_r = 2\frac{I_r}{c}. \quad (2.66)$$

where P_a is the radiation pressure due to absorbed photons and P_r the radiation pressure due to reflected photons. It should be noted that the intensity discussed in the context of the classical theory must consist of a discrete amount of photons, which may be expressed as $I = \frac{N_p \hbar \omega}{\Delta t A}$, where N_p is an integer and describes the amount of photons that cross the area A in a time span Δt . However, in cases where N_p is a large number, this effect can be neglected.

Considering quantum optics the fascinating experimental result has been reported that also interference effects for single photon experiments can be observed. A quite illustrative introduction to this topic is given by C. Braig et al. [BZKW03]. Following these experimental results it should be clarified that the intuition which may be build on the theory of Maxwell's equation, where we may think of electromagnetic radiation as continuous waves and describe interference as a superposition of waves is misleading. Instead, the underlying concept of the interference has been proven to be a kind of statistical process, which is in contradiction with observations of our macroscopically observable reality. Nevertheless, the interference effect which can be explained by quantum optics lead to the same result which have been derived by Eq. 2.41, considering a laser beam which consist of a enormous amount of photons.

In the experimental setup which is used in this work, and which will be discussed in detail in Section 5, electromagnetic radiation emitted by lasers will be used. This laser radiation may be approximated to be nearly monochromatic and the formulae of Section 2.1 can be used to describe the laser beam propagation. The fundamental principles of a laser will not be discussed further in this work. However, for the sake of completeness it should be mentioned that the underlying concept of a laser is strongly related to quantum mechanical concepts. For further information the interested reader is referred to [ST19, Chapter 13 and 14]. The detection of the laser intensity will be carried out with a photodiode in this work, however a detailed description of this detection principle will not be discussed in is work, but further information is given by [ST19, Chapter 18]. The underlying process in a photodiode is also a quantum effect, which describes the excitation of electrons by photons, resulting in a current/voltage which is measurable with an oscilloscope. However, this kind of measurement is related to different noise sources, which may also be referred to a quantum effect [ST19, p. 777]. Since the kind of noise is random the signal to noise ratio of a periodically repeating signal can be reduced by an averaging process, as it will be further discussed in Section 5. Also it should be mentioned that the ability of laser

radiation to generate an interference signal depends on coherence effects, which might have an impact on an interferometer measurement. However, as measurements presented in Section 5 will show, these effects may be neglected in good approximation in the context of this work. An introduction to the quite extended topic of optical coherence can be found in [ST19, Chapter 11].

3. Thermoelastic interaction of electromagnetic radiation with matter

When pulsed powerful electromagnetic radiation passes through a Bragg reflector a part of the pulse energy will be absorbed by electrons and a part of the absorbed energy will eventually be converted into heat. It may be assumed that the lattice thermalization mainly takes place in a time span of tens of picoseconds [YWW18] [RPJG⁺99] [WW17] [Maa18] [Rau21].

The rapid heating of the reflector causes thermal expansion. If the reflector is surrounded by vacuum, there is an absence of confinement in the direction normal to the surface. Therefore, considering Newton's third law, impulsively generated thermal stress subsequently drives a traveling compression/expansion wave, which is propagating inside the solid and will be reflected at the boundaries [TGMT86] [RPJG⁺99] [SMW⁺12] [YWW18]. The following chapter will provide the theoretical concepts to describe the propagation of such waves using a continuum theory and the assumptions of a local thermodynamic equilibrium.

3.1. Linear elasticity considering continuum mechanics

In this section a solid Bragg Reflector will be regarded as a continuum. A continuum may be regarded as a medium with a geometric configuration in the Euclidean space which exhibits continuous macroscopic properties. This assumption is suitable when the length scale of interest is large compared to the mean atomic distance ($\approx 1 \text{ \AA}$) [GM18, p. 145]. Further, it is assumed that neighboring atoms remain neighboring under the action of any loading conditions and no geometric discontinuities¹ in the solid are present.

Deformation An arbitrary deformation is illustrated in Fig. 3.1a for a two-dimensional geometry. Assuming that the initial and deformed shape of this geometry can be described in the same coordinate system, a mathematical relation which maps each point inside the geometry from an initial to the deformed shape is needed to describe the deformation of the geometry. For example choosing an arbitrary point inside the geometry as illustrated in Fig. 3.1a where the initial position of the point is located at \mathbf{r} and after the deformation it moved to \mathbf{r}' . The position change $\mathbf{r}' = \mathbf{r} + \mathbf{u}$ of the point is described by the displacement vector \mathbf{u} . The displacement vector is defined for every other arbitrary point inside the

¹Like cracks which can be regarded as an empty space inside the solid.

solid and thus the displacement vector field can be used to describe the deformation of the geometry. Of course this displacement vector field can be time dependent and therefore the displacement field can be used to describe the spatial and temporal change of a solid. It should also be noted that the introduced displacement field includes the description of translation and rotation of the entire geometry.

Infinitesimal strain tensor The displacement vector \mathbf{u} in a three-dimensional space is given by

$$\mathbf{u} = \begin{bmatrix} u \\ v \\ w \end{bmatrix} \equiv u_i, \text{ where } i = (1, 2, 3). \quad (3.1)$$

Considering elastic solids with large deformation as illustrated in Fig. 3.1a for a two dimensional case, the initial and deformed configurations can be significantly different and a line segment which was a straight line in the initial shape may now be curved. However, if a line element, much shorter than the radius of curvature of this curve is considered this will in good approximation still be a straight line in the deformed configuration. Using this assumptions the deformation of straight lines for a two-dimensional space is illustrated² in Fig. 3.1b. The illustrated change of the position in Fig. 3.1b shows a significant difference between the initial and the deformed position. Such deformations may be investigated in context of a finite strain theory [HY12]. However, the magnitude of the maximum displacements investigated in this work is in the nanometer range. Also, the change of the displacement considering geometrical scales on the micrometer range is in the picometer range, which gives the condition $\frac{\partial u_i}{\partial x_j} \ll 1$. Therefore, the approximation of infinitesimal strain theory can be used and the distinction between initial and deformed configurations can be dropped. The strain tensor under these circumstances may be expressed as [N⁺85, p. 105]:

$$\begin{aligned} \epsilon_{ij} &= \frac{1}{2} \left(\mathbf{u} \nabla + (\mathbf{u} \nabla)^T \right) \\ &= \begin{bmatrix} \frac{\partial u}{\partial x} & \frac{1}{2} \left(\frac{\partial u}{\partial y} + \frac{\partial v}{\partial x} \right) & \frac{1}{2} \left(\frac{\partial u}{\partial z} + \frac{\partial w}{\partial x} \right) \\ \frac{1}{2} \left(\frac{\partial v}{\partial x} + \frac{\partial u}{\partial y} \right) & \frac{\partial v}{\partial y} & \frac{1}{2} \left(\frac{\partial v}{\partial z} + \frac{\partial w}{\partial y} \right) \\ \frac{1}{2} \left(\frac{\partial w}{\partial x} + \frac{\partial u}{\partial z} \right) & \frac{1}{2} \left(\frac{\partial w}{\partial y} + \frac{\partial v}{\partial z} \right) & \frac{\partial w}{\partial z} \end{bmatrix} = \begin{bmatrix} \epsilon_{xx} & \epsilon_{xy} & \epsilon_{xz} \\ \epsilon_{yx} & \epsilon_{yy} & \epsilon_{yz} \\ \epsilon_{zx} & \epsilon_{yz} & \epsilon_{zz} \end{bmatrix}. \end{aligned} \quad (3.2)$$

The last two expressions are defined in Cartesian coordinates and for the calculation Eq. A.8 (Appendix A.1) has been used.

To understand the meaning of the normal and shear strain components in Eq. 3.2 it is helpful to consider the change of distances in the x - y plane given by the displacements of $u=u(x, y)$, $v=v(x, y)$ and $w=0$ as illustrated in Fig. 3.1b, in context of the condition $\frac{\partial u_i}{\partial x_j} \ll 1$. The normal strain in a given direction is defined as the change in length per

²This illustration does not refer directly to Fig. 3.1a. For such an illustration the distance change due to translation would be much bigger.

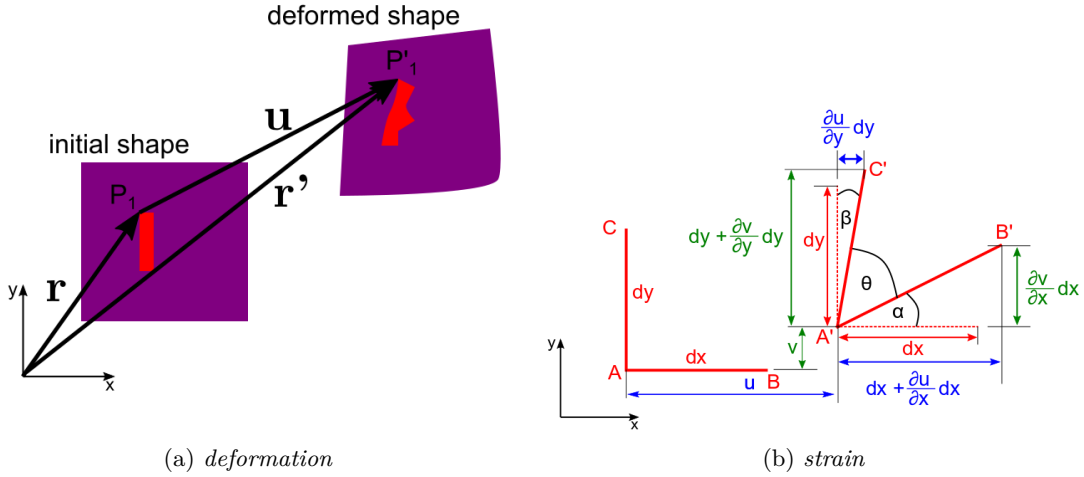


Figure 3.1.: Two-dimensional illustrations of (a) an arbitrary deformation and (b) the shearing and normal strain components.

unit length of a line which was originally oriented in a given direction. The normal strain is positive if the length of this line increases and negative if it decreases. Considering the change of length from the initial configuration ABC (Fig. 3.1b) to the deformed and translated configuration $A'B'C'$, the normal strain in x -direction can be derived by [Sad09, p. 35]:

$$\begin{aligned} \frac{A'B' - AB}{AB} &= \frac{A'B' - dx}{dx} = \frac{dx \sqrt{\left(1 + \frac{\partial u}{\partial x}\right)^2 + \left(\frac{\partial v}{\partial x}\right)^2} - dx}{dx} \\ &\approx \frac{dx \left(1 + \frac{\partial u}{\partial x}\right) - dx}{dx} = \frac{\partial u}{\partial x} = \epsilon_{xx}. \end{aligned} \quad (3.3)$$

Consistently with small deformation theory higher-order terms are neglected in the approximation of Eq. 3.3.

The shear strain is associated with two orthogonal directions and is defined as the change of the angle between two axes compared to an initial right angle. The sign of the shear strain depends on the coordinate system. Considering small deformations with $\alpha \approx \tan(\alpha)$ and $\beta \approx \tan(\beta)$ referring to Fig. 3.1b, the strain component is

$$\gamma_{xy} = \frac{\pi}{2} - \theta = \alpha + \beta \approx \frac{\frac{\partial v}{\partial x} dx}{dx + \frac{\partial u}{\partial x} dx} + \frac{\frac{\partial u}{\partial y} dy}{dy + \frac{\partial v}{\partial y} dy} \approx \frac{\partial v}{\partial x} + \frac{\partial u}{\partial y} \Rightarrow \epsilon_{xy} = \frac{1}{2} \gamma_{xy}. \quad (3.4)$$

Again in the approximation higher-order terms in the displacement gradients are neglected. The definition of the shear strain γ_{xy} Eq. 3.4 is called the engineering shear strain. However, the tensor formalism ϵ_{xy} of Eq. 3.2 is defined by one-half the angular change between orthogonal axes. Both definitions are commonly used and the factor of 2 is an endless source of confusion [Bow09, p. 24].

By considering a three-dimensional space all quantities of Eq. 3.2 can be derived with

similar geometrical considerations like the one in Fig. 3.1b [Sad09, p. 36].

Stress tensor Stress describes the internal forces in a solid. The unit of this quantity is force per area (N m^{-2}). A state of stress is given inside a solid body when one part exerts a force on a neighboring part. In a volume element two kinds of forces may occur. First, body forces, which act throughout the element having a magnitude proportional to the volume of the element. Secondly, forces exerted on the surface of the element, which are proportional to the area of the surface of the element. To give an illustrative example which is related to the context of this work the radiation pressure causes by absorption³ may be regarded as a kind of body force and the radiation pressure (Section 2.4) caused by reflection at a surface⁴ may be connected to a surface force.

In Fig. 3.2a the forces on the faces of a unit cube in a homogeneous⁵ stressed body are illustrated. The force transmitted across each face may be decomposed into three components. The indices of the stress tensor σ_{ij} denote the component of a force exerted by the material outside the cube upon the material inside in a direction j to a face of the cube which is perpendicular to direction i . For a homogeneous stress the forces on a opposite side of the faces illustrated in Fig. 3.2a must have the same magnitude and opposite direction. The components σ_{xx} , σ_{yy} and σ_{zz} are normal stresses the other elements of the tensor in Eq. 3.5 are shear stresses. The introduced sign convention gives a tensile stress for positive values of normal components and negative values give compressive stresses. The assumed statical equilibrium imposes the conditions $\sigma_{ij} = \sigma_{ji}$ to avoid a torque [GM18, p. 147]. This relation continues to hold even when the stress is inhomogeneously, when the body is not in statical equilibrium, and when body forces (but not body torques) are present [N⁺85, p. 87]. Defining the traction vector t_i^n , it can be proven that the components of stress σ_{ij} form a second rank tensor [N⁺85, p. 87]

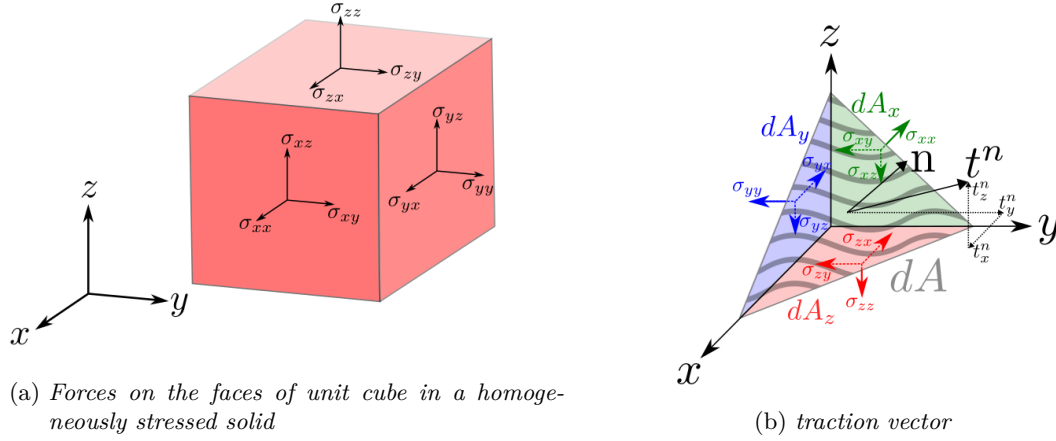
$$t_j^n = \sigma_{ij}n_i \quad \text{where} \quad \sigma_{ij} = \begin{bmatrix} \sigma_{xx} & \sigma_{xy} & \sigma_{xz} \\ \sigma_{yx} & \sigma_{yy} & \sigma_{yz} \\ \sigma_{zx} & \sigma_{yz} & \sigma_{zz} \end{bmatrix}. \quad (3.5)$$

The definition of the traction vector is illustrated in Fig. 3.2b. Selecting a small volume element with a part of its surface being dA within a stressed body and drawing its unit outer normal vector $\mathbf{n} = n_i$ perpendicular to dA , the force transmitted across the area can be denoted by $\mathbf{t}^n = d\mathbf{F}_r/dA$. The superscript n indicates the surface for which n_i is a unit normal vector and the reaction of the element under equilibrium condition to its surroundings is a force $d\mathbf{F}_r$ which acts on dA [HEG09, p. 2]. Choosing a small tetrahedron volume element as shown in Fig. 3.2 formed by three surfaces parallel to the coordinate planes and one inclined, the traction vector \mathbf{t}^n is defined by three components t_i^n along

³Considering a penetration depth sufficiently larger than the size of the element

⁴Considering an extinction length which is very short compared the dimensions of the element.

⁵A homogeneous stress is given, if the stress is homogeneous throughout the body, all part are in statical equilibrium, and no body-forces or body-torques are present [N⁺85, p. 82]



(a) Forces on the faces of unit cube in a homogeneously stressed solid

(b) traction vector

Figure 3.2.: (a) Forces on the faces of a unit cube in a homogeneously stressed solid. (b) Illustration of the traction vector.

the axes of the coordinate system. Noticing that $dA_i/dA = n_i$ [Bow09, p. 765] and when the height of the tetrahedron approaches zero, the balance of the forces acting on the element along the coordinate axes can be used to determine Eq. 3.5. It can be shown that the definition of traction is even valid for the case of non homogeneous stresses, when body forces are acting and when the body is not in statical equilibrium [N⁺85, p. 87] [HEG09, p. 3][N⁺85, p. 88].

With the previously defined quantities stress, strain and displacement it is possible to give a suitable description of an arbitrary point inside a solid considering small deformations. In three dimensions the displacement is given by a vector field, each point has a vector with three components. The strain at an arbitrary position is described by a tensor field, which can be calculated considering the infinitesimal changes of the displacement in each direction. The stress may be considered to be a measure for internal forces and is also given by a tensor field.

Constitutive law, stress-strain relations For an elastic deformation the strain is directly proportional to the stress. In this work only small deformations are considered and a linear elastic relation between stress and strain is assumed to be valid. Generally, a single crystal specimen is anisotropic. The relation between stress and strain using Einstein summation convention is [N⁺85, p. 132]

$$\begin{aligned}\sigma_{ij} &= C_{ijkl}\epsilon_{kl} \\ \epsilon_{kl} &= S_{klij}\sigma_{ij}.\end{aligned}\tag{3.6}$$

The elastic stiffness tensor C_{ijkl} and the compliance tensor S_{ijkl} are fourth-rank tensors that each have 81 components. The second-rank tensors in Eq. 3.6 are symmetric and therefore the elastic stiffness must have the following symmetries [Bow09, p. 77] [N⁺85, p. 131]:

$$C_{ijkl} = C_{klij} = C_{jikl} = C_{ijlk}.\tag{3.7}$$

This reduces the number of material constants to 21. The compliance tensor S_{ijkl} has the same symmetries as Eq. 3.7. Due to the symmetry of the tensors in Eq. 3.6 the stress-strain relations can be written in a more compact matrix form. Considering Cartesian coordinates and using the notation $1 \rightarrow xx$, $2 \rightarrow yy$, $3 \rightarrow zz$, $4 \rightarrow yz, zy$, $5 \rightarrow zx, xz$, $6 \rightarrow xy, yx$ (for example: $c_{11} \equiv C_{xxxx}$, $c_{12} \equiv C_{xxyy}$, $c_{66} \equiv C_{xyxy}$) the stiffness matrix \mathbf{C} and compliance matrix \mathbf{S} can be written as [Bow09, p. 78][GM18, p. 154][HNK] :

$$\begin{aligned} \boldsymbol{\sigma} &= \mathbf{C}\boldsymbol{\epsilon} \\ \boldsymbol{\epsilon} &= \mathbf{S}\boldsymbol{\sigma} \end{aligned} \quad (3.8)$$

$$\mathbf{C} = \begin{bmatrix} c_{11} & c_{12} & c_{13} & c_{14} & c_{15} & c_{16} \\ c_{12} & c_{22} & c_{23} & c_{24} & c_{25} & c_{26} \\ c_{13} & c_{23} & c_{33} & c_{34} & c_{35} & c_{36} \\ c_{14} & c_{24} & c_{34} & c_{44} & c_{45} & c_{46} \\ c_{15} & c_{25} & c_{35} & c_{45} & c_{55} & c_{56} \\ c_{16} & c_{26} & c_{36} & c_{46} & c_{56} & c_{66} \end{bmatrix} \quad \mathbf{S} = \begin{bmatrix} s_{11} & s_{12} & s_{13} & s_{14} & s_{15} & s_{16} \\ s_{12} & s_{22} & s_{23} & s_{24} & s_{25} & s_{26} \\ s_{13} & s_{23} & s_{33} & s_{34} & s_{35} & s_{36} \\ s_{14} & s_{24} & s_{34} & s_{44} & s_{45} & s_{46} \\ s_{15} & s_{25} & s_{35} & s_{45} & s_{55} & s_{56} \\ s_{16} & s_{26} & s_{36} & s_{46} & s_{56} & s_{66} \end{bmatrix}$$

$$\boldsymbol{\sigma} = \begin{bmatrix} \sigma_1 \\ \sigma_2 \\ \sigma_3 \\ \sigma_4 \\ \sigma_5 \\ \sigma_6 \end{bmatrix} \quad \boldsymbol{\epsilon} = \begin{bmatrix} \epsilon_1 \\ \epsilon_2 \\ \epsilon_3 \\ 2\epsilon_4 \\ 2\epsilon_5 \\ 2\epsilon_6 \end{bmatrix} .$$

Considering the symmetry of a cubic crystal it can be derived that only three independent⁶ elastic components exist and by choosing the basis vectors perpendicular to the symmetry planes as illustrated in Fig. 3.3, Eq. 3.8 can be written as [Bow09, p. 82][HNK]:

$$\mathbf{S} = \begin{bmatrix} s_{11} & s_{12} & s_{12} & 0 & 0 & 0 \\ s_{12} & s_{11} & s_{12} & 0 & 0 & 0 \\ s_{12} & s_{12} & s_{11} & 0 & 0 & 0 \\ 0 & 0 & 0 & s_{44} & 0 & 0 \\ 0 & 0 & 0 & 0 & s_{44} & 0 \\ 0 & 0 & 0 & 0 & 0 & s_{44} \end{bmatrix} \quad \mathbf{C} = \begin{bmatrix} c_{11} & c_{12} & c_{12} & 0 & 0 & 0 \\ c_{12} & c_{11} & c_{12} & 0 & 0 & 0 \\ c_{12} & c_{12} & c_{11} & 0 & 0 & 0 \\ 0 & 0 & 0 & c_{44} & 0 & 0 \\ 0 & 0 & 0 & 0 & c_{44} & 0 \\ 0 & 0 & 0 & 0 & 0 & c_{44} \end{bmatrix} . \quad (3.9)$$

It can be derived by using matrix inversion that the components of \mathbf{S} and \mathbf{C} in this case are related by [GM18, p. 156]

$$c_{44} = 1/s_{44}, \quad c_{11} - c_{12} = 1/(s_{11} - s_{12}), \quad c_{11} + 2c_{12} = 1/(s_{11} + 2s_{12}). \quad (3.10)$$

⁶The symmetry of the crystal causes comparing with Eq. 3.8 that $c_{11} = c_{22} = c_{33}$, $c_{44} = c_{55} = c_{66}$, $c_{12} = c_{13} = c_{23} = c_{21} = c_{31} = c_{32}$ and that the remaining components are zero [GM18, p. 156].

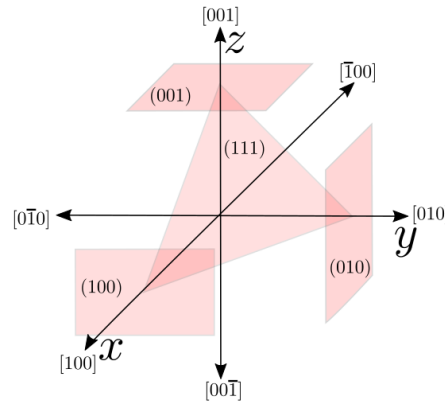


Figure 3.3.: Miller indices in a cubic crystal. By convention, the directions $[100]$, $[010]$, and $[001]$ are the x, y and z Cartesian coordinate axis.

It should be noted when solving a particular problem the orientation of a chosen coordinate system (x, y, z) relative to the boundaries of a solid (orientation of the lattice planes) could of course differ from the one chosen for the illustration in Fig. 3.3. In this case a transformation of the basis vectors can be carried out. However, it is important to notice that this transformation also changes the matrix components of Eq. 3.9. This elastic anisotropic effect considering a cubic crystal is discussed in the Appendix A.3.

Considering a single crystalline material elastic anisotropy has to be taken into account. However, for a polycrystalline material or in context of an approximation for particular single crystalline materials the elasticity may be considered to be isotropic. To describe the deformation of an elastic isotropic material it is common to used the following four technical material parameters [p. 160][GM18]:

- The Young's modulus E , which describes the relative change of a length $\Delta L/L$ in direction of a stress $\sigma = E\Delta L/L$.
- The Poisson's ratio $\nu = -\frac{\Delta D/D}{\Delta L/L}$, which is a measure for the change of length $\Delta D/D$ perpendicular to a direction of a stress, where the change of length in direction of the stress is $\Delta L/L$.
- The bulk modulus B gives the relation between a change in volume ΔV and a uniform stress on all sides of the solid (for example caused by a pressure P which has the same magnitude directed normal towards all sides of a cube with volume V):

$$P = -\sigma = -B\frac{\Delta V}{V}. \quad (3.11)$$

- The shear modulus gives the relation of shear stress σ and the resulting shear angle α_μ by: $\sigma = \mu\alpha_\mu$.

These four parameter are not independent of each other, since the following relations can

be derived [GM18, p. 160]:

$$\frac{1}{B} = \frac{3}{E}(1 - 2\nu), \quad \mu = \frac{E}{2(1 + \nu)}. \quad (3.12)$$

The matrices of Eq. 3.8, $\boldsymbol{\sigma} = \mathbf{C}\boldsymbol{\epsilon}$ and $\boldsymbol{\epsilon} = \mathbf{S}\boldsymbol{\sigma}$ can be written by using only two of the technical material parameters. Choosing the Young's modulus and the Poisson's ratio yields [Bow09, p. 70]:

$$\begin{aligned} \begin{bmatrix} \sigma_{xx} \\ \sigma_{yy} \\ \sigma_{zz} \\ \sigma_{xy} \\ \sigma_{yz} \\ \sigma_{xz} \end{bmatrix} &= \frac{E}{(1 + \nu)(1 - 2\nu)} \begin{bmatrix} 1 - \nu & \nu & \nu & 0 & 0 & 0 \\ \nu & 1 - \nu & \nu & 0 & 0 & 0 \\ \nu & \nu & 1 - \nu & 0 & 0 & 0 \\ 0 & 0 & 0 & \frac{1-2\nu}{2} & 0 & 0 \\ 0 & 0 & 0 & 0 & \frac{1-2\nu}{2} & 0 \\ 0 & 0 & 0 & 0 & 0 & \frac{1-2\nu}{2} \end{bmatrix} \begin{bmatrix} \epsilon_{xx} \\ \epsilon_{yy} \\ \epsilon_{zz} \\ 2\epsilon_{xy} \\ 2\epsilon_{yz} \\ 2\epsilon_{xz} \end{bmatrix} \\ \begin{bmatrix} \epsilon_{xx} \\ \epsilon_{yy} \\ \epsilon_{zz} \\ 2\epsilon_{xy} \\ 2\epsilon_{yz} \\ 2\epsilon_{xz} \end{bmatrix} &= \frac{1}{E} \begin{bmatrix} 1 & -\nu & -\nu & 0 & 0 & 0 \\ -\nu & 1 & -\nu & 0 & 0 & 0 \\ -\nu & -\nu & 1 & 0 & 0 & 0 \\ 0 & 0 & 0 & 2(1 + \nu) & 0 & 0 \\ 0 & 0 & 0 & 0 & 2(1 + \nu) & 0 \\ 0 & 0 & 0 & 0 & 0 & 2(1 + \nu) \end{bmatrix} \begin{bmatrix} \sigma_{xx} \\ \sigma_{yy} \\ \sigma_{zz} \\ \sigma_{xy} \\ \sigma_{yz} \\ \sigma_{xz} \end{bmatrix}. \end{aligned} \quad (3.13)$$

For the special case of an isotropic material which has a Poisson's ratio of approximately zero the elastic tensors are [Bow09, p. 71]

$$C_{ijkl} = \frac{E}{2}(\delta_{ik}\delta_{jl} + \delta_{il}\delta_{jk}) \quad \text{and} \quad S_{ijkl} = \frac{1}{2E}(\delta_{ik}\delta_{jl} + \delta_{il}\delta_{jk}). \quad (3.14)$$

where δ_{ij} is the Kronecker delta. The stress-strain relation given by Eq. 3.6 in this case becomes

$$\sigma_{ij} = E\epsilon_{ij} \quad \text{and} \quad \epsilon_{ij} = \frac{1}{E}\sigma_{ij}. \quad (3.15)$$

or in matrix form

$$\boldsymbol{\sigma} = E\boldsymbol{\epsilon} \quad \text{and} \quad \boldsymbol{\epsilon} = \frac{1}{E}\boldsymbol{\sigma}. \quad (3.16)$$

3.2. Thermodynamics of a solid crystal

A thermodynamic equilibrium occurs when the values of all the state variables, like strain, stress, temperature, velocity, entropy, and internal energy, are independent of time. Analyzing the thermoelastic behavior of a crystal and assuming the crystal possessing a center of symmetry⁷, the properties temperature T , entropy S , strain ϵ_{ij} and stress σ_{ij} may be described by reference to a equilibrium state. Starting with the first law of thermodynam-

⁷No piezo or pyroelectric effects have to be considered for a centrosymmetric structure of a single crystal diamond [HY07, p. 440] [N⁺85, p. 173]

ics and considering a unit volume, it is known that if a small amount of heat dQ flows into the crystal and a small amount of work dW is done on the crystal by external forces, the increase in the internal energy dU is a perfect differential $dU = dW + dQ$ [N⁺85, p. 175]. The work done per unit volume by a small change of the strain $d\epsilon_{ij}$ is given by $dW = \sigma_{ij}d\epsilon_{ij}$ [N⁺85, p. 136]. The second law of thermodynamics states that for a reversible change, it can be defined that $dQ = TdS$, where T is the absolute temperature (measured on the Kelvin scale), which yields

$$dU = dW + dQ = \sigma_{ij}d\epsilon_{ij} + TdS. \quad (3.17)$$

In Eq. 3.17 the strain ϵ_{ij} and entropy S are independent variables, which means the stress σ_{ij} and temperature T are determined when the quantities ϵ_{ij} and entropy S are given. The stress and temperature are called the depended variables in this context [N⁺85, p. 174]. If we want the stress and temperature to be the independent variables the function $\Phi_H = U - \sigma_{ij}\epsilon_{ij} - TS$ can be used. Differentiation gives $d\Phi_H = dU - \sigma_{ij}d\epsilon_{ij} - \epsilon_{ij}d\sigma_{ij} - SdT - TdS$ and using Eq. 3.17 yields:

$$d\Phi_H = -\epsilon_{ij}d\sigma_{ij} - SdT. \quad (3.18)$$

By the definition of Φ_H all quantities are function of σ_{ij} and T which gives

$$\left(\frac{\partial\Phi_H}{\partial\sigma_{ij}}\right)_T = -\epsilon_{ij} \quad \text{and} \quad \left(\frac{\partial\Phi_H}{\partial T}\right)_\sigma = -S. \quad (3.19)$$

Differentiating the first equation with respect to T and the second one with respect to σ_{ij} gives the Maxwell relation

$$-\frac{\partial^2\Phi_H}{\partial\sigma_{ij}\partial T} = \left(\frac{\partial\epsilon_{ij}}{\partial T}\right)_\sigma = \left(\frac{\partial S}{\partial\sigma_{ij}}\right)_T. \quad (3.20)$$

For a unit volume considering the independent variables σ_{ij} and T and the depended variables S and ϵ_{ij} it may be written [N⁺85, p. 174]:

$$\begin{aligned} d\epsilon_{ij} &= \left(\frac{\partial\epsilon_{ij}}{\partial\sigma_{kl}}\right)_T d\sigma_{kl} + \left(\frac{\partial\epsilon_{ij}}{\partial T}\right)_\sigma dT \\ dS &= \left(\frac{\partial S}{\partial\sigma_{kl}}\right)_T d\sigma_{kl} + \left(\frac{\partial S}{\partial T}\right)_\sigma dT. \end{aligned} \quad (3.21)$$

The relations occurring in Eq. 3.21 have physical meanings which can be connected to experimental measurable material properties. The elastic compliances tensor measured under isothermal (T is constant) conditions is

$$S_{ijkl}^T = \left(\frac{\partial\epsilon_{ij}}{\partial\sigma_{kl}}\right)_T. \quad (3.22)$$

The thermal expansion coefficient⁸ is given by

$$\alpha_{ij} = \left(\frac{\partial \epsilon_{ij}}{\partial T} \right)_{\sigma}. \quad (3.23)$$

The heat capacity per unit volume measured at constant stress is

$$C^{\sigma} = T \left(\frac{\partial S}{\partial T} \right)_{\sigma}, \quad (3.24)$$

which quantifies the heat developed when the temperature is changing, but the stress is held constant. The remaining relation $(\partial S / \partial \sigma_{kl})_T$ measures the entropy change caused by an isothermal stress change. Multiplied by T gives the produced heat when the crystal is isothermally stressed. From Eq. 3.20 it can be seen that this relation is also given by the thermal expansion coefficient $\alpha_{ij} = (\partial S / \partial \sigma_{kl})_T$.

If only small stress and temperature changes are considered a linear approximation may be used and integrating Eq. 3.21 gives

$$\begin{aligned} \epsilon_{ij} &= S_{ijkl}^T \sigma_{kl} + \alpha_{ij} \Delta T \\ \Delta S &= \alpha_{ij} \sigma_{ij} + (C^{\sigma} / T) \Delta T, \end{aligned} \quad (3.25)$$

where the material properties are assumed to have constant values and the strain ϵ_{ij} is taken to be zero when σ_{kl} and ΔT are zero. The temperature rise $\Delta T = T - T_0$ may be referred to an initial temperature rise T_0 and for $|\Delta T / T_0| \ll 1$ it may be used the approximation $T \approx T_0$, where T is the absolute temperature.

The Helmholtz free energy $\Phi_A = U - TS$ can be used to consider the temperature and strain as independent variables. Differentiating and using Eq. 3.17 gives

$$d\Phi_A = \sigma_{ij} d\epsilon_{ij} - S dT. \quad (3.26)$$

The Maxwell relation in this case yields

$$\left(\frac{\partial S}{\partial \epsilon_{ij}} \right)_T = - \left(\frac{\partial \sigma_{ij}}{\partial T} \right)_{\epsilon}. \quad (3.27)$$

For a unit volume considering the independent variables ϵ_{ij} and T and the depended

⁸There is no need to write α_{ij}^{σ} in this case, because the alternative coefficient $\alpha_{ij}^S = (\partial \epsilon_{ij} / \partial T)_S$ is meaningless, it would imply that each ϵ_{ij} is a function of T and S only, instead of a function of ten variables [N⁺85, p. 174].

variables σ_{ij} and S it may be written

$$\begin{aligned} d\sigma_{ij} &= \left(\frac{\partial \sigma_{ij}}{\partial \epsilon_{kl}} \right)_T d\epsilon_{kl} + \left(\frac{\partial \sigma_{ij}}{\partial T} \right)_\epsilon dT \\ dS &= \left(\frac{\partial S}{\partial \epsilon_{kl}} \right)_T d\epsilon_{kl} + \left(\frac{\partial S}{\partial T} \right)_\epsilon dT. \end{aligned} \quad (3.28)$$

The meaning of the relations in this case are the elastic stiffness tensor considering that the temperature is held constant:

$$C_{ijkl}^T = \left(\frac{\partial \sigma_{ij}}{\partial \epsilon_{kl}} \right)_T, \quad (3.29)$$

and the specific heat capacity per unit volume measured at constant strain

$$C^\epsilon = T \left(\frac{\partial S}{\partial T} \right)_\epsilon. \quad (3.30)$$

Also, it can be seen by using the Maxwell relation Eq. 3.27 that

$$\beta_{ij} = \left(\frac{\partial \sigma_{ij}}{\partial T} \right)_\epsilon = - \left(\frac{\partial S}{\partial \epsilon_{ij}} \right)_T. \quad (3.31)$$

Considering again small changes and a linear relation the integration of Eq. 3.28 gives

$$\begin{aligned} \sigma_{ij} &= C_{ijkl}^T \epsilon_{kl} + \beta_{ij} \Delta T \\ \Delta S &= -\beta_{ij} \epsilon_{ij} + (C^\epsilon / T) \Delta T, \end{aligned} \quad (3.32)$$

Considering Eq. 3.22 it can be seen that the relation given by Eq. 3.6 may give different values for a condition measured at constant temperature compared to a measurement at constant entropy. The relation between an adiabatically and an isothermally measured compliances tensor may be obtained by eliminating dT and putting $dS = 0$ in Eq. 3.21, which yields:

$$d\epsilon_{ij} = \left(\frac{\partial \epsilon_{ij}}{\partial \sigma_{kl}} \right)_T d\sigma_{kl} - \left(\frac{\partial \epsilon_{ij}}{\partial T} \right)_\sigma \left(\frac{\partial S}{\partial \sigma_{kl}} \right)_T d\sigma_{kl} / \left(\frac{\partial S}{\partial T} \right)_\sigma \quad (S \text{ is constant}). \quad (3.33)$$

Dividing by $d\sigma_{kl}$ gives:

$$\left(\frac{\partial \epsilon_{ij}}{\partial \sigma_{kl}} \right)_S - \left(\frac{\partial \epsilon_{ij}}{\partial \sigma_{kl}} \right)_T = - \left(\frac{\partial \epsilon_{ij}}{\partial T} \right)_\sigma \left(\frac{\partial S}{\partial \sigma_{kl}} \right)_T \left(\frac{\partial T}{\partial S} \right)_\sigma, \quad (3.34)$$

which may be written by considering Eq. 3.22, Eq. 3.23, Eq. 3.20 and Eq. 3.24 as:

$$S_{ijkl}^S - S_{ijkl}^T = -\alpha_{ij} \alpha_{kl} \frac{T}{C^\sigma}. \quad (3.35)$$

To investigate the difference between the heat capacity measured at constant entropy compared to a measurement at constant temperature, elimination of $d\sigma_{kl}$ and considering $d\epsilon_{kl} = 0$ in Eq. 3.21 can be used to obtain⁹:

$$C^\epsilon - C^\sigma = -T\alpha_{ij}\alpha_{kl}C_{klij}^T \quad (3.36)$$

The introduced material properties are not independent of each other and indeed the three tensors S_{ijkl}^T , α_{ij} and C^σ/T are sufficient to describe all first order thermoelastic effects [N⁺85, p. 177]. Assuming that the values on the right hand side of Eq. 3.35 and Eq. 3.36 are sufficiently small the approximation $C = C^\epsilon - C^\sigma$ and $S_{ijkl} = S_{ijkl}^S - S_{ijkl}^T$ may be used.

Due to the symmetry of the strain tensor $\epsilon_{ij} = \epsilon_{ji}$, the thermal expansion tensor should also be symmetric $\alpha_{ij} = \alpha_{ji}$, and for a cubic crystal like diamond it is also isotropic $\alpha_{ij} = \alpha\delta_{ij}$ [N⁺85, p. 107].

For an approximately isotropic elastic crystal where the Poisson's ratio can be neglected as expressed by Eq. 3.15 gives in this case by considering Eq. 3.25

$$\begin{aligned} \epsilon_{ij} &= \frac{1}{E}\sigma_{ij} + \alpha\delta_{ij}\Delta T \\ \Delta S &= \alpha\delta_{ij}\sigma_{ij} + (C/T)\Delta T, \end{aligned} \quad (3.37)$$

and for Eq. 3.32:

$$\begin{aligned} \sigma_{ij} &= E\epsilon_{ij} + \beta_{ij}\Delta T \\ \Delta S &= -\beta_{ij}\epsilon_{ij} + (C/T)\Delta T, \end{aligned} \quad (3.38)$$

Rearranging the first equation in Eq. 3.37 yields $\epsilon_{ij} = (1/E)(\sigma_{ij} - \beta_{ij}\Delta T)$, comparing with Eq. 3.38 it can be seen that for this case the following relation can be obtained

$$\beta_{ij} = -\alpha\delta_{ij}E, \quad (3.39)$$

which causes:

$$\sigma_{ij} = E(\epsilon_{ij} - \alpha\Delta T\delta_{ij}), \quad \text{where } \Delta T = T - T_0. \quad (3.40)$$

Considering the derived equation it may be useful to define different kinds of strain quantities. In the context of this work $\epsilon_{ij}^{el} = \epsilon_{ij} - \alpha\Delta T\delta_{ij}$ will be called the elastic strain and $\epsilon_{ij}^{th} = \alpha\Delta T\delta_{ij}$ the thermal strain. Considering Eq. 3.40 the total strain is given by $\epsilon_{ij} = \epsilon_{ij}^{el} + \epsilon_{ij}^{th}$.

The relation Eq. 3.40 will mainly be used in the context of this work to investigate thermoelastic interactions. However, similar relations may also be used for an anisotropic

⁹Using the relation $\left(\frac{\partial S}{\partial T}\right)_\epsilon - \left(\frac{\partial S}{\partial T}\right)_\sigma = -\left(\frac{\partial S}{\partial \sigma_{kl}}\right)_T \left(\frac{\partial \epsilon_{ij}}{\partial T}\right)_\sigma \left(\frac{\partial \sigma_{kl}}{\partial \epsilon_{ij}}\right)_T$, Eq. 3.29, Eq. 3.23, Eq. 3.24, Eq. 3.30 and Eq. 3.20.

solid [Bow09, p. 76]:

$$\begin{aligned}\sigma_{ij} &= C_{ijkl}[\epsilon_{kl} - \alpha_{kl}\Delta T], \text{ where } \epsilon_{kl} = \epsilon_{kl}^{el} + \epsilon_{kl}^{th} \text{ and } \Delta T = T - T_0, \\ \epsilon_{kl} &= S_{klij}\sigma_{ij} + \alpha_{kl}\Delta T.\end{aligned}\quad (3.41)$$

Considering thermal expansion the matrix equations given in Eq. 3.8 may be extended to $\boldsymbol{\sigma} = \mathbf{C}(\boldsymbol{\epsilon} - \boldsymbol{\alpha}\Delta T)$ and $\boldsymbol{\epsilon} = \mathbf{S}\boldsymbol{\sigma} + \boldsymbol{\alpha}\Delta T$ and for an isotropic solid with Young's modulus E and Poisson's ration ν it can be written [Bow09, p. 70]:

$$\begin{bmatrix} \sigma_{xx} \\ \sigma_{yy} \\ \sigma_{zz} \\ \sigma_{xy} \\ \sigma_{yz} \\ \sigma_{xz} \end{bmatrix} = \frac{E}{(1+\nu)(1-2\nu)} \begin{bmatrix} 1-\nu & \nu & \nu & 0 & 0 & 0 \\ \nu & 1-\nu & \nu & 0 & 0 & 0 \\ \nu & \nu & 1-\nu & 0 & 0 & 0 \\ 0 & 0 & 0 & \frac{1-2\nu}{2} & 0 & 0 \\ 0 & 0 & 0 & 0 & \frac{1-2\nu}{2} & 0 \\ 0 & 0 & 0 & 0 & 0 & \frac{1-2\nu}{2} \end{bmatrix} \begin{bmatrix} \epsilon_{xx} \\ \epsilon_{yy} \\ \epsilon_{zz} \\ 2\epsilon_{xy} \\ 2\epsilon_{yz} \\ 2\epsilon_{xz} \end{bmatrix} - \frac{E\alpha\Delta T}{1-2\nu} \begin{bmatrix} 1 \\ 1 \\ 1 \\ 0 \\ 0 \\ 0 \end{bmatrix}\quad (3.42)$$

$$\begin{bmatrix} \epsilon_{xx} \\ \epsilon_{yy} \\ \epsilon_{zz} \\ 2\epsilon_{xy} \\ 2\epsilon_{yz} \\ 2\epsilon_{xz} \end{bmatrix} = \frac{1}{E} \begin{bmatrix} 1 & -\nu & -\nu & 0 & 0 & 0 \\ -\nu & 1 & -\nu & 0 & 0 & 0 \\ -\nu & -\nu & 1 & 0 & 0 & 0 \\ 0 & 0 & 0 & 2(1+\nu) & 0 & 0 \\ 0 & 0 & 0 & 0 & 2(1+\nu) & 0 \\ 0 & 0 & 0 & 0 & 0 & 2(1+\nu) \end{bmatrix} \begin{bmatrix} \sigma_{xx} \\ \sigma_{yy} \\ \sigma_{zz} \\ \sigma_{xy} \\ \sigma_{yz} \\ \sigma_{xz} \end{bmatrix} + \alpha\Delta T \begin{bmatrix} 1 \\ 1 \\ 1 \\ 0 \\ 0 \\ 0 \end{bmatrix}.$$

Using index notation Eq. 3.42 can be written as [Bow09, p. 71]:

$$\epsilon_{ij} = \frac{1+\nu}{E}\sigma_{ij} - \frac{\nu}{E}\sigma_{kk}\delta_{ij} + \alpha\Delta T\delta_{ij}\quad (3.43)$$

$$\sigma_{ij} = \frac{E}{1+\nu} \left(\epsilon_{ij} + \frac{\nu}{1-2\nu}\epsilon_{kk}\delta_{ij} \right) - \frac{E\alpha\Delta T}{1-2\nu}\delta_{ij}\quad (3.44)$$

Relation of stress-pressure and strain-volume for a crystal with cubic lattice structure Using Cartesian coordinates and considering a macroscopic crystal in context of the infinitesimal strain approximation (see Section 3.1) the volume change ΔV of a unit cube with volume V is given by the dilation δ_V [GM18, p. 154]:

$$\delta_V = \Delta V/V = \epsilon_{xx} + \epsilon_{yy} + \epsilon_{zz}.\quad (3.45)$$

If cubic elastic properties are considered, which are given by Eq. 3.9 and the unit cube is experiencing a pressure P with equal magnitude from all sides so that the stress is given by $\sigma_{ij} = -P\delta_{ij}$ and causes a deformation with strains $\epsilon_{xx} = \epsilon_{yy} = \epsilon_{zz}$, the dilation is $\frac{1}{3}\delta_V = \epsilon_{xx} = \epsilon_{yy} = \epsilon_{zz}$. As mentioned before (Eq. 3.11) the bulk modulus may be defined by

$$B = -P\frac{V}{\Delta V}.\quad (3.46)$$

Considering the stress-strain relation Eq. 3.8 for a cubic crystal Eq. 3.9 it can be obtained for this case:

$$\begin{aligned} \epsilon_{xx} = -P(s_{11} + 2s_{12}), \quad \epsilon_{yy} = -P(s_{11} + 2s_{12}), \quad \epsilon_{zz} = -P(s_{11} + 2s_{12}) \quad \text{and} \quad (3.47) \\ -P = \epsilon_{xx}(c_{11} + 2c_{12}), \quad -P = \epsilon_{yy}(c_{11} + 2c_{12}), \quad -P = \epsilon_{zz}(c_{11} + 2c_{12}), \end{aligned}$$

which yields considering Eq. 3.46:

$$B = \frac{1}{3(s_{11} + 2s_{12})} = \frac{1}{3}(c_{11} + 2c_{12}) \quad (3.48)$$

For deformations which are isentropic ($dS = 0$) or at $T = 0$ ($TdS = 0$) the first law of thermodynamics Eq. 3.17 yields in this case:

$$dU = \sigma_{ii}d\epsilon_{ii} = -P\frac{dV}{V} \quad (3.49)$$

Considering the internal energy $\tilde{U} = UV$ instead of the internal energy per unit volume and rewriting Eq. 3.49 gives

$$P = -\frac{d\tilde{U}}{dV}. \quad (3.50)$$

The bulk modulus¹⁰ B which is a measure of how resistant a crystal is to compression may be defined by:

$$B = -V\frac{\partial P}{\partial V} \quad (3.51)$$

Inserting Eq. 3.50 into Eq. 3.51 gives:

$$B = -V\frac{\partial^2 \tilde{U}}{\partial V^2} \quad (3.52)$$

3.3. Heat conduction

The time dependent deformation of a crystal is connected to a change of the heat content of the solid and therefore causes a temperature changes. Controversy a temporal changing temperature field in the crystal causes a dynamic thermal expansion. These coupled effects are investigated in the context of a thermoelasticity theory [Now13, p. 1].

In the previous section it has been assumed that the thermodynamic properties are describable by reference to changes which are reversible. However, to investigate heat conduction and a time dependent thermoelastic problem, irreversible processes considering the second law of thermodynamics have to be taken into account. Using the laws of thermodynamics and considering small deformations, the following equation for an anisotropic solid can be derived, using Cartesian coordinates and the notation presented

¹⁰The bulk modulus is related to the parameter compressibility by $\kappa = -(1/V)(\partial V/\partial P)$ by $\kappa = 1/B$.

in Appendix A.1 [Tak79][HEG09, p. 63]:

$$(\lambda_{c_{ij}} T_{,j})_{,i} = T \beta_{ij} \epsilon_{ij} + c^\epsilon \rho \dot{T} - Q_{ext} \quad \text{where } T = T_0 + \Delta T \quad \text{and } \beta_{ij} = \alpha_{ij} C_{ijkl}, \quad (3.53)$$

where α_{ij} is the thermal expansion tensor, C_{ijkl} elastic stiffness tensor, ρ the mass density, c^ϵ the specific heat capacity per unit mass measured at constant strain and Q_{ext} is the heat produced per unit time and unit volume, which may be connected to the adsorbed and into heat converted energy, introduced by the electromagnetic radiation of a laser.

A detailed derivation of Eq. 3.53 considering small deformations of an isotropic crystal can be found in the first chapter of [Now13]. The derivation of this formula will be summarized in the following part of this section, it is based on a time dependent form of the energy conservation equation (first law to thermodynamics), which can be used to derive an expression for a local entropy balance [Now13, p. 5]

$$\dot{\Delta} S T = Q_{ext} - q_{i,i}^h \quad \text{where } T = T_0 + \Delta T. \quad (3.54)$$

Here $\dot{\Delta} S$ is the entropy production per unit volume and unit time. Conductive heat transfer in a solid can be understood as the heat transfer from places with higher temperature to places with lower temperature. This kind of process is irreversible and connected with an entropy production which may be described by Eq. 3.54 [Now13, p. 11]. The heat flux vector per unit area q_i^h may be described with the empirical Fourier law

$$q_i^h = -\lambda_{c_{ij}} \Delta T_{,j}. \quad (3.55)$$

Here $\lambda_{c_{ij}}$ is the coefficient of thermal conduction, which may be anisotropic. For an isotropic case the Fourier law is $q_i^h = -\lambda_c \Delta T_{,j}$, with $\lambda_c > 0$. It can be shown that the Fourier law satisfies the second law of thermodynamics (Clausius–Duhem inequality) [Now13, p. 6].

Considering the Helmholtz free energy for a small temperature increases ($|\Delta T/T_0| \ll 1$) and a material with isotropic elastic properties with Poisson's ratio ν and Young's modulus E it can be derived [Now13, p. 10]:

$$\Delta S = \left(\frac{E}{1-2\nu} \right) \alpha \epsilon_{ii} + (c^\epsilon \rho / T_0) \Delta T. \quad (3.56)$$

Inserting Eq. 3.56 into Eq. 3.54 and using the Fourier law Eq. 3.55 yields:

$$(\lambda_{c_{ij}} \Delta T_{,j})_{,i} = T \left(\left(\frac{E}{1-2\nu} \right) \alpha \epsilon_{ii} + \frac{c^\epsilon \rho}{T_0} \Delta T \right) - Q_{ext} \quad \text{where } T = T_0 + \Delta T \quad (3.57)$$

Noting that one of the assumptions for the derivation of this equation was $|\Delta T/T_0| \ll 1$ it is reasonable to linearize the second term on the right-hand side of 3.57 which yields

$$(\lambda_{c_{ij}} \Delta T_{,j})_{,i} = \left(\frac{E}{1-2\nu} \right) T \alpha \epsilon_{ii} + c^\epsilon \rho \dot{\Delta} T - Q_{ext}. \quad (3.58)$$

3.4. Equation of motion

The equation of motion based on the assumptions of Newton's law ($\mathbf{F}=\mathbf{ma}$) may be expressed in Cartesian coordinates by¹¹:

$$\sigma_{ij,j} + F_i = \rho \ddot{u}_i \quad (3.59)$$

where F_i are the components of a body force per unit volume and ρ is the mass density. Writing Eq. 3.59 in matrix form yields [Bow09, p. 49]

$$\nabla \cdot \boldsymbol{\sigma} + \mathbf{F} = \rho \ddot{\mathbf{u}}, \quad (3.60)$$

which may also be written as (see Appendix A.1 Eq. A.11)

$$\begin{aligned} \frac{\partial \sigma_{xx}}{\partial x} + \frac{\partial \sigma_{yx}}{\partial y} + \frac{\partial \sigma_{zx}}{\partial z} + F_x &= \ddot{u}_x \\ \frac{\partial \sigma_{xy}}{\partial x} + \frac{\partial \sigma_{yy}}{\partial y} + \frac{\partial \sigma_{zy}}{\partial z} + F_y &= \ddot{u}_y \\ \frac{\partial \sigma_{xz}}{\partial x} + \frac{\partial \sigma_{yz}}{\partial y} + \frac{\partial \sigma_{zz}}{\partial z} + F_z &= \ddot{u}_z \end{aligned} \quad (3.61)$$

Considering an elastic isotropic material with Poisson's ratio $\nu = 0$ expressed by Eq. 3.40 yields:

$$(E\epsilon_{ij} - E\alpha\Delta T\delta_{ij})_{,j} + F_i - \rho \frac{\partial^2 u_i}{\partial t^2} = 0 \quad (3.62)$$

The kinetic energy per unit volume of the solid under the action of surface and body forces is [HEG09, p. 58]:

$$K = \frac{1}{2} \rho \dot{u}_i \dot{u}_i \quad (3.63)$$

Speed of sound in an elastic isotropic solid Considering the propagation of a displacement wave in an elastic isotropic solid different types of waves, which possess a characteristic propagation speed may be classified and derived from the equation of motion. Considering a semi-infinite half-space which is initially at rest and experiences a time varying, spatially uniform pressure in direction normal to the surface it can be derived that a longitudinal wave (also called P-wave) is propagating with the speed v_L through the solid [Bow09, p. 241]:

$$v_L = \sqrt{\frac{E(1-\nu)}{\rho(1+\nu)(1-2\nu)}}. \quad (3.64)$$

Here ρ is the mass density, E is the value of the Young's modulus and ν the value of the Poisson's ratio. For a solid with a Poisson's ratio of nearly zero $\nu \approx 0$ Eq. 3.64 may be written as:

$$v_B = \sqrt{\frac{E}{\rho}} = \sqrt{\frac{3B}{\rho}}, \quad (3.65)$$

¹¹A derivation is given in Appendix A.2.

where B is the value to the bulk modulus (Eq. 3.12).

If a solid with semi-infinite half-space is initial in rest and is experiencing and time varying, spatial uniform anti-plane shear traction it can be derived that a transverse wave (also called shear wave or S-wave) is propagating with the speed v_T through the solid [Bow09, p. 241]:

$$v_T = \sqrt{\frac{E}{2(1+\nu)\rho}} \quad (3.66)$$

For the sake of completeness it should also be mentioned that considering a three-dimensional wave propagation there exist additional types of waves like Rayleigh waves [Bow09, p. 333], which travel near the surface. However, an analytical expression for such wave types will not be further discussed in the context of this work.

3.5. Thermoelastic axisymmetric assumption for isotropic material

In this section an elastic isotropic material, which is experiencing a radial, axial symmetric heat load will be discussed, by using cylindrical coordinates (Appendix A.1). The displacement in direction $\hat{\theta}$ is assumed to be zero in this case and the displacement vector is given by $\mathbf{u} = u\hat{\rho}_r + w\hat{\mathbf{z}}$. The benefit of these axisymmetric assumptions is that it reduces a three-dimensional problem into a two-dimensional problem, which is a great improvement for the calculation time regarding numerical solutions. Writing the infinitesimal strain tensor of Eq. 3.2 in cylindrical coordinates¹² it can be seen that the only non-zero strain components for this case are:

$$\epsilon_{\rho_r\rho_r} = \frac{\partial u}{\partial \rho_r} \quad \epsilon_{\theta\theta} = \frac{u}{\rho_r} \quad \epsilon_{zz} = \frac{\partial w}{\partial z} \quad \epsilon_{\rho_r z} = \frac{1}{2} \left(\frac{\partial u}{\partial z} + \frac{\partial w}{\partial \rho_r} \right). \quad (3.67)$$

The normal strains $\epsilon_{\rho_r\rho_r}$ and ϵ_{zz} , as well as the shear strain $\epsilon_{\rho_r z}$ have similar geometrical meanings as the strain given by Eq. 3.3 and Eq. 3.4. However, the strain $\epsilon_{\theta\theta}$ which may be referred to a hoop strain was not present in Cartesian coordinates. To give a phenomenological interpretation for this strain value the illustration in Fig. 3.4 may be helpful. In can be seen from this visualization that even if $u_1 = u_2$, which causes $\epsilon_{\rho_r\rho_r} = 0$, there is still a strain introduced in the direction $\hat{\theta}$.

The stress-strain relation for an isotropic material can be used without modification in cylindrical coordinates, as long as the matrices of Cartesian components of the various tensors are replaced by their equivalent matrices in cylindrical-polar coordinates [Bow09,

¹²Using Eq. A.9 of Appendix A.1.

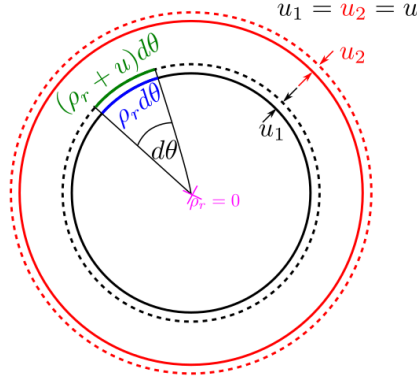


Figure 3.4.: For the Illustrated case the displacement in the radial direction is zero. However, the hoop strain $\epsilon_{\theta\theta} = \frac{(\rho_r+u)d\theta}{\rho_r d\theta} = \frac{u}{\rho_r}$ is non-zero.

p. 761]. Thus, if an isotropic material is considered, Eq. 3.42 can be rewritten as:

$$\begin{bmatrix} \sigma_{\rho_r\rho_r} \\ \sigma_{\theta\theta} \\ \sigma_{zz} \\ \sigma_{\rho_r z} \end{bmatrix} = \frac{E}{(1+\nu)(1-2\nu)} \begin{bmatrix} 1-\nu & \nu & \nu & 0 \\ \nu & 1-\nu & \nu & 0 \\ \nu & \nu & 1-\nu & 0 \\ 0 & 0 & 0 & \frac{1-2\nu}{2} \end{bmatrix} \begin{bmatrix} \epsilon_{\rho_r\rho_r} \\ \epsilon_{\theta\theta} \\ \epsilon_{zz} \\ 2\epsilon_{\rho_r z} \end{bmatrix} - \frac{E\alpha\Delta T}{1-2\nu} \begin{bmatrix} 1 \\ 1 \\ 1 \\ 0 \end{bmatrix} \quad (3.68)$$

$$\begin{bmatrix} \epsilon_{\rho_r\rho_r} \\ \epsilon_{\theta\theta} \\ \epsilon_{zz} \\ 2\epsilon_{\rho_r z} \end{bmatrix} = \frac{1}{E} \begin{bmatrix} 1 & -\nu & -\nu & 0 \\ -\nu & 1 & -\nu & 0 \\ -\nu & -\nu & 1 & 0 \\ 0 & 0 & 0 & 2(1+\nu) \end{bmatrix} \begin{bmatrix} \sigma_{\rho_r\rho_r} \\ \sigma_{\theta\theta} \\ \sigma_{zz} \\ \sigma_{\rho_r z} \end{bmatrix} + \alpha\Delta T \begin{bmatrix} 1 \\ 1 \\ 1 \\ 0 \end{bmatrix}$$

Using index notation and considering a Poisson's ratio of zero $\nu = 0$ Eq. 3.68 becomes

$$\sigma_{ij} = E\epsilon_{ij} - E\alpha\Delta T\delta_{ij}, \quad \epsilon_{ij} = \frac{1}{E}\sigma_{ij} + \alpha\Delta T\delta_{ij}, \quad \text{where } i = (r, \theta, z), \quad j = (r, \theta, z). \quad (3.69)$$

Here δ_{ij} is the Kronecker delta.

Writing out the equation of motion Eq. 3.60 in cylindrical coordinates by (using Eq. A.13 Appendix A.1) and taking only the none zero stress components of Eq. 3.68 into account yields:

$$\begin{aligned} \frac{\partial\sigma_{\rho_r\rho_r}}{\partial\rho_r} + \frac{\partial\sigma_{\rho_r z}}{\partial z} + \frac{1}{\rho_r}(\sigma_{\rho_r\rho_r} - \sigma_{\theta\theta}) + F_{\rho_r} &= \rho\ddot{u} \\ \frac{\partial\sigma_{\rho_r z}}{\partial\rho_r} + \frac{\partial\sigma_{zz}}{\partial z} + \frac{1}{\rho_r}\sigma_{\rho_r z} + F_z &= \rho\ddot{w}. \end{aligned} \quad (3.70)$$

As mentioned before the total strain $\epsilon_{ij} = \epsilon_{ij}^{el} + \epsilon_{ij}^{th}$ may be separated into an elastic strain ϵ_{ij}^{el} and a thermal strain component ϵ_{ij}^{th} , which for the case of an elastic isotropic material with a Poisson's ratio of zero is given by

$$\epsilon_{ij}^{el} = \frac{1}{E}\sigma_{ij} = \epsilon_{ij} - \alpha\Delta T\delta_{ij} \quad \text{and} \quad \epsilon_{ij}^{th} = \alpha\Delta T\delta_{ij}. \quad (3.71)$$

Considering an isotropic material where an elastic deformation takes place, the stored strain energy density defined as the work done per unit volume to deform a material from a stress free reference state to a loaded state is given by [Bow09, p. 76]

$$U_{el} = \frac{1}{2} \sigma_{ij} \epsilon_{ij}^{el} \quad (3.72)$$

and for the case of an elastic isotropic material with a Poisson's ratio of zero this gives

$$U_{el} = \frac{E}{2} \epsilon_{ij}^{el} \epsilon_{ij}^{el} = \frac{E}{2} (\epsilon_{rr} - \alpha \Delta T)^2 + \frac{E}{2} (\epsilon_{\theta\theta} - \alpha \Delta T)^2 + \frac{E}{2} (\epsilon_{zz} - \alpha \Delta T)^2 + \frac{E}{2} \epsilon_{rz}^2. \quad (3.73)$$

If heat dissipation is neglected U_{el} is stored as recoverable strain energy in the solid.

Considering an axisymmetric heat load and assuming the Fourier heat law (Eq. 3.55) to be valid, the heat transfer in the crystal described by Eq. 3.58 may be written, by assuming that for thermal conductivity only diagonal terms of $\lambda_{c_{ij}}$ are non-zero, in cylindrical coordinates (Eq. A.5 and Eq. A.7 Appendix A.1) as:

$$\frac{1}{\rho_r} \frac{\partial}{\partial \rho_r} \left(\rho_r \lambda_{\rho_r \rho_r} \frac{\partial \Delta T}{\partial \rho_r} \right) + \frac{\partial}{\partial z} \left(\lambda_{zz} \frac{\partial \Delta T}{\partial z} \right) = T \alpha \left(\frac{E}{1 - 2\nu} \right) (\epsilon_{\rho_r \rho_r} + \epsilon_{\theta\theta} + \epsilon_{zz}) + C^\epsilon \dot{\Delta T} - Q_{ext}. \quad (3.74)$$

To investigate a thermodynamic problem the coupled partial differential equations Eq. 3.61 and Eq. 3.53 have to be solved (or for an axisymmetric case with elastic isotropic material Eq. 3.70 and Eq. 3.74). However, depending of the kind of experiment, which is investigated, cases exist where the effect of the deformation on the temperature field are such small that they may be neglected. In this case the first term on the right-hand side of Eq. 3.53 (Eq. 3.74) can be neglected which decouples the equations and allows to first solve the temperature field and use the solution to solve the displacement field afterwards.

3.6. From classical thermodynamic theory to modern solid state physics

All thermoelastic formulae derived in the previous sections are based on the assumption that at least a local thermodynamic equilibrium exists, so that a meaningful local temperature value can be defined for each time step investigated for a thermoelastic problem. It is one main topic of this work to investigate if these assumptions can be used for a cryogenically cooled diamond Bragg reflector, by comparing experimental data with simulations based on the described theory of thermoelasticity.

The first and second law of thermodynamics which have been considered in the previous section are based on formulae which were historically derived by considering experiments

in the context of classical physics. In this context the work of James Prescott Joule (1818-1889) may be mentioned who discovered the relation between work and heat [Mes10, p. 252] which led to the development of the first law of thermodynamics. The formulation of the second law maybe refereed to Rudolf Julius Emanuel Clausius (1822-1888) connected to his restatement of the Carnot-Prozess. He also considered a kinetic theory of gases, which may be seen as a microscopic explanation for effects described by a thermodynamic theory [Lau57]. Ludwig Boltzmann (1844-1906) gave a statistical explanation of the second law of thermodynamics considering kinetic theory of gases. In context of this theory temperature may be considers as a measure of the average kinetic energy [Mes10, p. 253] of microscopic particles inside a macroscopic¹³ volume.

However, these theoretical concepts were developed by Boltzmann before the discovery of the quantum effects in physics. Historically, the work of Albert Einstein (1879-1955) regarding the temperature dependent heat capacity may be considered to be a beginning point for a theory describing thermodynamics in the context of a statistical theory including quantum effects. The result of this work will be introduced in the next section.

Erwin Schrödinger (1887-1961), may be named as one of many contributors for a quantum-mechanical theory. With the help of the Schrödinger equation a single crystalline material consisting of a periodic structure made of atoms¹⁴ may be described by a wave function of a quantum-mechanical system. From a quite modern perceptive *ab initio* (from first principles) methods may be considered to be a state of the art theory for describing thermodynamic properties of a crystal. In context of an *ab initio* method, a solution for a Schrödinger equation of crystal system can be calculated. However, it should be clarified that the historical steps which lead to a modern quantum-mechanical theory are quite extensive an will not be discussed further in this work.

Also this section should not be interpreted as a complete historical review reading the development of thermodynamics in context of modern physics. This section is just an attempt to clarify which underlying concepts are considered in the context of this work and how the century of their foundation may be historically classified.

As it will be discussed in detail in Section 7 the derivations of thermodynamic properties¹⁵ in the context of solid state physics (Section 4) are very useful to evaluate under which circumstances the formulae introduced in Section 3 are based on valid assumptions.

¹³Macroscopic may be connected in this context to a volume which is sufficiently big such that many particles are inside the volume so that a meaningful average value can be defined.

¹⁴Which may be approximated to consist of nuclei and electrons.

¹⁵Like the heat capacity, thermal conductivity and thermal expansion coefficient

4. Material properties of diamond

A Bragg reflector made of single crystalline diamond is investigated in this work. Diamond is composed of the single element carbon. The microscopic structure of diamond can be determined directly with the help of transmission electron microscopy [Har18] and is also observable in the diffraction pattern of X-rays. The knowledge of the micro structure can be used to develop theoretical concepts that describe the macroscopic material constants that have been introduced in Section 3.2 in the context of thermodynamics. On the other hand material constants can be measured with a suitable experimental setup. In the following section theoretical expressions and measured values available from literature will be presented and discussed.

Microscopic structure of diamond A diamond crystal consists of carbon atoms. In this work¹ a diamond crystal is considered which consist of a cubic lattice with a basis of two atoms, which are marked blue and green in Fig. 4.1a to be distinguished. The Bravais lattices in this case can be defined as face-centered cubic (fcc) and is illustrated in the middle of Fig. 4.1a, the cubic lattice constant is denoted by a . The blue marked atoms are located at the lattices points of the Bravais lattice and the green marked atoms are displaced by $a[\frac{1}{4}, \frac{1}{4}, \frac{1}{4}]^T$ from the position of a lattice point. The primitive cell consists of two atoms and is illustrated on the left of Fig. 4.1a. The primitive basis vectors are given by

$$\mathbf{a}_1 = \frac{a}{2} \begin{bmatrix} 0 \\ 1 \\ 1 \end{bmatrix}, \quad \mathbf{a}_2 = \frac{a}{2} \begin{bmatrix} 1 \\ 0 \\ 1 \end{bmatrix} \quad \text{and} \quad \mathbf{a}_3 = \frac{a}{2} \begin{bmatrix} 1 \\ 1 \\ 0 \end{bmatrix} \quad (4.1)$$

The same information about the lattice structure is also contained by a Wigner-Seitz primitive cell, which is a construction around a single lattice point and confined by an area which is nearer to this lattice point than any other lattice point [GM18, p. 6]. An illustration of a Wigner-Seitz primitive cell is given on the right of Fig. 4.1a.

In context of solid state physics it is very useful to define the reciprocal vectors, which are related to Eq. 4.1 by [GM18, p. 58]:

$$\mathbf{b}_1 = \frac{2\pi}{V_c} \mathbf{a}_2 \times \mathbf{a}_3, \quad \mathbf{b}_2 = \frac{2\pi}{V_c} \mathbf{a}_3 \times \mathbf{a}_1, \quad \mathbf{b}_3 = \frac{2\pi}{V_c} \mathbf{a}_1 \times \mathbf{a}_2 \quad \text{with} \quad V_c = \mathbf{a}_1 \cdot (\mathbf{a}_2 \times \mathbf{a}_3), \quad (4.2)$$

In reciprocal space an analogue construction like the Wigner-Seitz cell in real space can

¹It should be mentioned that also a hexagonal diamond structure (lonsdaleite) exist, which will not be discussed further in this work [GM18, p. 136].

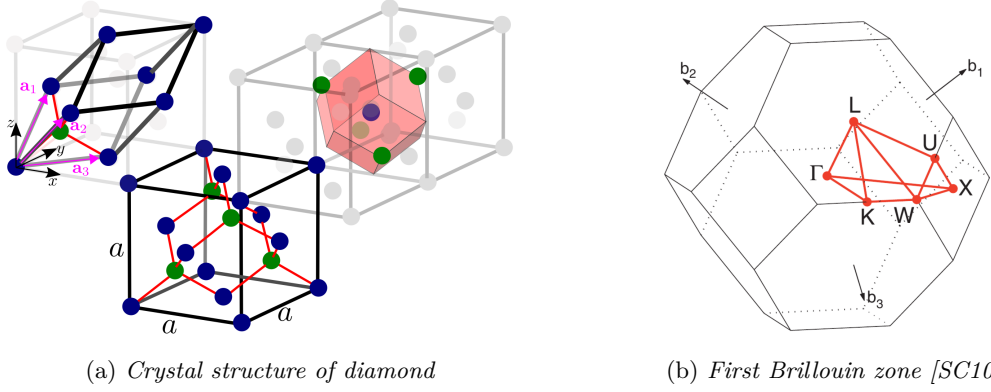


Figure 4.1.: (a) *Microscopic crystal lattice structure of cubic diamond with lattice constant $a = 3.566\,90(8)\text{ \AA}$. On the left a primitive cell is illustrated. In the middle a conventional unit cell based on a fcc Bravais lattice is shown. On the right a illustration of a Wigner-Seitz primitive cell is shown.* (b) *First Brillouin zone with marked symmetry points [SC10].*

be carried out. This construction is called the Brillouin zone [SC10]. In Fig 4.1b the first Brillouin zone for diamond is shown. The Brillouin zone is a meaningful definition to describe the phonon dispersion of diamond, which will be discussed in the following section. A complete visualization of the phonon dispersion of diamond can be achieved using the standard path in reciprocal space which is marked in Fig 4.1b (For detailed explanation see [SC10]).

A Bravais lattice can be defined by

$$\mathbf{R} = n_1\mathbf{a}_1 + n_2\mathbf{a}_2 + n_3\mathbf{a}_3, \quad (4.3)$$

and a reciprocal lattice by

$$\mathbf{G} = h\mathbf{b}_1 + k\mathbf{b}_2 + l\mathbf{b}_3, \quad (4.4)$$

where n_1, n_2, n_3, h, k and l are integers. The Bravais and the reciprocal lattices are related by $\exp(j\mathbf{G} \cdot \mathbf{R}) = 1$.

The diamond structure is formed by directed covalent bondings. The conventional unit cells of diamond, with a volume a^3 has eight atoms and each atom has four next neighbor atoms [GM18, p. 31]. The molar mass of carbon is $M=12\text{ g mol}^{-1}$. The lattice constant a of diamond varies only little with temperature changes. In the range from 50 K to 300 K it is $a = 3.566\,90(8)\text{ \AA}$ [SS10]. The mass density ρ can therefore be calculated by

$$\rho = \frac{8M}{a^3 N_A} \approx 3513\text{ kg/m}^3. \quad (4.5)$$

where N_A is the Avogadro constant. Due to the small variation of the lattice constant with the temperature, the value of ρ is assumed as temperature independent for the simulations carried out in this work. However, it should be noted that natural diamond typically contains about 1% of the isotope ^{13}C in otherwise pure ^{12}C crystals [PK13, p.203]. Due to the different molar mass of ^{13}C $M_{13} \approx 13\text{ g mol}^{-1}$ the average mass density in this case

is a little bit higher $\rho \approx 3516 \text{ kg/m}^3$.

Synthetic fabrication of single crystalline diamond Beside the rare possibility to find a natural diamond it is nowadays possible to fabricate single crystalline diamond synthetically. Two techniques, which are common to fabricate synthetic diamond crystals are:

High-pressure, high-temperature (HPHT) The basic principle of this technique is to subject a carbon-containing material to a high temperature ($>1800 \text{ K}$) and high pressure ($>5 \text{ GPa}$) environment. This treatment can cause a phase transition of graphite to diamond. The press systems employs a core reaction cell which contains some seed crystals beside a carbon source. To reduce the temperatures and pressure values, which are necessary for the phase transition, a metal solvent is used [PK13, p. 159].

Chemical vapor deposition (CVD) In this process the diamond crystal is grown on a substrate from a hydrocarbon gas mixture, inside an environment with controlled temperature and pressure values. For the substrate a HPHT diamond can be used. The mixture of hydrocarbon is injected into a chamber and heating can be carried out using for example a micro wave beam [PK13, p. 160]. At temperatures above 1100 K the gas mixture is ionized into chemically active radicals and a plasma is created, material can then nucleate on the surface of the substrate.

4.1. Thermomechanical properties

In Section 3 the dynamics of a elastic continuum have been introduced. In contrast to the continuum view on the material system, now the dynamics of a microscopic view will be considered. As mentioned before the microscopic structure of single crystalline diamond is well known. The solid crystal is built of atoms, which consist of electrons and nuclei. The electrons have the mass m and the charge $-e$. The nuclei have mass M and charge Ze . The interaction between these particles is assumed to be purely electromagnetic and the main contribution for this interaction are Coulomb interactions. Such a system is defined by the following Hamiltonian [GM18, p. 172] [Höl15, p. 9]:

$$\mathcal{H} = \hat{T}_n + \hat{T}_e + V_{ee}(\{\mathbf{r}\}) + \mathcal{V}(\{\mathbf{r}\}, \{\mathbf{R}\}) + V_{nn}(\{\mathbf{R}\}) + \Xi(t). \quad (4.6)$$

In this equation $\{\mathbf{r}\}$ is the position of the electrons and $\{\mathbf{R}\}$ the one of the nuclei. The first two terms are the kinetic energy operators for nuclei \hat{T}_n and electrons \hat{T}_e

$$\hat{T}_n = - \sum_k \frac{\hbar^2}{2M_k} \frac{\partial^2}{\partial \mathbf{R}_k^2} \quad \text{and} \quad \hat{T}_e = - \sum_i \frac{\hbar^2}{2m} \frac{\partial^2}{\partial \mathbf{r}_i^2}. \quad (4.7)$$

The remaining terms of Eq. 4.6 describes the particle-particle interactions. The interelectronic Coulomb potential is given by:

$$V_{ee}(\{\mathbf{r}\}) = \sum_{i<j} \frac{e^2}{4\pi\epsilon_0|\mathbf{r}_i - \mathbf{r}_j|}. \quad (4.8)$$

The electron-nuclear interaction is expressed by:

$$\mathcal{V}(\{\mathbf{r}\}, \{\mathbf{R}\}) = - \sum_{i,k} \frac{Ze^2}{4\pi\epsilon_0|\mathbf{r}_i - \mathbf{R}_k|}. \quad (4.9)$$

The Coulomb repulsion of the nuclei among each other is given by:

$$V_{nn}(\{\mathbf{R}\}) = \sum_{k<l} \frac{Z^2e^2}{4\pi\epsilon_0|\mathbf{R}_k - \mathbf{R}_l|}. \quad (4.10)$$

The last term in Eq. 4.6 is a possible time-dependent external vector potential $\Xi(t)$, which might result from a laser beam.

If relativistic effects and spin can be neglected such a system can be completely described by a Schrödinger equation

$$\mathcal{H}\psi(\{\mathbf{r}\}, \{\mathbf{R}\}, t) = j\partial_t\psi(\{\mathbf{r}\}, \{\mathbf{R}\}, t). \quad (4.11)$$

If the Schrödinger equation Eq. 4.11 for Eq. 4.6 can be solved all the information is given to describe the macroscopic thermomechanical material parameters of the diamond crystal. However, for such a high dimensional system a direct solution is not directly calculable. Nevertheless, for appropriated assumptions there are ways to find solutions for such problems with methods based on first-principles (ab initio) density functional theory (DFT). The calculation of such a simulation and the underlying theoretical concepts and approximation, are extensive and will not be covered in this work. For a detailed introduction to this topic the interested reader is referred to [RLB19] [Höl15]. In the following section simpler theoretical models than DFT will be introduced and the solutions will be compared to DFT calculations available from literature.

Elastic constants The elastic constants of cubic diamond have been measured by various experimental methods and have been calculated with different theoretical approaches [Hes12][KC93] [SWM⁺12]. For the simulations in this work the following values for the stiffness tensor are used [CL05]:

$$c_{11} = (1043 \pm 5) \text{ GPa}, c_{12} = (128 \pm 5) \text{ GPa} \quad \text{and} \quad c_{44} = (534 \pm 17) \text{ GPa}. \quad (4.12)$$

Using Eq. 3.10 gives the values for the compliance tensor

$$s_{11} = 0.985 \text{ TPa}^{-1}, s_{12} = -0.108 \text{ TPa}^{-1} \quad \text{and} \quad s_{44} = 1.873 \text{ TPa}^{-1}. \quad (4.13)$$

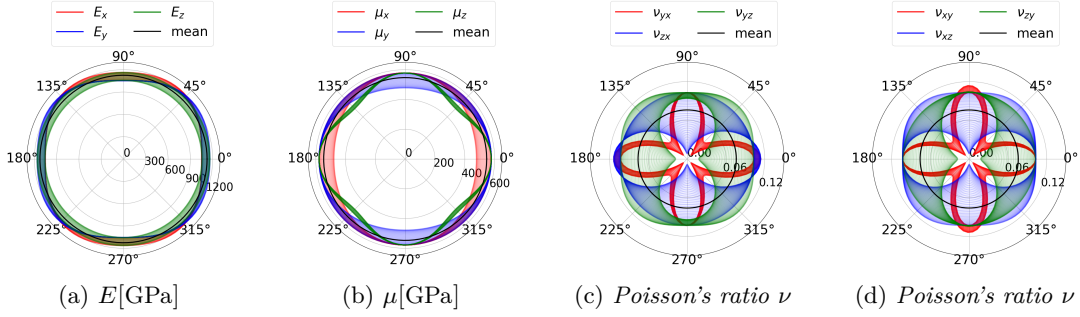


Figure 4.2.: Illustration of the elastic properties of SC diamond in various orientations calculated with the method described in Appendix A.3 (a) values of Young's modulus $E_{mean}=1125$ GPa, $E_{min}=1053$ GPa, $E_{max}=1207$ GPa (b) values of the shear modulus $\mu_{mean}=546$ GPa, $\mu_{min}=478$ GPa, $\mu_{max}=578$ GPa (c) and (d) values of the Poisson's ratio $\nu_{mean}=0.076$, $\nu_{min}=0.008$, $\nu_{max}=0.114$.

These values are in good agreement with measured values. However, it should be mentioned that the reported values for diamond of different qualities and various experimental methods show a quite broad variation of about 10% [Hes12].

The measured variation of elastic constants for cubic diamond in the temperature range 60 K to 400 K is less than a percent [SWM⁺12] and therefore the values of Eq. 4.12 are considered to be approximately temperature independent in the context of this work.

Substituting the values of Eq. 4.12 in Eq. A.21 (Appendix A.3) to assess the elastic anisotropy it can be obtained that diamond has a value of $A_{iso} = 1.167$ which is near the isotropic value of $A_{iso} = 1$. As described in the Appendix A.3 the variation of the Young's modulus E_i , the Poisson's ratio ν_{ij} and the shear modulus μ_i can be calculated in different orientation of the crystal structure regarding the axis of a Cartesian coordinate system. Considering the directional dependence which is illustrated in Fig. 4.2 it can be seen that Young's modulus and also the shear modulus vary only little with orientation. The Poisson's ratio ν_{ij} differs substantially with orientation. The maximum value is 0.114 and the minimum value is 0.008. However, it should be noted that the maximum of ν_{ij} is still quite small.

The bulk modulus calculated with Eq. 3.48 using the values of Eq. 4.12 is:

$$B = \frac{1}{3}(c_{11} + 2c_{12}) = 433 \text{ GPa} \quad (4.14)$$

Considering the diamond crystal to be approximately isotropic and using the mean value of the Poisson's ratio $\nu_{mean} = 0.076$ and the Young's modulus $E_{mean} = 1125$ GPa gives considering Eq. 3.12

$$B_{iso} = \frac{E_{mean}}{3(1 - 2\nu_{mean})} = 436 \text{ GPa} \quad (4.15)$$

Considering the quite small value of the Poisson's ratio for diamond an approximation may be used where the Poisson's ratio is nearly zero. However, this approximation has a significant impact on the value of the Bulk modulus, which can be in this case be calculated

by

$$B_{iso,\nu=0} = \frac{E_{mean}}{3} = 375 \text{ GPa} \quad (4.16)$$

Using the approximation of an isotropic material and further assuming a Poisson's ratio of zero will introduce a systematical error considering thermoelastic simulations. However, the benefit is that for an isotropic material the axisymmetric case could be used (Section 3.5) and for the case where the Poisson's ratio is assumed to be zero the stress-strain is given by the simple relation Eq. 3.15. The verification and limits of these approximation will be discussed in detail in the Section 6 by comparing simulation results with experimental data.

Phonon dispersion relation The thermal properties like heat capacity, thermal expansion and thermal conductivity for an insulating material like diamond may be described by effects which can be related to lattice vibrations in form of quantized phonon properties [GM18, p. 213].

In the Section 3 the dynamics of an elastic continuum has been discussed. In contrast to the continuum view on the material system, now the dynamics of a microscopic view will be considered. As mentioned before the microscopic structure of single crystalline diamond is well known. Starting with this knowledge, theories can be developed which explain the macroscopic measurable material parameter, which have been introduced in Section 3. Considering the motion of the lattice atoms around their rest position gives a description for the lattice dynamics. Including quantum effects leads to the definition of a phonon, which may be considered as a collective excitation of the atomic displacement in the periodic crystal. This quasiparticle can have different polarizations corresponding to longitudinal and transverse waves. Further, different phonon modes namely acoustical and optical modes, can be defined. A detailed introduction to this extensive topic can be found in various textbooks [GM18], also the PhD theses of P. Rauer [Rau21] and C. Maag [Maa18], should be mentioned in this context, where the basics of lattice vibrations are explained in more detail than in this work. The phonon dispersion relation, relates the wavelength (or wavenumber) to the frequency (energy) of the phonon. The phonon dispersion relation can be determined experimentally by investigating inelastic scattering processes of neutrons and photons with the crystal [GM18, p. 204]. In Fig. 4.3 a comparison of experimental data for diamond carried out with inelastic neutron scattering [WYDC67] and calculations based on an ab initio theory is shown for particular points of the first Brillouin zone (Fig. 4.1b). The ab initio calculation has been carried out considering a super cell of 128 atoms by using the code *exciting* (version: nitrogen) [GKM⁺14] the input file for the calculation can be found in the Appendix A.4. With the knowledge of the phonon dispersion relation a equation for the internal energy \tilde{U} can be formulated

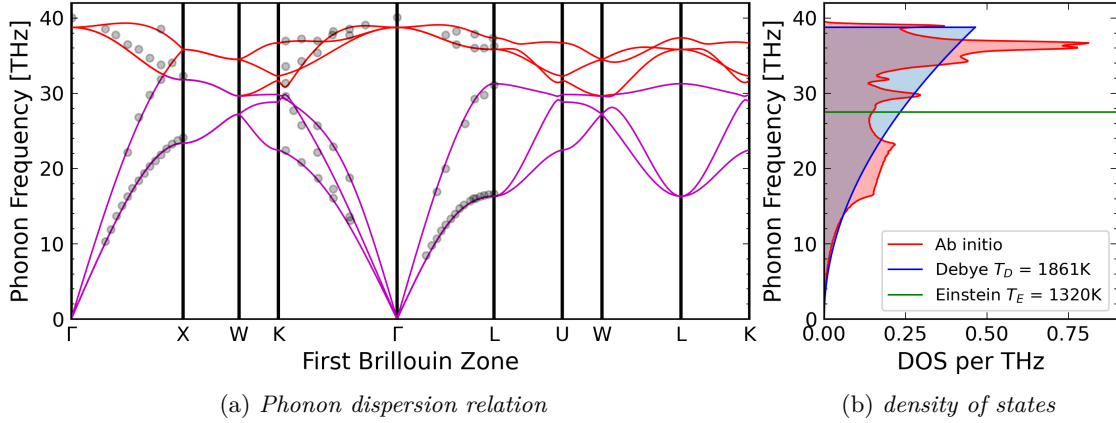


Figure 4.3.: In both figures the phonon frequency in THz is given considering the same range of values. It should also be mentioned that the considered frequency is given by $\omega/2\pi$, where ω is the angular frequency. (a) Phonon dispersion relation of diamond considering the first Brillouin zone Fig. 4.1b. The measurement result of inelastic neutron scattering [WYDC67] are illustrated by black dots. The results of an *ab initio* calculations (Appendix A.4) are represented by solid lines. The optical modes are marked red and the acoustics modes are marked magenta. (b) Density of states (DOS) for a diamond unit cell. The integration over the frequency range results in a value of $3Nr' = 6$ (red area). Beside the DOS calculated from an *ab initio* calculations, the Debye and Einstein approximation are shown, considering an Debye temperature of $T_D = 1861$ K and an Einstein temperature of $T_E = 1320$ K. The integral of the DOS per frequency gives per definition also a value of 6 (blue area) and the green line of the Einstein approximation has a value of 6 (which is not illustrate for a better visualization) at the frequency value of $\omega_E/2\pi$ and is zero every else.

by [GM18, p. 221]

$$\langle \tilde{U} \rangle = \tilde{U}_{eq} + \sum_{\mathbf{q},p} \frac{1}{2} \hbar \omega_{\mathbf{q}p} + \sum_{\mathbf{q},p} \hbar \omega_{\mathbf{q}p} \langle n_{\mathbf{q}p} \rangle, \text{ where } \langle n_{\mathbf{q}p} \rangle = \frac{1}{\exp\left(\frac{\hbar \omega_{\mathbf{q}p}}{k_B T}\right) - 1} \text{ and } p = 1, 2, \dots, 3r'. \quad (4.17)$$

Here k_B is the Boltzmann constant, \hbar reduced Planck's constant, ω is the angular frequency of a phonon with wave vector \mathbf{q} , and p are the possible polarizations given by the number r' of atoms in a unit cells. The number of modes in the crystal is given by $3N' = 3Nr'$, where N is the number of unit cells and N' is the amount of the atoms. The values of the wave vector \mathbf{q} can be connected to values of the Brillouin zone, small values near zero of \mathbf{q} correspond to the Γ point of the first Brillouin zone (Fig. 4.1b) and a large wavelength value. The Bose-Einstein distribution is represented by $\langle n_{\mathbf{q}p} \rangle$, which takes into account quantum mechanical effects [GM18, p. 219]. The constant \tilde{U}_{eq} represents the contribution of the static crystal lattice. The second term on the right hand side is connected to the ground state and the third represents contribution of thermally excited phonons.

The phonon group velocity is connected to the dispersion relation (Fig. 4.3a) and is given by [GM18, p. 182]

$$\mathbf{v}_g = \nabla_{\mathbf{q}} \omega(\mathbf{q}). \quad (4.18)$$

Considering a macroscopic crystal (consisting of a sufficiently large number of unit cells) the sum in Eq. 4.17 may be approximated as an integral expression by considering the phonon density of states (DOS) for the frequency space $D(\omega)$ [GM18, p. 222]:

$$\langle \tilde{U} \rangle = \tilde{U}_{eq} + \sum_p \int \frac{1}{2} \hbar \omega D_p(\omega) d\omega + \sum_p \int \hbar \omega D_p(\omega) \langle n(\omega, T) \rangle d\omega, \quad (4.19)$$

$$\text{where } \langle n(\omega, T) \rangle = \frac{1}{\exp\left(\frac{\hbar \omega}{k_B T}\right) - 1} \text{ and } p = 1, 2, \dots, 3r'$$

The integration of the DOS function gives

$$3N' = \int_{\omega_{min}}^{\omega_{max}} D(\omega) d\omega. \quad (4.20)$$

Heat capacity From the first law of thermodynamics it follows, that the heat capacity \tilde{C}_V measured at constant volume can be defined as [GM18, p. 214]

$$\tilde{C}_V \equiv \left(\frac{\partial \tilde{Q}}{\partial T} \right)_V = \left(\frac{\partial \tilde{U}}{\partial T} \right)_V, \quad (4.21)$$

where \tilde{Q} is an amount of heat and \tilde{U} the internal energy. It should be noted that in this case the properties are not considered per unit volume. However, the heat Q and internal energy U per unit volume which have been introduced in Section 3.2 are related by $\tilde{Q} = VQ$ and $\tilde{U} = VU$.

The heat capacity \tilde{C}_V used in Eq. 4.21 is also related to the heat capacity measured at constant strain per unit volume $\tilde{C}_V = C^\epsilon V$ and the heat capacity measured per unit mass c^ϵ measured at constant strain is given by:

$$c^\epsilon = \frac{\tilde{C}_V}{m} = \frac{\tilde{C}_V}{\rho V} = \frac{C^\epsilon}{\rho} \quad (4.22)$$

Inserting Eq. 4.17 into Eq. 4.21 gives:

$$\tilde{C}_V = \left(\frac{\partial \langle \tilde{U} \rangle}{\partial T} \right)_V = \sum_{\mathbf{q}, p} \frac{\partial}{\partial T} \frac{\hbar \omega_{\mathbf{q}p}}{\exp\left(\frac{\hbar \omega_{\mathbf{q}p}}{k_B T}\right) - 1} \quad (4.23)$$

Considering an approximation for the low temperature range under the assumption $k_B T \ll \hbar \omega_{\mathbf{q}p}$ it can be derived that the heat capacity is given by [GM18, p. 224]:

$$\tilde{C}_V = V \frac{2\pi^2}{5} k_B \left(\frac{k_B T}{\hbar v_s} \right)^3, \quad c^\epsilon = \frac{2\pi^2}{\rho 5} k_B \left(\frac{k_B T}{\hbar v_s} \right)^3 \quad (4.24)$$

where v_s is the mean speed of sound of the three acoustic modes and Eq. 4.22 has been used to calculate c^ϵ .

A phenomenological description of the temperature dependent heat capacity of diamond may be given by the Einstein-approximation. The underlying assumption for this

approximation is that a crystal which possesses N' atoms has $3N'$ number of modes which all have the same frequency ω_E , which is denoted as the Einstein-frequency. For such a condition the DOS (Eq. 4.20) are given by $D(\omega) = 3N'\delta(\omega - \omega_D)$, where δ is the Dirac delta function (Fig. 4.3b). Inserting Eq. 4.19 into Eq. 4.23 gives in this case:

$$\tilde{C}_{V,einstein} = 3N'k_B \left(\frac{T_E}{T}\right)^2 \frac{\exp(T_E/T)}{(\exp(T_E/T) - 1)^2}, \text{ where } T_E = \frac{\hbar\omega_E}{k_B}. \quad (4.25)$$

The Einstein temperature T_E characterizes the material specific heat capacity and may be obtained by comparisons with experimental data. As illustrated in Fig. 4.4 the value for a diamond crystal is about $T_E = 1320$ K. The number of atoms in a macroscopic diamond crystal with volume V may be calculated by $N' = 8V/a^3$, where a is the lattice constant. Considering the density given by Eq. 4.5 the mass may be calculated by $m = V\rho = MN'/N_a$. Thus, given by Eq. 4.22 the specific heat capacity per unit mass is:

$$c_{einstein}^e = 3k_B N_{kg} \left(\frac{T_E}{T}\right)^2 \frac{\exp(T_E/T)}{(\exp(T_E/T) - 1)^2}, \text{ where } N_{kg} = \frac{N_A}{M}, \quad (4.26)$$

where N_{kg} is the number of atoms per unit mass. Considering $T \gg T_E$ it can be seen that Eq. 4.26 is approximately $3N_{kg}k_B$. This result is also known as the Dulong-Petit law and can be also derived with classical assumptions (without considering quantum effects) using the theory of statistical mechanics [GM18, p. 216]. Considering the Dulong-Petit value for the heat capacity of diamond gives $c_{DP}^e = 3N_{kg}k_B = 2078.6 \text{ J kg}^{-1} \text{ K}$. Comparing this value with measured values of the heat capacity Fig. 4.4 [DeS53] shows that this classical approximation gives wrong² result for diamond because it cannot explain the strong temperature dependence (even at room temperature) of diamond. Considering sufficiently low temperatures it can be seen that for some high frequency modes the following inequality has to be considered:

$$\hbar\omega \gg k_B T. \quad (4.27)$$

A classical mode could take any amount of energy $k_B T$ from a heat bath. However, taking into account quantum mechanical effects a mode with frequency ω under the condition $\hbar\omega \gg k_B T$ cannot take energy from the heat bath and stays in the ground state. Therefore, with decreasing temperature some of the modes with higher frequencies will stay in the ground state, which causes a decreasing heat capacity. Considering Eq. 4.27 an absolute temperature value of 300 K may be related³ to a phonon frequency of 6.25 THz. As it can be seen from Fig. 4.3 this causes that for diamond most of the modes are in the ground state even at room temperature, which explains the strong deviation of the Dulong-Petit law. For high temperature values (sufficiently higher than the Einstein temperature) all modes can take energy from the heat bath ($k_B T \gg \hbar\omega$) and the approximation of the

²However, it should be mentioned that the Dulong-Petit law gives quite accurate values for a heat capacity at room temperature for many different materials. The strong deviation in the considered case is a special case due to the special material properties of diamond.

³Calculating the phonon frequency by $\frac{k_B T}{\hbar 2\pi}$.

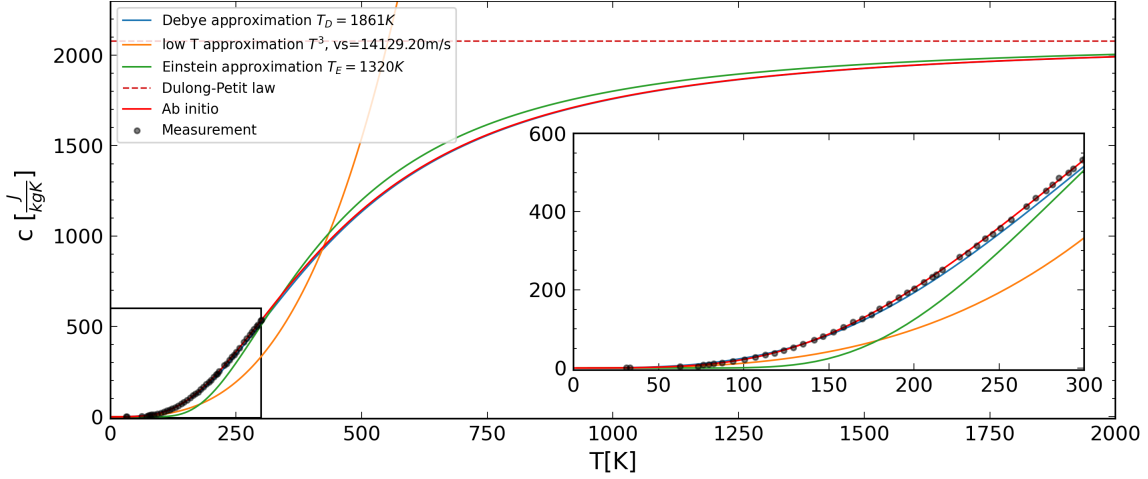


Figure 4.4.: Heat capacity calculated with an *ab initio* method (Appendix A.4) compared to measured data [DeS53]. Also shown are heat capacity values calculated with the Debye approximation Eq. 4.29 ($T_D = 1861$ K), the Einstein approximation Eq. 4.26 ($T_E = 1320$ K) and the low temperature approximation Eq. 4.24.

Dulong-Petit law may be used. However, it should be mentioned in this context that for diamond at temperatures values above about 1800 K graphitization processes have to be taken into account and for temperature values about 2400 K, diamond will be converted completely to graphite in the time span of a few minutes [DE72].

The Debye approximation uses similar assumptions like the Einstein approximation. However, in this case the phonon dispersion is assumed to consist of three acoustic branches with linear dispersion ($\omega_p = v_p q$, where $p = 1, 2, 3$) and the DOS are given by $D_p(\omega) = \frac{V}{2\pi^2} \frac{\omega^2}{v_p^3}$. Inserting Eq. 4.19 into Eq. 4.23 gives in this case [GM18, p. 228]:

$$C_{V,debye} = 9N'k_B \left(\frac{T}{T_D}\right)^3 \int_0^{T_D/T} \frac{x^4 e^x}{(e^x - 1)^2} dx, \text{ where } T_D \equiv \frac{\hbar\omega_D}{k_B} = \frac{\hbar v_{mean}}{k_B} \left(6\pi^2 \frac{N'}{V}\right)^{1/3} \quad (4.28)$$

where ω_D is the Debye frequency, and a mean phonon velocity v_{mean} has been considered. The Debye temperature T_D may be obtained from experimental data and has at room temperature a value of about $T_D = 1861$ K (at $T = 300$ K) [DeS53]. For $T_D = 1861$ K and using $N'/V = N_a \rho / M$, thus v_{mean} is $11\,144.6 \text{ m s}^{-1}$. For phonon wavelengths λ_{ph} which are much bigger than the lattice constant ($\lambda_{ph} \gg a$) a continuum approximation may be considered. For such a case the phonon velocity may be connected to the speed of a longitudinal (Eq. 3.64) and transverse (Eq. 3.66) sound waves [GM18, p. 182] and v_{mean} may be calculated by $v_s = (2v_T + v_L)/3 = 14\,129.20 \text{ m s}^{-1}$, where the mean Young's modulus $E_{mean} = 1125$ GPa and mean Poisson's ratio $\nu_{mean} = 0.07$ have been used for the calculation. Such an approximation may be used considering low temperatures, because the only modes which are not in the ground state are in this case phonon modes with long wavelengths near the Γ -point of the first Brillouin zone. Considering the low temperatures range it can be obtained from measurements of the heat capacity that the

Debye temperature in this case is about $T_D = 2242$ K (at $T = 60$ K) [DeS53], which gives a mean velocity of $v_{mean} = 13\,426.19$ m s⁻¹, which is close to the continuum speed of sound value v_s .

Following the same arguments as before for the Einstein approximation the heat capacity per unit mass can be calculated with

$$c_{debye}^e = 9N_{kg}k_B \left(\frac{T}{T_D}\right)^3 \int_0^{T_D/T} \frac{x^4 e^x}{(e^x - 1)^2} dx, \text{ where } N_{kg} = \frac{N_A}{M} \quad (4.29)$$

Comparing the values calculated with the ab initio method for the heat capacity with measured values [DeS53] shows very good agreement (Fig. 4.4). Also the Debye approximation considering a Debye temperature of $T_D = 1861$ K shows a quite good agreement with the measurements. Using the Einstein approximation shows clear deviations from the measured values and cannot explain the low temperature approximation calculated with Eq. 4.24. However for an Einstein temperature of $T_E = 1320$ K it gives results which describe the temperature dependence of the diamond heat capacity correctly to some extent.

Comparing the Einstein and Debye approximation it should be clarified that these approximations were not invented to simplify the calculations which can be carried out by ab initio methods, but were postulated before such ab initio methods were invented.

Phonon-phonon scattering To describe thermal expansion and thermal conductivity, scattering processes have to be taken into account. Without phonon-phonon scattering processes, phonons inside a crystal would be entirely decoupled and a once excited lattice vibration would exist forever. Under such conditions a thermal equilibrium could not appear. The most common phonon-phonon scattering process is a three-phonon process where either two phonons are converted into a new one, or one phonon is converted into two new phonons. Considering conservation of energy for this scattering process gives:

$$\hbar\omega_3 = \hbar\omega_1 + \hbar\omega_2. \quad (4.30)$$

Further a conservation law for the quasimomentum can be defined:

$$\mathbf{q}_3 + \mathbf{G} = \mathbf{q}_1 + \mathbf{q}_2. \quad (4.31)$$

The reciprocal lattice vector \mathbf{G} has to be chosen in a way that all wave vectors \mathbf{q} are inside the first Brillouin zone. In this context scattering processes with $\mathbf{G} = 0$ are called normal scattering. For $\mathbf{G} \neq 0$ they are called Umklapp scattering, which regards to a change in the direction of converted wave vectors.

Higher scattering processes involving more than three phonons are also possible but less likely and therefore may be neglected [GM18, p. 236].

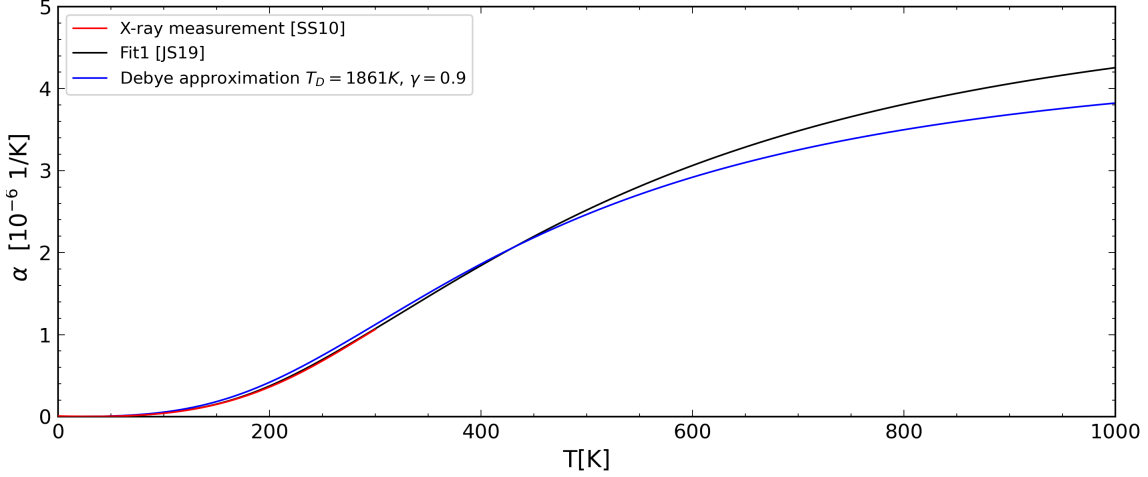


Figure 4.5.: Change of the linear thermal expansion coefficient $\alpha(T)$ measured with X-ray diffraction data [SS10] and fit given by [JS19], which were obtained by taking into account various result of measured values known from literature.

Thermal expansion coefficient Considering a perfect single crystalline (SC) diamond the macroscopic structure is built of a periodic arrangement of many unit cells like the one illustrated in Fig. 4.1a. Therefore the change of the lattice parameter a is directly connected to the macroscopic property of the thermal expansion coefficient introduced in Section 3.2 (Eq. 3.23), which may be formulated as:

$$\alpha(T) = \frac{1}{a(T)} \left(\frac{\partial a(T)}{\partial T} \right)_{\sigma} \xrightarrow{\Delta T \rightarrow 0} \alpha_{ij} = \left(\frac{\partial \epsilon_{ij}}{\partial T} \right)_{\sigma} \quad (4.32)$$

where $\alpha(T)$ can be interpreted as an approximated constant value if only small temperature variations ΔT are considered. Measuring the lattice constants of SC diamond at different temperatures using X-ray diffraction gives the progression of the linear thermal expansion coefficient which can be fitted to a polynomial function for the temperature range from near zero Kelvin to room temperature (300 K) [SS10]:

$$a(T) = 3.56682 \text{ \AA} + 2.5 \times 10^{-8} \text{ \AA/K}^1 T - 5.19 \times 10^{-10} \text{ \AA/K}^2 T^2 + 4.96 \times 10^{-12} \text{ \AA/K}^3 T^3 \\ + 1.11 \times 10^{-16} \text{ \AA/K}^4 T^4 + 1.92 \times 10^{-16} \text{ \AA/K}^5 T^5 - 3.46 \times 10^{-19} \text{ \AA/K}^6 T^6 \quad (4.33)$$

Inserting 4.33 into 4.32 the thermal expansion coefficient illustrated in Fig. 4.5 can be calculated.

Measurements conditions In Section 3.2 it has been mentioned that the heat capacity measured at constant strain could give a different result compared to a measurement at constant stress (Eq. 3.36). Taking into account Eq. 4.22 gives:

$$c_{\epsilon} - c_{\sigma} = -\frac{T}{\rho} \alpha_{ij} \alpha_{kl} C_{ijkl} \quad (4.34)$$

where $c^\sigma = \frac{C^\sigma}{\rho}$ is the heat capacity per unit mass measured at constant stress. For a cubic crystal it can be obtained by using $\alpha_{ij} = \alpha\delta_{ij}$, that Eq. 3.9 and Eq. 3.48 results in $\alpha_{ij}\alpha_{kl}C_{ijkl} = 3\alpha^2(c_{11} + 2c_{12}) = 9\alpha^2B$. Considering that the thermal expansion coefficient at room temperature is about $1 \times 10^{-6} \text{ K}^{-1}$ (Fig. 4.5) and the bulk modulus is 433 GPa (Eq. 4.14) gives by Eq. 4.34 $c_\epsilon - c_\sigma = 0.332 \text{ J K}^{-1} \text{ kg}^{-1}$. This value is much smaller than the heat capacity value (Fig. 4.4), which is about $534 \text{ J K}^{-1} \text{ kg}^{-1}$ for room temperature. Considering the temperature dependence of the thermal expansion coefficient (Fig. 4.5) and the heat capacity (Fig. 4.4) it can be obtained that the value of $c_\epsilon - c_\sigma$ is not only much smaller at room temperature, but also for any other temperature value. Thus, it can be assumed in good approximation that $c_\epsilon \approx c_\sigma$ and therefore in the following part of this work the heat capacity per unit mass c will be used without distinguishing between the values measured at constant strain or constant stress.

As also mentioned in Section 3.2 the elastic properties may give different results measured at constant temperature compared to a measurement at constant entropy, given by the relation Eq 3.35:

$$S_{ijkl}^S - S_{ijkl}^T = -\alpha_{ij}\alpha_{kl} \frac{T}{c\rho}. \quad (4.35)$$

Considering again room temperature values gives $-\alpha^2 \frac{T}{c\rho} = 0.00016 \text{ TPa}^{-1}$ which is much smaller than the values of the components of the compliance tensor Eq. 4.13. Also in this case $\alpha^2 \frac{T}{c\rho}$ is not only much smaller at room temperature, but for any value of the temperature, considering the temperature dependence of the thermal expansion coefficient (Fig. 4.5) and the heat capacity (Fig. 4.4). Thus, the difference for the elastic properties measured at constant strain compared to the ones measured at constant entropy can be neglected in good approximation.

Grüneisen parameter The volume dependence of the phonon frequencies may be described by the Grüneisen parameter, which will be introduced in this section. The thermal expansion coefficient can only be measured if the crystal is free of stress. From a thermodynamic view this means that the derivative of the Helmholtz free energy with respect to the volume must disappear, which demands that the pressure P must disappear for all temperatures. Considering thermodynamic relations and the definition of the internal energy Eq. 4.17, an equation for the pressure can be derived [GM18, p. 239]:

$$P = -B \frac{\delta V}{V} - \frac{\partial}{\partial V} \sum_{\mathbf{q},p} \frac{1}{2} \hbar \omega_{\mathbf{q}p} - \sum_{\mathbf{q},p} \frac{\partial \hbar \omega_{\mathbf{q}p}}{\partial V} \frac{1}{\exp\left(\frac{\hbar \omega_{\mathbf{q}p}}{k_B T}\right) - 1}. \quad (4.36)$$

In this equation B is the bulk modulus and $\delta V = V - V_0$ is the change of volume regarding to an initial volume V_0 .

The definition of thermal expansion coefficient for a finite volume V and the definition

for the bulk modulus (Eq. 3.51) gives [GM18, p. 241]

$$\alpha = \frac{1}{3V} \left(\frac{\partial V}{\partial T} \right)_P = -\frac{1}{3V} \left(\frac{\partial V}{\partial P} \right)_T \left(\frac{\partial P}{\partial T} \right)_V = \frac{1}{3B} \left(\frac{\partial P}{\partial T} \right)_V. \quad (4.37)$$

Inserting Eq. 4.36 into Eq. 4.37 yields

$$\alpha = -\frac{1}{3B} \sum_{\mathbf{q},p} \left(\frac{\partial \hbar \omega_{\mathbf{q}p}}{\partial V} \right) \frac{\partial}{\partial T} \frac{1}{\exp\left(\frac{\hbar \omega_{\mathbf{q}p}}{k_B T}\right) - 1}. \quad (4.38)$$

Recalling the definition of Eq. 4.23 and Eq. 4.22 the equation for the specific heat capacity per volume is

$$C^\epsilon = \sum_{\mathbf{q},p} C_{\mathbf{q}p}^\epsilon, \text{ where } C_{\mathbf{q}p}^\epsilon = \frac{\hbar \omega_{\mathbf{q}p}}{V} \frac{\partial}{\partial T} \frac{1}{\exp\left(\frac{\hbar \omega_{\mathbf{q}p}}{k_B T}\right) - 1}. \quad (4.39)$$

The definition of the Grüneisen parameter is

$$\gamma_{\mathbf{q}p} \equiv -\frac{V}{\omega_{\mathbf{q}p}} \frac{\partial \omega_{\mathbf{q}p}}{\partial V} = -\frac{\partial(\ln \omega_{\mathbf{q}p})}{\partial(\ln V)} \text{ and } \gamma \equiv \frac{\sum_{\mathbf{q},p} \gamma_{\mathbf{q}p} C_{\mathbf{q}p}^\epsilon}{\sum_{\mathbf{q},p} C_{\mathbf{q}p}^\epsilon}. \quad (4.40)$$

With this definition it follows

$$\alpha = \frac{\gamma C^\epsilon}{3B}. \quad (4.41)$$

Considering again the Debye approximation, the frequencies of the normal modes scale linearly with ω_D and therefore Eq. 4.40 becomes in this case

$$\gamma_{\mathbf{q}p} = -\frac{\partial(\ln \omega_D)}{\partial(\ln V)} = \gamma = \frac{3B\alpha}{C^\epsilon}. \quad (4.42)$$

Considering a Debye temperature of $T_D = 1861$ K and a mean Grüneisen parameters of $\gamma = 0.9$ gives acceptable agreement with measured values in the temperature range from near zero up to 400 K as illustrate in Fig. 4.5. However, this may be considered just as a rough estimation, which may visualize that there is some similarity between the function of the heat capacity and the thermal expansion coefficient. A more sophisticated fitting approach would be to consider the Grüneisen parameter as a mode and temperature dependent parameter [Par77]. The Grüneisen parameter can also be calculated with an ab initio method [XWCH91], however this kind of calculation will not be carried out in this work. Instead a semi-empirical multi-frequency Einstein mode, approximating the Grüneisen parameters will be introduced to describe the values of the thermal expansion of diamond by [JS19] [Ree75]

$$\alpha = \sum_{i=1}^n X_i \left(\frac{T_{E_i}}{T} \right)^2 \frac{\exp(T_{E_i}/T)}{(\exp(T_{E_i}/T) - 1)^2}. \quad (4.43)$$

It has been obtained by fitting Eq. 4.43 to available experimental data from the literature

that using the values:

$$\begin{aligned} X_1 &= 0.0096 \times 10^{-6} \text{ K}^{-1}, T_{E_1} = 159.3 \text{ K} \\ X_2 &= 0.2656 \times 10^{-6} \text{ K}^{-1}, T_{E_2} = 548.5 \text{ K} \\ X_3 &= 2.6799 \times 10^{-6} \text{ K}^{-1}, T_{E_3} = 1237.9 \text{ K} \\ X_4 &= 2.3303 \times 10^{-6} \text{ K}^{-1}, T_{E_4} = 2117.8 \text{ K} \end{aligned}$$

gives good agreement with the experimental data in the temperature range up to 1000 K [JS19] as illustrated in Fig. 4.5.

Heat transfer Contrary to the thermal properties discussed so far the heat conductivity is a non-equilibrium property, which is describing the heat flux and is caused by a temperature gradient. In the previous discussion about the specific heat capacity the properties $\langle \tilde{U} \rangle$ and $\langle n_{\mathbf{qp}} \rangle$ (Eq. 4.17) were described by assuming a thermal equilibrium, which is characterized by a fixed temperature. To describe heat conductivity a situation where the spatial variation of the temperature is small may be considered, so that it can be assumed to be constant in a particular region. This region must of course be bigger than the atomic distance in the crystal. However, to set a limit for which spatial dimensions this approximation is valid is not a trivial task. It depends on the problem under consideration, as well as on the material properties. This statement is going to be discussed in detail in this section.

In a first approximation it will be assumed that neighboring regions have only a small temperature difference and each of the neighboring regions is defined by a homogeneous temperature value and mean amount of phonons $\langle n_{\mathbf{qp}} \rangle$. Therefore, $\langle n_{\mathbf{qp}} \rangle$ is now a space dependent function. To describe thermal conductivity, the heat flux \mathbf{q}^h as a function of $\langle n_{\mathbf{qp}} \rangle$ will now be investigated. Considering now a one-dimensional⁴ heat flux, where an amount \tilde{Q} of heat is transferred in x -direction during a time span τ across a surface A . The transferred amount of heat may be determined by [GM18, p. 244]

$$Q = \frac{\tilde{U}}{V} A v_x \tau = \mathbf{q}_x^h A \tau. \quad (4.44)$$

where v_x is the mean velocity of the phonons which transport the energy. This velocity is given by the group velocity $\partial\omega/\partial q_x$. In Eq. 4.44 $\frac{\tilde{U}}{V}$ is the energy density inside a considered cuboid volume given by $A v_x \tau$. The heat flux in x -direction \mathbf{q}_x^h is the transferred amount of heat \tilde{Q} per area A and time τ . Using Eq. 4.17 to describe the internal energy \tilde{U} of the phonon system, the heat flux becomes:

$$\mathbf{q}_x^h = \frac{1}{V} \sum_{\mathbf{q}, p} \hbar \omega_{\mathbf{qp}} \left(\frac{1}{2} + \langle n_{\mathbf{qp}} \rangle \right) v_{x, \mathbf{qp}}, \text{ where } v_{x, \mathbf{qp}} = \frac{\partial \omega_{\mathbf{qp}}}{\partial q_x}. \quad (4.45)$$

⁴Here a temperature profile varying only in x -direction but constant in the $y - z$ plane at each position in x -direction is considered.

From this equation it follows that considering neighboring parts which are in thermal equilibrium, the heat flux \mathbf{q}_x^h is zero, because the occupation numbers for positive and negative wave vectors are equal and due to symmetry of the dispersion relation it follows that $v_x(\mathbf{q}) = -v_x(-\mathbf{q})$. Therefore, the sum in Eq. 4.45 is equal to zero. A non-zero heat flux exists if the mean phonon number $\langle n_{\mathbf{qp}} \rangle$ deviates from a reference thermal equilibrium $\langle n_{\mathbf{qp}} \rangle_0$:

$$\mathbf{q}_x^h = \frac{1}{V} \sum_{\mathbf{q},p} \hbar \omega_{\mathbf{q},p} (\langle n_{\mathbf{qp}} \rangle - \langle n_{\mathbf{qp}} \rangle_0) v_{x,\mathbf{qp}}. \quad (4.46)$$

The spatial change of $\langle n_{\mathbf{qp}} \rangle$ over time can be connected to two different processes. First, some phonons can diffuse into another spatial area and second, phonon-phonon scattering can occur, producing new phonons:

$$\frac{d\langle n_{\mathbf{qp}} \rangle}{dt} = \left. \frac{d\langle n_{\mathbf{qp}} \rangle}{dt} \right|_{\text{diffusion}} + \left. \frac{d\langle n_{\mathbf{qp}} \rangle}{dt} \right|_{\text{scattering}}. \quad (4.47)$$

This equation is a special case of the Boltzmann transport equation. Using the assumption that $\frac{d\langle n_{\mathbf{qp}} \rangle}{dt} = 0$ gives an approximately stationary state, where it is assumed that $\langle n_{\mathbf{qp}} \rangle$ depends on space but not on time. Another approximation may be used by considering that the temporal change of the phonon occupation number due to scattering can be described by a mean scattering time τ , which is independent of the phonon energy:

$$\left. \frac{d\langle n_{\mathbf{qp}} \rangle}{dt} \right|_{\text{scattering}} = -\frac{\langle n_{\mathbf{qp}} \rangle - \langle n_{\mathbf{qp}} \rangle_0}{\tau}. \quad (4.48)$$

The diffusion term is connected to a temperature gradient. In a time span Δt all phonons that were localized at $x - v_x \Delta t$ will arrive at position x , which gives

$$\left. \frac{d\langle n_{\mathbf{qp}} \rangle}{dt} \right|_{\text{diffusion}} = \lim_{\Delta t \rightarrow 0} \frac{1}{\Delta t} [\langle n_{\mathbf{qp}}(x - v_x \Delta t) \rangle - \langle n_{\mathbf{qp}}(x) \rangle] = -v_x \frac{\partial \langle n_{\mathbf{qp}} \rangle}{\partial x} = -v_x \frac{\partial \langle n_{\mathbf{qp}} \rangle_0}{\partial T} \frac{\partial T}{\partial x}. \quad (4.49)$$

The approximation on the right hand side of this equation, where $\langle n_{\mathbf{qp}} \rangle$ has been replaced by $\langle n_{\mathbf{qp}} \rangle_0$ is possible if a static situation and local thermal equilibrium is assumed [GM18, p. 246].

Inserting Eq. 4.49 and Eq. 4.48 into Eq. 4.47 gives an expression for $\langle n_{\mathbf{qp}} \rangle - \langle n_{\mathbf{qp}} \rangle_0$, which can be then inserted into Eq. 4.46:

$$\mathbf{q}_x^h = -\frac{1}{V} \sum_{\mathbf{qp}} \hbar \omega_{\mathbf{q},p} v_x^2 \tau \frac{\partial \langle n_{\mathbf{qp}} \rangle_0}{\partial T} \frac{\partial T}{\partial x}. \quad (4.50)$$

For an isotropic solid it can be defined that $\langle v_x^2 \rangle = \frac{1}{3} v^2$, because in this case the magnitude of the phonon velocity is given by $v_x^2 + v_y^2 + v_z^2 = v^2$ and $v_x^2 = v_y^2 = v_z^2$. By using Eq. 4.39, the Fourier heat law, which has been introduced before as an empirical law (Eq. 3.55) can be derived:

$$\mathbf{q}_x^h = \lambda_c \frac{\partial T}{\partial x}, \text{ where } \lambda_c = \frac{1}{3} C^e v l \text{ and } l = v \tau. \quad (4.51)$$

From this equation it can be seen that heat capacity and the group velocity have a direct influence on the thermal conductivity. Therefore, phonons near the edge of the Brillouin zone or optical phonons have only little impact on the heat transport. It should be noted that, for the derivation of Eq. 4.51 it has been neglected that the considered properties are frequency dependent, also that phonons can be defined to be acoustic and optical phonons and their particular polarization has been ignored.

In Eq. 4.51 also the mean free path l has been introduced, which will be discussed in detail in the following part of this section. Considering the temperature dependence of the thermal conductivity the properties c_V and l are expected to have the major influence. The temperature dependence of c_V has already been discussed. For the mean free path, different scattering processes have to be considered, regarding a diamond crystal with finite size. If various scattering processes appear independently of each other, a total scattering rate may be calculated by summation, with the connection of the scattering rate $1/\tau_i \propto 1/l_i$ [GM18, p. 248]:

$$\frac{1}{l} = \frac{1}{l_{ph-ph}} + \frac{1}{l_D} + \frac{1}{l_{iso}}. \quad (4.52)$$

Phonon-phonon scattering, l_{ph-ph} The three phonon-phonon scattering process has already been introduced in this section. Considering that two phonons are converted into a new one, it can be expected that this process appear more frequently for higher phonon densities. Therefore, the scattering probability should be proportional to $n_{ph}(T)$ and $l_{ph} \propto 1/n_{ph}(T)$. For normal scattering processes the total momentum and energy (Eq. 4.30 and Eq. 4.31) is constant. Therefore, the equilibrium distribution of the phonons at a temperature T can propagate with a certain drift velocity along the crystal. These scattering processes do not hinder the thermal conductivity at all. For a finite value of the heat conductivity not only processes, which have a finite mean free path are necessary, but also processes like Umklapp scattering needed to cause thermalization. For Umklapp scattering the momentum \mathbf{G} is transferred to the lattice. This momentum transfer leads to the thermal resistance of the lattice [GM18, p. 248].

Since, the sum of two phonon wave vectors has to be outside of the first Brillouin zone to generate Umklapp scattering, the Debye approximation may be used to define the mean energy for such phonons by $k_B T_D/2$ [GM18, p. 249]. The occupation probability in this case is given by $\langle n \rangle = 1/(\exp(\frac{T_D}{2T}) - 1)$. For $T \ll T_D$ it can be obtained $\langle n \rangle \propto \exp(-\frac{T_D}{2T})$ and $T \gg T_D$ gives $\langle n \rangle \propto \frac{T}{T_D}$. This causes for the mean free path $l_{ph} \propto \exp(\frac{T_D}{2T})$ for $T \ll T_D$ and $l_{ph} \propto \frac{T_D}{T}$ for $T \gg T_D$.

Defect scattering, l_D Defects inside the crystal and at its boundaries lead to scattering of phonons. The probability of such a scattering process only depends on the density of defects n_D and scattering cross-section σ_D and is therefore nearly independent of the surrounding temperature. For the scattering of phonons which have a wavelength λ_{th} much bigger than the diameter of the defect area $a_D \ll \lambda_{th}$, Rayleigh scattering can be

considered. The scattering cross-section in this case is

$$\sigma_D \simeq \pi a_D^2 (a_D q)^4. \quad (4.53)$$

The mean free path in this case is related to $l_D \propto \frac{1}{n_D \sigma_D}$ [GM18, p. 249].

Boundary scattering For small solids or cases where all mean free paths in Eq. 4.52 are greater than the characteristic lengths of the solid, a dominant scattering process may be the diffusive scattering at the boundaries of the solid. However, the scattering of phonons at boundaries does not need to be diffusive, but can also be specular depending on the particular structure of the crystal surface. For a perfect smooth surface there would be no diffuse scattering at all. A surface may be characterized by its variation from its mean plane (i.e. roughness) and by the distance between two roughness features (i.e. correlation length). A reduced mean-free-path can be calculated in this context by considering that, depending on a particular phonon momentum and angle of incidence at the surface, there exists a probability for the phonon to be scattered inside the solid or at a boundary [MM16].

Isotope scattering, l_D In single crystalline material the isotope concentration can have a significant impact regarding the phonon scattering. The random distribution of different isotope masses disturbs the periodicity of a perfect crystal and leads to scattering processes [GM18, p. 250]. However, a detailed discussion about the effect of the isotope concentration will not be carried out in this work. For further information about this topic the interested reader is referred to the work of P. Rauer [Rau21].

Low temperature limit Considering that the mean free path caused by phonon-phonon scattering increases exponentially in the low temperature range $l_{ph} \propto \exp(\frac{T_D}{2T})$ for $T \ll T_D$, it can be concluded that the mean free path is dominated by defect and boundary scattering effects. For single crystal materials with low defect concentration the mean free path can be larger than the spatial dimension of the crystal and the mean free path is related to scattering effects at the crystal boundaries.

Thermal conductivity Diamond has the highest thermal conductivity of any known material at temperatures above about 100 K. However, the exact value strongly depends on the quality of the specimen. Synthetic single crystals which are prepared with carbon isotopically enriched in ^{12}C can reach values of $3300 \text{ W m}^{-1} \text{ K}^{-1}$ at 300 K and SC CVD diamond have show values of about $2200 \text{ W m}^{-1} \text{ K}^{-1}$ [PK13, p.285]. In Fig. 4.6 the thermal conductivity calculated with an ab initio method for a diamond with an isotope concentration of 1.1% ^{13}C for two different thicknesses of 100 μm and 150 μm are shown. The calculation have been carried out by P. Rauer and details about the used method can be found in his PhD thesis [Rau21]. Also shown in Fig. 4.6 are measurements of a diamond

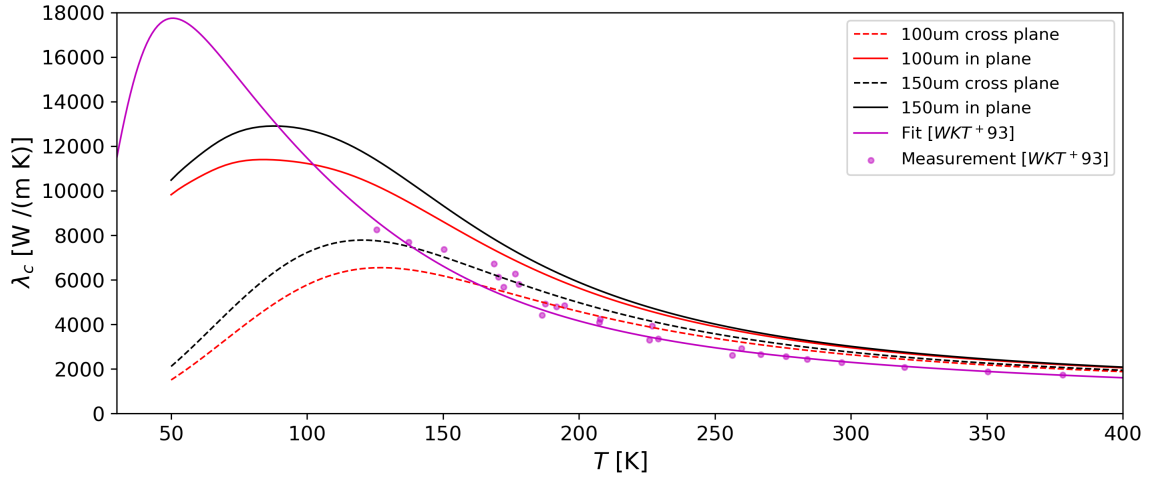


Figure 4.6.: Thermal conductivity of SC diamond with an isotope concentration of 1.1% ^{13}C . Calculated for a 100 μm and 150 μm thick crystal with an *ab initio* method by P. Rauer [Rau21] and measured values by [WKT⁺93], with a SC diamond crystal of size 1 mm \times 2 mm \times 4 mm.

crystal with an isotope concentration of 1.1% ^{13}C , where a crystal with spatial dimension in the millimeter range has been investigated [WKT⁺93]. The illustrated temperature dependence in Fig. 4.6 may be related to the derived relation of the thermal conductivity in Eq. 4.51: $\lambda_c = \frac{1}{3}C^\epsilon v l$. As mentioned before the value of the heat capacity and the phonon mean free path l shows a significant temperature dependence. The increase of the thermal conductivity at low temperatures can be related to the increase of the value of the heat capacity. With increasing temperature the reduced mean free path due to phonon-phonon scattering can be related to the decrease of the value of the thermal conductivity for higher temperatures.

The heat transfer in diamond in the low temperature range may be connected to a ballistic heat transport where phonons can propagate through the crystal without being scattered. Under such condition the heat conductivity which has been derived under the assumptions of a diffuse heat transport (Eq. 4.49) has no clear defined meaning anymore. However, considering the failure of the diffuse assumption there will be a temperature region where the simulations carried out under the assumption of a diffuse heat transport may still predict useful results. This kind of region will be investigated by the experiments in this work which will be explained in detail in the next sections.

To get a rough estimation for the value of the mean free path Eq. 4.51 may be considered to be calculated:

$$l = \frac{3\lambda_c}{c\rho v}. \quad (4.54)$$

Here the relation of Eq. 4.22 has been used. Considering the mean velocity obtained from the Debye approximation (11 144.6 m s^{-1}) and using the heat capacity values calculated with an *ab initio* method (Fig. 4.4) the mean free path calculated with Eq. 4.54 as illustrated in Fig. 4.7a can be obtained.

In the measurements of this work only diamond crystals with an isotope concentration

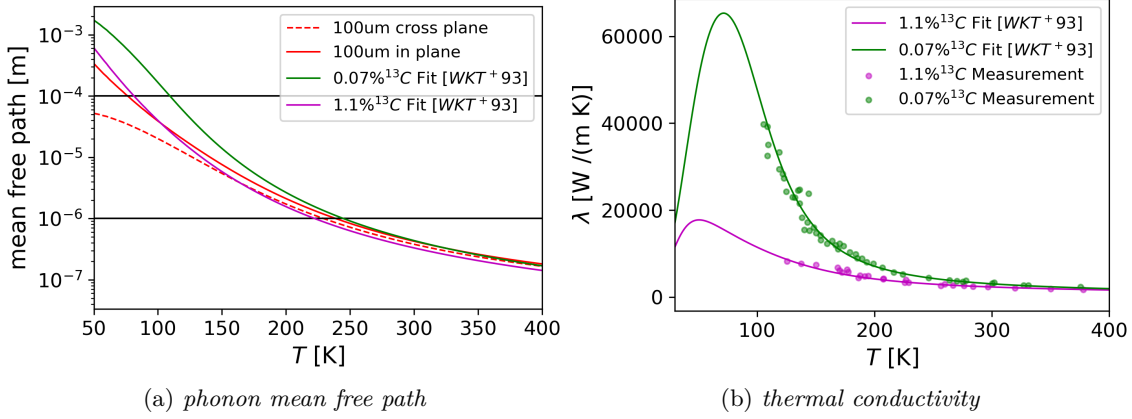


Figure 4.7.: (a) Mean free path calculated with Eq. 4.54. (b) Measured impact of isotope concentration on the value of the thermal conductivity [WKT+93].

of about 1.1%¹³C are investigated. However, it should be mentioned that a low isotope concentration could give a much higher conductivity like the measurements of SC diamond with a isotope concentration of 0.07%¹³C [WKT+93] (Fig. 4.7b).

4.2. Optical properties

The optical refractive index at room temperature of diamond has been measured for various wavelengths [PT64]. Important for the experimental setup used in this work are wavelength values of $\lambda = 213$ nm and $\lambda = 532$ nm. For $\lambda = 213$ nm a refractive index of $n = 2.7764$ and a absorption coefficient of $\alpha_k = 2008.8 \text{ cm}^{-1}$ (penetration depth of $\zeta = \frac{1}{\alpha_k} = 4.978 \text{ }\mu\text{m}$) has been measured. At $\lambda = 532$ nm the absorption coefficient is nearly zero and the refractive index is $n = 2.4250$. Considering Eq. 2.51, Eq. 2.52 and Eq. 2.55 of Section 2 the reflectance under normal incidence is $R = 0.22128$ for a wavelength of $\lambda = 213$ nm and $R = 0.1731$ for a wavelength of $\lambda = 532$ nm. A measurement of the temperature dependence of the refractive index in the range 93 K to 713 K for the wavelengths of 435.8 nm and 546.1 nm is illustrated in Fig. 4.8. The reduction of the refractive index at these wavelength with decreasing temperature from 123 K to 93 K has a very small value so that it could not be determined by the measurements [Ram47].

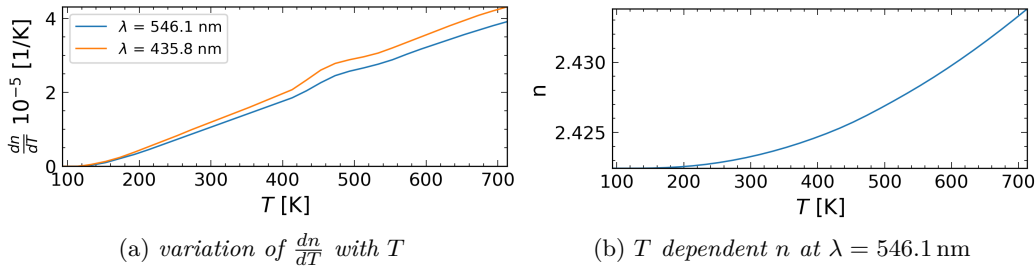


Figure 4.8.: (a) Change of the refractive index with temperature in the range from 93 K to 713 K at the wavelengths 435.8 nm and 546.1 nm [Ram47]. (b) Value of the refractive index calculated by numerical integration of the change of the refractive index with temperature. The value at room temperature is $n = 2.4232$.

5. Experimental setup and measurements

To investigate the nondestructive interaction of powerful electromagnetic radiation with a diamond Bragg reflector an experimental pump-probe setup has been built up. In the context of this work the intensity change of a continuous wave single frequency laser (i.e. probe) probes a material interaction, which is initialized by a pulsed laser (i.e. pump). The effect of the photon-material interaction of the probe with the Bragg reflector in terms of absorption is assumed to be negligible. As mentioned in the introduction of this work (Section 1) the pump laser is chosen to imitate the heat load expected of a saturated XFEL X-ray pulse. The probe is combined with a Michelson interferometer, which enables a measurement of the displacement in normal direction to the crystal surface. The experimental setup is explained in detail in the following section and is illustrated in Fig. 5.5.

Diamond crystals For the pump-probe measurements in this work a single crystal diamond fabricated by *Applied Diamond, Inc* has been investigated. The crystal has the nominal dimensions $4\text{ mm} \times 4\text{ mm} \times 100\text{ }\mu\text{m}$, the orientation $\langle 100 \rangle$ and a wedge angle which is about 0.1° , which corresponds to a thickness variation of about $\tan(0.1^\circ) \times 4\text{ mm} = 7\text{ }\mu\text{m}$. The manufacturing tolerance for the crystal thickness is $\pm 10\text{ }\mu\text{m}$. The wedge angle is used to separate the laser spots that are reflected at the front side and the back side of the crystal as illustrated in Fig. 5.1. The crystal was fabricated by a microwave plasma CVD technique. The manufacturer information is that the ^{13}C content of the diamond is about 1.1%.

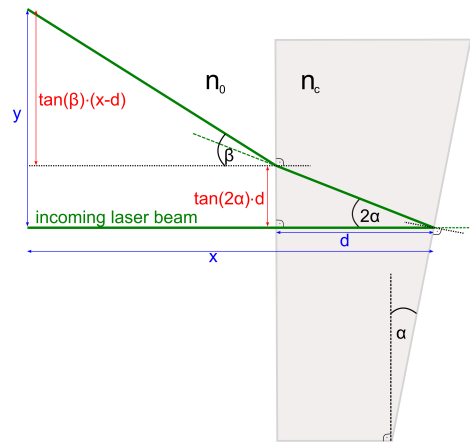


Figure 5.1.: *Illustration of the wedged angle, here denoted by α . The laser spots of a reflected laser beam can be spatially separated with a wedged crystal. The refractive index of diamond is denoted n_c and n_0 is the refractive index of the vacuum.*

Crystal holder An illustration of the crystal holder is given in Fig. 5.2. The holder is made of oxygen-free high thermal conductivity (OFHC) copper. The clamping can be adjusted with a linear piezo stage (*model: SLC1720, company: SmarAct*), which moves a

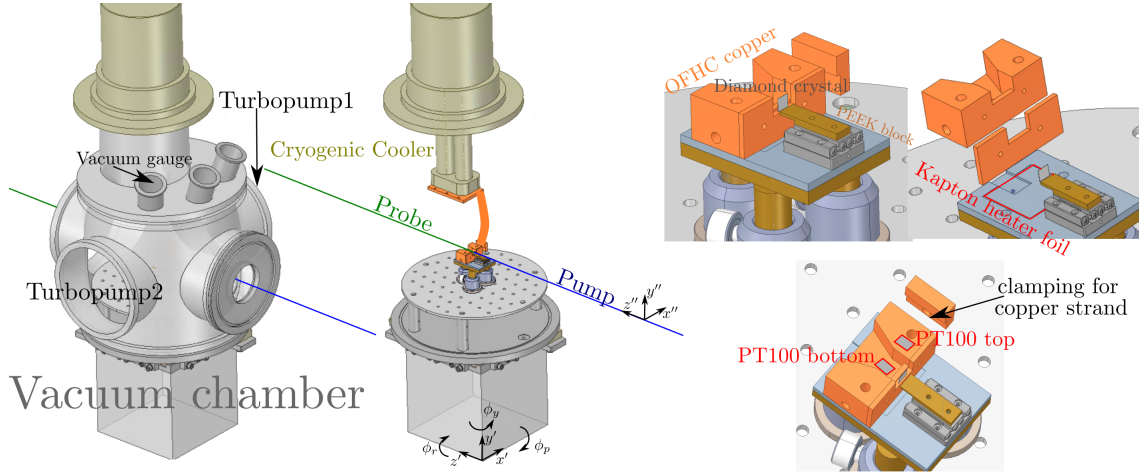


Figure 5.2.: Illustration of the vacuum chamber and the crystal holder.

block of PolyetherEtherKetone (PEEK). The temperature of the holder is measured with two PT100 resistors at the bottom and the top of the holder as illustrated in Fig. 5.2. The resistors are clamped mechanically. The bottom of the holder is made of stainless steel. Between the steel plate and the copper a kapton heater foil (*model*: 317-KAPH-1/1-V3, *company*: allecra) is placed of size 25 mm x 25 mm.

Cryogenic cooling A single-stage cryogenic pulse tube cooler (*model*: PTS 8030-HT, *company*: TransMIT) is connected to the holder with a OFHC copper strand. The heater and PT100 sensors of the holder are connected to a PID controller (*model*: 330, *company*: LakeShore), which adjusts the temperature of the holder to the desired temperature value.

Vacuum chamber The vacuum chamber is illustrated in Fig. 5.2. The pressure in the chamber is measured with an active wide range vacuum gauge (*model*: ATMION, *company*: VACOM). Two turbopumps (*model*: HIPACE80, *company*: PFEIFFER) and (*model*: TMU 261, *company*: PFEIFFER) are used to create a vacuum pressure $P < 10^{-6}$ mbar.

Alignment The alignable axes ($x'-y'-z'$, $x''-y''-z''$, $\phi_r-\phi_y-\phi_p$) of the experimental setup are illustrated in Fig. 5.2. The vacuum chamber is on top of some positioning stages, which allows to move the chamber in $x'-y'-z'$ -direction with micrometer precision. Three additional stages can also be used to tilt the chamber around the roll ϕ_r , the yaw ϕ_y and the pitch ϕ_p axes. The chamber is design in a way that the intersection point of these axes meet at the position of the crystal. All motors can be addressed with digital position values. The pump laser is also on top of the same positioning $x'-y'-z'$ stages like the vacuum chamber. It is further possible to align the position of the pump laser relative to the crystal position in y'' and z'' -direction mechanically and in x'' -direction with digital addressing. The probe laser is placed on an optical table with fixed position.

Knife edge method Putting an opaque crystal into the holder and moving it step wise through the beam, while measuring the average power behind the crystal gives data that can be used to calculate the laser spot size. This technique is called the knife edge method [ASL⁺09] and is illustrated in Fig. 5.3c. Assuming the z -direction is parallel to the direction of the beam propagation, the intensity of a Gaussian beam in Cartesian coordinates at a fixed position z is given by (see Eq. 2.33) :

$$I(x, y) = I_0 \exp(-2[(x - x_0)^2 + (y - y_0)^2]/W^2), \text{ where } \rho_r^2 = x^2 + y^2, \quad (5.1)$$

where W is the beam radius at the fixed position z . As illustrated in Fig. 5.3c, moving a knife which is parallel to the y -axis through the beam in x -direction gives the normalized transmitted power obtained by the integral:

$$P_N(x, y) = \frac{\int_{-\infty}^x \int_{-\infty}^{\infty} I(x', y') dy' dx'}{\int_{-\infty}^{\infty} \int_{-\infty}^{\infty} I(x', y') dy' dx'} \quad (5.2)$$

$$P_N(x) = \frac{1}{2} \left[1 + \operatorname{erf} \left(\frac{\sqrt{2}(x - x_0)}{W} \right) \right] \quad (5.3)$$

The fitting of Eq. 5.3 can be carried out by using a Python script containing the *scipy* module and using *scipy.optimize.curve_fit*.

Pump laser The pump laser is a pulsed UV laser (*model*: FQSS 213-50, *company*: CryLas), which operates at a wavelength of 213 nm and emits pulses with a repetition frequency of 20 Hz. The pulse duration is about ≈ 1.5 ns, the exact temporal profile $U(t)$ has been measured with an ultrafast photodiode (*model*: UPD-200-UP, *company*: ALPHALAS) in combination with an oscilloscope (*model*: WaveMaster 8 Zi-B, *company*: Teledyne LeCroy). The variations of the pulse shape and amplitude from pulse to pulse are less than $\pm 5\%$ and the averaged signal considering a few tens of sweeps is such stable that the oscilloscope measures a nearly static signal, thus these kind of variations can be neglected in the context of this work. The temporal profile of the laser is illustrated in Fig. 5.3b and has been normalized with: $U(t)/(\int_0^T U(t') dt')$, where T is the time span illustrated in Fig. 5.3b.

The spot size of the laser has been determined with two different techniques. The first is to place the screen of a UV converter (*model*: BSF08R12N, *company*: DataRay Inc.) in combination with a beam profiler (*model*: LBP2-HR-VIS, *company*: Newport) at the position¹ of the crystal. With this method the shape of the laser beam can determined as illustrated in Fig. 5.3d. The second method is the knife edge method (Fig. 5.3c). For the UV laser, diamond is a opaque material, therefore the edge of the diamond crystal can be used to partly cut the laser spot. Moving the diamond in $5 \mu\text{m}$ steps through the beam and measuring the average laser power at each step yields the curve plotted

¹For this measurement the holder and the crystal have to be removed from the vacuum chamber.

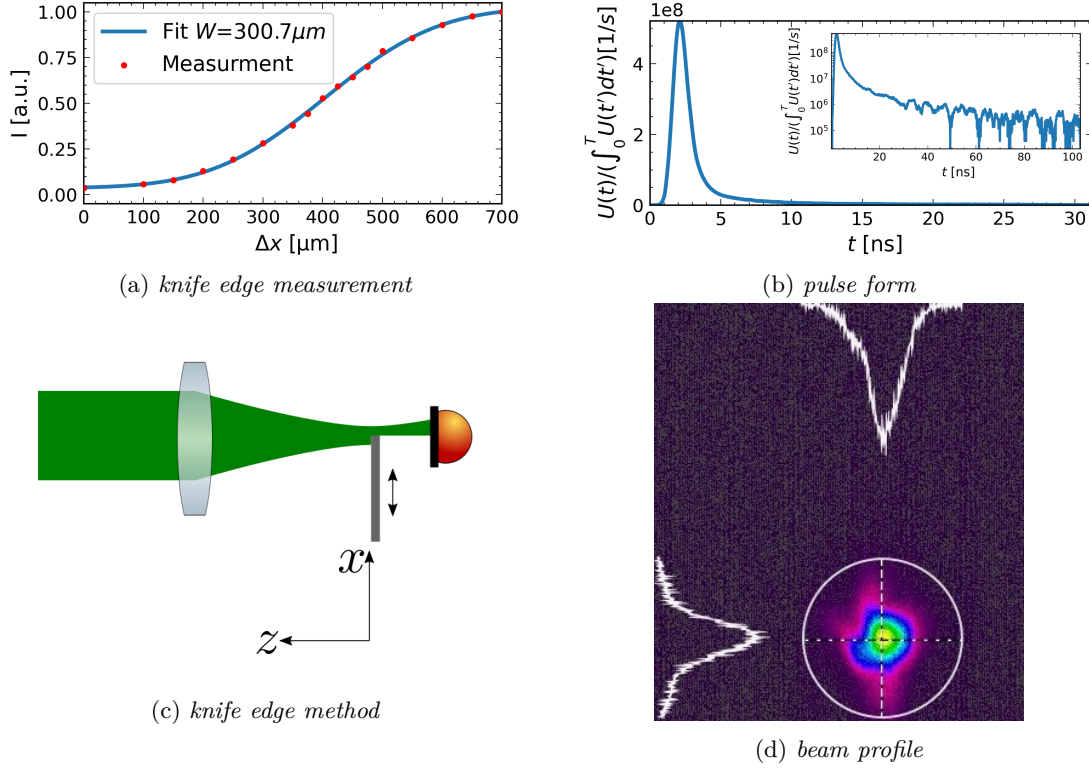


Figure 5.3.: (a) Measurement of beam radius W . (b) Temporal profile of pump laser pulse (c) Sketch of knife edge method. The y -axis is in direction out of plane in this illustration. (d) Spatial profile measured with beam profiler.

in Fig. 5.3a. Assuming a Gaussian profile and fitting this curve with Eq. 5.3 gives the radius $W = 300.7 \mu\text{m}$. The pulse energy of $E_p = (44.6 \pm 5.0) \mu\text{J}$ has been measured with a thermal sensor at the position of the crystal.

Measurements of temperature dependent absorption coefficient As mentioned in Section 4.2 the value of the absorption coefficient is $\alpha_k = 2008.8 \text{ cm}^{-1}$ at room temperature. To measure the temperature dependence of α_k a photodiode (*model*: DET10A/M, *company*: Thorlabs) is placed behind a SC HPHT crystal to measure the pulse intensity of the UV laser, which has a wavelength of 213 nm. The crystal has a thickness of $(100 \pm 10) \mu\text{m}$. The crystal used for these measurements is not the crystal used for the measurements presented in the following pump-probe experiment. However, it has nearly the same geometrical shape as the CVD diamond used in the pump-probe experiment. The ^{13}C content of the HPHT diamond crystal might be a bit higher than 1.1%, as reported by the manufacturer *Applied Diamond, Inc.*

The photodiode, which is used for the measurements is aligned² such that the signal reaches a maximum value. The peak value of the pulse shape (comparable to Fig. 5.3b) measured with the oscilloscope has a value of about $U = 3 \text{ V}$. The temperature of the holder is reduced step wise and the change of the voltage is measured by noting the peak

²The pump laser radius was larger than the detector size for these measurements.

value of an average signal (500 sweeps) of the pulse shape at each temperature³ value. At the last measurement point the photodiode was realigned and it could be noted that the diode was still at the position where the signal has been at its maximum.

Ignoring for simplicity that the reflectance may also be temperature dependent the ratio of the voltage value U_0 measured at room temperature and the voltage value, which is proportional to the intensity (Eq. 2.60) measured at a lower temperature $U(T)$ may be referred to:

$$\frac{U(T)}{U_0} = \frac{\exp(-d(T)\alpha_k(T))}{\exp(-d_0\alpha_{k0})}, \quad (5.4)$$

where $\alpha_{k0} = 2008.8 \text{ cm}^{-1}$ is the absorption coefficient at room temperature, $d_0 = 100 \text{ }\mu\text{m}$ the thickness of the diamond crystal and $d(T)$ the temperature dependent thickness of the diamond crystal which may be calculated by:

$$d(T) = d_0 + \Delta d(T), \quad \text{where} \quad \Delta d(T) = d_0 \int_{T_0}^T \alpha(T') dT'. \quad (5.5)$$

Here $T_0 = 300 \text{ K}$ is the room temperature value and $\alpha(T)$ is the temperature dependent thermal expansion coefficient. Using Eq. 5.4, Eq. 5.5 and the values of the fitted function for the thermal expansion coefficient (Fig. 4.5) the following equation may be used to measure the deviation of the absorption coefficient in relation to the room temperature value:

$$\alpha_k(T) - \alpha_{k0} = -\frac{\ln\left(\frac{U(T)}{U_0}\right) - d_0\alpha_{k0}}{d(T)} - \alpha_{k0}. \quad (5.6)$$

As shown in Fig 5.4 the measured deviation is much smaller than the room temperature value $\alpha_{k0} = 2008.8 \text{ cm}^{-1}$ and the corresponding penetration depth $\zeta = 1/\alpha_k$ may be considered to be approximately $\zeta \approx \frac{1}{2012 \text{ cm}^{-1}} \approx 5 \text{ }\mu\text{m}$ in the temperature range from 60 K to 300 K. For the sake of completeness it should be clarified that the reflectance change due to temperature change has not been measured in this work. Thus a change of the reflectance could also cause the deviation illustrated in Fig 5.4. Also, it cannot be excluded that the deviation is higher than illustrated in Fig 5.4 because the reflectance change might compensate the measured change of the absorption coefficient. A measurement of the reflectance would also be possible but not with the alignment of the current experimental setup and thus it has not been carried out in this work. Taking into account the thickness tolerance of the crystal $\Delta d_0 = 10 \text{ }\mu\text{m}$ the following error calculation, which has been used for the calculation of the error bars in Fig 5.4, may be used:

$$\Delta(\alpha_k(T) - \alpha_{k0}) = \left| \frac{\partial \alpha_k(T)}{\partial d_0} \Delta d_0 \right| = \left| \frac{\ln\left(\frac{U(T)}{U_0}\right)}{d_0^2(1 + \int_{T_0}^T \alpha(T') dT')} \Delta d_0 \right|. \quad (5.7)$$

³The temperature values are measured at the bottom position of the holder. The temperature difference to the values measured at the top of the holder is illustrated by the error bars in Fig. 5.4.

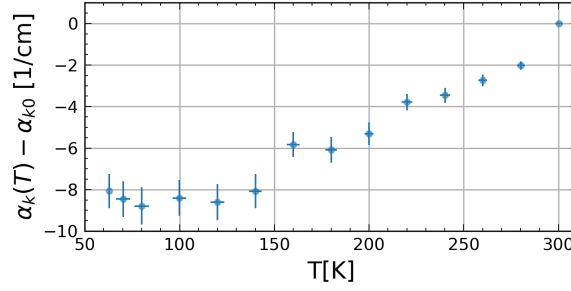


Figure 5.4.: Measured temperature dependent absorption coefficient for SC HPHT diamond at a wavelength of 213 nm.

5.1. Michelson interferometer

To build up a Michelson interferometer a linearly polarized single frequency continuous wave laser (*model*: Sapphire SF, *company*: COHERENT) operating at a wavelength of 532 nm with an output power of $P = 150$ mW is used. This laser has a linewidth of $\Delta\nu < 1.5$ MHz and a M^2 of < 1.05 . The factor $M^2 = W_{0R}\theta_{dR}\pi/\lambda$ is a numerical measure describing the deviation of a real laser beam with beam waist radius W_{0R} and angular divergence $\theta_{dR} = \lambda/\pi W_{0R}$ from the idealized Gaussian beam discussed in Section 2 [ST19, p. 85]. The M^2 value of the CW laser is near the value of an ideal Gaussian beam ($M^2 = 1$), thus it may be approximated as an ideal Gaussian beam for a rough calculation considering focusing optics. In context of paraxial ray optics the q -parameter (Eq. 2.26) of a Gaussian beam may be used in combination with the ABCD law [ST19, p. 93] to describe the focusing of the beam by various kinds of lenses. Taking into account the focal length of the lenses and the distance of the lenses to the beam waist the beam propagation may be predicted to some extent. The position of the beam radius and the distance of the waist measured from the output of the laser housing has been specified by the manufacturer of the CW laser. Using these information, for the needs of this work the focusing and collimating of the laser beam by various kinds of lenses as sketched in Fig. 5.5 could be predicted with sufficient accuracy. For the calculations the software *Just Another Mode Matching Tool* (JamMt) has been used⁴. The lenses of the experimental setup illustrated in Fig. 5.5 are used to collimate and focus the beam in a way that the focal planes lay on the surface of the diamond crystal and at the detector areas.

At the PBS₂ (*model*: CCM1-PBS25-532, *company*: THORLABS) (see Fig. 5.5) the beam is separated into an in x -direction linearly polarized part with magnitude $|E_{T0}|$, which is transmitted and an in y -direction linearly polarized part with magnitude $|E_{R0}|$ which is reflected (see Section 2 Eq. 2.45). The path of the reflected beam propagating in the direction to the diamond crystal will be called the signal arm of the interferometer in the following part of this work and the transmitted path which is propagating in direction of the mirror which is mounted on a piezo will be called the reference arm. The ratio of the

⁴Using the approximation of an idealized Gaussian beam and considering the focal lengths of the lenses in context of a thin lens approximation.

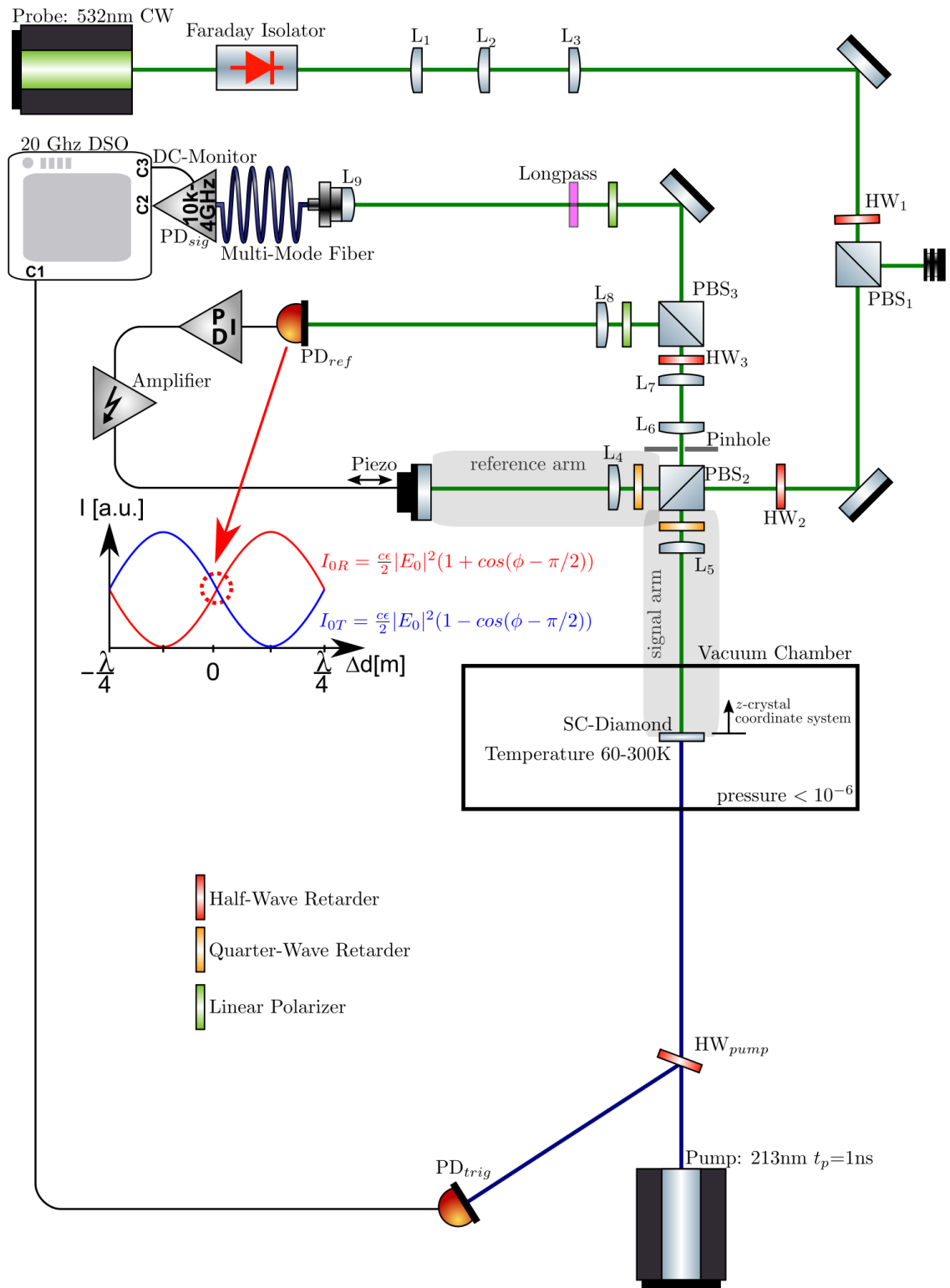


Figure 5.5.: *Experimental pump-probe setup used in this work illustrated with the ComponentLibrary by Alexander Franzen, which is licensed under a Creative Commons Attribution-NonCommercial 3.0 Unported License. A detailed description of the experimental setup is given in Section 5.1.*

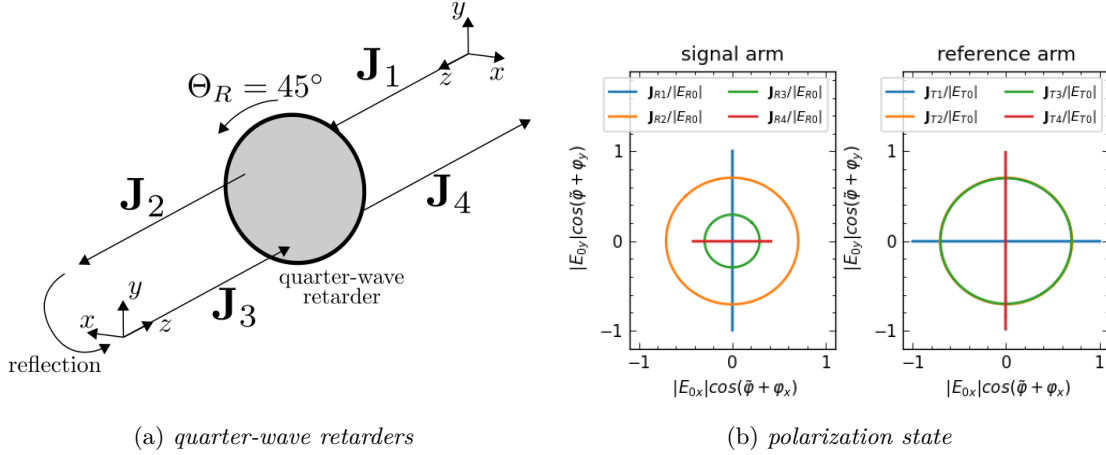


Figure 5.6.: (a) Illustration of beam path in the signal and reference arm of the interferometer. (b) Polarization states of in the signal and reference arm, calculated with Jones matrices introduced in Section 2.

magnitude of the transmitted and reflected electric field (or intensity) can be adjusted by the half-wave retarder (*model*: WPH10ME-532, *company*: THORLABS) HW_2 in front of the PBS_2 . To understand the purpose of the quarter-wave retarders (*model*: WPQ10E-532, *company*: THORLABS) in the reference and signal arm the illustration in Fig. 5.6 may be helpful. The reflected beam at the PBS_2 , which can be associated with the Jones vector \mathbf{J}_{R1} and which is propagating in direction to the diamond crystal (signal arm) is illustrated by the blue line in the left plot of Fig. 5.6b, where the amplitude has been normalized such that the magnitude of the Jones vector is $|\mathbf{J}_{R1}| / |E_{R0}| = 1$. The Jones vector \mathbf{J}_{R1} is linear polarized in y -direction. After the quarter-wave retarder which is rotated⁵ by $\Theta_R = 45^\circ$ the wave is circularly polarized⁶ but still has a magnitude of $|\mathbf{J}_{R2}| / |E_{R0}| = 1$, the phase difference is $\arg(E_{R0y2}) - \arg(E_{R0x2}) = 90^\circ$. After the reflection which can be calculated with the Jones matrix of Eq. 2.53 and the refractive index of diamond (Section: 4.2) the magnitude is reduced $|\mathbf{J}_{R3}| / |E_{R0}| = 0.4164$. Also, the polarization state is now circular with a phase difference of $\arg(E_{R0y3}) - \arg(E_{R0x3}) = -90^\circ$. Considering the sign convention⁷ used in this work the reflected wave is now facing a quarter-wave retarder rotated by $\Theta_R = -45^\circ$. After propagating through the quarter-wave retarder the wave is linearly polarized in x -direction having a magnitude of $|\mathbf{J}_{R4}| / |E_{R0}| = 0.4164$. Due to the linear polarization in x -direction the wave is now transmitting through the PBS_2 . It should be noted that without the quarter-wave retarder the reflected beam would be polarized in y -direction and thus it would be reflected at the PBS_2 , resulting in a beam propagation directed back into the output of the laser housing. The propagation of the beam in the reference arm can be explained with the same underlying concept (and is illustrated in right plot of Fig. 5.6b). The quarter-wave retarder causes in this case that the reflected wave from the mirror after the quarter-wave retarder is polarized in y -direction which

⁵The used convention for the rotation is described in Section 2.1.3

⁶For the calculations the Jones matrices described in Section 2.1.3 have been used.

⁷The sign convention is explained in Section 2.1.3.

causes a reflection at the PBS₂. However, due to the high reflectance of the silver⁸ mirror the magnitude after reflection, given by $|\mathbf{J}_{R4}| / |E_{R0}| = 0.9916$ is significantly higher. To achieve that the magnitude of the electric field, which is coming from the signal arm is equal to the one of the reference arm, the half-wave retarder HW₂ can be aligned appropriately. The setup is adjusted in a way that the beam waists coming from each interferometer arm are equal and the spatial position of the beam shape is nearly the same. For the alignment the beam profile has been measured at various positions in the experimental setup. The Jones vectors of the two beams after the PBS₂, which are propagating in direction of the PBS₃ (*model*: PBS12-532 , *company*: THORLABS) can be denoted by a Jones vector coming from the signal arm \mathbf{J}_{sig} and a Jones vector coming from the reference arm \mathbf{J}_{ref} :

$$\mathbf{J}_{sig} = \begin{pmatrix} |E_{0x1}|e^{i\varphi_{x1}} \\ 0 \end{pmatrix} \quad \mathbf{J}_{ref} = \begin{pmatrix} 0 \\ |E_{0y2}|e^{i\varphi_{y2}} \end{pmatrix}. \quad (5.8)$$

The half wave retarder HW₂ in front of PBS₂ is aligned such that: $|E_{0x1}| = |E_{0y2}| = |E_0|$.

It should be mentioned that due to the transparency of diamond at a wavelength of 532 nm the laser is reflected at both the front and back side of the crystal. A crystal with perfect parallel surfaces would give an overlap of the beam reflected at the front and back side of the crystal and thus needed to be considered as an additional contribution to \mathbf{J}_{sig} . However, due to the wedge of the crystal (Fig. 5.1) the undesired reflection can be cut away by the pinhole after PBS₂.

The interference of monochromatic Gaussian beams has been discussed in Section 2.1.3. The size and position of the laser beams from the signal and reference arm have been aligned in a way that the beam radii are nearly equal and such that the center of both beams is nearly at the same position. The maximum intensity for such aligned interfering Gaussian beams is given by Eq. 2.41. Considering Eq. 2.43 it can be seen that the polarization states of Eq. 5.8 will not interfere with each other and the intensity is $I_0 = \frac{c\epsilon}{2}|E_0|^2$. However, after the half-wave retarder HW₃ (*model*: WPH05ME-532 , *company*: THORLABS), which is rotated by angle of $\Theta_R = 22.5^\circ$, the polarization state of \mathbf{J}_{sig} and \mathbf{J}_{ref} are changed to:

$$\mathbf{J}_{sig} = |E_0|e^{i\varphi_1} \frac{1}{\sqrt{2}} \begin{pmatrix} 1 \\ -1 \end{pmatrix} \quad \mathbf{J}_{ref} = |E_0|e^{i\varphi_2} \frac{1}{\sqrt{2}} \begin{pmatrix} -1 \\ -1 \end{pmatrix} \quad (5.9)$$

The values of φ_1 and φ_2 can be aligned, by changing the position of the diamond crystal and the reference mirror, respectively. The PBS₃ transmits the in x -direction polarized part of the beams and reflects the in y -direction polarized part. Thus, by considering Eq. 2.43 the transmitted intensity becomes $I_{0T} = \frac{c\epsilon}{2}|E_0|^2(1 - \cos(\varphi_1 - \varphi_2))$ and the reflected $I_{0R} = \frac{c\epsilon}{2}|E_0|^2(1 + \cos(\varphi_1 - \varphi_2))$. The phase difference $\phi = \varphi_1 - \varphi_2$ can be

⁸For the calculation the literature values of the refractive index $n = 0.054$ and the absorption coefficient $\alpha_k = 8.0996 \times 10^5 \text{ cm}^{-1}$ have been used [JC72].

calibrated by changing the path difference Δd , which could be realized⁹ for example by changing the position¹⁰ of one interferometer arm while holding the position of the other constant: $\phi = \frac{4\pi\Delta d}{\lambda}$. The mirror of the reference arm is mounted on a piezo (*model*: P-885.11, *company*: Physik Instrumente). The reflected part of PBS₃ is measured with a photodiode (*model*: DET10A/M, *company*: Thorlabs), which is connected to the input of an analog PID controller (*model*: SIM960, *company*: Stanford Research Systems). The output of the PID controller is connected to the input of a modified¹¹ piezo amplifier (*model*: E-617.00F, *company*: Physik Instrumente), which stabilizes the working point of the interferometer by controlling the position of the mirror in the reference arm of the interferometer at a position in the middle between destructive and constructive interference, as illustrated in Fig. 5.5. The transmitted part of the PBS₃ is collected by a high speed photoreceiver (*model*: 1591NF, *company*: Newport). The high speed photoreceiver can be used in two different operation modes AC and DC. In DC mode the photoreceiver measures with the full band width from zero to 4.5 GHz. The AC mode uses a bandwidth of 10 kHz to 4.5 GHz. The voltage measured in the DC mode with the oscilloscope is proportional to the intensity of the interfering beams $U \sim I_{0T}$. If the interferometer is aligned correctly the single beam intensity from the signal and reference arm should be equal. The single beam intensity can be observed by blocking one of the interferometer arms and measuring the constant voltage value with the oscilloscope (*model*: WaveMaster 8 Zi-B, *company*: Teledyne LeCroy) using the DC mode. Setting the working point to be the zero position, the function of the displacement w (Eq. 3.1) of the reflecting diamond surface in z -direction gives:

$$U(w) = 2U_s \left(1 + \cos \left(\frac{4\pi w}{\lambda} - \frac{\pi}{2} \right) \right). \quad (5.10)$$

Here the coordinate system of the crystal deformation has been defined¹² so that a positive displacement in z -direction is given in the direction marked near the crystal in Fig. 5.5. The intensity of the interfering beams is stabilized with the PID controller at the working point to a value of $U_0 \approx 2U_s$. Here U_s is the value for a single beam, which can be measured if one of the interferometer arms is blocked. As illustrated in Fig. 5.7 the working point is localized, at a value which is half of the maximum achievable value. Considering only small values for w of a few nm the first Taylor series term may be used as an approximation:

$$U(w) \approx 2U_s + \frac{U_s 8\pi}{\lambda} w. \quad (5.11)$$

⁹Under the assumption that the refractive index of the medium through which the beams propagate has a constant value.

¹⁰In the propagation direction of the beam.

¹¹It was recognized that the amplifier produces a high frequency oscillation with time periods of a few microseconds and an amplitude of a few nanometers. This undesired noise signal could be eliminated by installing a simple RC low pass to the output of the amplifier.

¹²With this convention it can be seen that $w = -\Delta d$ which causes $I_{0T} \sim (1 - \cos(\frac{4\pi\Delta d}{\lambda} - \frac{\pi}{2})) = (1 - \cos(\frac{-4\pi w}{\lambda} - \frac{\pi}{2})) = (1 + \cos(\frac{4\pi w}{\lambda} - \frac{\pi}{2}))$

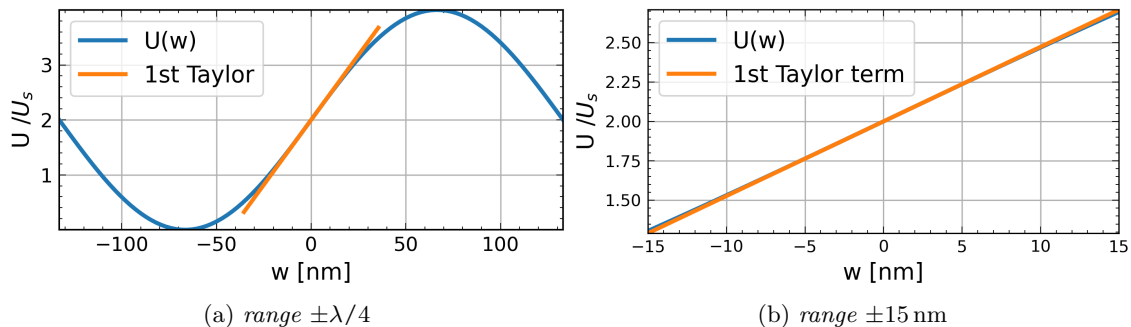


Figure 5.7.: (a) Function of the voltage calculated with Eq. 5.10, which could be measured with the oscilloscope when the interferometer is stabilized with a PID controller at the working point $U_0 \approx 2U_s$ as a function of the displacement w of the diamond surface. (b) Zoom of the linear range Eq. 5.11.

If only displacements smaller than a few nanometers are considered then the conversion factor between the voltage change of the signal measured with the oscilloscope is proportional to the displacement. The conversion factor in this case is given by the second term on the right hand side of Eq. 5.11.

If the interferometer is not stabilized, a time varying signal as illustrated in Fig. 5.8 is measured. The main reason for this instability is probably that the vacuum chamber is standing on a heavy granite block and the interferometer on an optical table, which means that each interferometer arm has a different damping response to surrounding vibrations. Also it should be mentioned that the reference arm and a part of the signal arm propagate through air and local density fluctuations (temperature changes, air draught) may change the local value of the refractive index of air resulting in a change of the optical path length of the wave propagation. However, with the help of a PID controller, which is adjusting the position of the working point, these random variations can be compensated as illustrated in Fig. 5.8. Regarding these measurements it should be mentioned that the high speed photoreceiver (*model*: 1591NF, *company*: Newport) can output a voltage up to about 1 V before reaching saturation¹³, thus there might be a systematic error regarding voltage value higher than 1000 mV. As show in Fig. 5.8 the intensity of the interfering beams can vary between a minimum of nearly zero and a maximum which is about four times the single beam value. This may be considered as a verification of the assumption that the laser beams can be considered as interfering monochromatic waves. It shows that the beams have been aligned sufficiently accurate to have a spatial overlap which fulfills the predicted case discussed in Section 2 (interference of Gaussian beams). It should be mentioned that in general when the interference of a real laser beam is investigated temporal and spatial coherence may be considered, because the described intensity range from zero to four times of the intensity of a single beam for interfering beams could be reduced due to incoherence effects. An introduction to this topic can be found in textbooks [ST19, Chapter 11] [Hec16, Chapter 12]. However, for the needs of this work

¹³For higher output values the response might become non linear.

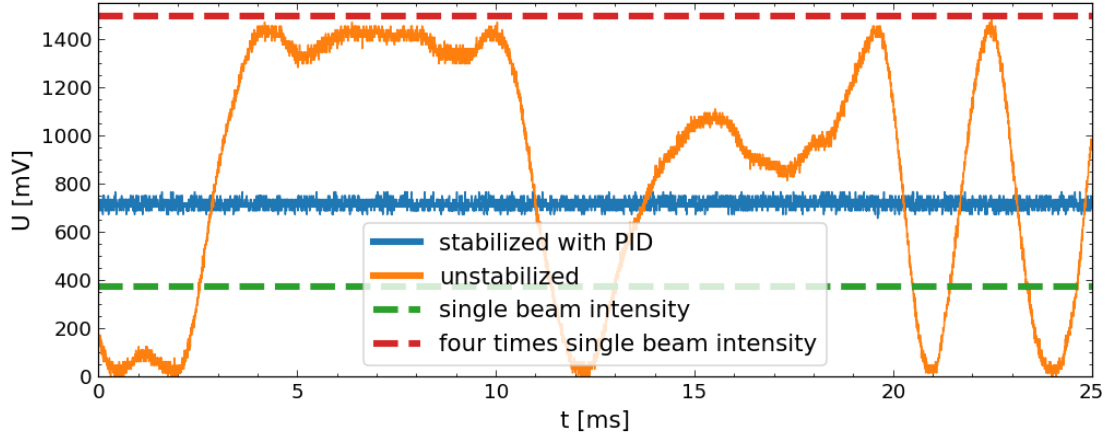


Figure 5.8.: Measurement using the DC mode of the high speed photoreceiver. Comparing working point stabilization to a signal which is measured over the same time range for an unstabilized condition. The voltage value measured for the single beam intensity in the illustrated measurement was 374 mV.

the measurement shown in Fig. 5.8 indicate that the interference of the beams can be considered in good approximation as the interference of nearly perfectly coherent waves.

Considering Fig. 5.5 the use of some of the illustrated components have not been explained so far. These components do not effect the principle of the interferometer, which has been discussed in the text above, however for the sake of completeness they will now be explained. The lenses L_1 (*model*: AC254-080-A, *company*: Thorlabs), L_2 (*model*: AC254-060-A, *company*: Thorlabs) and L_3 (*model*: AC254-125-A, *company*: Thorlabs) are used to collimate the beam. The beam radius after L_3 of the collimated beam is about $W \approx 1250 \mu\text{m}$. A polarizing beamsplitter PBS_1 in combination with a rotatable half-wave retarder gives control over the intensity, which is transmitted or reflected by the PBS as described in Section 2.1 Fig.2.3a. The PBS_1 (*model*: CCM1-PBS25-532, *company*: THORLABS) in combination with the half-wave retarder HW_1 (*model*: VA5-532, *company*: Thorlabs) is used to reduce the laser intensity for a safe alignment procedure. The lenses L_4 and L_5 are of the same type (*model*: AC254-300-A, *company*: Thorlabs) and are used to focus the beam. The beam size at the focal spot lying on the surface of the crystal and the reference mirror is $\omega_0 = 45.4 \mu\text{m}$ and has been measured with the knife edge method¹⁴ (Fig. 5.9). The shape of the beam has nearly the same diameter in all directions in the xy -plane, which has been obtained with a beam profiler at the position of the crystal. The lenses L_6 (*model*: AC254-100-A, *company*: Thorlabs) and L_7 (*model*: AC254-040-A, *company*: Thorlabs) are used to reduce the size of the beam radius to a collimated beam with a radius of about $500 \mu\text{m}$. The linear polarizers (*model*: LPVISC100-MP2, *company*: Thorlabs) are used to reduce the intensity of the beams to avoid exceeding the maximum intensity values which have been specified by the manufacturers for the photodiodes. The lens L_8 (*model*: AC254-400-A, *company*: Thorlabs) is used to focus the beam onto the

¹⁴For the measurement a $100 \mu\text{m}$ thick silicon crystal has been used.

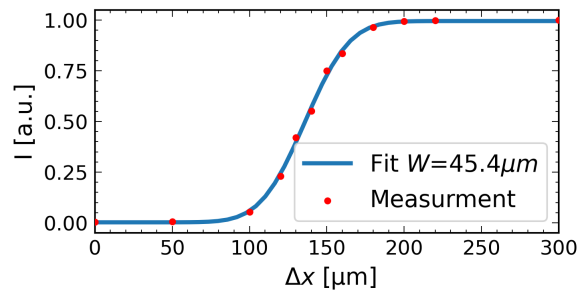


Figure 5.9.: Knife edge measurement of probe laser spot.

sensor area of the photodiode. The lens L_9 (*model*: F220FC-532, *company*: Thorlabs) is used to focus the beam into the entrance of a multimode fiber (*model*: M42L02, *company*: Thorlabs), which is connected to the photoreceiver. The photoreceiver is directly¹⁵ connected to the input of the oscilloscope. The Faraday isolator¹⁶ (*model*: IO-5-532-HP, *company*: Thorlabs) is used to avoid back reflection into the laser, which might occur due to reflections at the surfaces of the lenses and PBSs. Metallic mirrors (*model*: PF10-03-P01, *company*: Thorlabs) are used to change the direction of the beam propagation. It should be mentioned that the reflection at these mirrors may also influence the polarization state [ST19, p. 210], however these effect is not discussed further in this work, because even if the beam is elliptically polarized due to a reflection at a metallic mirror at some point in the setup, the PBS_2 would still only transmit the linearly polarized wave in x -direction and reflect a wave polarized in y -direction. The phase difference thus may be different as assumed in the discussion above, however the phase difference in this setup can be aligned arbitrarily by changing the position of the reference mirror (or the position of the diamond crystal). Thus, the explanations given for the interferometer above are also valid if the wave at the position HW_2 is elliptically polarized. The pump laser passes a half-wave retarder HW_{pump} before reaching the diamond crystal. The pump laser is partly reflected at the surface of the half-wave retarder and the reflected beam is propagating in direction of the sensor area of a photodiode (*model*: DET10A/M, *company*: Thorlabs). This is the only need for the HW_{pump} in this experimental setup. It should be mentioned that for this purpose also a partly transparent plate could be used. The impact of the polarization state of the pump laser on the material interaction has not been investigated further in this work and is assumed to have not a relevant impact on the experiment.

5.2. Pump-probe measurement

In this section the implementation of the pump-probe measurements is described in detail and the data measured with the experimental setup will be presented. A detailed discussion about the origin of these signals is postponed to Section 6.

¹⁵No cable is needed to connect the photoreceiver to the oscilloscope.

¹⁶This optical isolator transmit the light only in one direction. For a detailed description of the technical concept see [ST19, p. 238].

For all measurements in this section the probe beam is reflected at the back side of the crystal, regarding to the side where the pump beam enters the crystal. As illustrated in Fig. 5.5 each pump laser pulse sends a trigger signal to channel 1 of the digital storage oscilloscope. The ultrafast photodiode is connected to channel 2 and measures the deviation from the working point. In addition a DC monitor signal of the photoreceiver is connected to channel 3. This signal is very helpful when signals in AC mode¹⁷ are measured, because it gives the ability to check if the working point stabilization works. If the working point stabilization works correctly the DC monitor channel of the oscilloscope shows a constant signal with the desired value.

The oscilloscope has a bandwidth of 20 GHz. This bandwidth should be sufficiently high to recognize the complete high frequency content of the signal provided by the photodiode with frequency bandwidth up to 4.5 GHz. The 4.5 GHz corresponds to a time span of about 222 ps, which may be considered the maximum temporal resolution of the experimental setup. The maximum displacement value considered in this work is in the range of about 1 nm. Therefore, an approximately linearly connection of the measured signal in mV and the displacement is given by Eq. 5.11. The trigger signal defines the beginning of a measurement which is displayed on the screen of the oscilloscope. It is assumed that the crystal returns to an undisturbed state after a time span of $T=50$ ms, which is related to the repetition rate of the pump laser, or in other words, it is assumed that the signal created by the pump laser pulse has no influence on the following signal introduced by the next pump pulse. Further it is assumed that the signal is reproducible, which seems reasonable because the intensity of the pump laser (Fig. 5.3b) is very stable in shape and amplitude. Further, the beam profile illustrated in Fig. 5.3d is such stable, that no spatial fluctuations are noticeable on the micrometer range measured with the beam profiler. The pump-probe experiments have been carried out at different temperature values of the holder. The crystal is placed in vacuum and therefore no convective heat transport has to be assumed. Further, neglecting the radiative heat transfer it can be assumed that the crystal has nearly the same temperature as the value that has been measured with the PT100 resistors of the holder. The temperature of the holder is measured at two different points of the holder as illustrated in Fig. 5.2. As shown in Table 5.1 the temperature values are slightly different at each point and the temperature difference of the two points may be considered as an estimation for the tolerance of the crystal temperature value. The values of the spot sizes are shown in Fig 5.9 and Fig 5.3a. The interaction point of the pump and probe beam is illustrated in Fig. 5.10a. The probe laser is aligned in the center¹⁸ of the pump laser spot.

¹⁷If the AC mode of the photoreceiver is used, the stable DC signal, which is given when the working point stabilization is used, is not measured. Thus, the oscilloscope measures a signal of nearly 0 mV.

¹⁸A rough alignment is carried out by observing the position of the laser spot on the crystal with a camera. Fine alignment is carried out positioning the probe laser to maximizing the signal amplitude. As it will be discussed in detail in section 6.3 the maximum measurable displacement value can be expected to be located at the center position of the pump beam.

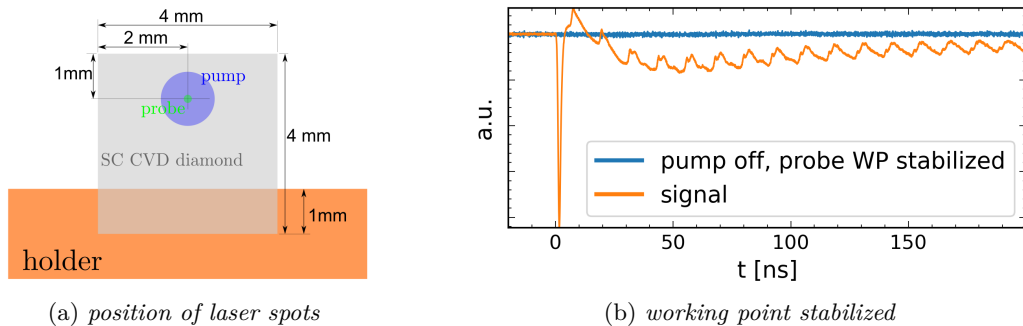


Figure 5.10.: (a) Locations of the pump/probe laser on the diamond crystal for the measurements carried out with a SC CVD diamond crystal. (b) Comparison of a signal measured with blocked pump laser (pump off) to a signal change caused by the absorption of the pump laser.

T_{plot} [K]	300	260	220	180	140	100	60
T_{top} [K]	300.0	260.0	220.0	179.99	139.19	103.45	60.01
T_{bottom} [K]	298.5	258.2	217.9	177.63	141.86	106.23	56.83

Table 5.1.: Temperature values measured with PT100 at bottom and top of the holder.

An important value for an oscilloscope measurement is the sampling rate which defines how much data points (samples) are taken per second. The maximum sampling rate which can be used by the oscilloscope is 80 GHz (80×10^9 samples per second). The sampling rate should be sufficiently high to cover all the features of interest in a signal, but considering a finite time span of the measurement it may be useful to reduce the sampling rate to reduce the amount of collected data. Also it should be noted that an oscilloscope can only store a limited amount of data in memory, which gives a limitation for the sampling rate considering measurements of larger time spans. The maximum time span which can be measured at a given sampling rate is given by the maximum amount of samples which can be stored by the oscilloscope (measured in points per signal) divided by the sampling rate. To reduce the noise of the measurements averaging over thousands of sweeps has been carried out. The averaging process is described in detail in the following part of this section. However, in this context it should be mentioned that this assumption may be wrong, when the response of the crystal gives a statistically varying signal for each pump pulse. If such a signal would have occurred in the measurements presented in this section it might be averaged out by the averaging process over thousands of sweeps.

Since the amplitude of the pump laser has a stable temporal shape it is useful to use averaging of many sweeps to reduce the signal to noise ratio of the measurement. The averaging process will be explained by the following example: Considering a single shot measurement, the oscilloscope outputs an amount of discrete data points for the measured amplitude (measured in Volt) and corresponding time steps. The amount of data points is given by the sampling rate multiplied by the period of the considered time span. For example considering a time span of 100 ns and a sampling rate of 40 GHz gives 4000 data

points. Since the data points have a constant time stepping value the time between two following points in the example is 25 ps. For convenience in the following example just one arbitrary time step (denoted by \tilde{t}) and its corresponding voltage value (denoted by \tilde{U}) from the in total 4000 possible points will be discussed. Now considering a second measurement (which may also be denoted by a new sweep), where the same time stepping is used, but 4000 new voltage points are measured, the voltage value at the arbitrary point in time for the first sweep may be denoted by \tilde{U}_1 and the voltage value for the second sweep by \tilde{U}_2 . Further, considering N sweeps the voltage value at the \tilde{N} 's sweep is $\tilde{U}_{\tilde{N}}$ and an averaging voltage value \tilde{U}_{avg} can be calculated by:

$$\begin{aligned}
 \text{Average value at 1st sweep: } & \tilde{U}_{avg1} = \tilde{U}_1 \\
 \text{Average value at 2nd sweep: } & \tilde{U}_{avg2} = \frac{\tilde{U}_1 + \tilde{U}_2}{2} \\
 \text{Average value at 3rd sweep: } & \tilde{U}_{avg3} = \frac{\tilde{U}_1 + \tilde{U}_2 + \tilde{U}_3}{3} = \frac{\tilde{U}_3}{3} + \frac{2\tilde{U}_{avg2}}{3} \\
 & \vdots \\
 \text{Average value at } N\text{th sweep: } & \tilde{U}_{avgN} = \frac{\tilde{U}_N}{N} + \frac{(N-1)\tilde{U}_{avgN-1}}{N}
 \end{aligned}$$

However, this averaging process is not only carried out for one arbitrary data point by the oscilloscope, but for all 4000 points considering the example. Thus, an averaging of the measured signal can be carried out by several sweeps to reduce the signal to noise ratio (provided that the noise which is superimposed the signal is random). The oscilloscope used in this work can take up to 1000000 sweeps.

5.2.1. Investigation of the connection between measured signal and the displacement of the crystal surface

Before presenting the measured displacement it has to be investigated if the measured signal of the oscilloscope can really be directly connected to the displacement of the crystal. Therefore, three different cases which could affect the signal are discussed in this section.

First a measurement has been carried out to see if the radiation of the pump laser has a direct impact on the signal. For this purpose the pump laser was activated, while the probe laser has been turned off. In front of the ultrafast photodiode which measures the signal an optical longpass filter (*model*: FEL0400, *company*: THORLABS) has been placed, which strongly attenuates wavelengths smaller than 400 nm. By using the longpass filter¹⁹ the signal of the ultrafast photodiode shows a nearly zero value indicating no direct impact of the pump laser on the measured signal.

Second, the working point stabilization has to be investigated. For this purpose a measurement has been carried out where pump and probe laser are activated, but the transmitted radiation after HW_{pump} (Fig. 5.5) in front of the pump laser has been blocked.

¹⁹Without the longpass filter a signal of the shape given in Fig. 5.3b can be measured.

Therefore, no pump laser radiation is reaching the crystal, but a trigger signal is still sent to the oscilloscope. In this case a constant value located at the working point which is adjusted by the PID controller is expected. As mentioned before, in the AC mode of the photodiode the output signal should be a constant value around zero. In Fig. 5.10b such a measurement is presented which shows a straight line as expected. This measurement proves that no surrounding noise sources show a noticeable effect to the signal. The measured time span in this case was 200 ns which corresponds to a frequency of 5 MHz and is far beyond the frequency range that can be controlled by the working point stabilization. The bandwidth of the PID controller is specified by the supplier with 100 kHz and the piezo amplifier shows for frequencies greater 10 kHz a very weak amplification. Therefore, an effect of the working point stabilization seems unlikely for time spans up to a few μs .

The third type of measurement, which has to be considered is the change of the reflectance due to the photon-matter interaction. This gives a change of the intensity of the signal arm, which then differs from the intensity of reference arm. The blue lines in Fig. 5.11 show the measurements of the intensity change due to change of the reflectance. These measurements have been carried out by blocking the reference arm of the interferometer. The measurements carried out with a blocked reference arm have been compared to the signal measured with the interferometer setup (Fig. 5.11). Both measurements were carried out in AC mode of the photodiode. In all measurements a peak at the beginning of the signal at $t = 0$ ns is visible, which is connected to a change of the reflectance. For the reflectance measurements it further can be seen that after this peak a signal with opposite sign regarding to the zero value $t < 0$ ns is present which has a much smaller value than the peak at $t = 0$ ns and possess oscillations. In Fig. 5.11a it can be seen that the overall signal measured with the interferometer apart from the peak in the beginning is much greater than the reflectance signal. However, at low temperatures as shown in Fig. 5.11b the difference is smaller than compared to the signal measured at room temperature.

The reflectance signal (blue line in Fig. 5.11) can affect the interferometer signal and the change for the reflectance may be connected to a change of the refractive index and/or the absorption coefficient (see Eq. 2.55). However, it should be noted that a change of the reflectance in this case is connected to the assumptions of the Maxwell's equations given by Eq. 2.6. These assumptions may be wrong regarding the interpretation of the measurement. As it will be discussed in Section 7 the change of the reflectance seems not to have a direct simple connection to a temperature change or a displacement field. Since the origin of reflectance change signal is unknown it is hard to predict which impact this kind of signal will have on the interferometer signal. Nevertheless, the reflectance signal causes, apart from the peak in the beginning of the signal, a significant smaller voltage change measured by the oscilloscope, which motivates to neglected this effect in the following presentation of the measurements. However, it should be reminded, that the reflectance change signal can give a systematic error to the interferometer signal which could not be predicted in this work.

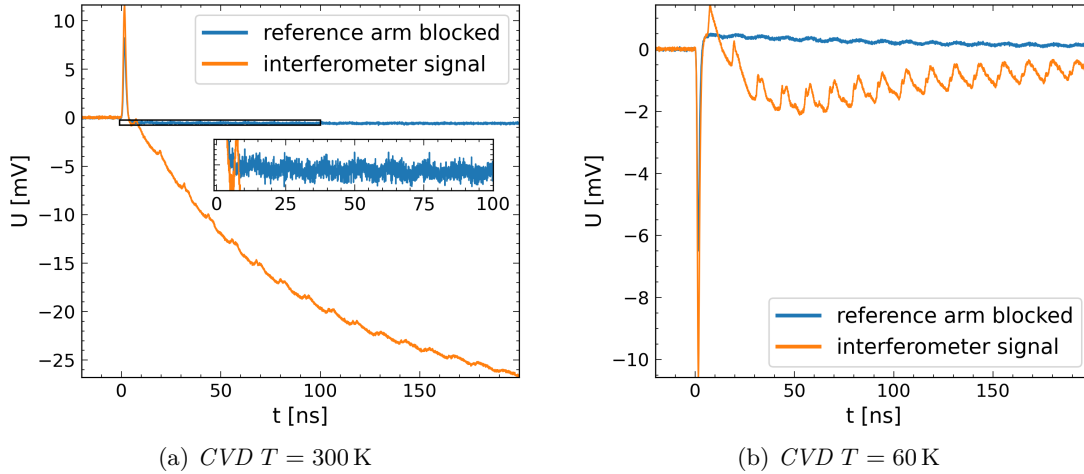


Figure 5.11.: Comparison of signal change due to a reflectance change which can be measured if the reference arm is blocked and an interferometer signal. The voltage value for single beam intensity for these measurements was 400 mV. (a) Measurement with a holder temperature of $T = 300$ K. (b) Measurement at $T = 60$ K.

Surprisingly, the amplitude of the peaks, which occur after $t = 0$, and the following oscillations are changing the magnitude and also the sign with decreasing temperature. Also it has been observed that amplitude and sign of the initial peak not only strongly depend on the temperature but also on the position of the pump laser beam relative to the probe laser beam. For example at an initial temperature value of 300 K it has been observed that moving the probe beam about $50 \mu\text{m}$ in lateral direction away from the center of the beam gives a peak with similar peak amplitude but an opposite sign. Moving the probe beam step wise away from the center it has been observed that the peak periodically changes the sign with distances of about $100 \mu\text{m}$ and the maximum reached value is reduced with increasing distance from the center. This effect could be investigated in detail with the experimental setup presented in this work to understand its origin and possible use for scientific applications. Investigating this topic in detail may be an interesting topic for upcoming projects.

Another assumption used to interpret the interferometer signal is that the area over which the probe beam spot extends has a nearly constant displacement value, thus the interferometer measurement is directly connected to a particular displacement value on the surface of the crystal. The validation of this approximation will be discussed in Section 6.3.

5.2.2. Development of displacement after photon-matter interaction

The time span of a few hundred nanoseconds corresponds to a frequency of a few MHz and is in particular interesting for this work because it represents the repletion rate of modern X-ray free electron laser facilities like the European XFEL. The heat load which is given by the absorption of a few tens of microjoules in this pump-probe experiment represents a similar heatload as expected for a saturated CBXFEL X-ray pulse [Rau21]. In Fig. 5.12

the displacement after the photon-matter interaction is shown. For these measurements a sampling rate of 40 GHz has been used. The measurements were taken by using the AC mode of the photodiode. With the approximations discussed in the previous section the conversion factor to calculate the displacement is given by Eq. 5.11. The voltage value measured for a single beam is $U_s = 400 \text{ mV}$, which gives a conversion factor of $0.0529 \text{ nm mV}^{-1}$. The crystal is assumed to be in rest (displacement is set zero) before the interaction. The time zero is set to the rise of the peak introduced by the reflectance change. The different initial temperature values are given by Table 5.1. The negative overall rise of the displacement observed in all measurements represents that the sample surface moves in the direction of the pump laser beam. The maximum value of this overall rise is reduced with decreasing temperature value. In all measurements periodic fringes are present which are repeated in a time span of about 12.08 ns (frequency 82.78 MHz). The repetition rate of the fringes does not change noticeable with temperature. This is visualized by the vertical lines in Fig. 5.12.

The lower limit of the bandwidth of the photodiode in AC mode is 10 kHz which corresponds to a time period of 0.1 ms. The measurements with this time range, using a sampling rate of 10 GHz, have been carried out at the temperature values 300 K, 220 K and 60 K. The corresponding measured temperature values of the holder are given in Table 5.1. For a better visualization different zoom levels starting at the time of the photon-matter interaction are shown in Fig. 5.13. From Fig. 5.13c it can be seen that nearly the maximum magnitude of the displacement is reached a few hundred nanoseconds after the startup time, as has been discussed before (Fig. 5.12). As illustrated in Fig. 5.13a the amplitude of the previously discussed fringes decreases significantly on a time scale of about 1000 ns. On larger time scales as shown in Fig. 5.13b and Fig. 5.13c it can be seen that the displacement created in the startup regime is followed by some oscillations which have all together a peak to peak amplitude in the range of the maximum value in the startup regime. The amplitude of these oscillations does not decrease noticeably on the time scale of 0.1 ms. It should be noted that for the sake of a comparable visualization all the illustrations in Fig 5.13 consider the same displacement range and also the starting point located at -1000 ns is the same for all of the three plots. To analyze the frequency components of the time varying signal in Fig. 5.13 a Fourier transformation has been carried out for values²⁰ $t > 20 \text{ ns}$. The computation is carried out with a Python script using the *scipy* [JOP⁺] module *scipy.fft*. The amplitude has been scaled by $2/N$, where N is the number of samples. As illustrated in Fig. 5.14a frequency components greater than a few MHz have a quite small amplitude. In Fig. 5.14b it can be seen that the amplitude of frequencies smaller than 1 MHz decreases significantly with the initial temperature of the crystal. Some modes are present at all temperatures that have been investigated, like the mode at around 0.9 MHz, whereas others are only present at low temperatures like the one at 0.4 MHz. As indicated by the frequencies around 5 MHz in Fig. 5.14c the

²⁰The choice of 20 ns is taken to exclude the effect of the reflectance peak directly after $t = 0$

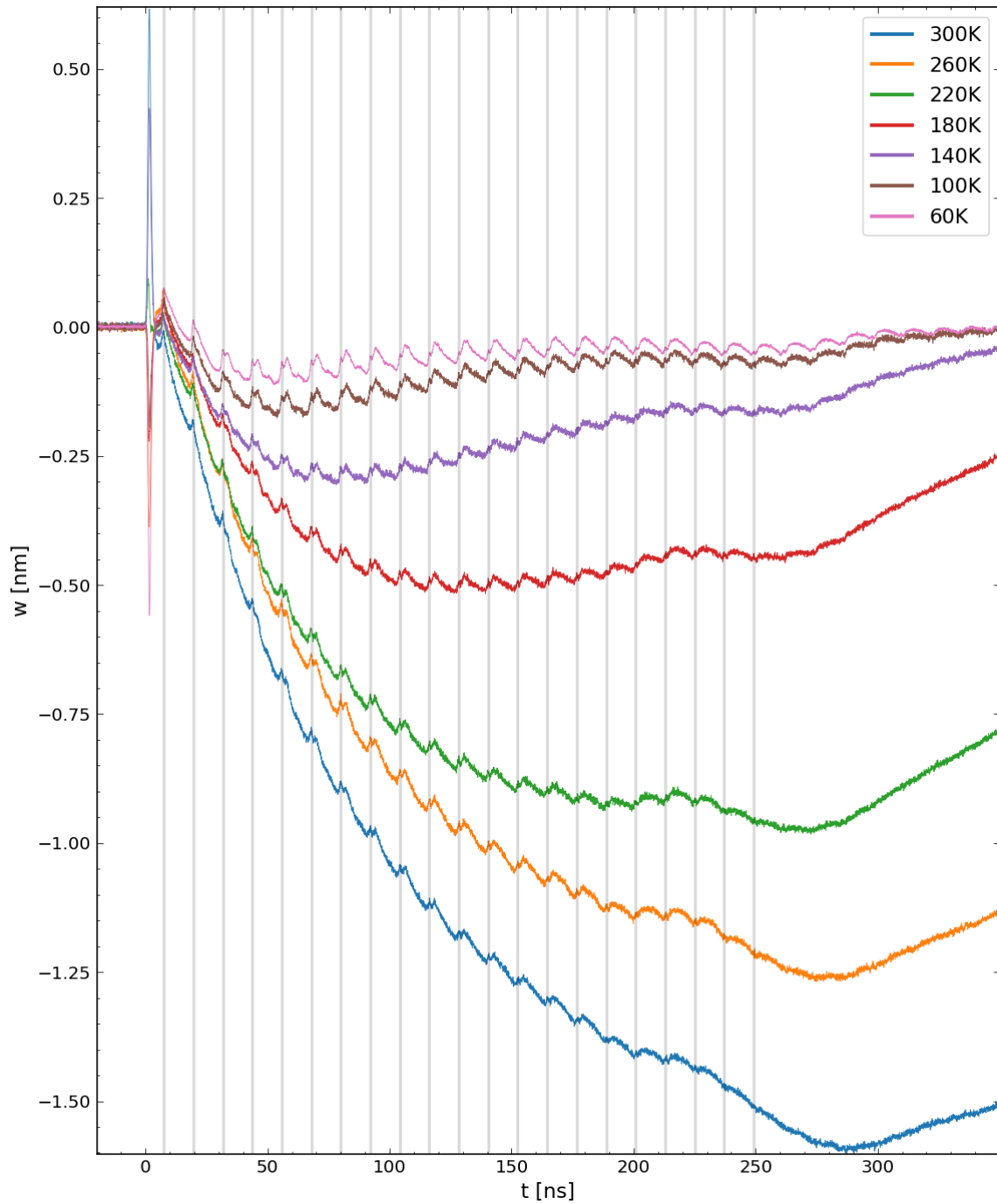
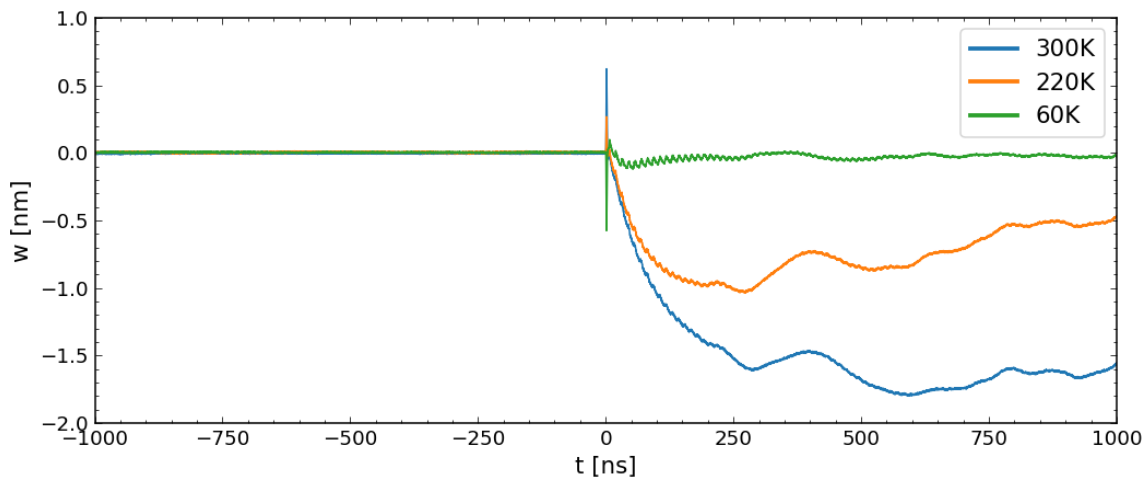


Figure 5.12.: Interferometer measurements of the time span of a few hundred nanoseconds after phonon-matter interaction considering a pump-probe experiment at different initial temperature values for a SC CVD diamond.

amplitude values in this frequency range have comparable magnitudes for all temperature values which have been measured. However, the variation of the particular frequency values of the modes depends even more clearly on the temperature in this frequency range. The fringes which have been mentioned in the previous discussion about Fig. 5.12 have frequencies of about 82.78 MHz. This range is shown in Fig. 5.14d. This illustration shows that there is a significant increase of the amplitude of these fringes at low temperatures.



(a) first 1000 ns

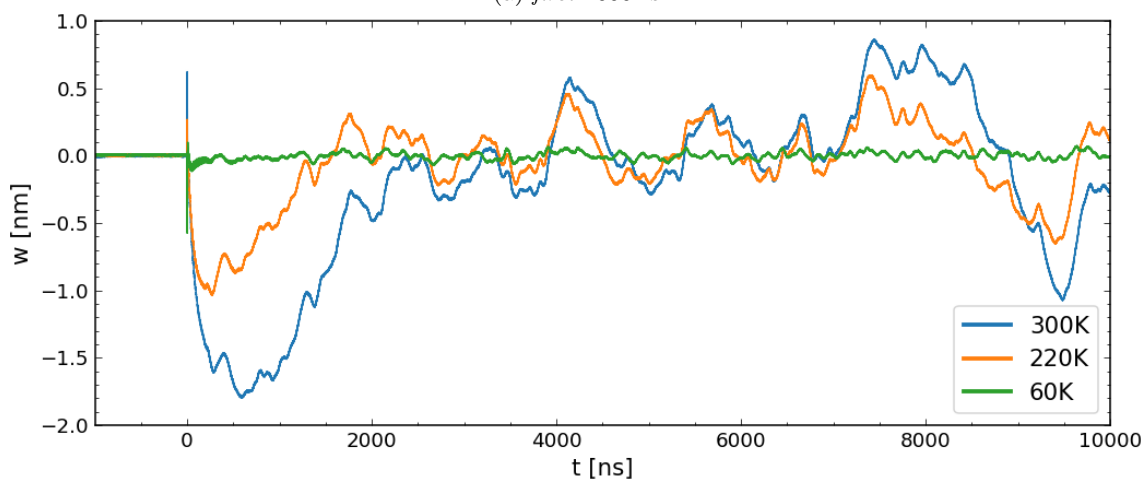
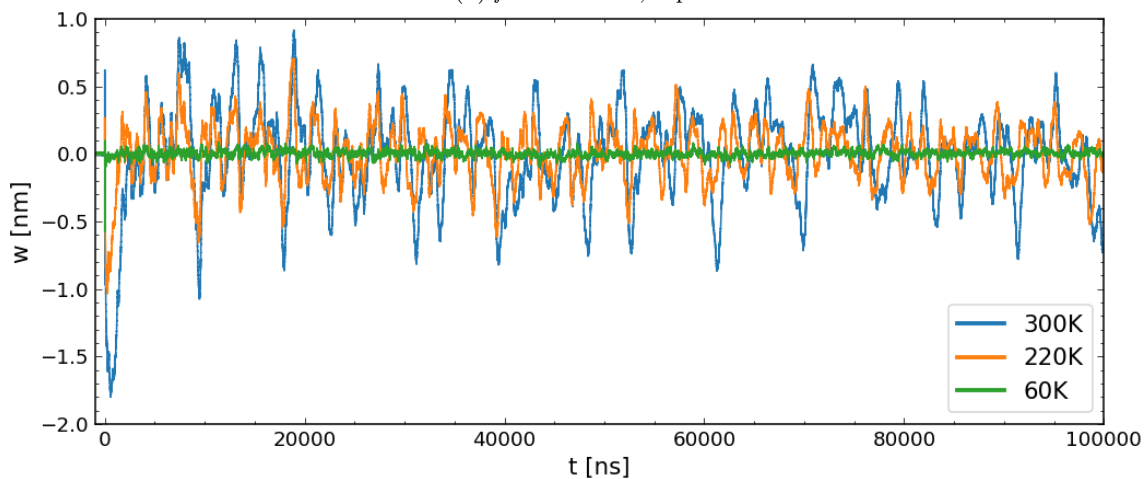
(b) first 10 000 ns, 10 μ s(c) first 100 000 ns, 100 μ s, 0.1 ms

Figure 5.13.: Interferometer measurements using the full bandwidth in AC mode of the photodiode, investigating the CVD diamond sample at different initial temperature values. For a better visualization different time ranges of the measurement are shown. In (a) the first 1000 ns, in (b) the first 10 000 ns and in (c) the first 100 000 ns or 0.1 ms are shown.

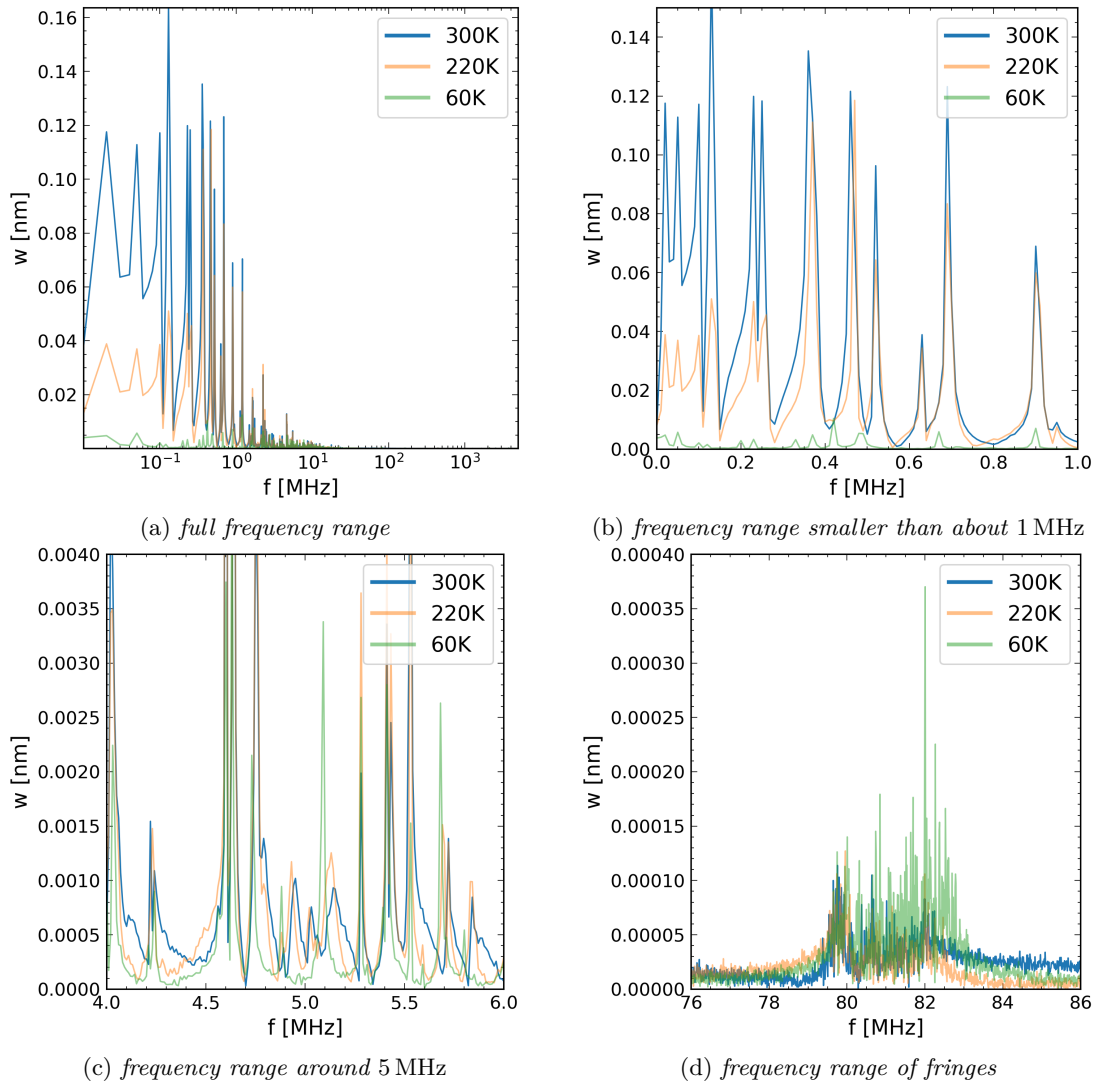


Figure 5.14.: (a) Full frequency range of the time varying signal in Fig.5.13 with a logarithmic scale of the frequency. (b) Frequency components smaller than 1 MHz. (c) Values around 5 MHz. (d) Frequency components that correspond to the fringes of Fig.5.12.

6. Calculation of thermoelastic problems considering a diamond Bragg reflector

A detailed description about the experimental setup and theoretical concepts which are used in the context of this work has been given in the previous sections. Before proceeding it may be good to recall the main topic, which is investigated in this work:

The change of X-ray diffraction conditions by nondestructive deformation of the crystal lattice spacing introduced by dynamical thermal expansions, which is created by absorbed energy of pulsed XFEL radiation.

For an experimental investigation of this topic a pump-probe experiment (see Section 5) has been built up, using an optical UV pump laser. A simulation for this pump-probe experiment will be presented in Section 6.3. To distinguish the different effects, which are causing the shape of the measured and simulated signal presented in Section 6.3 it is useful to investigate simplified cases. These simplified cases describe wave propagation effects separately which are superimposed in the final observed wave propagation presented in Section 6.3. In this work different types of thermoelastic introduced wave effects have been identified, which may be used to interpret the total measured signal. These are namely a one-dimensional kind of wave propagation (Section 6.1.2), a radial propagating wave caused by a heat bump effect (Section 6.2.1) and a diffusivity affected wave (Section 6.2.4) influenced by a rapid rises and fall of a temperature profile. The one-dimensional kind of wave propagation has already been simulated and measured by several researchers [TGMT86] [SMW⁺12]. However, a radial propagating wave caused by a heat bump effect and the diffusivity affected wave have not been measured and discussed in the current literature so far to the best knowledge of the author.

A simulation for thermoelastic effects considering the heat load given for a saturated CBXFEL is presented in Section 6.4. For this simulation an absorbed energy profile simulated by P. Rauer [Rau21] is used (Fig. 6.35, Section 6.4). The total absorbed energy per saturated CBXFEL pulse is about 45 μJ . Since, the absorbed energy per pulse of the UV laser for the pump-probe experiment is about 35 μJ , a similar amount of energy is adsorbed by the crystal. Nevertheless, the radius considered for the pump-probe experiment is about 300 μm and the penetration depth is 5 μm . Since the beam radius for the saturated CBXFEL pulse is about 50 μm and most of the absorbed energy can be connected to a penetration depth of roughly 20 μm , there is a significant difference comparing the shape of the heat load profiles. The shape of the heat load profile has a direct impact

on the shape of the resulting wave propagation. However, the kind of wave propagation may still be connected of a superposition of the already, mentioned three types of wave propagation.

For the simulation of the pump-probe experiment in Section 6.3 as well for the CBXFEL Section 6.4 the assumption of the Fourier law has been used. As discussed in Section 4 this assumption is critical at low temperatures and therefore systematic errors may be present. However, the kind of heat transfer at low temperatures which causes a development of a thermoelastic generated wave may also depend on the shape of the heat profile, due to the reached temperature rise and connected mean free path, as it will be discussed in detail in Section 6.4.

The theoretical principles to investigate the thermoelastic interaction of powerful electromagnetic fields with a diamond Bragg reflector have been derived in the previous sections under the assumptions of continuum mechanics and the existence of a local thermodynamic equilibrium. Also the diffuse heat transfer (Fourier law) has been considered, which could be verified in the context of solid state physics under the assumption that the scales of interest are much larger than the phonon mean free path. The derived equations will be now shortly summarized.

Considering Cartesian coordinates the coupled PDEs which can be used to describe a thermoelastic problem are given by Eq. 3.59, Eq. 3.41 and Eq. 3.53

$$\begin{aligned} \sigma_{ij,j} + F_i &= \rho \ddot{u}_i, \text{ where } \sigma_{ij} = C_{ijkl}[\epsilon_{kl} - \alpha_{kl}\Delta T] \\ (\lambda_{c_{ij}} T_{,j})_{,i} &= T\beta_{ij}\epsilon_{ij} + c\rho\dot{T} - Q_{ext} \text{ where } T = T_0 + \Delta T \text{ and } \beta_{ij} = \alpha_{ij}C_{ijkl} \end{aligned} \quad (6.1)$$

The radiation pressure discussed in Section 2.4, which is occurring when a powerful X-ray pulse is reflected by a Bragg reflector, may be considered as a body force F_i per unit volume. However, considering this effect it has been shown that the created strain wave is about two orders of magnitude smaller compared to heat load effects, thus it is assumed that this effect can be neglected and thus the impact of F_i will not be discussed further in this work. Additional information about this topic can be found in a proceeding paper which was published during this PhD project [BTM⁺18].

To solve the coupled partial differential equations (Eq. 6.1), initial and boundary conditions have to be defined [Bal89]. Considering a time dependent problem where at $t = 0$ the solid is at rest and has a homogeneous initial temperature T_0 , the initial conditions are:

$$u_i(\mathbf{r}, t = 0) = 0, \quad \dot{u}_i(\mathbf{r}, t = 0) = 0 \quad (6.2)$$

$$T(\mathbf{r}, t = 0) = T_0 \quad (6.3)$$

Boundary conditions The boundary conditions for Eq. 6.9 are called the kinematic boundary condition and for Eq. 6.11 the boundary condition are named thermal boundary conditions in the context of this work.

Kinematic boundary condition The mechanical boundary conditions can be defined on the surface S_M , which is enclosing a three-dimensional solid, with one of the following equations:

$$u_i|_{S1_M} = \hat{u}_i \quad (6.4)$$

$$\sigma_{ij}n_i|_{S2_M} = \hat{t}_j \quad (6.5)$$

which defines the traction \hat{t}_j and/or displacement \hat{u}_i at arbitrary points on the boundary surface of the solid. In cases where the boundary condition Eq. 6.5 is zero, inserting the definitions of Eq. 6.10 into Eq. 6.5 gives:

$$E\epsilon_{ij}n_i = E\alpha\Delta Tn_i \quad (6.6)$$

This shows that in this case $E\alpha\Delta Tn_i$ behaves like a surface force on the boundary [Mur13, p. 5]

Thermal boundary conditions On the same total surface of the solid as mentioned for the kinematic boundary condition $S_T = S_M$, the thermal boundary conditions can be partly defined on S_T by:

$$T|_{S1_T} = \hat{T} \quad (6.7)$$

$$q_i^h n_i|_{S2_T} = \hat{q}_n^h + a_h(T_R - T_S) \quad (6.8)$$

where q_i^h is the heat flux per unit area, a_h is a heat transfer coefficient, T_S the surface temperature and T_R the constant temperature of a thermal reservoir which is connected to the surface area $S2_T$.

The derived coupled PDEs Eq. 6.1 in combination with the boundary condition may be denoted as the strong form, which can be used to describe a thermoelastic problem. The strong form can be rewritten as an integral expression which is called the weak form. These weak form is suitable to be solved by numerical methods. To solve the coupled thermoelastic equation a special weighted residual method, the Galerkin-method may be used to apply the finite element method (FEM). These are the underlying assumption used by the software COMSOL multiphysics® which is used to solve thermoelastic problems in this work. An introduction to this concept is given by an example in Appendix A.6, where a one-dimensional FEM is discussed in detail. Using this method it is also possible to take into account temperature dependent material parameters (for further information see Appendix A.6).

For the simulations carried out in this work an axisymmetric heat load is investigated in detail and solved with FEM. For these calculations the approximation has been used that the elastic stiffness tensor is isotropic and temperature independent. Assuming that body

force effects can be neglected the equation of motion in this case is given by Eq. 3.70:

$$\begin{aligned} \frac{\partial \sigma_{\rho_r \rho_r}}{\partial \rho_r} + \frac{\partial \sigma_{\rho_r z}}{\partial z} + \frac{1}{\rho_r} (\sigma_{\rho_r \rho_r} - \sigma_{\theta \theta}) &= \rho \ddot{u} \\ \frac{\partial \sigma_{\rho_r z}}{\partial \rho_r} + \frac{\partial \sigma_{zz}}{\partial z} + \frac{1}{\rho_r} \sigma_{\rho_r z} &= \rho \ddot{w}. \end{aligned} \quad (6.9)$$

For the special case of an elastic isotropic solid with a Poisson's ratio of zero, the stress-strain relation is given by Eq. 3.69

$$\begin{aligned} \sigma_{\rho_r \rho_r} &= E \epsilon_{\rho_r \rho_r} - E \alpha \Delta T, \quad \text{where } \epsilon_{\rho_r \rho_r} = \frac{\partial u}{\partial \rho_r} \\ \sigma_{\theta \theta} &= E \epsilon_{\theta \theta} - E \alpha \Delta T, \quad \text{where } \epsilon_{\theta \theta} = \frac{u}{\rho_r} \\ \sigma_{zz} &= E \epsilon_{zz} - E \alpha \Delta T, \quad \text{where } \epsilon_{zz} = \frac{\partial w}{\partial z} \\ \sigma_{\rho_r z} &= E \epsilon_{\rho_r z}, \quad \text{where } \epsilon_{\rho_r z} = \frac{1}{2} \left(\frac{\partial u}{\partial z} + \frac{\partial w}{\partial \rho_r} \right) \end{aligned} \quad (6.10)$$

The equation describing heat transfer Eq. 3.74 for the special case of an elastic isotropic solid with a Poisson's ratio of zero is

$$\frac{1}{\rho_r} \frac{\partial}{\partial \rho_r} \left(\rho_r \lambda_{\rho_r \rho_r} \frac{\partial \Delta T}{\partial \rho_r} \right) + \frac{\partial}{\partial z} \left(\lambda_{zz} \frac{\partial \Delta T}{\partial z} \right) = T \alpha E (\epsilon_{\rho_r \rho_r} + \epsilon_{\theta \theta} + \epsilon_{zz}) + c \rho \dot{\Delta T} - Q_{ext}, \quad (6.11)$$

where the temperature rise $\Delta T = T - T_0$ is referred to an initial temperature rise T_0 and T is the absolute temperature value. In the following section analytical and numerical solutions for special cases of Eq. 6.9 and Eq. 6.11 will be discussed. As it will be shown in Section 6.3, these special cases give an insight to the characteristic effects which describe the wave propagation caused by an axisymmetric heat load for a diamond crystal.

If the material-photon interaction can be described with the previously introduced continuum assumptions, the calculated displacement field from the thermoelastic simulation can be used to describe the change of the X-ray diffraction conditions expressed by dynamical diffraction theory of a deformed crystal [Rau21]. If the spatial and temporal profile of the absorbed¹ laser pulse energy and the material parameters of the Bragg reflector are known, the thermoelastic interaction may be described by solving the partial differential equations (PDE) Eq. 6.9 and Eq. 6.11. However, finding an analytical solution of a three-dimensional problem with these equations is not a trivial task. Even if numerical solutions are used, careful consideration about the simulation parameters are required to avoid numerical errors and unnecessarily long computation times.

In this work a finite element method (FEM) has been chosen to solve the PDEs, which describe thermoelasticity. The steps, which lead to the final simulation results carried out in this work are based on some approximations, which are discussed in the following

¹Assuming that all of the absorbed energy is converted into heat and the thermalization can be approximated as instantaneously.

section. Before directly describing the assumptions of the applied FEM simulation, it is useful to consider first simplified problems of the thermoelastic interaction which have a simple analytical solution. The reproduction of these analytical solutions with the FEM may be a good starting point to understand which simulation parameters are necessary to carry out a sufficiently accurate simulation. For the sake of simplicity first problems at room temperature under the assumption of constant² material parameters for a diamond crystal will be discussed:

constant [unit]	ρ [kg/m ³]	E [GPa]	α [K ⁻¹]	c [J K ⁻¹ kg ⁻¹]	λ_c [W m ⁻¹ K ⁻¹]
value	3513	1125	1E-6	517	2000

Table 6.1.: *Material constants of diamond at a temperature of 300 K, where ρ is the mass density E Young's modulus, α the linear thermal expansion coefficient, c the specific heat per unit mass and λ_c the thermal conductivity*

6.1. Analytical solutions

In the following section two analytic solutions are examined. First a solution for a temperature profile, which is calculated by ignoring the mechanical coupling and heat conductivity. The second is a one-dimensional strain wave caused by an instantaneous temperature rise.

6.1.1. Initial temperature profile created by absorption of a laser pulse

Recalling Eq. 2.62 it may be assumed for a laser with an ultra-short pulse duration that the instantaneously absorbed energy E_{abs} in a cylindrical crystal with radius R_0 and thickness d is given by the integral of the energy density $\Phi_E(\rho_r, z)$ over the crystal domain. The fraction γ_h ($0 < \gamma_h < 1$) expresses the part of the absorbed energy E_{abs} , which is converted into heat

$$E_Q = E_{abs}\gamma_h. \quad (6.12)$$

Neglecting heat conduction and the time dependent strain fields Eq. 6.11 reduces to

$$Q_{ext}(\rho_r, z) = c\rho \frac{\partial T(\rho_r, z)}{\partial t}. \quad (6.13)$$

Integration over time and assuming an instantaneous thermalization, the energy density $\Phi_Q(\rho_r, z)$ can cause an instantaneous temperature rise, which considering a small temperature rise gives the relation

$$\Phi_Q(\rho_r, z) = c\rho\Delta T(\rho_r, z) \quad (6.14)$$

²The assumption of nearly constant material parameters is a good approximation if a temperature range of only a few kelvin is considered.

The integration of Eq. 6.14 over the crystal domain gives E_Q . Thus, considering Eq. 2.62 gives the relation

$$\begin{aligned} E_Q &= \gamma_h \int_0^d \int_0^{2\pi} \int_0^{R_0} \Phi_E(\rho_r, z) \rho_r d\rho_r d\theta dz = \int_0^d \int_0^{2\pi} \int_0^{R_0} \Phi_Q(\rho_r, z) \rho_r d\rho_r d\theta dz \quad (6.15) \\ &= \frac{\gamma_h(1-R)2E_p}{\zeta\pi W^2} \int_0^d \int_0^{2\pi} \int_0^{R_0} \exp\left(-\frac{2\rho_r^2}{W^2}\right) \exp(-z/\zeta) \rho_r d\rho_r d\theta dz \\ &= c\rho \int_0^d \int_0^{2\pi} \int_0^{R_0} \Delta T(\rho_r, z) \rho_r d\rho_r d\theta dz, \end{aligned}$$

where E_p is the pulse energy of the laser, R the reflectance considering normal incidence, W the beam radius and ζ the penetration depth. If the density ρ and specific heat capacity c are independent³ of the temperature, $\Phi_E(\rho_r, z)$ and ΔT must have the same spatial distribution. Therefore, the temperature rise distribution is given by

$$\Delta T(\rho_r, z) = \Delta T_{max} \exp\left(-\frac{2\rho_r^2}{W^2} - \frac{z}{\zeta}\right), \quad \text{with} \quad \Delta T_{max} = \frac{\gamma_h(1-R)2E_p}{\zeta\pi W^2 c\rho}. \quad (6.16)$$

From Eq. 6.16 the relations $T_{max} \propto 1/W^2$ and $T_{max} \propto 1/\zeta$ can be derived. It should be noted that T_{max} is independent of the material size, given by the values of d and R_0 in this formulation. However, the amount of the absorbed energy depends on the crystal size and can be calculated by solving the integral of Eq. 6.15. The solution for this integral has been introduced by Eq. 2.63, which gives:

$$E_{abs} = E_p(1-R) \left(1 - \exp\left(-\frac{2R_0^2}{W^2}\right)\right) (1 - \exp(-d/\zeta)). \quad (6.17)$$

For a crystal with lateral size $R_0 \gg W$ the absorbed energy is

$$E_{abs} = E_p(1-R)(1 - \exp(-d/\zeta)). \quad (6.18)$$

If $R_0 \gg W$ and $d \gg \zeta$ the absorbed energy is

$$E_{abs} = E_p(1-R). \quad (6.19)$$

The temperature profile given by Eq. 6.16 is useful for discussing the validity of a one-dimensional simplification. This simplification will be explained by an example, considering an absorption length of $\zeta = 100 \mu\text{m}$, a reflectance of $R \approx 0$, a complete conversion of the absorbed energy into heat $\gamma_h = 1$, a pulse energy of $E_p = 100 \mu\text{J}$ and a beam radius of $W = 500 \mu\text{m}$. Using these values and the material parameters of Table 6.1 gives the temperature profile shown in Fig. 6.1a inside a range which may be associated with a cylindrical diamond crystal with a radius of $R_0 = 1000 \mu\text{m}$ and a thickness of $d = 200 \mu\text{m}$. If a pump-probe experiment with a probe laser spot $W_p \ll W$ is considered,

³Whether these assumptions are valid depends on the material and the considered temperature range.

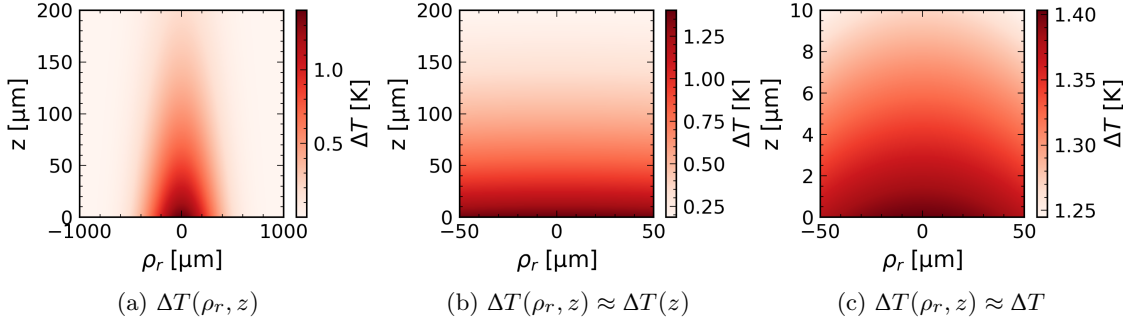


Figure 6.1.: ΔT calculated with Eq. 6.16 using the values, $W = 500 \mu\text{m}$, $E_p = 100 \mu\text{J}$, $\zeta = 100 \mu\text{m}$ and material parameters of Table 6.1, (a) $\Delta T(\rho_r, z)$ in a cylindrical crystal with $R_0 = 1000 \mu\text{m}$ and $d = 200 \mu\text{m}$. (b) ΔT considering the area covered by a probe beam radius of $W_p \approx 20 \mu\text{m}$. In this case the temperature may be considered only to be a function of z -direction. (c) Considering an area covered by a probe beam radius of $W_p \approx 20 \mu\text{m}$ and a crystal thickness of $d = 10 \mu\text{m}$. In such case a nearly uniform temperature profile may be assumed.

the temperature profile may be assumed to be independent of the ρ_r -direction, which can be considered as a one-dimensional temperature profile problem where lateral boundary effect can be neglected. This case is illustrated by Fig. 6.1b, showing the temperature profile in a small region near the center of the pump beam. This approximation gets more accurate if $W \gg d$. If in addition a thinner crystal of thickness $d = 10 \mu\text{m}$ would be investigated the temperature profile may be considered to be approximately constant. As shown in Fig. 6.1c the temperature variation in this range is rather small. In this case the accuracy of the approximation could be further improved by $\zeta \gg d$ in combination with $W \gg d$.

6.1.2. One-dimensional thermoelastic models for pump-probe experiments

Thermoelastic models considering propagation of one-dimensional strain waves have been successfully used by Thomsen et al. [TGMT86] and Stoupin et al. [SMW⁺12] to verify their measured signals in pump-probe experiments. For a case of a pump-probe experiment where the pump beam W and a probe beam with size W_p fulfills $W \gg W_p$ a one-dimensional approximation of Eq. 6.16 can be used:

$$\Delta T(z) = \Delta T_{max} \exp\left(-\frac{z}{\zeta}\right), \text{ where } \Delta T_{max} = \frac{2E_p(1-R)\gamma_h}{W^2\pi c\rho\zeta} \quad (6.20)$$

With this assumptions and assuming further that Poisson's ratio can be neglected the equation Eq. 6.9 and Eq. 6.10 can be written as:

$$\begin{aligned} \sigma_{zz} &= E \frac{\partial w(z, t)}{\partial z} - \alpha E \Delta T(z) = E(\epsilon_{zz} - \epsilon_{zz}^{th}) = E\epsilon_{zz}^e, \\ \rho \frac{\partial^2 w(z, t)}{\partial t^2} &= \frac{\partial \sigma_{zz}}{\partial z}. \end{aligned} \quad (6.21)$$

In these formulae E is the Young's modulus, α the linear thermal expansion coefficient, ρ the density, ϵ_{zz}^e the elastic strain and ϵ_{zz}^{th} the thermal strain. Considering a free standing crystal placed in vacuum, the boundary conditions for Eq. 6.21 are that the stress σ_{zz} is zero at $z = 0$ and $z = d$, which causes

$$\left. \frac{\partial w(z, t)}{\partial z} \right|_{z=0} = \epsilon_{zz}(z, t) \Big|_{z=0} = \alpha \Delta T(0), \quad \left. \frac{\partial w(z, t)}{\partial z} \right|_{z=d} = \epsilon_{zz}(z, t) \Big|_{z=d} = \alpha \Delta T(d). \quad (6.22)$$

The initial conditions are $\epsilon_{zz}(z, 0) = \frac{\partial w(z, 0)}{\partial z} = 0$ and $\frac{\partial w(z, t)}{\partial t} = 0$. The analytical solution for Eq. 6.21 is given by [SMW⁺12]

$$\epsilon_{zz}(z, t) = \alpha(\Delta T(z) - \frac{1}{2}[F(z - vt) + F(z + vt)]). \quad (6.23)$$

This solution has only a physical meaning in the range of $z = 0$ to $z = d$ (the domain of the solid), $v = \sqrt{\frac{E}{\rho}}$ is the speed of sound for longitudinal waves (see Eq. 3.65). The function $F(x)$ is $F(x) = \Delta T(x)$ in the range $0 < x < d$ and for values $x = z - vt$ or $x = z + vt$ outside this range the following iterative function⁴ may be used to calculate the propagating strain wave which is reflected at the boundaries located at $z = 0$ and $z = d$:

```

1 def F(x):
2     n=floor(x/d)
3     if n == 0:
4         return dT(x)
5     elif n < 0:
6         return -F(-x)
7     elif n > 0:
8         return - F(2*d-x)

```

Here the function in line 4 is given by $\Delta T(x)$ (Eq. 6.20).

From Eq. 6.23 it can be seen that the solution for the strain consists of a time independent part indicated by the first term and a traveling wave given by the second and third term, which propagates with the velocity v . Considering Eq. 6.21 it can be seen that the time independent part is the thermal strain and the traveling wave is connected to the elastic strain.

By integration of the strain function Eq. 6.23 and considering boundary condition for the displacement Eq. 6.22, the displacement function may be calculated by:

$$w(z, t) = \int_0^z \epsilon_{zz}(z, t) dz \quad (6.24)$$

with $\int_0^z \Delta T(z') dz' = -\Delta T_{max} \zeta (e^{-\frac{z}{\zeta}} - 1)$

and $\int_0^z \Delta T(z' \pm vt) dz' = -\Delta T_{max} \zeta (e^{-\frac{z \pm vt}{\zeta}} - 1)$

⁴Considering the programming language Python and the floor function from the NumPy module.

this yields :

$$w(z, t) = \alpha(-\zeta\Delta T(z) - \frac{1}{2}[G(z - vt) + G(z + vt)]) \quad (6.25)$$

Here $G(x)$ is $G(x) = -\zeta\Delta T(x)$ in the range $0 < x < d$ and to take into account the reflection at the boundaries (condition Eq. 6.22) the following iterative function may be used:

```

1 def G(x):
2     n=floor(x/d)
3     if n == 0:
4         return -zeta*dT(x)
5     elif n < 0:
6         return G(-x)
7     elif n > 0:
8         return G(2*d-x)

```

Where the function in line 4 is given by $-\zeta\Delta T(x)$ (Eq. 6.20).

Using the values from Table 6.1 gives a speed of sound of $v = 17\,903 \text{ m s}^{-1}$. Considering a crystal thickness of $d = 100 \mu\text{m}$ the strain and displacement waves given by Eq. 6.23 and Eq. 6.25 indicates that both values are a periodic functions of time with a repetition rate of $T_p = 2d/v = 11.18 \text{ ns}$. The time span of T_p has been used to illustrate the strain and displacement wave at various time steps shown in Fig. 6.2 and Fig. 6.3. Two different temperature profiles have been considered in these figures. The figures (a) have been calculated with a temperature rise profile $\Delta T(x)$ which corresponds to a penetration depth of $\zeta = 5 \mu\text{m}$ and a maximum temperature rise value of $T_{max} = 1.75 \text{ K}$. In figures (b) a constant temperature rise $\Delta T = 1 \text{ K}$ has been assumed. It should be mentioned that a constant temperature rise would need a penetration depth of $\zeta \rightarrow \infty$, however as mentioned in the previous section a constant temperature rise is a good approximation for $\zeta \gg d$. In case of a constant temperature rise the function $F(x)$, which is related to the strain propagation (Eq. 6.23) has a constant value. Integration of strain (Eq. 6.24) gives a slightly different solution compared to Eq. 6.25:

$$w(z, t) = \alpha(z\Delta T - \frac{1}{2}[L(z - vt) + L(z + vt)]) \quad (6.26)$$

Here $L(x)$ is $L(x) = x\Delta T$ in the range $0 < x < d$. And the iteration is given by

```

1 def L(x):
2     n=floor(x/d)
3     if n == 0:
4         return x*dT
5     elif n < 0:
6         return L(-x)
7     elif n > 0:
8         return L(2*d-x)

```

where the dT in line 4 is the constant temperature rise value ΔT .

In Fig. 6.2 and Fig. 6.3 it can be seen that the assumption of an instantaneous temperature rise causes a kink discontinuity in the displacement field, which causes a jump discontinuity in the strain field. These discontinuities are moving with the speed of sound v . In Fig. 6.4 the first nanosecond of the wave propagation of Fig. 6.2 and Fig. 6.3 are illustrated. These illustrations may be a good way to explain the creation of the strain wave. Now the situation of a constant temperature rise as shown in Fig. 6.4b will be considered. Given by Eq. 6.21, an initial temperature rise temperature creates a negative (compressing) thermal stress, which has a value of $\sigma_{zz} = -\alpha E \Delta T(z)$ at $t = 0$ due to the initial condition for the strain to be zero. However, due to the boundaries conditions the stress must be zero at $z = 0$ and $z = d$ and this, as explained by Eq. 6.6, gives a force per area at the boundaries, which has the same magnitude as the stress inside the crystal. Phenomenologically this represents the assumption that the crystal is surrounded by vacuum and so there is no reaction force in its area, which allows the material a free expansion in the area $z < 0$ and $z > d$ at both ends of the crystal. It is visualized in Fig. 6.4b that for $t > 0$ this gives rise to the development of a negative displacement at $z = 0$ and a positive displacement at $z = d$. At $t = 0$ an arbitrary element inside the crystal experiences the same force (stress) from both sides due to the homogeneous temperature rise profile. But a tiny time step after $t=0$ the expansion at the boundaries takes away the stress at one side for an element inside the crystal just beneath the surface. Given by Eq. 6.21 the elastic strain $\epsilon_{zz}^e = \epsilon_{zz} - \epsilon_{zz}^{th}$ is proportional to the value of the stress, therefore the green line in Fig. 6.4b illustrates the spatial and temporal shape of the stress. The temporal development of the green line in Fig. 6.4b shows that due to the expansions in the direction of the boundaries a cascade of stress relaxation inside the crystal takes place. This is also visible by the blue line in Fig. 6.4b and Fig. 6.2b, which shows the propagation of the total strain. It can be seen that the positive strain, which indicates an expansion initiated at the surface and given by the solution Eq. 6.23 is propagating with the speed of sound into the material. This propagation of strain is directed from both boundaries into the crystal.

In Fig. 6.5a the time span is illustrated were the expanding strain wave meet each other. At $t \approx 2.8$ ns it can be seen by the green line that the elements in the middle of the crystal experience now a positive (tensile) stress⁵, which increases the magnitude of the displacement. The (tensile) stress is build up with the speed of sound towards the boundaries. However, caused by the boundary conditions that the stress is zero at $z = 0$ and $z = d$ the strain gets reflected as illustrated in Fig. 6.5b at $t \approx 5.6$ ns. A phenomenological explanation for the reflection is that when a stress is expanding (pushing) the material in the area where there is just vacuum, the crystal gives a reaction force, which pulls the material back into the solid crystal. Directly after the reflection an element just beneath the surface which felt lately a (tensile) stress is relaxed to zero strain by the reaction force of the boundary and it follows a reverse development of the strain and displacement function,

⁵As mentioned before the elastic strain ϵ_{zz}^e is proportional to the stress due to Eq. 6.21.

which has been described before. When the discontinuity of the strain and displacement function later reaches the opposite boundary the initial condition $\epsilon_{zz} = 0$ is met again. After the following reflection then an identical cycle of the wave propagation begins.

The wave propagation in case of the spatial varying temperature rise profile with $\zeta \ll d$ can be explained similarly to the previously discussed case of a spatial constant temperature rise. However, a main difference is that at $t = 0$ the thermal expansion causes a stress profile which is nearly zero⁶ at the boundary $z = d$. This is illustrated in Fig. 6.4a. It causes that the material is not only expanding into the vacuum area as described before, but also a compression (negative strain) into the crystal. This is forming a strain pulse with a width of twice the penetration depth ζ , consisting of a compressed area in front to the propagation direction and a tensile strain behind as illustrated in Fig. 6.2a.

As described before the strain and displacement are a periodic function in time. If the displacement is measured at the back side⁷ of the crystal $w(d, t)$ a periodic function as shown in Fig. 6.6 can be measured. It should be noted that in the assumptions of this calculation no damping has been considered which leads to the unphysical result that such a strain/displacement wave could propagate infinitely long, repeating a periodic signal like the ones illustrated in Fig. 6.2 and Fig. 6.3.

⁶The temperature in Eq. 6.20 is exponentially decreasing with z , and for $d > \zeta$ the value is very small.

⁷It should be mentioned that for the presented iteration code it is not possible to calculate the displacement directly at $z = d$, this would cause an endless loop. However, instead a value slightly smaller than d like $d - 1$ pm may be used to carry out a calculation.

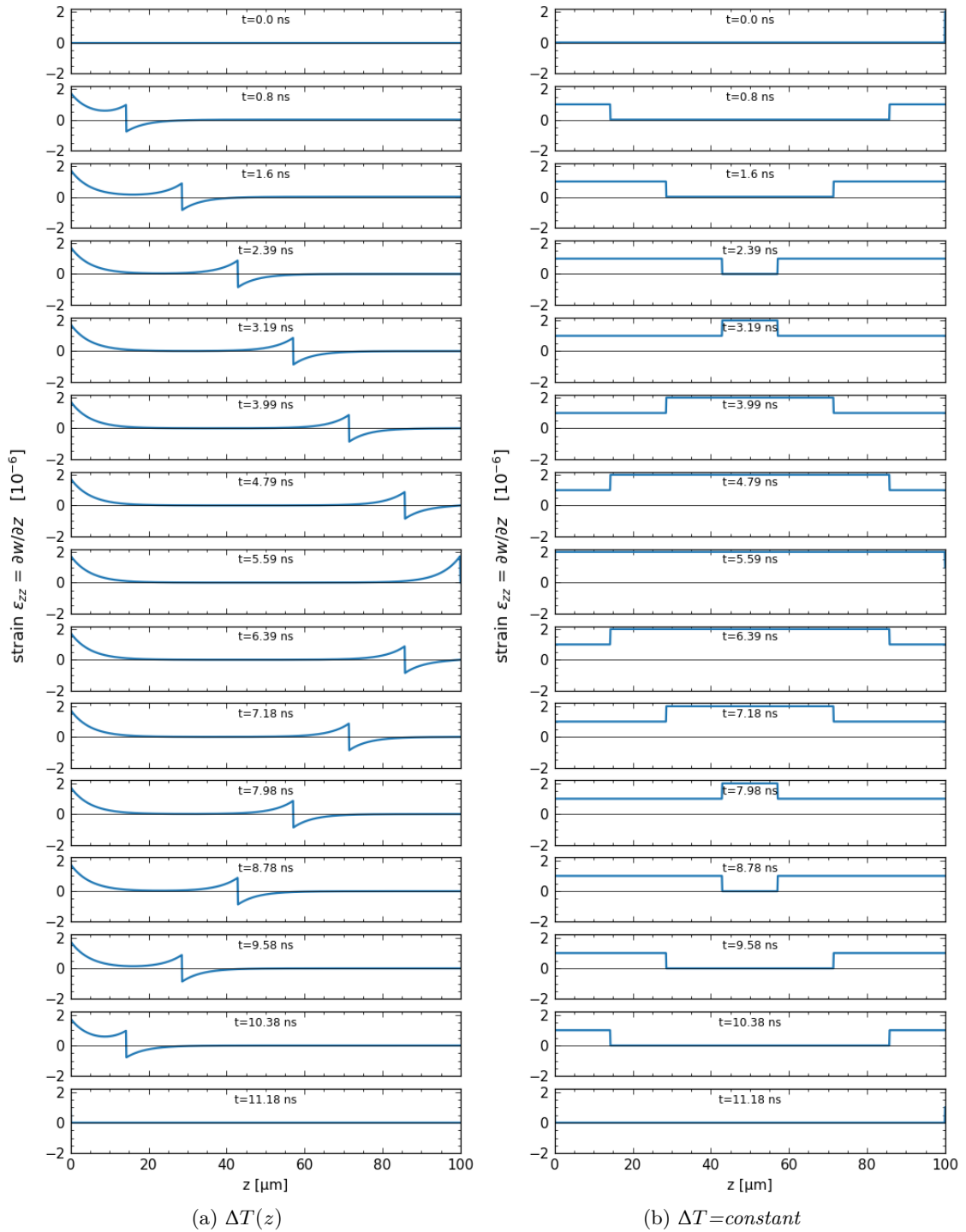


Figure 6.2.: The blue line shows the propagation of the strain ϵ_{zz} calculated with Eq. 6.23 using the material parameters of Table 6.1. The domain which is considered in all illustrated plots ranges from $z = 0$ to $z = d = 100 \mu\text{m}$. For the simulation show in (a) $\zeta = 5 \mu\text{m}$ and $T_{max} = 1.75 \text{ K}$ was used. In (b) a homogeneous temperature of $\Delta T = 1 \text{ K}$ was chosen for the calculation.

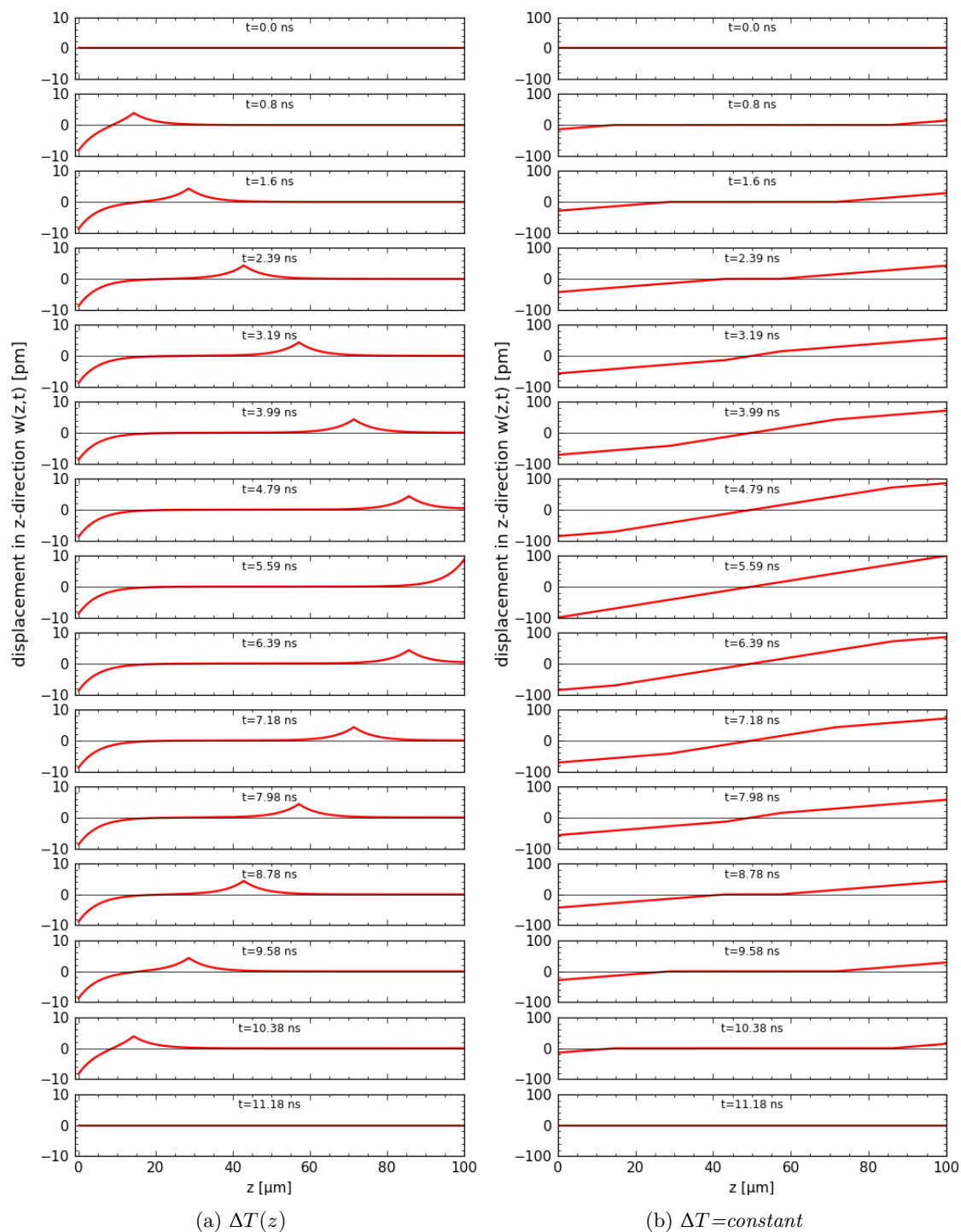


Figure 6.3.: The red line shows the propagation of the displacement in picometers using the material parameters of Table 6.1. The domain which is considered in these plots ranges from $z = 0$ to $z = d = 100 \mu\text{m}$. The simulation in (a) has been calculated by using Eq. 6.25. Here the penetration depth $\zeta = 5 \mu\text{m}$ and $T_{max} = 1.75 \text{K}$ have been used. In (b) a homogeneous temperature of $\Delta T = 1 \text{K}$ was chosen for the calculation with Eq. 6.26.

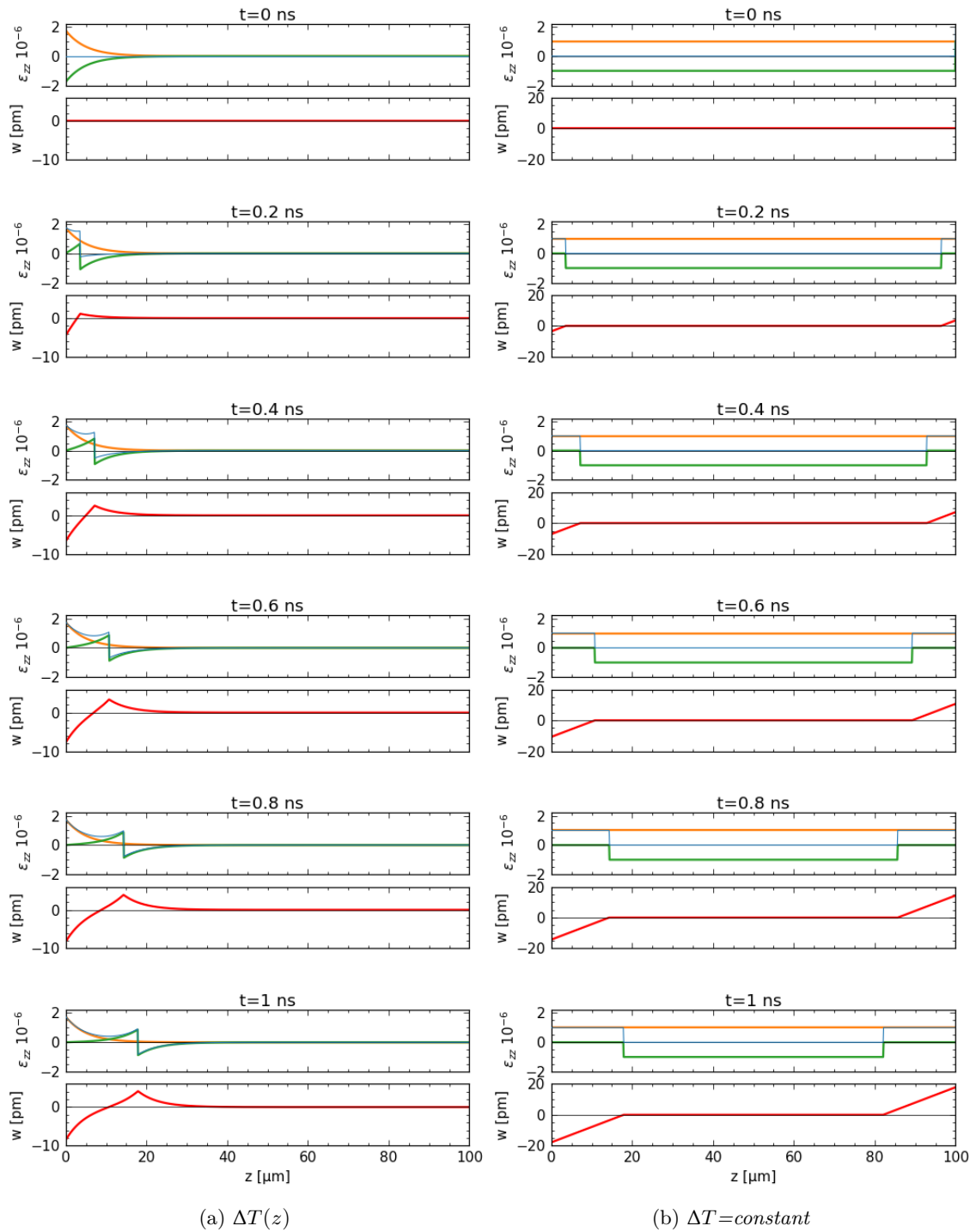


Figure 6.4.: The blue line shows the propagation of the total strain ϵ_{zz} . The orange line is the thermal strain $\epsilon_{zz}^{th} = \alpha E \Delta T(z)$, which has a time independent value in this case. The green line is the elastic strain $\epsilon_{zz}^e = \epsilon_{zz} - \epsilon_{zz}^{th}$. The displacement in z -direction w is illustrated by the red line. For the calculations the same equations as described by Fig. 6.2 and Fig. 6.3 have been used. In (a) the penetration depth $\zeta = 5 \mu\text{m}$ and $T_{max} = 1.75 \text{K}$ have been used. In (b) a homogeneous temperature of $\Delta T = 1 \text{K}$ was chosen.

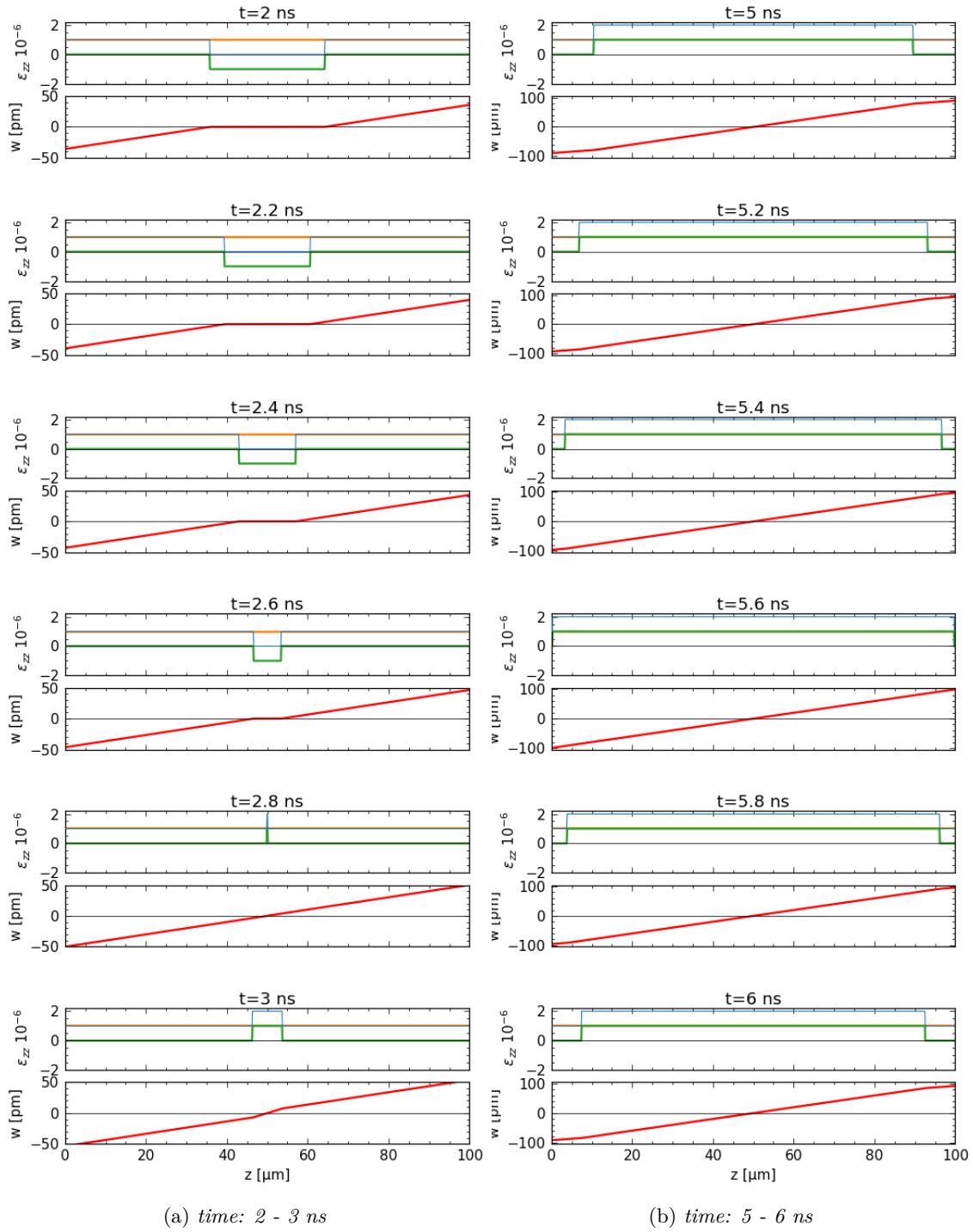


Figure 6.5.: The blue line shows the propagation of the total strain ϵ_{zz} . The orange line is the thermal strain $\epsilon_{zz}^{th} = \alpha E \Delta T(z)$, which has a time independent value in this case. The green line is the elastic strain $\epsilon_{zz}^e = \epsilon_{zz} - \epsilon_{zz}^{th}$. For the calculation the same equation as described by Fig. 6.2b and Fig. 6.3b have been used. The displacement in z -direction w is illustrated by the red line. (a) Time span in the range from 2 ns to 3 ns. (b) Time span for reflection in the range from 5 ns to 6 ns.

dimensional strain wave. The kinetic energy with these approximations can be calculated by

$$E_K(t) = \frac{A\rho}{2} \int_0^d \dot{w}^2(z, t) dz \quad (6.30)$$

and the elastic energy with

$$E_{el}(t) = \frac{AE}{2} \int_0^d (\epsilon_{zz} - \alpha\Delta T(z))^2 dz. \quad (6.31)$$

Assuming $\zeta \ll d$ and considering the temperature profile Eq 6.20 the elastic energy at $t = 0$ is⁸

$$E_{el}(0) = \frac{AE\alpha^2\zeta\Delta T_{max}^2}{4} \quad (6.32)$$

Considering $R = 0$ and $\gamma_h = 1$ the corresponding pulse energy is equal to the absorbed energy (Eq. 6.19) and the into heat converted energy (Eq. 6.12) $E_p = E_{abs} = E_Q$ and using Eq. 6.16 it can be derived that

$$\frac{E_{el}(0)}{E_p} = \frac{E\alpha^2}{2c\rho} \Delta T_{max}(W, \zeta, E_p), \text{ where } \Delta T_{max}(W, \zeta, E_p) = \frac{2E_p}{W^2\pi c\rho\zeta}. \quad (6.33)$$

Using the values of Table 6.1 the material dependent prefactor for diamond at room temperature is $\frac{E\alpha^2}{2c\rho} = 3 \times 10^{-7} \text{ K}^{-1}$. The energy density $\frac{E_p}{W^2\zeta}$ determines the value of ΔT_{max} and therefore the ratio $\frac{E_{el}(0)}{E_p}$, which determines the part of the laser converted pulse energy into elastic energy. Considering a moderate⁹ temperature rise it can be seen that $E_{el}(0) \lll E_Q$.

Considering a pump laser pulse with the beam parameters $W = 300 \mu\text{m}$, $\zeta = 5 \mu\text{m}$, which is introducing an instantaneous temperature rise of $\Delta T_{max} = 1.75 \text{ K}$ the energies illustrated in Fig. 6.7a for the time of one cycle $2d/v = 11.18 \text{ ns}$ can be calculated by numerical integration. In this case Eq. 6.32 gives $E_{el}(0) = 0.304 \text{ pJ}$ which is also visible by the numerical solution shown in Fig. 6.7a. In Fig. 6.7b the numerical solution for a case of a constant temperature rise of $\Delta T = 1 \text{ K}$ and a beam radius $W = 300 \mu\text{m}$ has been considered. It is visualized that in both cases shown in Fig. 6.7 the elastic energy and kinetic energy are periodically converted into each other and that the maximum elastic energy is present at $t = 0$. A graphical explanation for this effect can be seen by considering the green line in Fig. 6.4b which represents the elastic strain and noting by Eq. 6.31 that the square of the integral of the elastic strain is proportional of E_{el} .

When considering an experiment the kind of one-dimensional wave propagation which has been discussed in this section is of course always connected to a three-dimensional kind of wave propagation. However, to distinguishes these kinds of waves from other types of three-dimensional waves, the previously described wave propagation will be called a **one-dimensional wave** in the following part of this work.

⁸ $E_{el}(0) = \frac{AE}{2} \int_0^d (-\alpha\Delta T(z))^2 dz$

⁹It should be noted that the assumption of temperature independent material constants is only valid for a temperature rise of a few Kelvin.

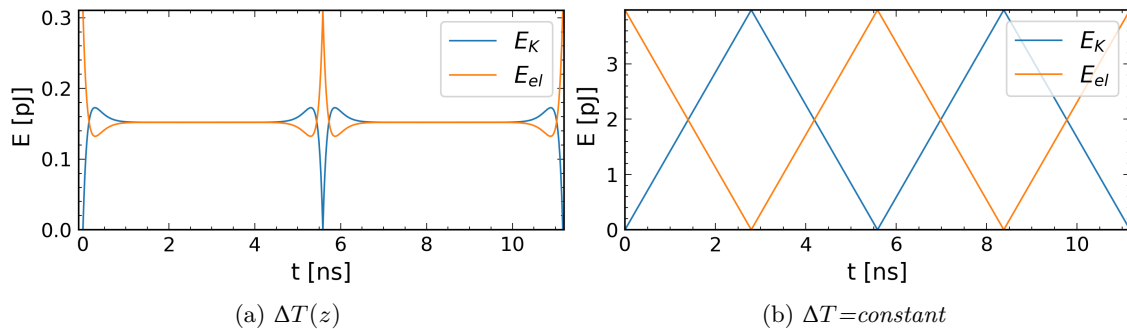
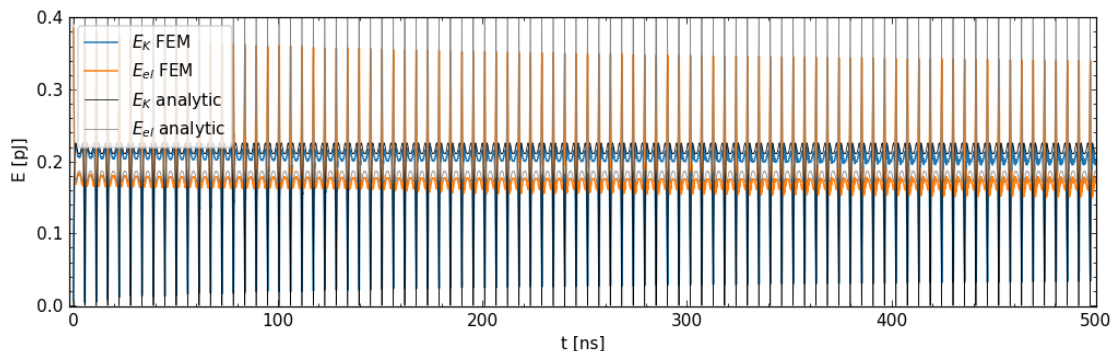


Figure 6.7.: Numerical integration of Eq. 6.31 considering a beam radius of $W = 300 \mu\text{m}$. (a) Spatial dependent temperature profile $\Delta T(z)$ with $\Delta T_{max} = 1.75 \text{ K}$ and $\zeta = 5 \mu\text{m}$. (b) Constant temperature rise of $\Delta T = 1 \text{ K}$.

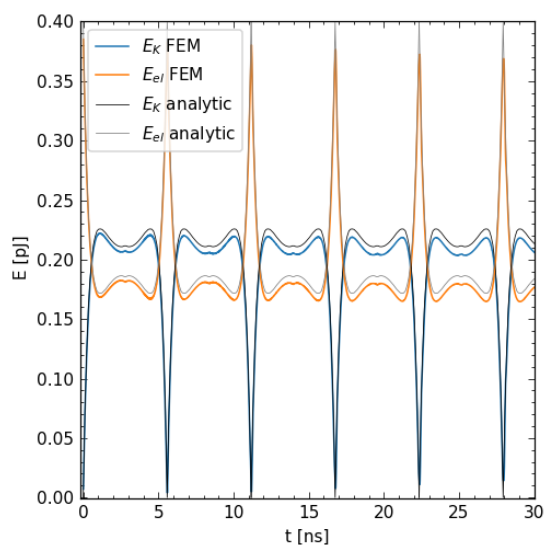
6.2. Solving thermoelastic equations with the finite element method

The finite element method (FEM) is a numerical method that can be used to solve coupled partial differential equations. For the calculations the software COMSOL multiphysics® 5.5 is used in this work. The Structural Mechanics Module and the Heat Transfer Module of this software can be used to solve thermoelastic problems described by the equations Eq. 6.9 and Eq. 6.11. An example for a simple FEM code is given in Appendix A.6. The concepts explained by this FEM code are similar to the one used in COMSOL multiphysics® and may give a good introduction to the underlying concepts of the particular FEM used by COMSOL multiphysics® which are chosen to solve thermoelastic problems in this work.

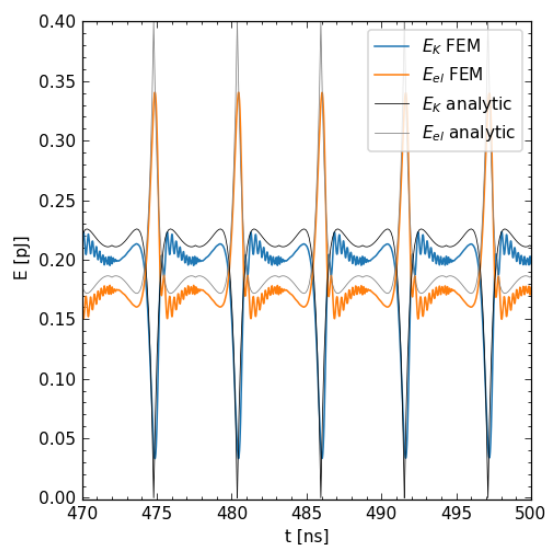
Reproducing the one-dimensional solution with the FEM Before investigating a time dependent three-dimensional thermoelastic problem it should be verified that the chosen parameters for a FEM simulation can reproduce the analytical solution of the one-dimensional wave propagation. For this verification Eq. 6.21 is solved with the Coefficient Form PDE module of COMSOL multiphysics® using quadratic shape functions, a uniform mesh of $1 \mu\text{m}$ per element, a uniform time stepping of 10 ps and the generalized alpha method as time-depend solver. For the beam parameters, $\zeta = 20 \mu\text{m}$ and $\Delta T_{max} = 1 \text{ K}$ have been chosen. The crystal thickness d is $100 \mu\text{m}$ and for the energy calculations a beam radius of $W = 300 \mu\text{m}$ is assumed. In Fig. 6.8 the comparison of the analytic solution for the displacement and energies is given. It is noticeable that the numerical errors of the FEM simulation introduce some kind of damping and also some high frequency oscillations as illustrated in Fig. 6.8c. However, it may be assumed from this comparison that the calculated values with the FEM simulation with the chosen parameters give still reliable information about the thermoelastic problem which has been investigated. It should be mentioned that with the same simulation parameters but a value of $\zeta = 5 \mu\text{m}$ as it has been used in Fig. 6.3a the numerical errors concerning the oscillation are much clearer



(a) Elastic and kinetic energy



(b) Zoom for the first 30 ns



(c) Zoom for the last 30 ns

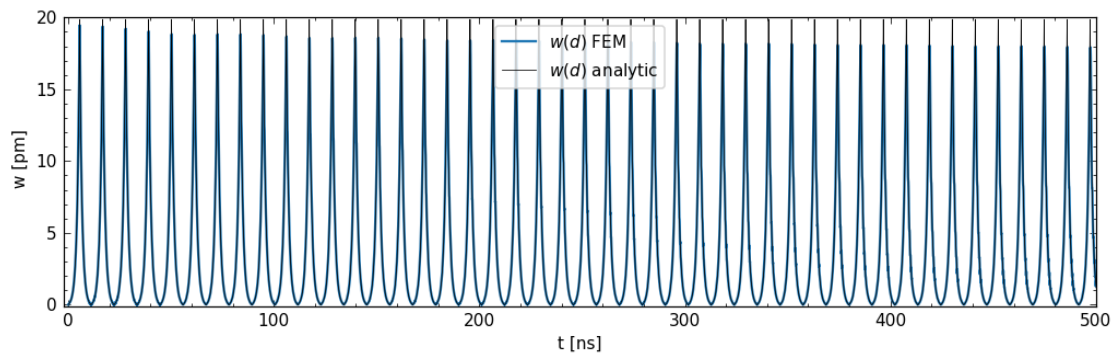
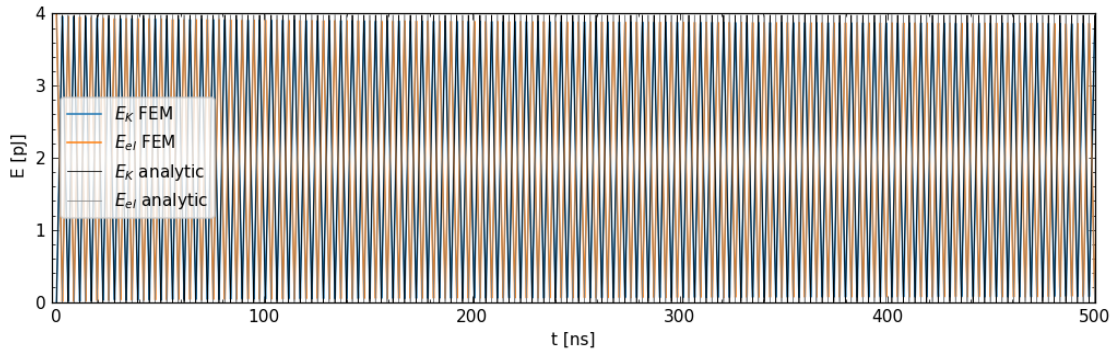
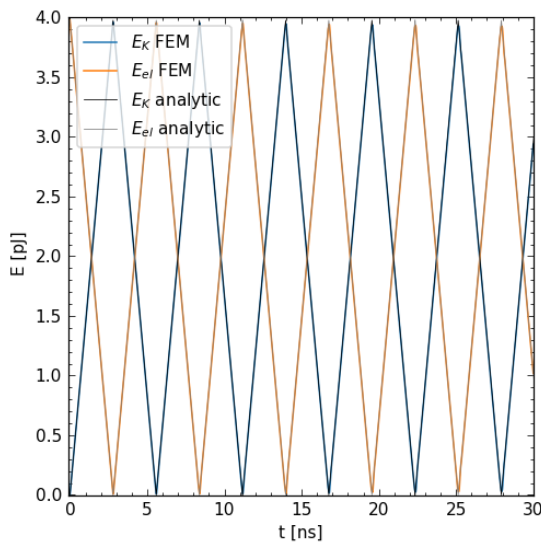
(d) Displacement at $z = d$

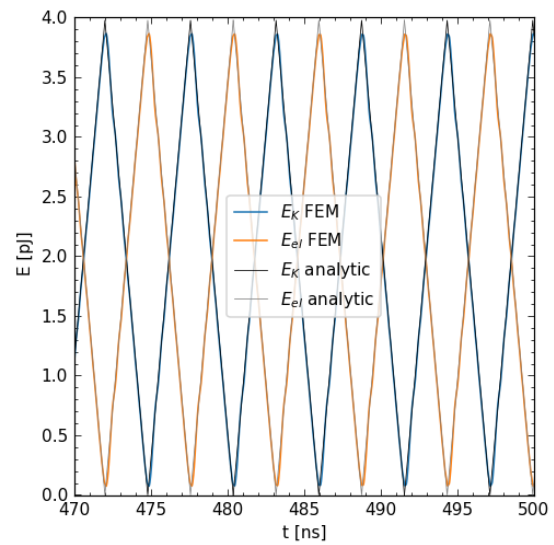
Figure 6.8.: Comparison of FEM simulation with analytical solution for a time span of 500 ns using a uniform mesh of $1\ \mu\text{m}$ and a uniform time stepping of 10 ps, considering a spatial dependent temperature rise with $\Delta T_{\max} = 1\ \text{K}$ and $\zeta = 20\ \mu\text{m}$. In (a) the elastic and kinetic energy is shown. A zoom of this plot for the first 30 ns is given in (b) and for the last 30 ns in (c). In (d) the displacement at $z = d$ is illustrated.



(a) Elastic and kinetic energy



(b) Zoom for the first 30 ns



(c) Zoom for the last 30 ns

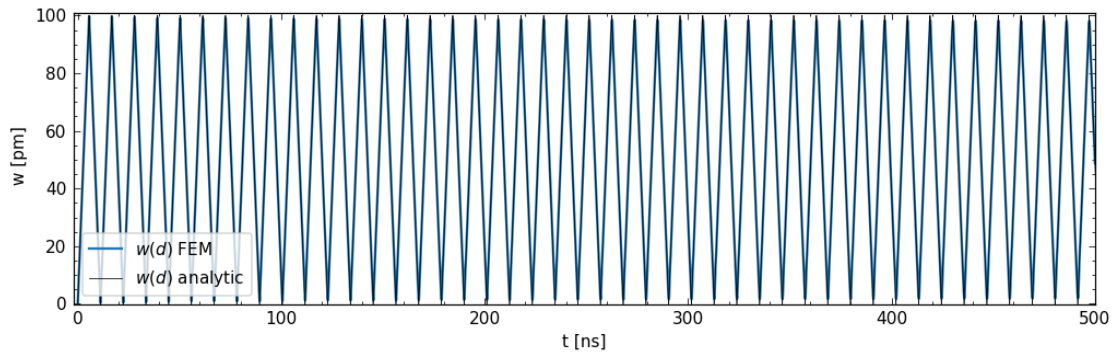
(d) Displacement at $z = d$

Figure 6.9.: Comparison of FEM simulation with analytical solution for a time span of 500 ns using a uniform mesh of $1 \mu\text{m}$ and a uniform time stepping of 10 ps, considering a spatial constant temperature rise of $\Delta T(z) = 1 \text{ K}$. In (a) the elastic and kinetic energy is shown. A zoom of this plot for the first 30 ns is given in (b) and for the last 30 ns in (c). In (d) the displacement at $z = d$ is illustrated.

present. To keep the simulation time as short as possible but sufficiently accurate to explain the thermoelastic wave propagation caused by a temperature rise with $\zeta \ll d$ it is supposed that choosing $\zeta = 20 \mu\text{m}$ and $d = 100 \mu\text{m}$ is a good compromise. For the case of a spatially constant temperature rise of $\Delta T(z) = 1 \text{ K}$, the FEM simulation using the same parameters as before shows less numerical errors as illustrated in Fig. 6.9.

6.2.1. Thermoelastic axisymmetric simulations considering a time independent temperature profile

In this section a three-dimensional thermoelastic problem is investigated considering axial symmetric¹⁰ wave propagation introduced by a time independent axisymmetric temperature profile given by Eq. 6.16, which has the maximum temperature value in the center of a cylindrical crystal. In this context, "time independent" means that no heat conduction is considered, but the temperature profile can occur instantaneously at $t = 0$ and causes thereby thermoelastic waves.

Quasi-static As a starting point for this investigation the consideration of a quasi-static case where no heat conduction is present may be helpful. Such a situation can be considered approximately for a situation where the development of the temperature rise is built up sufficiently slow, so that kinetic energy (Eq. 3.63) is small enough to be neglected. Further, the heat conduction process in this case should be so slow that the temperature profile can be approximated to be static for a certain time span. Assuming that a temperature profile given by Eq. 6.16 is time independent will cause a static displacement field in a constrained crystal. To investigate an axisymmetric displacement field a cylindrical diamond crystal (Fig. 6.10a) with radius $R_0 = 900 \mu\text{m}$, height $d = 100 \mu\text{m}$ as illustrated in Fig. 6.10a is considered. The chosen kinematic boundary conditions (Eq 6.4 and Eq 6.5) for the crystal surface are as follows: The displacement is zero at positions for $\rho_r = R_0 \rightarrow u_i|_{S_{1M}} = \hat{u}_i = 0$ and that there is no constraining force at positions $z = 0$ and $z = d \rightarrow \sigma_{ij}n_i|_{S_{2M}} = \hat{t}_j = 0$. The maximum of the temperature profile is located at ($z = 0$ and $\rho_r = 0$). The value of the maximum temperature is $T_{max} = 1 \text{ K}$ and the value for W is $300 \mu\text{m}$. For the calculations the elastic material constants of diamond are approximated to be isotropic with a Poisson's ratio of $\nu = 0$ and a Young's modulus $E = 1125 \text{ GPa}$ as discussed in Section 4 Fig. 4.2. The stress-strain relation for this problem is given by Eq. 6.10. Due to the axisymmetry only the cross section domain must be calculated, which is marked red in Fig. 6.10b. Thus, due to the axisymmetry in this case a three-dimensional problem can be represented by the solution of a two-dimensional problem.

Due to the assumption of a time independent temperature profile the time derivative terms in Eq. 6.9 can be neglected. Considering these simplifications equation Eq. 6.9 then is solved with the FEM in a cylindrical coordinate system using a two-dimensional ax-

¹⁰Using the condition mentioned in Section 3.5

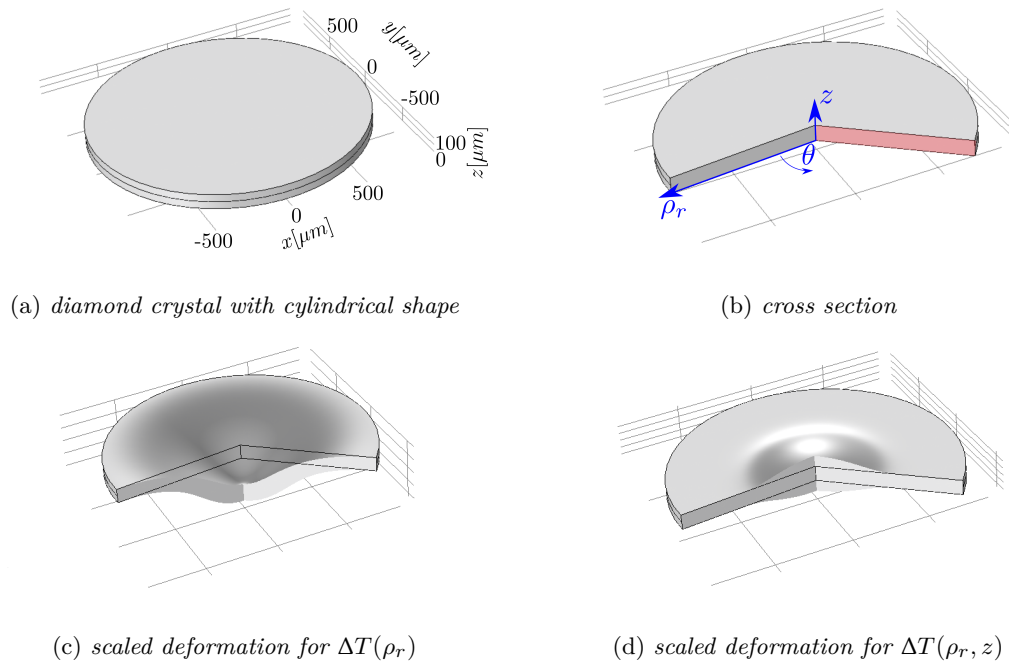


Figure 6.10.: (a) Cylindrical crystal shape which is assumed for the FEM simulation. (b) Cross section of the cylindrical crystal. (c) Deformation scaled by a factor 1500000 caused by the temperature profile shown in Fig. 6.11a. (d) Deformation scaled by a factor 1500000 caused by the temperature profile shown in Fig. 6.11b.

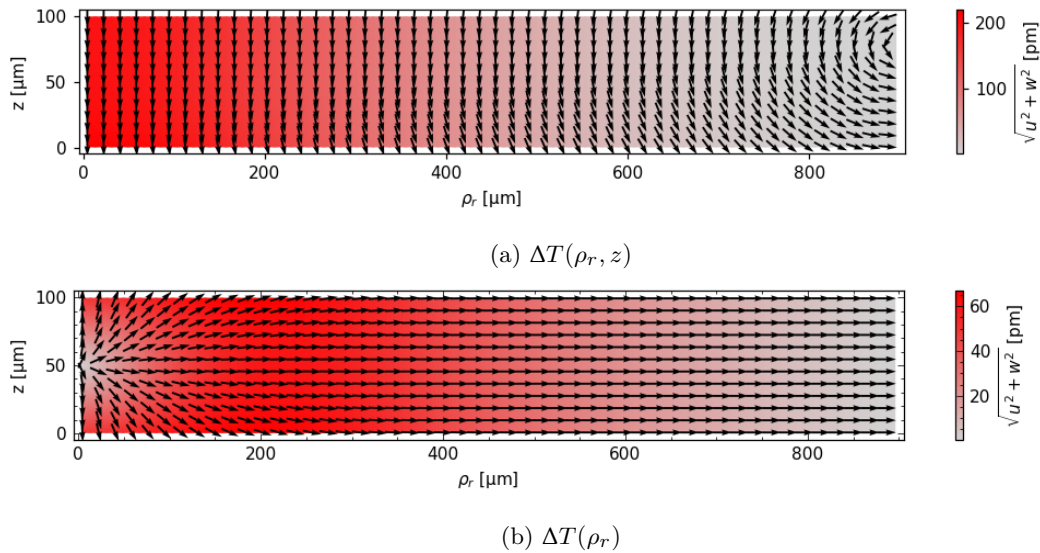


Figure 6.11.: In (a) the magnitude of the displacement field calculated for at temperature profile: $\Delta T(\rho_r, z) = \Delta T_{max} \exp\left(-\frac{2\rho_r^2}{W^2} - \frac{z}{\zeta}\right)$ with $W = 300 \mu\text{m}$, $\zeta = 20 \mu\text{m}$ and $T_{max} = 1 \text{ K}$ is illustrated. The maximum displacement value is 220 pm at $(z = 0, \rho_r = 0)$. In (b) a temperature profile $\Delta T(\rho_r) = \Delta T_{max} \exp\left(-\frac{2\rho_r^2}{W^2}\right)$ with $T_{max} = 1 \text{ K}$ which is constant in z direction has been considered.

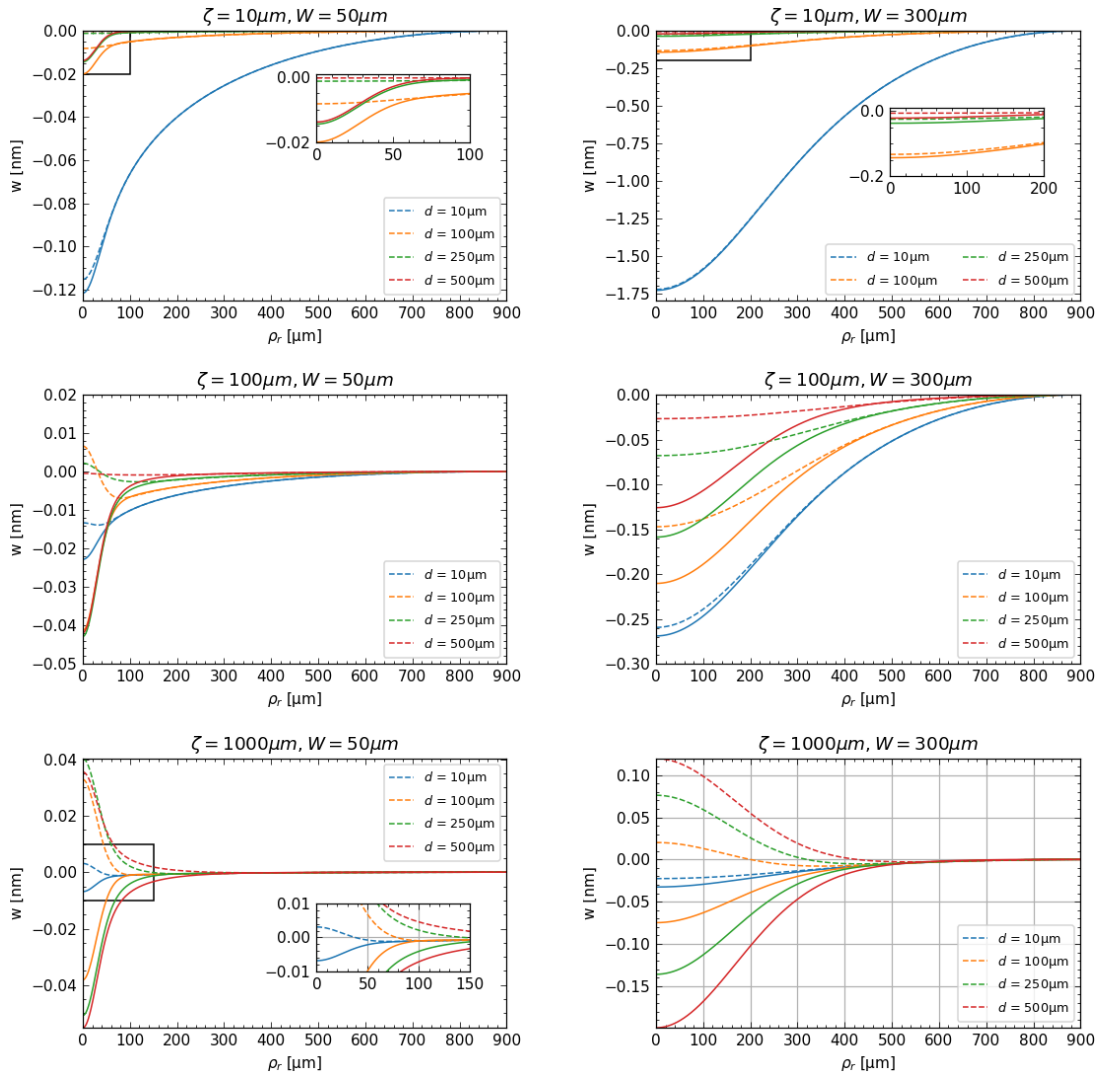


Figure 6.12.: Displacement in z -direction w at the front side $z = 0$ (solid lines) and the back side $z = d$ (dashed lines) for a cylindrical diamond crystal with $R_0 = 1000 \mu\text{m}$ experiencing a thermal expansion of a constant temperature profile $\Delta T(\rho_r, z) = \Delta T_{\max} \exp\left(-\frac{2\rho_r^2}{W^2} - \frac{z}{\zeta}\right)$ with $T_{\max} = 1 \text{ K}$ and various values of d , ζ and W .

isymmetric simulation with quadratic shape functions and a uniform quad mesh with element size of $1 \mu\text{m}$. In Fig. 6.11a the magnitude of the displacement field calculated for a temperature profile described by Eq. 6.16 with $\zeta = 20 \mu\text{m}$ is illustrated. In Fig. 6.11b a temperature profile which is constant in z -direction has been considered. The direction of the vector field is illustrated with normalized arrows in both illustrations. The displacement fields for these temperature profiles look quite different. For the z -direction dependent temperature profile in Fig. 6.11a it can be seen that the temperature profile causes a displacement pointing in negative z -direction at the front ($z = 0$) and at the back side ($z = d$) in the center region (around $\rho_r = 0$) of the crystal. This is caused by the constraints of the crystal (fixed constraint at $\rho_r = R_0$) in combination with a spatial varying thermal expansion. The thermal expansion causes a thermal stress which results in a deformation shape illustrated in Fig. 6.10c, where the magnitude of the deformation

is scaled by a factor of 1500000 for visualization purpose. The maximum value of the displacement is located at $(z = 0, \rho_r = 0)$ and has a value of 220 pm. The displacement field caused by the in z -direction constant temperature profile shows a symmetry regarding the mid line (at $z = d/2$) of the crystal. At $(z = 0, \rho_r = d)$ the displacement has a value of 49.9 pm pointing in positive z -direction and at $(z = 0, \rho_r = 0)$ the value is also 49.9 pm, but pointing in negative z -direction. However, the maximum magnitude of the displacement is in this case located at the positions $(z = 0, \rho_r = 190 \mu\text{m})$ and $(z = d, \rho_r = 190 \mu\text{m})$ and has a value of 67 pm. The deformation for this temperature profile is illustrated in Fig. 6.10d and is also scaled by a factor of 1500000.

The kind of deformation, which has been described in this section will be called a **heat bump** in the following part of this work.

It should be noted that the heat bump effects illustrated in Fig. 6.11 are rather special cases. A more general investigation of the heat bump effect is given by the illustrations in Fig. 6.12, where various combinations of different values for W , ζ and d are shown. To obtain a better overview only the displacement w in z -direction at the surface $z = 0$ (solid lines) and at $z = d$ (dashed lines) are shown. For all FEM¹¹ simulation results shown in Fig. 6.12 a temperature profile $\Delta T(\rho_r, z) = \Delta T_{max} \exp\left(-\frac{2\rho_r^2}{W^2} - \frac{z}{\zeta}\right)$ with $T_{max} = 1$ K and a diamond crystal (Table 6.1) with radius $R_0 = 900 \mu\text{m}$ have been considered. It can be seen clearly that the shape of the temperature given by ζ and W , as well the thickness d of the crystal have a major impact on the resulting shape of deformation. The shape of these deformations is relevant for the excitation of eigenfrequencies, which will be discussed in Section 6.2.5.

Instantaneous temperature rise Now a case with an instantaneous temperature rise will be considered. However, heat conduction is still assumed to be neglected. The material geometry, parameters and the temperature profiles which are used for the simulations are the same ones used for the quasi static case. The PDE which has to be solved in this case is given by Eq. 6.9 and the stress-strain relation by Eq. 6.9. This PDE has been solved then with the FEM¹².

The total kinetic E_{kin} and elastic energy E_{el} can be calculated with Eq. 3.73 and Eq. 3.63 by integrating over the crystal domain:

$$\begin{aligned} E_{el} &= \int_0^d \int_0^{2\pi} \int_0^{R_0} U_{el}(\rho_r, z, t) \rho_r d\rho_r d\theta dz \\ E_{kin} &= \int_0^d \int_0^{2\pi} \int_0^{R_0} K(\rho_r, z, t) \rho_r d\rho_r d\theta dz. \end{aligned} \quad (6.34)$$

Considering the terms in Eq. 3.73 and Eq. 3.63 these integrals can be separated into the sums $E_{el} = E_{el_{zz}} + E_{el_{\rho_r\rho_r}} + E_{el_{\theta\theta}} + E_{el_{\rho_r z}}$ and $E_{kin} = E_{kin_z} + E_{kin_{\rho_r}}$, where the separate

¹¹Using quadratic shape functions a uniform quad mesh with an element size of 1 μm .

¹²Using quadratic shape functions a uniform quad mesh with an element size of 1 μm and the generalized alpha time solver using a uniform time stepping of 10 ps. The choice for this time stepping is motivated by the previously discussion about reproducing the one-dimensional solution.

terms are:

$$\begin{aligned}
E_{el_{\rho_r\rho_r}} &= \pi E \int_0^d \int_0^{R_0} (\epsilon_{\rho_r\rho_r}(\rho_r, z, t) - \alpha\Delta T(\rho_r, z, t))^2 \rho_r d\rho_r dz & (6.35) \\
E_{el_{zz}} &= \pi E \int_0^d \int_0^{R_0} (\epsilon_{zz}(\rho_r, z, t) - \alpha\Delta T(\rho_r, z, t))^2 \rho_r d\rho_r dz \\
E_{el_{\theta\theta}} &= \pi E \int_0^d \int_0^{R_0} (\epsilon_{\theta\theta}(\rho_r, z, t) - \alpha\Delta T(\rho_r, z, t))^2 \rho_r d\rho_r dz \\
E_{el_{\rho_r z}} &= \pi E \int_0^d \int_0^{R_0} \epsilon_{\rho_r z}^2(\rho_r, z, t) \rho_r d\rho_r dz \\
E_{kin_z} &= \rho\pi \int_0^d \int_0^{R_0} \dot{w}^2(z, t) \rho_r d\rho_r dz \\
E_{kin_{\rho_r}} &= \rho\pi \int_0^d \int_0^{R_0} \dot{u}^2(z, t) \rho_r d\rho_r dz.
\end{aligned}$$

With the calculated solution of the FEM simulation for the displacement field the energies in Eq. 6.35 can be calculated for each time step.

In Fig. 6.13 energies for the z -dependent temperature profile with $\zeta = 20\ \mu\text{m}$ and $T_{max} = 1\ \text{K}$ are illustrated. It can be seen from Fig. 6.13b that the energy from the rough estimation for the energy of the analytic solution has nearly the same value as $E_{el_{zz}}, E_{el_{\rho_r\rho_r}}$ and $E_{el_{\theta\theta}}$ at $t = 0$. However, it is important to notice that each energy component $E_{el_{zz}}, E_{el_{\rho_r\rho_r}}$ and $E_{el_{\theta\theta}}$ has this energy so that the total energy at $t = 0$ (Fig. 6.13a) is about three times the value of the analytical estimation where the three-dimensional effect have been ignored. The periodic exchange of the kinetic and elastic energy in z -direction (Fig. 6.13b) shows a similar development for the first few nanoseconds compared to the one-dimensional case (Fig. 6.8a). However, the amplitude of these energy oscillations is decreasing significantly on time scales of a few hundred nanosecond, which cannot be explained by the one-dimensional solution, but is an effect connected to the three-dimensional propagation of the strain wave.

In Fig. 6.13b it can also be seen that the hoop strain $E_{el_{\theta\theta}}$ is decreasing significantly in the startup range. This energy seems to be converted mainly into kinetic and elastic energy in the ρ_r -direction. Also it should be noted that the elastic energy of $E_{el_{\rho_r z}}$ is small in comparison to the other energies. The displacement in z -direction at position ($z = d, \rho_r = 0$) for this simulation is illustrated in Fig. 6.8. The vertical lines in Fig. 6.14a and Fig. 6.13 mark the period $T_z = 2d/v = 11.18\ \text{ns}$ of the one-dimensional wave illustrated in Fig. 6.8d. The first peak in Fig. 6.14a at $T_z/2$ has nearly the same magnitude and shape as for the one-dimensional case which is propagating in z -direction. In the next periods a peak which corresponds to the wave propagating in z -direction is still noticeable; However, the magnitude is reduced. Also, a rise of a negative displacement is superimposed to the displacement peak. This displacement development can be connected to the previously described heat bump. However, in this case the heat bump needs time to develop which causes a radial strain wave. To investigate the propagation of this radial wave a FEM simulation with a coarser mesh of an element size of $5\ \mu\text{m}$ and a uniform time stepping

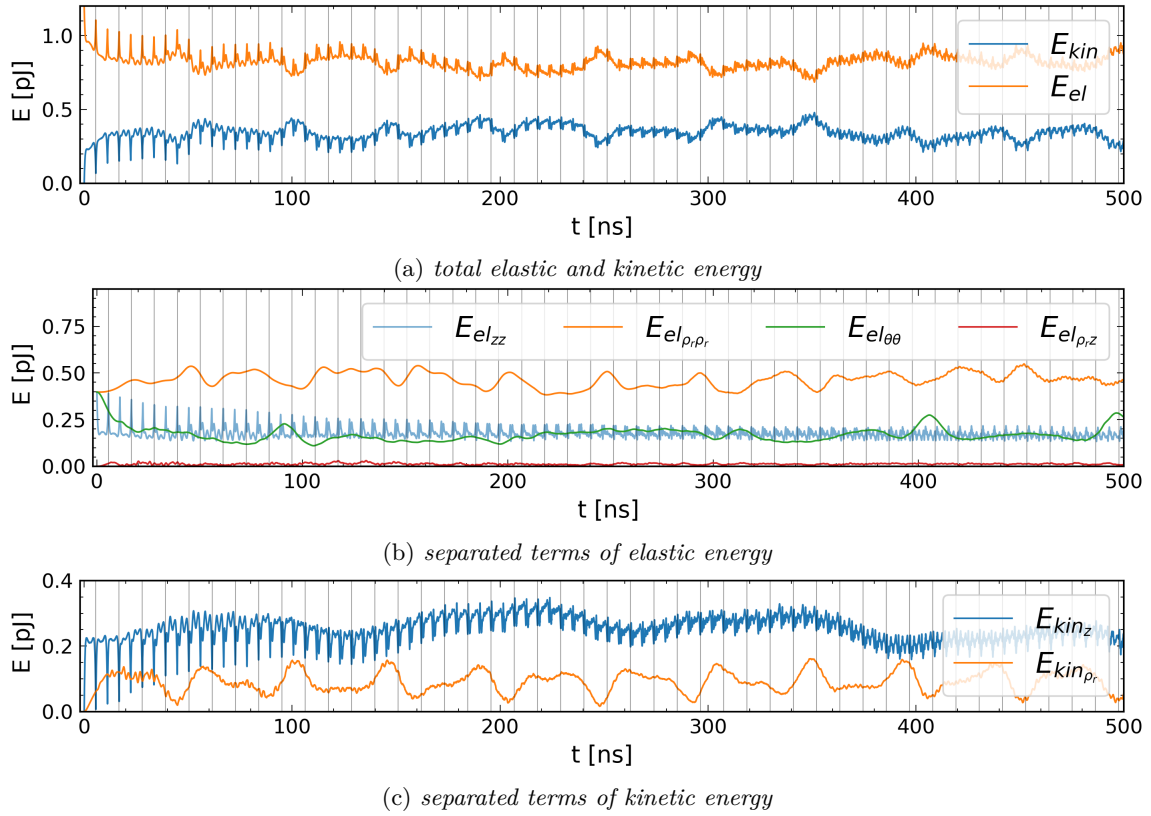


Figure 6.13.: Energies integrated over the crystal domain for (a) the total elastic and kinetic energy, (b) the separated terms of elastic energy and (c) the separated terms of kinetic energy, calculated with the FEM for a cylindrical crystal with radius $R_0 = 900 \mu\text{m}$ and height $d = 100 \mu\text{m}$ which is experiencing an instantaneous temperature rise of a temperature profile $\Delta T(\rho_r, z) = \Delta T_{max} \exp\left(-\frac{2\rho_r^2}{W^2} - \frac{z}{\zeta}\right)$ with $\zeta = 20 \mu\text{m}$ and $T_{max} = 1 \text{K}$ where no heat conduction is considered.

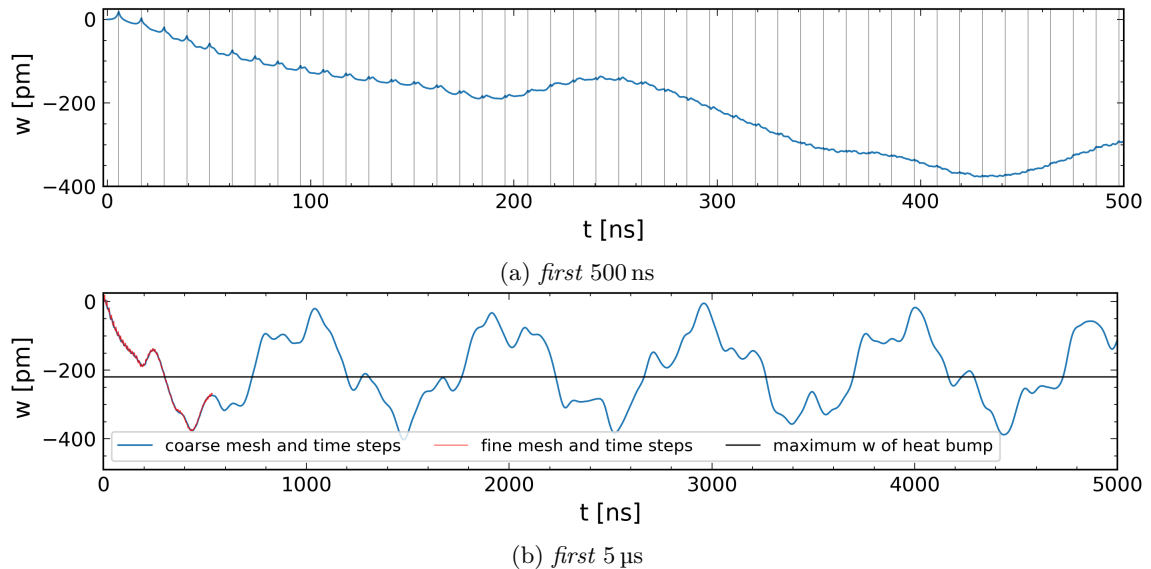


Figure 6.14.: Illustration of the displacement in z -direction at position $(z = d, \rho_r = 0)$, calculated for the same temperature profile and crystal as described in Fig. 6.13, using FEM with parameters: (a) fine uniform quad mesh with element size $1 \mu\text{m}$ and uniform time stepping 10ps and (b) coarse uniform quad mesh with element size $5 \mu\text{m}$ and uniform time stepping 5ns .

of 5 ns has been used. The choice of these simulation parameters is motivated by the observation that the oscillation in z -direction, which have a significant amount of high frequency content, become less important for a description of the displacement at point ($z = d, \rho_r = 0$) considering time spans greater than about hundred nanoseconds. The comparison of the simulation illustrated in Fig. 6.14b shows that the coarse simulation parameter seem to be accurate enough to describe the development of the displacement for time scales in the microsecond range. From this illustration it can be seen that there is no strictly repeated periodical pattern, but a non-periodic oscillation for the illustrated time span. These oscillation are oscillating around the value known from quasi static case (220 pm, see Fig. 6.11) and have a peak-to-peak value which is roughly about twice this value (≈ 440 pm).

To illustrate the development of the radial wave, a FEM simulation with the same condition as described before has been carried out, with the only difference that the radius¹³ of the crystal has now a value of $R_0 = 2000$ μm . As illustrated in Fig. 6.15 it can be seen that the radial wave is build up from the center and is propagating towards the side boundary of the crystal. Due to the boundary of the crystal in ρ_r -direction, which is reached after a time span of about 100 ns to 150 ns this kind of wave will be reflected. However, the impact on the development of the displacement at the position ($\rho_0 = 0, z = 0$) will be delayed, because the radial wave needs time to travel back to the center of the crystal. It should be mention that the radial wave propagation shows a quite different behavior compared to the one-dimensional wave propagation described in Section 6.1, which gave a periodic repeating function after reflection at the boundaries. For the case of the radial wave the temporal development of the displacement field after reflection is quite chaotic and does not show simple periodic behavior. In other words for the considered simulation the kind of displacement wave propagation illustrated in Fig. 6.15 is only observed in the start up range and is not repeated afterwards. In Fig. 6.16 the comparison of the displacement in z -direction at position ($\rho_0 = 0, z = d$) for the simulation of the cylindrical crystals with radii R_0 are shown. It can be seen that in the startup range the displacement shows the same development, however after a characteristic dip in the development of the displacement the further development is completely different. The characteristic dip can be connected to the arrival of the radial wave which is reflected at the side boundaries. Another feature which is visualized by Fig. 6.16 is that the maximum value of the displacement which is reached does not only depend on the value of the temperature rise, but also on the radius of the crystal, which can be explained by considering that the heat bump effect depends on the crystal radius and the crystal constraints (Fig. 6.12).

In Fig. 6.17 the energies calculated for a temperature profile constant in z -direction with $\Delta T = 1$ K is illustrated. Also in this case the estimation of the one-dimensional solution (Fig. 6.9) gives a quite accurate value for the elastic energy $E_{el_{zz}}$ at $t = 0$. However,

¹³The larger radius is chosen because the development of the radial wave in the range of the first tens of nanoseconds in this case can be illustrated without taking into account a major contribution of side boundary reflection effects.

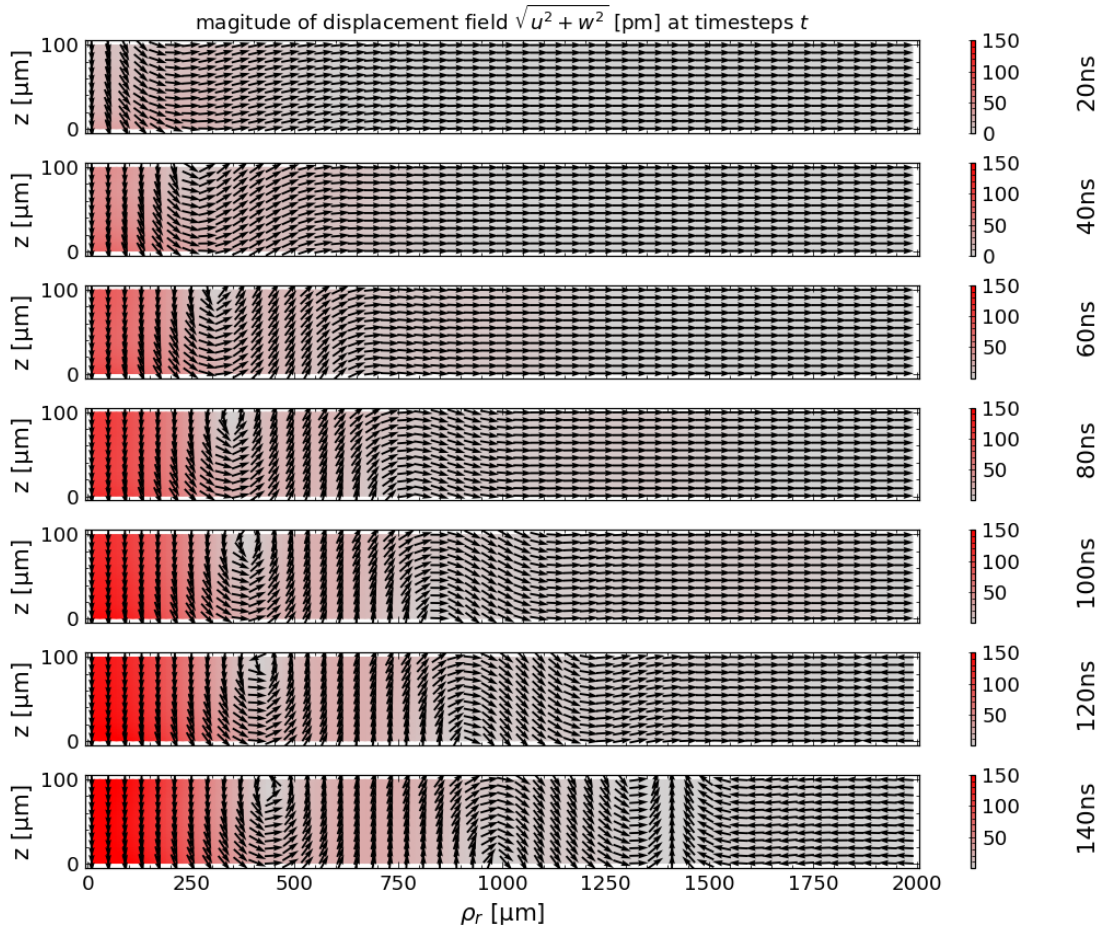


Figure 6.15.: Temporal development of the heat bump effect after an instantaneous temperature rise $\Delta T(\rho_r, z) = \Delta T_{max} \exp\left(-\frac{2\rho_r^2}{W^2} - \frac{z}{\zeta}\right)$ with $\zeta = 20 \mu\text{m}$, $W = 300 \mu\text{m}$ and $T_{max} = 1 \text{ K}$.

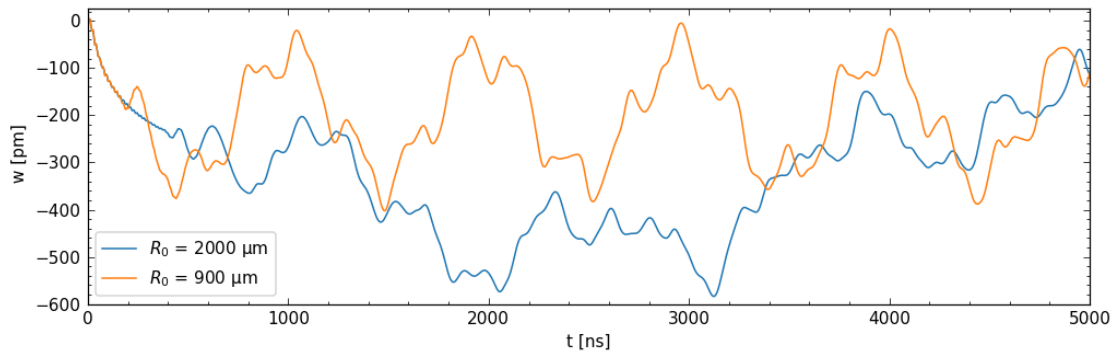


Figure 6.16.: Comparison of a FEM simulation using the same parameters as in Fig. 6.14b, except of the radius R_0 of the cylindrical crystal, which is here assumed to be $2000 \mu\text{m}$.

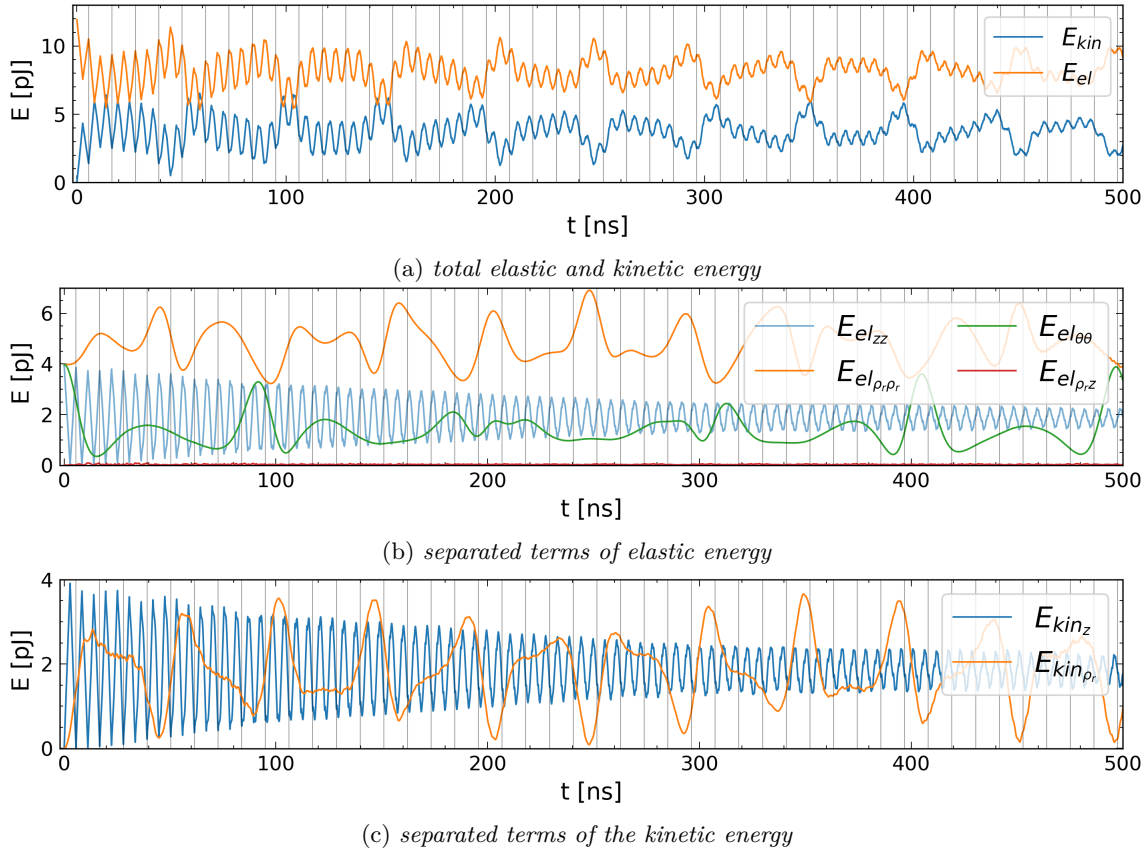


Figure 6.17.: Energies integrated over the crystal domain for (a) the total elastic and kinetic energy, (b) the separated terms of elastic energy and (c) the separated terms of kinetic energy, calculated with FEM for a cylindrical crystal with radius $R_0 = 900 \mu\text{m}$ and height $d = 100 \mu\text{m}$ which is experiencing an instantaneous temperature rise of a temperature profile $\Delta T(\rho_r) = \Delta T_{max} \exp\left(-\frac{2\rho_r^2}{W^2}\right)$ with $T_{max} = 1 \text{ K}$ where no heat conduction is considered.

also in this case the same energy amount like for $E_{el_{zz}}$ is present for $E_{el_{\rho_r\rho_r}}$ and $E_{el_{\theta\theta}}$. Also, like observed before for the z -dependent temperature profile the hoop strain $E_{el_{\theta\theta}}$ decreases significantly in the first nanoseconds and the energy is converted into elastic and kinetic energy in the ρ_r -direction. The periodic energy exchange for the elastic and kinetic energy in z -direction is similar like in the one-dimensional case (Fig. 6.9) considering the first nanoseconds as indicated by the vertical lines indicated in Fig. 6.17. However, in the first 200 ns the amplitude drops significant and for t greater than about 300 ns there is a significant change of periodicity noticeable. The vertical markings are also used in Fig. 6.18, where the displacement at position $(\rho_r = 0, z = d)$ is illustrated. It can be seen that for t greater than about 300 ns the oscillation are less periodic and oscillate around the value of the heat bump at position $(\rho_0 = 0, z = d)$ shown in Fig. 6.11b.

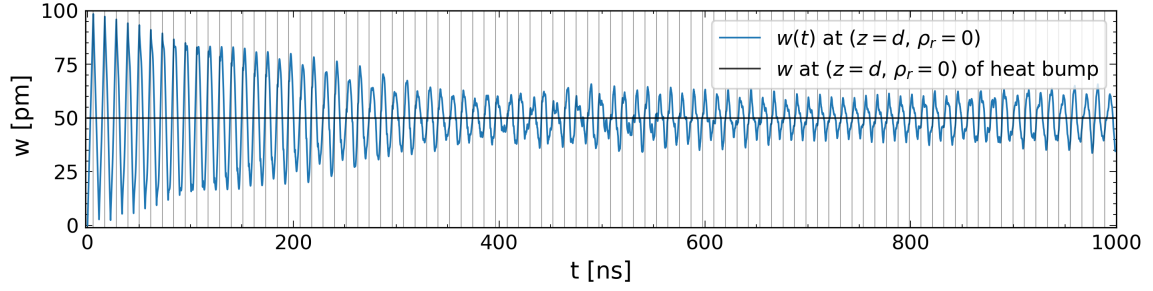


Figure 6.18.: Illustration of the displacement w in z -direction at position $(z = d, \rho_r = 0)$, which has been calculated for the same temperature profile and crystal as described in Fig. 6.17, using FEM simulation with a uniform quad mesh, element size $1 \mu\text{m}$ and uniform time stepping 10 ps .

6.2.2. Time dependent temperature profile

In the discussed examples of this section so far an instantaneous temperature rise has been assumed. Now a finite time span for the temperature rise will be discussed.

Considering Eq. 6.11 in this context the introduced heat per unit time and unit volume Q_{ext} by a pulsed electromagnetic radiation with a Gaussian beam profile may be expressed by using Eq. 2.62:

$$Q_{ext} = \mathfrak{T}(t) \frac{(1-R)2E_p\gamma h}{\zeta\pi W^2} \exp\left(-\frac{2\rho_r^2}{W^2}\right) \exp(-z/\zeta), \quad (6.36)$$

The used constants in Eq. 6.36 have the same meaning as described by Eq. 6.15, $\mathfrak{T}(t)$ is a function which has the unit s^{-1} and is normalized so that

$$\int_0^\infty \mathfrak{T}(t) dt = 1. \quad (6.37)$$

The absorbed energy in a time span covering the complete rise and fall time of $\mathfrak{T}(t)$ is given by Eq. 6.17. The function $\mathfrak{T}(t)$ can be interpreted in the context of this work as the temporal profile of the pump laser pulse under the assumption that the thermalization, which is describing the conversion of the absorbed energy into heat takes place on timescales much faster than the rise and fall time of the temporal laser pulse profile. However, for laser pulse durations much shorter than the characteristic time scales of the thermalization process $\mathfrak{T}(t)$ may also be used to describe the thermalization process.

A particular choice of $\mathfrak{T}(t)$ is given by a normalized¹⁴ Gaussian function (Fig. 6.19a)

$$\mathfrak{T}(t) = \frac{1}{\sqrt{2\pi\tau_0^2}} \exp\left(-\frac{(t-5\tau_0)^2}{2\tau_0^2}\right) \quad (6.38)$$

The full width at half maximum (FWHM) value of the Gaussian function is $t_p = 2\sqrt{2\ln 2}\tau_0$

¹⁴In fact the integral function is not exactly $\int_0^\infty \mathfrak{T}(t) dt = 1$ because the values at $t < 0$ are not zero. However the value at $t = 0$ is already very small (compared to the maximum value of $\mathfrak{T}(t)$) and the magnitude for value $t < 0$ decreases exponentially and thus can be neglected.

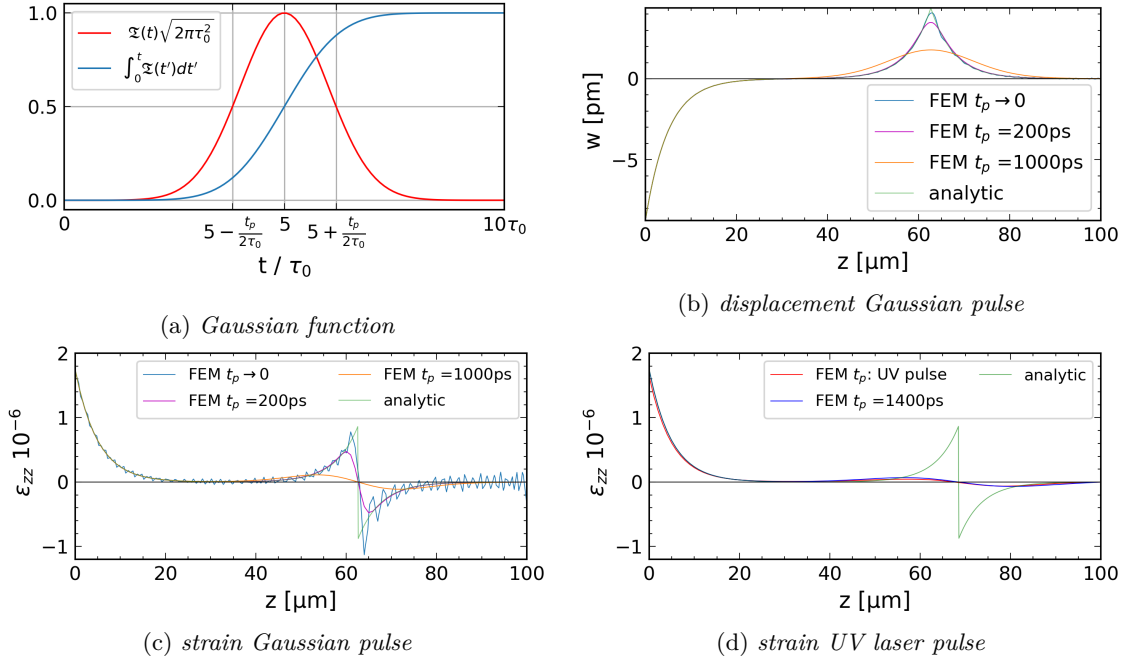


Figure 6.19.: (a) *Gaussian function with a maximum value located at $5\tau_0$. The FWHM range is marked by the range between $5\tau_0 - \frac{t_p}{2}$ and $5\tau_0 + \frac{t_p}{2}$.* (b) *Displacement and (c) strain of a FEM solution for a temporal dependent one-dimensional temperature profile at time $t = 3.5 \text{ ns} + 5\tau_0$.* (d) *Strain introduced by the temporal profile of the pump laser illustrated in Fig. 5.3b.*

and therefore for a given t_p value τ_0 can be calculated by $\tau_0 = \frac{t_p}{2\sqrt{2 \ln 2}}$.

Another choice of $\mathfrak{Z}(t)$ which is of particular interest for the needs of this work is given by the measured temporal profile of the UV laser pulse illustrated in Fig. 5.3b.

For simplicity a one-dimensional problem, which is similar to the previously described one-dimensional wave propagation expressed by Eq. 6.21 will now be considered to investigate the effect of a finite temperature rise. Considering a small temperature rise, the heat capacity c and the density ρ can be approximated to be temperature independent. For a case where the impact of the temporal changing strain field on temperature and the heat conduction can be neglected Eq. 6.11 becomes in this case

$$c\rho \frac{\partial T}{\partial t} = Q_{ext}, \quad \text{where } T = T_0 + \Delta T. \quad (6.39)$$

For a pump laser a one-dimensional development of a temperature profile can be considered by assuming $W \gg \zeta$. The temperature profile, assuming that all the absorbed energy is converted into heat ($\gamma_h = 1$), can be expressed by inserting Eq. 6.36 into Eq. 6.39 which yields by considering $W \gg \zeta$:

$$\Delta T(t, z) = \Delta T_{max} \exp(-z/\zeta) \int_0^t \mathfrak{Z}(t') dt' \quad \text{where } \Delta T_{max} = \frac{2E_p(1-R)\gamma_h}{W^2 \pi c \rho \zeta}. \quad (6.40)$$

For the UV pulse (Fig. 5.3b) the integral in Eq. 6.40 can be solved numerically and the

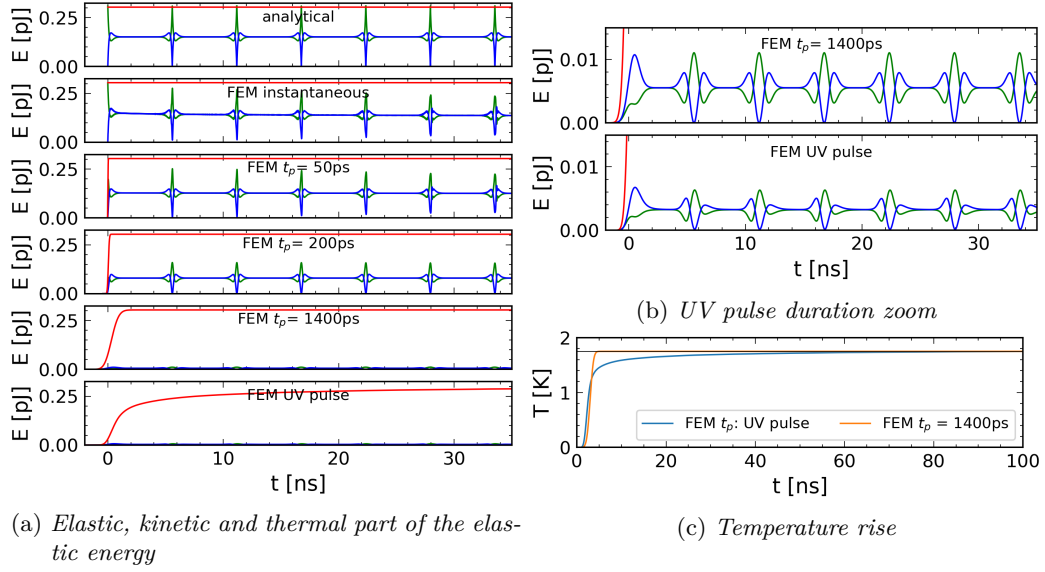


Figure 6.20.: (a) Energies calculated for a case with a beam radius of $W = 300 \mu\text{m}$ a penetration depth of $\zeta = 5 \mu\text{m}$ and a maximum temperature rise $\Delta T_{max} = 1.75 \text{K}$. The red line illustrates the thermal part of the elastic energy calculated with Eq. 6.42, the green line represents the elastic energy, which is given by Eq. 6.31 and the kinetic energy illustrated by the blue line, is calculated with Eq. 6.30. Several finite time spans for the temperature profile to built up have been considered and are compared with analytical and FEM solutions for an instantaneous temperature rise. (b) A zoom for the elastic and kinetic energy for pulse duration in the nanosecond range, which are also illustrated in (a). (c) Time span to reach saturation comparing the UV pulse Fig. 5.3b shape with a Gaussian pulse with similar FWHM value.

integral of the Gaussian function Eq. 6.38 is in good approximation (Fig. 6.19a)

$$\int_0^t \mathfrak{T}(t') dt' = \frac{1}{2} \left(1 + \operatorname{erf} \left(\frac{t - 5\tau_0}{\tau_0 \sqrt{2}} \right) \right). \quad (6.41)$$

Inserting Eq. 6.40 into Eq. 6.21 gives a partial differential equation which can be solved with the Coefficient Form PDE module of COMSOL multiphysics®. For the calculation quadratic shape functions, a uniform mesh of $1 \mu\text{m}$ per element, a uniform time stepping of 5ps and the generalized alpha method for time-dependent solver have been used.

In Fig. 6.19 the calculated displacement (Fig. 6.19b) and strain (Fig. 6.19c) for different values of t_p , considering a temporal Gaussian profile (Fig. 6.19a), are show at the time $t = 3.5 \text{ns} + 5\tau_0$. The chosen parameters for $\zeta = 5 \mu\text{m}$ and $\Delta T_{max} = 1.75 \text{K}$ are the same as the ones used to calculate the values of Fig. 6.2a and Fig. 6.3a. The analytic solution is also illustrated in Fig. 6.19. For $t_p \rightarrow 0$ the solution of the FEM simulation should give the same values as the analytic function, but due to numerical errors these values differ. However, it should be noted that the calculated variable in this FEM simulation is only the displacement w , and the strain is just the numerical derivation $\frac{\partial w}{\partial z}$ of this solution. Therefore, the deviation of the strain compared to the analytical function shouldn't be overvalued.

In Fig. 6.19b it is clearly visible that for $t_p > 0$ the propagating displacement peak is

reduced. The phenomenological explanation for the wave propagation is nearly the same as before (see Section 6.1.2), but in this case the temperature rise is build up on timescales where the wave can propagate a significant distance $\Delta z = vt_p$ during the time where the temperature rise is building up. This results that the observed discontinuity occurring for an instantaneous temperature rise is smeared out for case where the temperature development needs a finite time. Therefore the amplitude of the traveling displacement and strain wave will decrease considering a finite time span of the development of a temperature profile. As illustrated in Fig. 6.19 larger values of t_p result in a lower amplitude of the strain and displacement wave. For values much bigger than one nanosecond the resulting wave may have a negligible amplitude.

Inserting the numerical integration for the UV laser pulse shape (Fig. 5.3b) solution of Eq. 6.40 into Eq. 6.21 and by considering $\zeta = 5 \mu\text{m}$ and $\Delta T_{max} = 1.75 \text{ K}$, gives by using the FEM¹⁵ the strain illustrated in Fig. 6.19d at time $t = 15 \text{ ns} + \tau_{max}$. Here, τ_{max} is the time where the pulse shape in Fig. 5.3b reaches its maximum. By comparing this solution with the analytical solution and the strain calculated for a temporal Gaussian pulse at $t = 15 \text{ ns} + 5\tau_0$ with $t_p = 1400 \text{ ps}$ which is approximately the HWHM value for the UV laser pulse it can be seen that the considered UV laser pulse gives a strain pulse with slightly lower magnitude than the temporal Gaussian pulse. Also it can be seen that the strain at $z = 0$ for the UV laser is slightly smaller. This effect can be explained by considering the temporal profile of the UV pulse in Fig. 5.3b shown in Fig. 6.19d. Since heat conduction has been neglected in the considered example the temperature profile which is final reached is the same in all illustrated case. Therefore the final temperature rise causes the same static displacement and strain value in Fig. 6.19 at $z = 0$. However, for the UV laser this final temperature isn't reached at the illustrated time step.

The kinetic and elastic energy may be calculated with Eq. 6.30 and Eq. 6.31. Due to the temperature dependence of the temperature profile it is now also useful to consider the thermal part of the elastic energy E_{th} which may be calculated by:

$$E_{th}(t) = \frac{AE}{2} \int_0^d (\alpha \Delta T(z, t))^2 dz. \quad (6.42)$$

Considering the area $A = \pi(W/2)^2$ and a beam radius of $W = 300 \mu\text{m}$ the energies show in Fig. 6.20a can be calculated. From these illustrations it can be seen that the time in which the temperature profile is build up has a strong impact on the magnitude of the elastic and kinetic energy considering the one-dimensional displacement/strain wave propagation for a diamond crystal. Also it can be seen that for the chosen FEM simulation parameters quite strong numerical errors are present when a short rise time or an instantaneous temperature rise is considered. These errors may be referred to the quite small penetration depth, because comparing the results to Fig. 6.8 where a larger value for the penetration depth was used showed less errors. For the case of a pulse duration in the nanosecond range,

¹⁵choosing, quadratic shape functions, a uniform mesh of $1 \mu\text{m}$ per element, a uniform time stepping of 5 ps and the generalized alpha method for time-dependent solver

which corresponds to the value of the UV laser pulse (Fig. 5.3b) used for the experiments of this work, a zoom of the elastic and kinetic energy from Fig. 6.20a is shown for better visualization in Fig. 6.20b.

In the following sections a Gaussian temporal profile with $t_p = 200$ ps and the temporal profile of the UV laser (Fig. 5.3b) will be discussed further. These temporal profiles are of particular interest for this work, because the temporal profile of the UV laser will be used to simulate the pump-probe experiment (Section 6.3) and the Gaussian temporal profile with $t_p = 200$ ps will be chosen as an assumption for the thermalization time span after absorption of a femtosecond X-ray photon pulse to simulate the heat load of a saturated XFEL pulse (Section 6.4).

6.2.3. Temperature dependent material parameters

The temperature dependence of material parameters are known from Section 4 and may be taken into account by considering that the material parameters in Eq. 6.9 and Eq. 6.11 are a function of temperature, which causes that the PDEs are now nonlinear. However, in COMSOL multiphysics® such problems can still be calculated by updating the matrices which contain material dependent parameters during a time dependent FEM simulation (see Appendix A.6). Also, non-linear changes can be considered by the software using the Newton-Raphson method.

It should be noted that for the derivation of the thermoelastic PDEs no temperature dependence of the material parameter was considered. From a physical point of view the modification of the PDEs with material dependent constants may be regarded as the assumption that all parts of the solid can be assumed to be in a kind of local thermodynamic equilibrium¹⁶ at each numerical time step and the local temperature dependent material parameters are given by the values introduced in Section 4.

To investigate the effect of a temperature rise, with temperature dependent material parameters, a good starting point may be to consider a one-dimensional case with a temperature variation only in z -direction where heat conduction is neglected. Further, neglecting the coupling of the strain to the temperature Eq. 6.11 becomes:

$$0 = c(T)\rho \frac{\partial T}{\partial t} - Q_{ext}, \quad \text{where } T = T_0 + \Delta T \quad (6.43)$$

The external heat source may be given by a pump laser with a Gaussian beam profile, which has a beam radius of $W = 300 \mu\text{m}$ at position $z = 0$ where it meets the surface of a diamond crystal under normal incidence. The considered thickness of the crystal is $d = 100 \mu\text{m}$. The penetration depth is assumed to be $\zeta = 5 \mu\text{m}$. The pulse energy after reflection is $(1 - R)E_p = 2 \mu\text{J}$ and is assumed to be converted completely into heat. The temporal profile of the laser pulse is assumed to be a Gaussian function described by Eq. 6.38 with FWHM $t_p = 200$ ps. To hold the assumption of a one-dimensional

¹⁶So that a meaningful definition of a thermodynamic temperature is given.

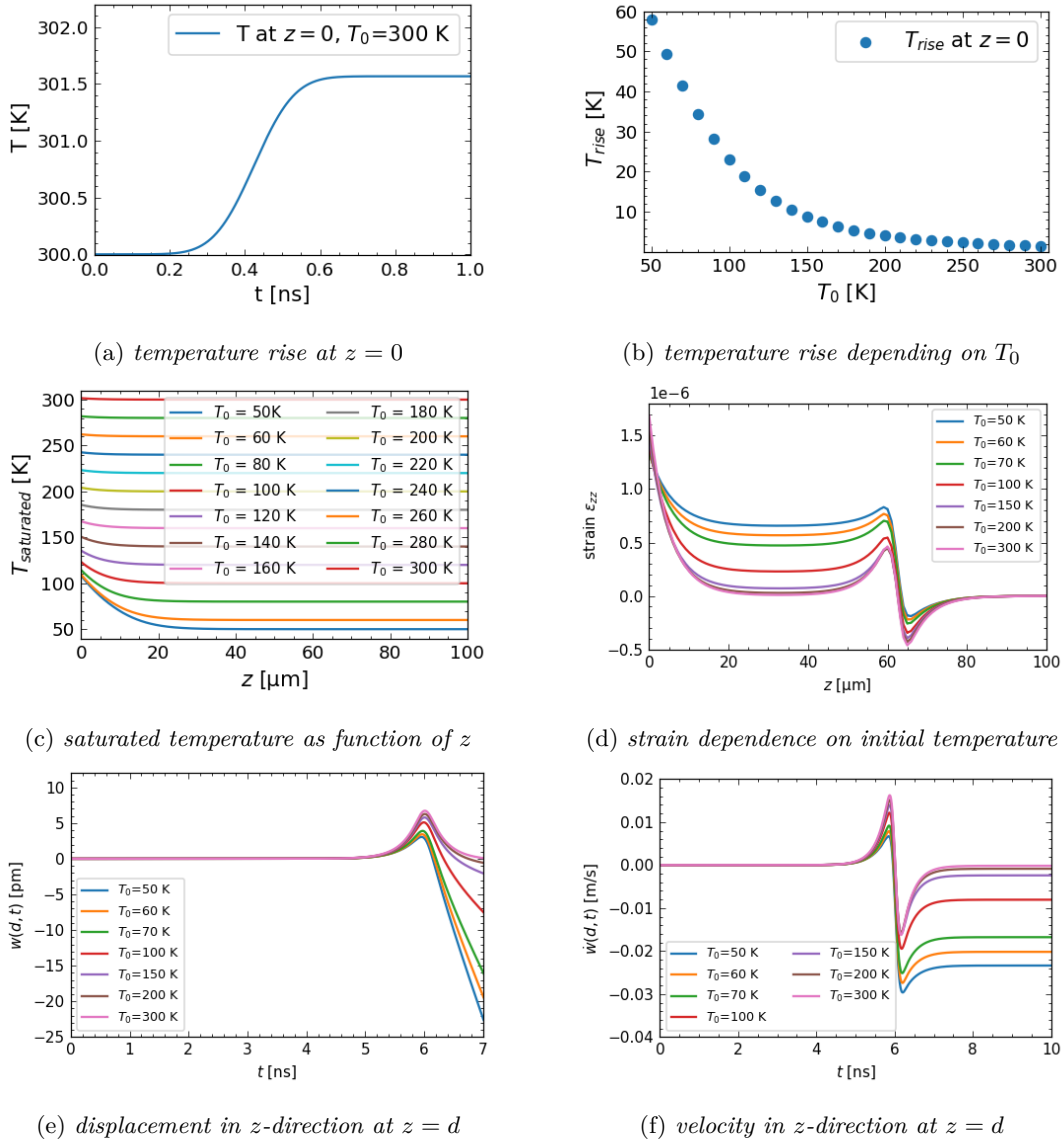


Figure 6.21.: One-dimensional FEM simulation, considering a pump beam with beam radius $W = 300 \mu\text{m}$, a pulse energy after reflection of $(1 - R)E_p = 2 \mu\text{J}$, a penetration depth of $\zeta = 5 \mu\text{m}$ and a crystal thickness of $d = 100 \mu\text{m}$. The temperature dependence of the heat capacity and thermal expansion coefficient of diamond has been taken into account. In (a) the temporal development for an initial temperature of $T_0 = 300 \text{K}$ is shown. After about $t = 0.8 \text{ns}$ the temperature saturates. (b) Temperature rise given by the saturated temperature minus the initial temperature T_0 calculated for different initial temperatures. (c) Spatial dependence of the saturated temperature for different initial temperature values T_0 . (d) Strain ϵ_{zz} for different values of T_0 at the time $t = 3.5 \text{ns} + 5\tau_0$. (e) Displacement in z -direction at the position $z = d$. (f) Velocity \dot{w} at position $z = d$.

temperature profile, only the temperature profile near $\rho_r \approx 0$ is considered. With these assumptions it follows from Eq. 6.38 and Eq. 2.62 that the external heat source for the thermoelastic problem is given by

$$Q_{ext}(z, t) = \mathfrak{T}(t) \frac{2(1-R)E_p}{\zeta\pi W^2} \exp(-z/\zeta), \quad (6.44)$$

where $\mathfrak{T}(t) = \frac{1}{\sqrt{2\pi\tau_0^2}} \exp\left(-\frac{(t-5\tau_0)^2}{2\tau_0^2}\right)$ and $t_p = 2\sqrt{2 \ln 2}\tau_0$.

Solving Eq. 6.43 with the FEM¹⁷ by using the temperature dependent value¹⁸ for $c(T)$ (Fig. 4.6) gives a dependence of the temperature rise of the initial temperature T_0 due to the temperature dependence to the heat capacity. The temperature rise at position $z = 0$ is illustrated for an initial temperature of $T_0 = 300$ K in Fig. 6.21a. It can be seen that the temperature saturates after a time of about $t \approx 4t_p$. This should be not surprising. Because no heat conduction is considered, the temporal Gaussian function will cause a static temperature profile and the time, which it takes for the temperature to build up, corresponds to the width of the Gaussian function Eq. 6.38. The value of the temperature rise ΔT_{rise} in the considered problem is given by the subtraction of the initial temperature T_0 from the temperature value at saturation. The value of the maximum ΔT_{rise} at $z = 0$ is illustrated in Fig. 6.21b for different initial temperatures. In Fig. 6.21c the spatial dependence of the saturated temperature is shown for different initial temperature values.

The solution of the calculated temperature rise can be used to calculate the displacement with Eq. 6.9:

$$E \frac{\partial^2 w}{\partial z^2} - E\alpha_s(T, T_0) \frac{\partial \Delta T}{\partial z} - \rho \frac{\partial^2 w}{\partial t^2} = 0. \quad (6.45)$$

Using the FEM¹⁹ and taking into account the temperature dependence for the secant thermal expansion $\alpha_s(T, T_0)$ (Fig. 4.5, Appendix A.5) the displacement in z -direction w has been calculated for different initial temperatures. The strain in z -direction given by $\epsilon_{zz} = \frac{\partial w}{\partial z}$ at a time $t = 3.5 \text{ ns} + 5\tau_0$ is illustrated in Fig. 6.21d. It can be seen that the strain significantly increases for temperatures lower than 150 K, whereas for temperatures in the range 200 K to 300 K the value is nearly the same. The displacement at position $z = d$ is illustrated in Fig. 6.21e and shows that for low temperatures there is a decrease of the displacement noticeable at the peak around 6 ns, followed by rise of a negative displacement. From Fig. 6.21f it can be seen that the temperature dependence of material properties causes a constant velocity \dot{w} at position $z = d$ after the reflection of the displacement/strain wave, which has a greater magnitude for low temperature and causes the negative displacement rise.

¹⁷Using quadratic shape functions, a uniform mesh size of 1 μm , a uniform time stepping of 5 ps and the generalized alpha time solver

¹⁸Here the heat capacity calculated with the Debye approximation has been used.

¹⁹Using quadratic shape functions, a uniform mesh size of 1 μm , a uniform time stepping of 5 ps and the generalized alpha time solver

6.2.4. Thermal conductivity

The initial temperature profile created by an ultrashort laser pulse, where an instantaneous thermalization has been assumed can be expressed by Eq. 6.16:

$$\Delta T(\rho_r, z) = \Delta T_{max} \exp\left(-\frac{2\rho_r^2}{W^2} - \frac{z}{\zeta}\right), \text{ with } \Delta T_{max} = \frac{\gamma_h(1-R)2E_p}{\zeta\pi W^2 c\rho}. \quad (6.46)$$

If the impact of the temporally changing strain field can be neglected and an isotropic thermal conductivity is considered, the temporal development of the temperature field may be calculated by solving Eq. 3.58:

$$(\lambda_c(T)T_{,i})_{,i} = c(T)\rho\dot{T} - Q_{ext}, \text{ where } T = T_0 + \Delta T \quad (6.47)$$

If no external heat source is present and only a small temperature rise ΔT is considered, so that thermal conductivity and heat capacity can be approximated to be nearly constant, Eq. 6.47 can be expressed as

$$a_T(T_0)(T_{,i})_{,i} = \frac{\partial T}{\partial t}, \text{ where } a_T = \frac{\lambda_c(T_0)}{\rho c(T_0)} \text{ and } T = T_0 + \Delta T. \quad (6.48)$$

Here a_T is the thermal diffusivity. A phenomenological explanation of a_T may be given by noticing that $(T_{,i})$ is the gradient of a scalar field (temperature) and thus a_T is related to the capability of the material to change a spatial temperature difference in a finite time span. The values of the thermal diffusivity a_T as a function of the initial temperatures T_0 for a diamond crystal are illustrated in Fig. 6.22a. For the calculation the temperature dependent material parameters of [WKT⁺93] (Fig 4.6, Section 4) have been used.

For a solid with insulating boundaries where an amount of energy E_Q from a pulsed laser is absorbed and converted into heat energy inside the solid, there will be, as determined by Eq. 6.47, after some time due heat conduction a nearly spatially independent constant equilibrium temperature rise ΔT_{eq} . However, from Eq. 4.21 it can be seen that the value of the temperature rise depends on the value of the heat capacity. Considering the spatial integration of Eq. 4.21 over the volume of the crystal and assuming a constant temperature rise gives

$$\Delta T = \frac{E_Q}{V\rho c(T_0)}. \quad (6.49)$$

For a volume $V = \pi R_0^2 d$ of a cylindrical diamond crystal where the radius is assumed to be $R_0 = 900 \mu\text{m}$ and the thickness $d = 100 \mu\text{m}$, the amount of heat energy of $E_Q = 2 \mu\text{J}$ causes a temperature rise which depends on the initial temperature T_0 as illustrated in Fig. 6.22b. It can be seen that the equilibrium temperature rise T_{eq} does not exceed values of one Kelvin, which verifies the approximation to use a constant heat capacity for the calculation with Eq. 6.49 at each initial temperature value T_0 .

In Fig. 6.22b also the equilibrium temperature rise T_{eq} for a one-dimensional case is illustrated, as given by Eq. 6.44. For a one-dimensional temperature rise which only

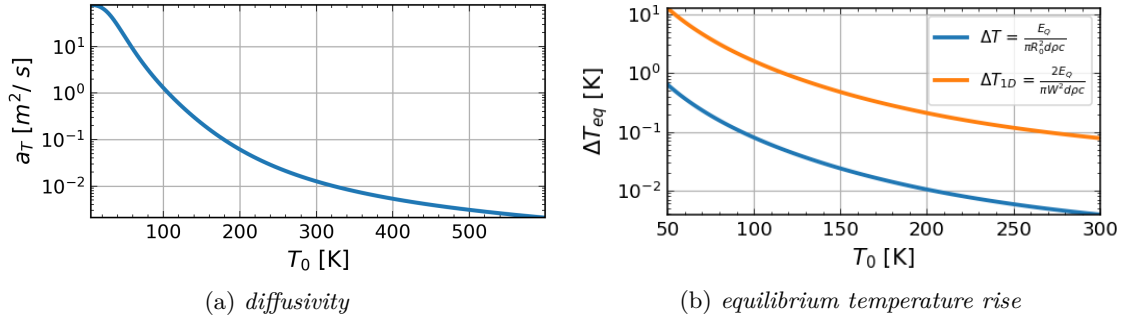


Figure 6.22.: (a) Values of diffusivity a_T as a function of the initial temperature T_0 for a diamond crystal. (b) Equilibrium temperature rise of a cylindrical diamond crystal with insulating boundaries (blue line), with thickness $d = 100 \mu\text{m}$ and radius $R_0 = 900 \mu\text{m}$ after absorption of an amount of heat energy $E_Q = 2 \mu\text{J}$, compared to a one-dimensional case (orange line) where the amount of heat per area is $\frac{2E_Q}{\pi W^2}$ and $W = 300 \mu\text{m}$.

varies in z -direction a heat energy per area $\frac{2E_Q}{\pi W^2}$ (Eq. 6.44) may be used to calculate the equilibrium temperature rise for a crystal with thickness d by integration of Eq. 4.21 over the crystal domain in z -direction:

$$\Delta T_{1D} = \frac{2E_Q}{\pi W^2 d \rho c(T_0)}. \quad (6.50)$$

The values for the one-dimensional scenario in Fig. 6.22b have been calculated by considering a beam radius of $W = 300 \mu\text{m}$, a thickness of $d = 100 \mu\text{m}$ and an amount of heat energy $E_Q = 2 \mu\text{J}$. However, in this case the assumption of constant heat capacity becomes critical at low temperature, where the predicted equilibrium value is in the range of a few Kelvin. Also it has to be mentioned that the consideration of this one-dimensional scenario is kind of artificial, because it neglects the heat conduction in radial direction. However, this approximation is useful for the discussion of one-dimensional heat conduction and resulting displacement/strain waves that will be considered in the following part of this section.

To investigate the temporal change of a three-dimensional axisymmetric temperature profile introduced by a pump laser in a cylindrical diamond crystal Eq. 6.11 is solved with the FEM²⁰, by neglecting the effect of the temporal strain change on the temperature field. In the simulation a crystal with thickness $d = 100 \mu\text{m}$ and radius $R_0 = 900 \mu\text{m}$ is considered. For the thermal conductivity the values calculated by [Rau21] are used²¹ (Fig 4.6, Section 4). The pump laser is chosen to have a Gaussian beam profile with $W = 300 \mu\text{m}$ which is centered in the middle of the crystal. For the temporal profile a Gaussian function with $t_p = 200 \text{ps}$ (Eq. 6.38) and the UV laser pulse (Fig. 5.3b) are considered. The pulse energy after the reflection is assumed to be $(1 - R)E_p = 2 \mu\text{J}$ and a complete conversion of the absorbed energy into heat is assumed. The penetration

²⁰Using, quadratic shape functions, a uniform mesh size of $5 \mu\text{m}$, a uniform time stepping of 10ps and the generalized alpha time solver

²¹Here λ_{zz} is the cross plane value and $\lambda_{\rho_r \rho_r}$ the in plane value shown in Fig 4.6.

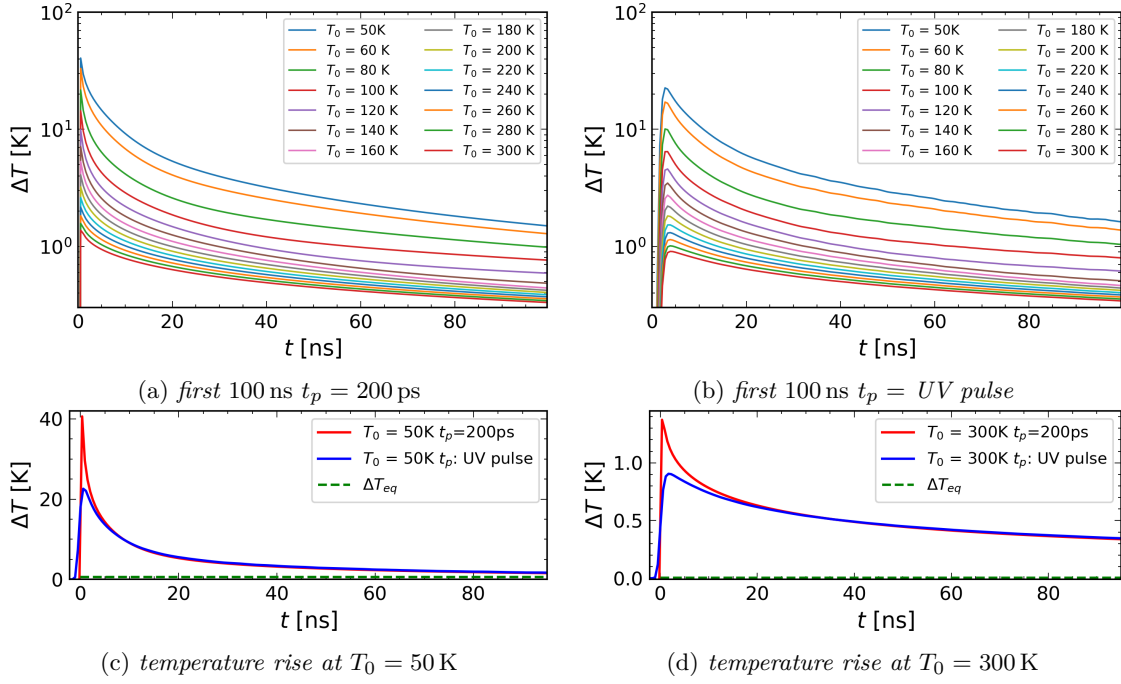


Figure 6.23.: The temporal development of the temperature rise in a cylindrical crystal with $R_0 = 900 \mu\text{m}$ and $d = 100 \mu\text{m}$ at position ($z = 0$, $\rho_r = 0$) introduced by a pump laser with $W = 300 \mu\text{m}$, $d = 100 \mu\text{m}$, $E_Q = 2 \mu\text{J}$ and $\zeta = 5 \mu\text{m}$ (Eq. 6.36), depending on the initial temperature T_0 illustrated for the first 100 ns calculated for (a) a temporal Gaussian profile with $t_p = 200$ ps and (b) for the UV laser pulse shape Fig. 5.3b. Comparing the impact of the temporal shape (c) at $T_0 = 50$ K and (d) $T_0 = 300$ K. The green dotted line marks the equilibrium temperature rise calculated with Eq. 6.49

depth is $\zeta = 5 \mu\text{m}$. With this assumption the external heat source can be expressed by Eq. 6.36. Due to the spatial profile of the pump laser the maximum temperature rise occurs at ($z = 0$, $\rho_r = 0$). The temporal change of the temperature rise at this position is illustrated in Fig. 6.23. As mentioned before the temperature rise depends, due to the temperature dependence of the heat capacity on the value of the initial temperature of the crystal. This is illustrated in Fig. 6.23, for the first 100 ns of the temporal development of the temperature rise at position at ($z = 0$, $\rho_r = 0$). It should be noted that if no heat conduction would be assumed the temperature at ($z = 0$, $\rho_r = 0$) would saturate at the same value as given by the one-dimensional problem in Fig. 6.21b. However, due to the finite pulse duration and the high thermal conductivity of diamond especially at low temperatures the temperature cannot be build up to the value of the saturated temperature rise illustrated in Fig. 6.21b. Due to the longer pulse duration of the UV pulse (Fig. 6.23b) compared to the Gaussian pulse (Fig. 6.23a) the temperature rise is significantly smaller for the UV pulse. This means that when considering a temporal finite temperature rise, the value of the maximum temperature rise not only depends on the temperature dependent material constants, but also on the finite value of the pulse length and/or on the timescales on which thermalization takes place. Also, it should be noted that due to the higher value of the diffusivity at low temperatures (in the range of 50 K) the maximum temperature rise at position ($z = 0$, $\rho_r = 0$) tends faster to the value of an equilibrium temperature

rise. This is illustrated for the initial temperature value of 300 K and 50 K in Fig. 6.23c and Fig. 6.23d, respectively. Considering the development of a heat bump which has been discussed in Section 6.2.1 it should be realized that a heat bump can only be built up if there exists a non-equilibrium temperature field. However, if the time scales on which the heat bump is build up is larger than the time scales which are needed for the temperature profile to reach a nearly equilibrium state, the displacement magnitude of the heat bump will decrease. In this context it should be noted for time spans longer than a few nanoseconds the decrease of the temperature is similar considering the different pulse duration illustrated in Fig. 6.23c and Fig. 6.23d. This leads to the conclusion that temporal development of the heat bump effect will be dominated by the diffusivity of the material and is not sensitive to the exact value to the pulse duration up to values of about one nanosecond, for a diamond crystal. The effect of the strong diffusivity a_T in diamond has also a significant impact on the one-dimensional strain wave at low temperatures, as will be shown by the following example. Using the same example as in Section 6.2.3 but this time considering the effect of thermal conductivity gives, with Eq. 6.11 and Eq. 6.9:

$$\begin{aligned} \frac{\partial}{\partial z} \left(\lambda_c \frac{\partial T}{\partial z} \right) &= c\rho \frac{\partial T}{\partial t} - Q_{ext}, \quad \text{where } T = T_0 + \Delta T \\ E \frac{\partial^2 w}{\partial z^2} - E\alpha_s \frac{\partial \Delta T}{\partial z} - \rho \frac{\partial^2 w}{\partial t^2} &= 0. \end{aligned} \quad (6.51)$$

Solving²² Eq. 6.51 with the FEM²³ gives the results shown in Fig. 6.24, which can be compared to the FEM solutions illustrated in Fig. 6.21 where heat conduction was neglected. As illustrated in Fig. 6.24a and already mentioned for the three-dimensional temperature rise the saturated temperature value (Fig. 6.21b) is not reached due to the finite pulse duration. After $t = 10$ ns the temperature rise for $T_0 = 50$ K is reduced to a value near the equilibrium temperature rise illustrated in Fig 6.22b. The rapid change of the temperature due to the thermal diffusivity causes a different shape of the strain pulse (Fig. 6.24c) and also prevents the creation of a significant constant velocity at $z = d$ after reflection (Fig. 6.24g). For a shorter pulses duration the resulting strain and displacement magnitude are significantly higher than for longer pulse duration, which is visible by comparing Fig. 6.24 for the UV laser and the Gaussian pulse. For the UV laser shape the peak value of the displacement at $z = d$ significantly increases for low temperatures. Also the calculation of the thermal (Eq. 6.42), kinetic (Eq. 6.30) and elastic (Eq. 6.31) energies represents this effect as illustrated in Fig. 6.25. However, it should be noted that even if the energy values reached for a shorter pulsed duration are significantly higher, compared to a longer pulse duration, the increases with lowering the initial temperature for the kinetic energy and elastic energy is higher for the longer pulses duration illustrated in Fig. 6.25. In other words, the ratio of the kinetic or elastic energy given in Fig. 6.25 obtained by dividing the

²²Using the cross plane thermal conductivity for a 100 μm crystal (Fig 4.6, Section 4) and the heat capacity calculated with the Debye approximation (Fig 4.4, Section 4).

²³Using, quadratic shape functions, a uniform mesh size of 1 μm , a uniform time stepping of 5 ps and the generalized alpha time solver

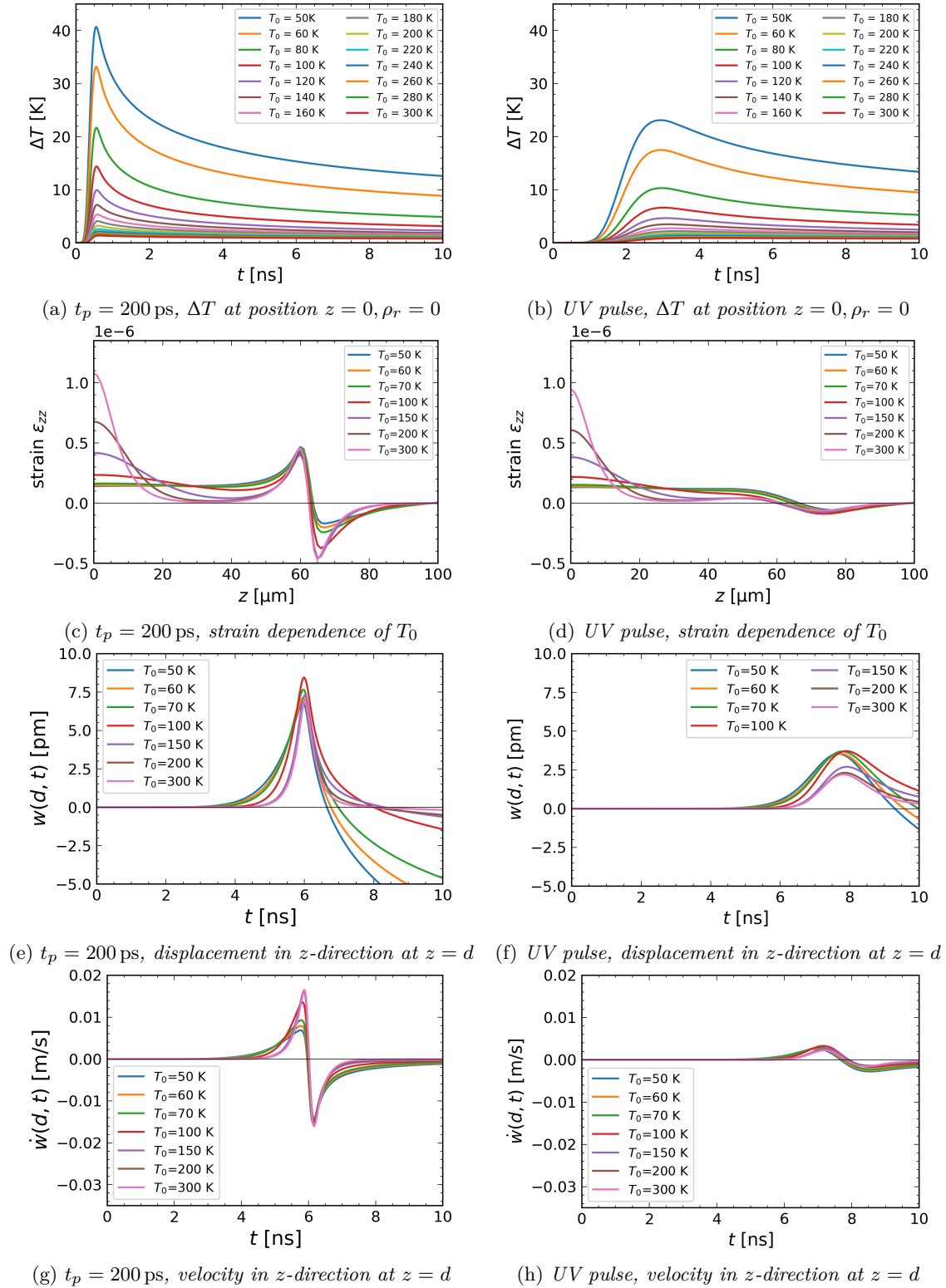


Figure 6.24.: One-dimensional wave propagation considering a pump beam with beam radius $W = 300 \mu\text{m}$, a pulse energy after reflection of $(1 - R)E_p = 2 \mu\text{J}$, a penetration depth of $\zeta = 5 \mu\text{m}$ and a crystal thickness of $d = 100 \mu\text{m}$. Considering thermal conductivity and comparing a Gaussian temporal profile $t_p = 200$ ps (left side of the illustration) and the UV laser pulse (Fig. 5.3b) (right side of the illustration). (a) and (b) Temperature rise ΔT at position ($z = 0, \rho_r = 0$) for different initial temperature values T_0 . (c) Strain ϵ_{zz} for different values of T_0 at the time $t = 3.5 \text{ ns} + 5\tau_0$ and (d) at $t = 3.5 \text{ ns} + 2.175 \text{ ns}$. (e) and (f) Displacement in z -direction at position $z = d$. (g) and (h) Velocity \dot{w} at position $z = d$.

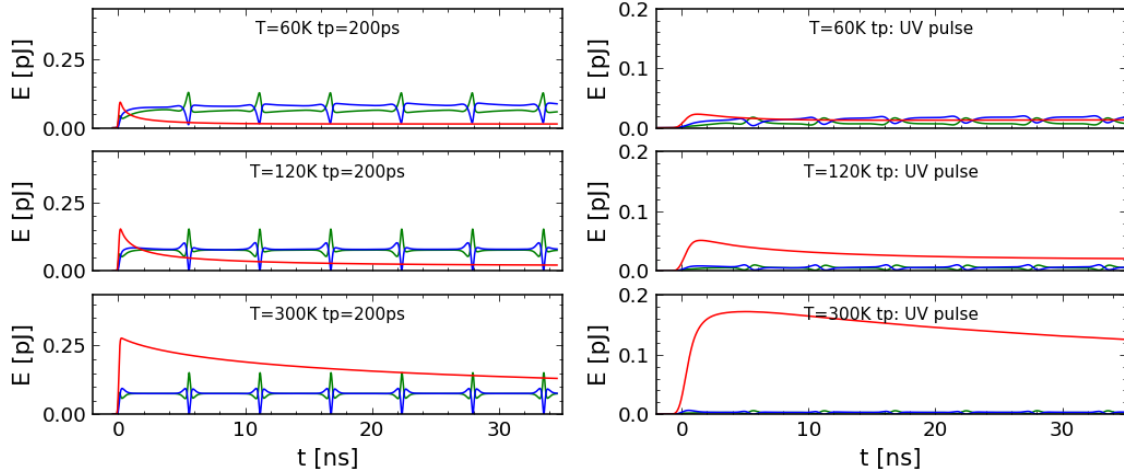


Figure 6.25.: Energy development for a one-dimensional wave propagation using the parameters described in Fig. 6.24. Comparing the effect of a Gaussian temporal profile $t_p = 200$ ps and the UV laser pulse (Fig. 5.3b). The red line represents the thermal part of the elastic energy (Eq. 6.42), the blue line the kinetic (Eq. 6.30) and the green line the elastic (Eq. 6.31) energy.

values for the short pulse by the longer one, considering a particular initial temperature value, decreases with lowering the initial temperature for the considered case.

6.2.5. Excitation of eigenfrequencies

In this section eigenfrequencies, also synonymously called natural frequencies, are introduced in the context of a vibrating solid.

Suppose a crystal with known geometry and material parameters is forced to be deformed into an arbitrary shape which can be described by a displacement field and the continuum theory introduced in Section 3. If then the forces which cause this deformation are suddenly released, the following motion of the solid can have a very complicated shape. These motions may also appear in a non-periodic way. However, there are particular initial displacement fields which will cause a harmonic and periodic motion with a corresponding frequency called the eigenfrequency and a periodic shape changing of the three-dimensional solid called the eigenmode or synonymously mode shape.

The calculation of eigenfrequencies and eigenmodes for a three-dimensional geometry are carried out with the FEM [Bow09, p. 503] using COMSOL multiphysics® in this work. However, considering the solution of a simple one-dimensional problem may be helpful to understand the meaning of eigenfrequencies and eigenmodes. Therefore, again the one-dimensional equation Eq. 6.21 will be considered. If no temperature profiles are present Eq. 6.21 becomes

$$\begin{aligned} \sigma_{zz} &= E \frac{\partial w(z, t)}{\partial z} \\ \rho \frac{\partial^2 w(z, t)}{\partial t^2} &= \frac{\partial \sigma_{zz}}{\partial z}. \end{aligned} \quad (6.52)$$

This gives a homogeneous wave equation for the displacement

$$\frac{\partial^2 w(z, t)}{\partial t^2} = v_l^2 \frac{\partial^2 w(z, t)}{\partial z^2}, \text{ where } v_l = \sqrt{\frac{E}{\rho}}, \quad (6.53)$$

which has to fulfill the boundary conditions $\sigma_{zz} = 0$ at $z = 0$ and $z = d$. Using the ansatz $w(z, t) = \Re[\tilde{w}(z)e^{j(\omega t)}]$ for the displacement, where \tilde{w} is a complex number containing the information of amplitude and phase and inserting this ansatz into Eq. 6.53 gives

$$\frac{\partial^2 \Re[\tilde{w}(z)]}{\partial z^2} + k^2 \Re[\tilde{w}(z)] = 0, \text{ where } k = \frac{\omega}{v_l}. \quad (6.54)$$

A solution for this equation is $\Re[\tilde{w}(z)] = \Re[w_{amp} e^{j(-kz + \phi_{\mathfrak{W}})}]$. This solution can also be written as $\Re[\tilde{w}(z)] = w_{amp} \cos(-kz + \phi_{\mathfrak{W}})$. To satisfy the boundary conditions this solution must fulfill $\left. \frac{\partial \Re[\tilde{w}(z)]}{\partial z} \right|_{z=0} = 0$ and $\left. \frac{\partial \Re[\tilde{w}(z)]}{\partial z} \right|_{z=d} = 0$. The derivation of the solution gives $\frac{\partial \Re[\tilde{w}(z)]}{\partial z} = w_{amp} k \sin(-kz + \phi_{\mathfrak{W}})$. Thus, solutions fulfilling the boundary condition are given for $\phi_{\mathfrak{W}} = 0$, $k_n = \frac{n\pi}{d}$, $n = 0, 1, 2, \dots, \infty$. The eigenfrequencies in this case are given by $f_n = \frac{\omega_n}{2\pi} = \frac{nv_l}{2d}$ and the corresponding eigenmodes are $\mathfrak{W}_n(z) = \cos(k_n z)$.

Considering again the cylindrical crystal (Fig. 6.10a) with R_0 , thickness $d = 100 \mu\text{m}$ and assuming no traction or constraints at the surface of the crystal, it is known from the one-dimensional solution that the crystal should possess eigenfrequencies at $f_0 = 0$, $f_1 = 89.51 \text{ MHz}$, $f_2 = 179.03 \text{ MHz}$ and $f_2 = 268.54 \text{ MHz}$. Indeed, these eigenfrequencies can be also calculated with the eigenfrequency solver of COMSOL multiphysics® considering a three-dimensional cylindrical crystal with arbitrary R_0 . But these eigenmodes have a rather special shape, they only oscillate in z -direction. However, for a three-dimensional solid, modes can oscillate in various directions depending on the geometry and boundary conditions. In this context it should be mentioned that the eigenmodes of the analytical solution would not be present if there would be a fix constraint at the sides of the crystal at position $\rho_r = R_0$.

For this work it is important to investigate which eigenfrequencies may be excited by a pulsed heat load. In this context it should be noted that the eigenfrequencies and eigenmodes of the crystal will depend on the kind of constraints, the elastic material parameters and damping effects. A real crystal may have different elastic properties compared to the literature values, because of a non-perfect lattice which can contain various kinds of defects. Also, the kind of damping effects due to defects and clamping are often unknown. Thus, the prediction of the eigenfrequencies and eigenmodes which will be excited in a real crystal is a challenging task. Nevertheless, an investigation of eigenfrequencies where damping is neglected and a perfect crystal with ideal clamping and elastic constant is considered may be a good starting point to understand which kind of eigenmodes could be excited in a particular frequency range.

To investigate the kind of three-dimensional eigenfrequencies, which exist for a cylindrical crystal, a crystal with $R_0 = 500 \mu\text{m}$, $d = 100 \mu\text{m}$ and a fixed constraint at the side

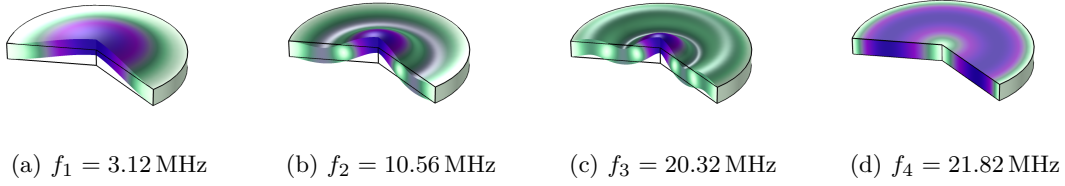


Figure 6.26.: first four axisymmetric eigenfrequencies/modes for a cylindrical crystal with radius $R_0 = 500 \mu\text{m}$ and thickness $d = 100 \mu\text{m}$.

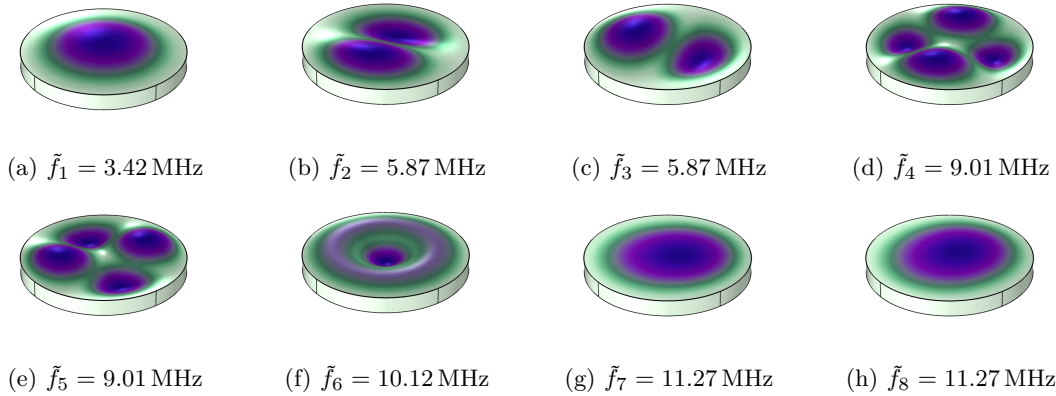


Figure 6.27.: first eight three-dimensional eigenfrequencies/modes for a cylindrical crystal with radius $R_0 = 500 \mu\text{m}$ and thickness $d = 100 \mu\text{m}$.

surface $\rho_r = R_0$ is considered. The results for the first four eigenfrequencies calculated with the FEM²⁴ considering axisymmetric modes are illustrated in Fig. 6.26. It should be mentioned that for this crystal also none axisymmetric modes exist which can also be calculated with the FEM. The FEM simulation results for a three-dimensional calculation are shown in Fig. 6.27. The mode²⁵ given by Fig. 6.27a is related to the mode shown in Fig. 6.26a and the mode Fig. 6.27f to the mode Fig. 6.26c.

In Section 6.2.1 the temporal development of a displacement field introduced by an instantaneously temperature rise $\Delta T(\rho_r, z) = \Delta T_{max} \exp\left(-\frac{2\rho_r^2}{W^2} - \frac{z}{\zeta}\right)$ with $\zeta = 20 \mu\text{m}$, $W = 300 \mu\text{m}$ and $T_{max} = 1 \text{K}$ (Fig. 6.14b) and an in z -direction constant temperature profile (Fig. 6.18) inside a cylindrical diamond crystal have been investigated. The crystal side boundaries were considered to be fixed constraints, the radius was $R_0 = 900 \mu\text{m}$ and thickness was $d = 100 \mu\text{m}$. The first four eigenmodes of this crystal have a similar shapes as illustrated in Fig. 6.26. However, the values of the eigenfrequencies are in this case $f_1 = 1.0117 \text{MHz}$, $f_2 = 3.7308 \text{MHz}$, $f_3 = 7.7802 \text{MHz}$ and $f_4 = 12.122 \text{MHz}$. Considering the Fourier transformation²⁶ of displacement in z -direction (Fig. 6.14b) as illustrated in Fig. 6.28a it can be seen that the frequencies of the eigenfrequencies are clearly related to temporal changing displacement. The fourth eigenfrequencies (at 12.122 MHz) has a

²⁴using a uniform quad mesh with $5 \mu\text{m}$ per element.

²⁵The difference of the eigenfrequency value may be reduced by using a mesh with higher resolution, however for the three-dimensional simulation in this work tetrahedral elements with size $10 \mu\text{m}$ are used to keep the computation time short.

²⁶Carried out with a Python script contain the *scipy* [JOP⁺] module *scipy.fft*

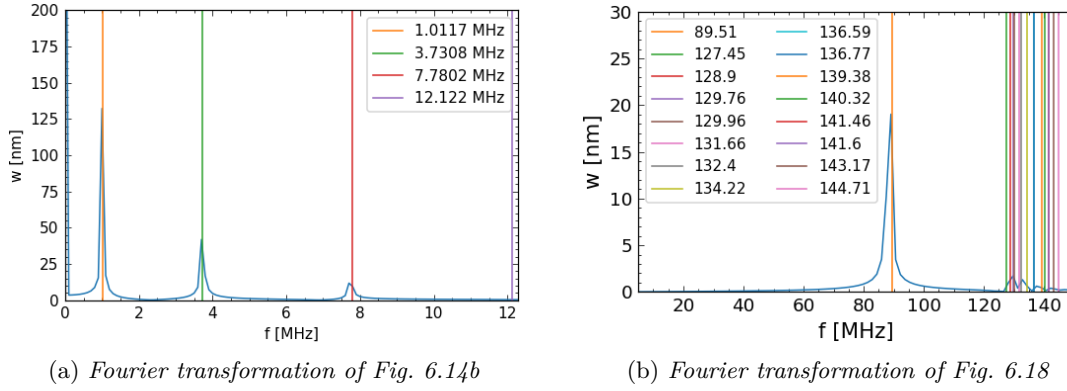


Figure 6.28.: Fourier transformation of the temporal development of the displacement in z -direction observed at position ($z = d$, $\rho_r = 0$) for (a) the displacement illustrated in Fig. 6.14b and (a) the displacement illustrated in Fig. 6.18.

radial shape and is not present in Fig. 6.28a investigated in this case.

For the Fourier transformation of the in z -direction constant temperature profile illustrated in (Fig. 6.14b) it can be seen that the frequency with the highest amplitude can be connected to a mode with a frequency similar to the one known from the analytic solution. There are also higher frequency components visible in the range from 125 MHz to 145 MHz. In this range a variety of different modes with quite chaotic shape are present has is has been obtained by a FEM simulation of the eigenfrequencies.

An topic which has not been investigated in this work is how eigenfrequencies/modes may be excited by a pulsed heat load with a fixed repetition rate. However, from the investigations of this work it may already be concluded that not only the repetition rate of heat load but also, the shape of the heat load profile which may be related to particular beam radius and a penetration depth may have an important impact of a possible excitation of eigenmodes.

6.3. Simulation of the pump-probe experiment

It can be seen clearly in (Fig. 5.12, Section 5) that the experimental data show features, which are familiar from the simulation results of the previous section. The periodic fringes can be connected to the one-dimensional wave propagating in z -direction (Fig. 6.6a), which has been discussed in detail in Section 6.1. The rise of the overall displacement value can be connected to the radial wave propagation (Fig. 6.15), which is caused by the heat bump effect (see Section 6.2.1). The decrease of the maximum reached overall displacement for lower initial temperatures observed in the measurements can be connected to the higher diffusivity (Fig. 6.22a, Section 6.2.4) for diamond at lower initial temperatures. The higher diffusivity causes a reduction of the heat bump effect, because a nearly equilibrium temperature (see Section 6.2.4) is reached on shorter timescales than the time which is needed for the heat bump effect to be build up (see Section 6.2.1). The increase of the displacement magnitude in the frequency range around 80 MHz (Fig. 5.14d, Section 5)

observed in the measurements can be connected to an increase of the magnitude of the one-dimensional displacement wave, which is probably caused mainly by the strong diffusivity of diamond at low temperatures (see Fig. 6.24 and Fig. 6.25, Section 6.2.4). The oscillations in the microsecond range observed in the measurements (Fig. 5.13) can be connected to the radial wave propagation and reflection at the side boundaries (see Fig 6.16, Section. 6.2.1). The measured frequencies (Fig. 5.14, Section 5) may be connected to the particular eigenfrequencies of the diamond crystal (see Fig. 6.28a Section 6.2.5). However, the prediction of the excitation of particular eigenfrequencies is challenging, because it depends on the clamping conditions and the three-dimensional shape of the crystal as well as on the spatial and temporal shape of the heat load as discussed in Section 6.2.5.

However, in all FEM simulations carried out in this work the assumption of the Fourier heat law has been used. From the discussion in Section 4 regarding the thermal conductivity it is known that this assumption is very critical for low temperatures, where the mean free path reaches values of a few micrometers. The thermoelastic simulation which is describing the pump-probe experiment of this work has to take into account temperature variations in the micrometer range²⁷, therefore the assumptions of the Fourier law may be expected to fail at low temperatures. This aspect may be investigated by comparing the simulation results with the experimental data.

For the simulation of the pump-probe experiment the elastic properties of diamond are approximated to be temperature independent and isotropic with a Poisson's ratio of 0.076 and a Young's modulus of $E_{mean} = 1125$ GPa as discussed in Section 4. For the temperature dependent heat capacity $c(T)$ the values calculated with the ab initio method are used (Fig. 4.4). The used function for the temperature dependent thermal expansion coefficient (Eq. 4.43) is given by the fitted values derived by P. Jacobson et al. [JS19] (Fig. 4.5) and is used to calculate the secant thermal expansion coefficient (Appendix A.5). The isotope content is assumed to be 1.1%. Thus, the density is assumed to be $\rho \approx 3516$ kg/m³ (as derived in Section 4). For the temperature dependent thermal conductivity the values for a 100 μm thick diamond crystal calculated by P. Rauer [Rau21] are used (Fig. 4.6). Considering Eq. 6.11 the value of the cross plane thermal conductivity (Fig. 4.6) is represented by λ_{zz} and the in-plane value is represented by $\lambda_{\rho_r\rho_r}$. The measured pump beam radius $W = 300.7$ μm (Fig. 5.3a) is approximated by a perfect Gaussian beam. The pump laser has a wavelength of 213 nm. From Section 4.2 and Section 5 (Fig. 5.4) it is known that the values for the penetration depth ζ and the reflectance R in this case are ≈ 5 μm and 0.221 28, respectively. As discussed in Section 5 these values are assumed to be nearly temperature independent. It is assumed that the absorbed energy of the total pulse energy $E_p = 44.6$ μJ is converted completely into heat energy which gives, by considering Eq. 6.19, $E_{abs} = (1 - R)E_p = 34.7$ μJ . With the temporal pulse shape $\mathfrak{T}(t) = \frac{U(t)}{\int_0^{T_m} U(t')dt'}$ illustrated in Fig. 5.3b and the assumption that thermalization takes place on much shorter time scales than the rise time of the laser

²⁷Because the penetration is about 5 μm and the crystal thickness is 100 μm

pulse, the spatial and time dependent heat per unit volume can be expressed by Eq. 2.62:

$$Q_{pump}(\rho_r, z, t) = \mathfrak{T}(t) \frac{2E_{abs}}{\zeta \pi W^2} \exp\left(-\frac{2\rho_r^2}{W^2}\right) \exp(-z/\zeta) \quad (6.55)$$

The dimensions of the crystal are $4 \text{ mm} \times 4 \text{ mm} \times 100 \text{ }\mu\text{m}$. However, for the FEM simulations a cylindrical crystal with radius $R_0 = 2000 \text{ }\mu\text{m}$ is considered. With this simplification and the assumption that the pump laser beam is centered in the center of the crystal an axisymmetric simulation can be carried out, which significantly²⁸ reduces the calculation time for the FEM simulation. The thermal boundary conditions for the surface of the crystal are chosen to be thermal insulating $q_i^h n_i|_{S_{2T}} = 0$. This choice is motivated by noticing that, for a single pump laser pulse absorbed by the crystal, only a small equilibrium temperature rise is expected using Eq. 6.49. For example, considering $T_0 = 50 \text{ K}$ gives an equilibrium temperature of $T_{eq} = 1.5 \text{ K}$ and for higher initial temperature values the equilibrium temperature is even smaller. For the mechanical boundary conditions it is assumed that the displacement is zero at the side boundary of the crystal $\rho_r = R_0 \rightarrow u_i|_{S_{1M}} = \hat{u}_i = 0$ (fixed constraint). Furthermore, it is assumed that at the bottom and top of the crystal (the remaining part of the crystal surface) there is no traction $\sigma_{ij} n_i|_{S_{2M}} = \hat{t}_j = 0$.

The periodic fringes in Fig. 5.12, Section 5 marked by the vertical lines, can be connected to the propagation of a one-dimensional displacement wave in z -direction (see also Fig. 6.14a). The measured periodicity is $T_p = 12.08 \text{ ns}$. From the analytic solution for the one-dimensional wave propagation Eq. 6.25 it can be seen that the periodicity of the fringes T_p is connected to the thickness of the crystal by:

$$T_p = \frac{2d}{v} \quad (6.56)$$

Using a Young's modulus $E = 1125 \text{ GPa}$ and a Poisson's ratio of $\nu = 0.076$, which have been discussed in Section 4 the longitudinal speed of sound is given by Eq. 3.64:

$$v_L = \sqrt{\frac{E(1-\nu)}{\rho(1+\nu)(1-2\nu)}} = 18000.5 \text{ m s}^{-1} \quad (6.57)$$

Inserting the longitudinal speed of sound²⁹ and the measured periodicity into Eq. 6.56 gives a thickness of $d = 108.72 \text{ }\mu\text{m}$. This thickness value is used for the cylindrical crystal in the FEM simulation. It should be noted that the thickness value is inside the tolerance for the crystal thickness specified by the manufacturer: $(100 \pm 10) \text{ }\mu\text{m}$. However, it should

²⁸For a three-dimensional simulation there would be much more degrees of freedom and the global matrix to solve (Appendix A.6) would contain much more elements.

²⁹It should be mentioned that considering the three-dimensional wave propagation the one-dimensional wave propagation might only be assumed as a fully decoupled kind of wave propagation for the case where Poisson's ratio is zero (see Eq. 3.68 and Eq. 3.70 in context of Eq. 6.21). However, since the Poisson's ratio for diamond is quite small a systematic error which might be introduced by a non zero Poisson's ratio is assumed to be small.

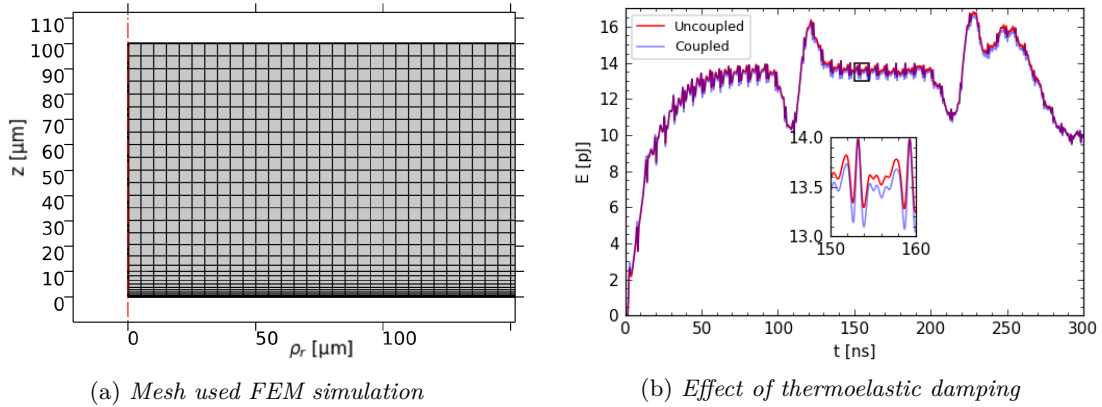


Figure 6.29.: (a) Mesh with increasing element size in z -direction. The mesh has the same distribution along the complete ρ_r -direction, of the crystal. However, for better visualization only the first $\approx 100 \mu\text{m}$ are shown in the illustration. (b) FEM Simulation considering the pump-probe experiment at initial temperature $T_0 = 300 \text{ K}$. For the uncoupled calculation the effect of the temporal changing strain field has been neglected. For the coupled simulation the coupled PDEs Eq. 6.11 and 6.9 have been solved simultaneously.

also be noted that due to the wedge angle (Fig 5.1) the crystal thickness is not constant and the assumption of a constant thickness for the FEM simulation will introduce a systematic error. For the FEM simulation of the pump-probe experiment a uniform quad mesh with an element size of $5 \mu\text{m}$ combined with boundary layers at $z = 0$ with increasing size in z -direction for the first $\approx 20 \mu\text{m}$ as illustrated in Fig. 6.29a is used. The finer mesh at the area near $z = 0$ is used to resolve the exponential decrease of the heat source, which is caused by the penetration depth of $\zeta \approx 5 \mu\text{m}$. However, the created displacement/strain wave as discussed in Section 6.2.2 (Fig. 6.19d) is smeared out due to the temporal pulse shape of the UV laser and a quite coarse mesh of $5 \mu\text{m}$ should be sufficient³⁰ to resolve the propagation of this wave. For the time solver the generalized alpha solver with a time stepping of 50 ps is used. The simulation time span of 300 ns , which will be investigated in detail in the following part of this section may be considered to be the start up regime for the thermoelastic wave propagation. This time span is of particular interest for the needs of this work, because as mentioned in Section 1 it corresponds to the repetition rate of fourth generation XFEL facilities.

For all the simulations presented in Section 6.1 and Section 6.2 the impact of the displacement/strain field on the temperature rise (thermoelastic damping) represented by the first term on the right hand side of Eq. 6.11 has been neglected, also in all the simulations it has been assumed that the Poisson's ratio is zero. Using the Structural Mechanics Module and the Heat Transfer Module of the software COMSOL multiphysics® 5.5 it is possible to solve the coupled PDEs Eq. 6.11 and³¹ Eq. 6.9 for an axisymmetric problem simultane-

³⁰To verify this assumption a simulation using a much finer mesh with $1 \mu\text{m}$ element size has been carried out. Investigating the first 40 ns of the simulation show in Fig. 6.30 comparing the solution with the coarse mesh there was no significant difference noticeable.

³¹Using the stress-strain relation Eq. 3.68.

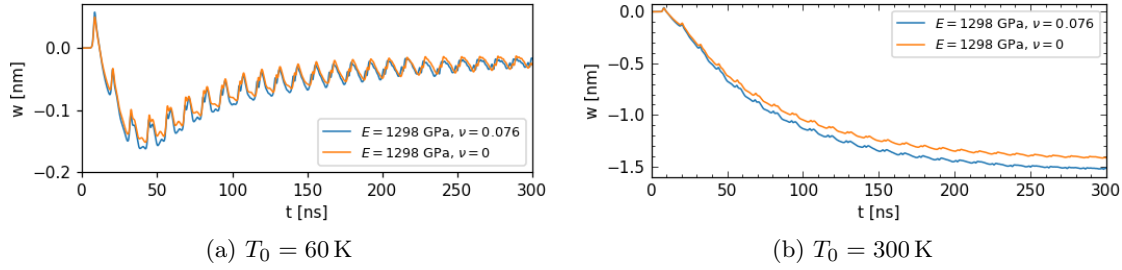


Figure 6.30.: Displacement at position ($z = d$, $\rho_r = 0$) for the initial temperature values $T_0 = 60$ K and $T_0 = 300$ K, calculated with FEM simulation considering the pump-probe experiment described in Section 5.

ously. The results for a simulation, which is taking into account thermoelastic damping effects, is illustrated by the temporal development of the kinetic energy (Eq. 3.63) integrated over the crystal domain in Fig. 6.29b, considering an initial temperature of 300 K and the previously described assumptions for the pump-probe experiment simulation. Comparing this result with a solution carried out with a simulation where the effect of thermoelastic damping is neglected, and the PDEs Eq. 3.74 and Eq. 3.70 can be decoupled, it can be seen that the results show only very small deviations, as indicated by the zoom plot in Fig. 6.29b. Thus, these kind of effects are assumed to be not important considering the investigated time span of a few hundreds of nanoseconds. Also it should be noted that the first term on the right hand side of Eq. 6.11 (or Eq. 3.74), which characterizes the thermoelastic damping is proportional to the value of the absolute temperature and the value of the thermal expansion coefficient. Considering that the elastic material properties (Section 4) are nearly temperature independent for temperatures lower 300 K and that the thermal expansion coefficient (Fig. 4.5) decreases with decreasing temperature, it seems reasonable to assume that thermoelastic damping effects at lower temperatures are even less important compared to cases at room temperature.

Comparing the results simulated for initial temperatures of $T_0 = 300$ K and $T_0 = 60$ K carried out with a non-zero Poisson's ratio ($\nu = 0.076$) with the solutions where the Poisson's ratio is set to zero, it can be seen that there is a significant difference noticeable (Fig. 6.30). However, it also can be seen that the features, which can be noticed in the temporal development of the displacement in z -direction at the position ($z = d$, $\rho_r = 0$) are very similar in both cases. Therefore it seems reasonable to assume that for the investigated time span the temporal development of the displacement can be characterized mainly by effects, which have been investigated in Section 6.2 and Section. 6.1, where the Poisson's ratio has been neglected.

In Fig. 6.30 the results for displacement in z -direction at the position ($z = d$, $\rho_r = 0$) for the initial temperature values of $T_0 = 60$ K and $T_0 = 300$ K are illustrated. These are the displacement values at an exact point which would need an infinitesimal small radius of the probe beam to be resolved. However, the probe laser spot of the interferometer has a finite beam radius of $W_{probe} \approx 45.4 \mu\text{m}$, thus it has to be considered that the displacement measured with the probe beam at positions $\rho_r \neq 0$ can differ from the values of the

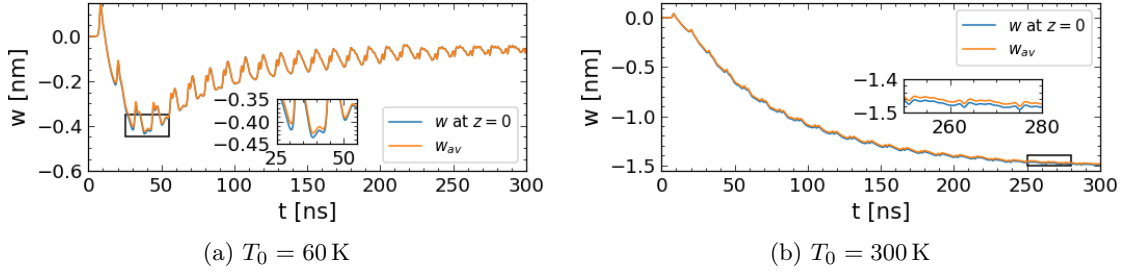


Figure 6.31.: Comparison of the displacement at position ($z = d$, $\rho_r = 0$) with the displacement averaged over the probe beam size at (a) initial temperature $T_0 = 60$ K and (b) initial temperature $T_0 = 300$ K.

displacement illustrated in Fig. 6.30. To investigate the impact of this effect an average value w_{av} for the displacement field $w(\rho_r)$ at $z = d$ weighted with the intensity profile $I_{probe}(\rho_r) = I_0 \exp\left(-\frac{2\pi\rho_r^2}{W_{probe}^2}\right)$ of the probe laser can be calculated by:

$$w_{av} = \frac{\int_0^{2\pi} \int_0^\infty w(\rho_r) I_{probe}(\rho_r) \rho_r d\rho d\theta}{\int_0^{2\pi} \int_0^\infty I_{probe}(\rho_r) \rho_r d\rho d\theta} = \frac{\int_0^\infty w(\rho_r) \exp\left(-\frac{2\pi\rho_r^2}{W_{probe}^2}\right) \rho_r d\rho}{\int_0^\infty \exp\left(-\frac{2\pi\rho_r^2}{W_{probe}^2}\right) \rho_r d\rho}. \quad (6.58)$$

Using discrete values for the displacement from the FEM solution the integral may be approximated as a sum

$$w_{av} = \frac{\sum_{i=0}^n I_{probe}(\rho_{r_i}) w_i(\rho_{r_i}) \rho_{r_i}}{\sum_{i=0}^n I_{probe}(\rho_{r_i}) \rho_{r_i}}. \quad (6.59)$$

Since $I_{probe}(\rho_r)$ becomes very small for $z > W_{probe}$ it is sufficient to consider a range from $\rho_r = 0$ to $\rho_r = 65 \mu\text{m}$ in this case. For the summation discrete values with a uniform spacing of $5 \mu\text{m}$ have been used. A comparison of the calculated values at ($z = d$, $\rho_r = 0$) to the averaged displacement w_{av} are shown in Fig. 6.31, which indicates that in the considered case the displacement at position ($z = d$, $\rho_r = 0$) gives nearly the same values as the averaged displacement.

The different shape of the crystal in the simulation will give some systematic error, due to the different kind of constraints at the side boundaries, compared to the real crystal shape used in the pump-probe experiment. However, the simulation results are in quite good agreement with the experimental data considering the comparison illustrated Fig. 6.33. It should be clarified at this point that for the FEM simulations material parameters known from ab initio calculations and literature values have been used, which means none of the material properties for the crystal used in the pump-probe experiment have been measured. Also it should be noted that the Poisson's ratio is strongly orientation dependent (Fig 4.2) and has been approximated as a mean value for the simulation. Further, the measured spot size of the pump beam is not a perfect Gaussian beam (Fig. 5.3d) and the pulses energy was measured with a quite broad uncertainty $E_p = (44.6 \pm 5.0) \mu\text{J}$. Also the wedge angle which causes a thickness variation of about $7 \mu\text{m}$ might have an impact on the wave

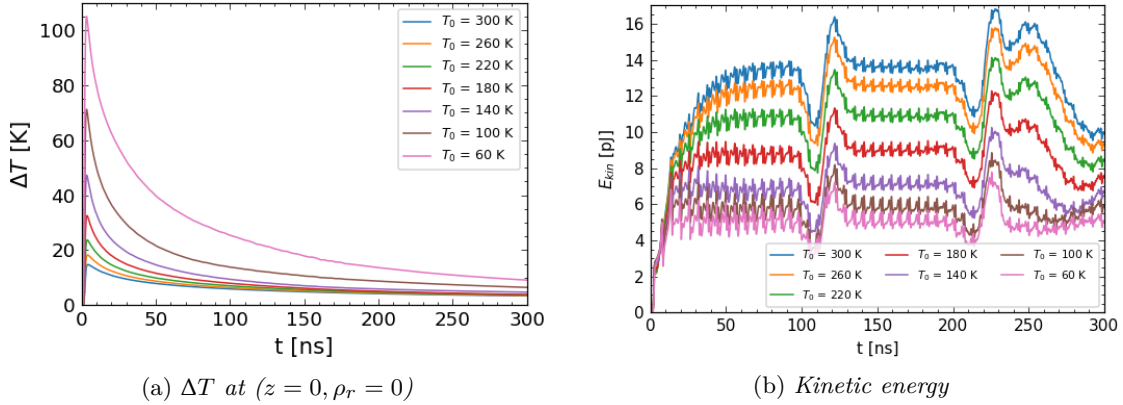


Figure 6.32.: (a) Maximum temperature rise predicted by the FEM simulation for the pump-probe measurement. (b) Kinetic energy integrated over the crystal domain considered for the FEM simulation.

propagation which cannot be taken into account by the axisymmetric FEM simulation. Under these circumstance one should not expect a perfect agreement of simulation and experimental data and it has to be admitted that a compensation of different errors cannot be excluded. However, on the other hand the good agreement of the measurement in amplitude and shape with the simulation data may be seen as a strong indicator that the underlying theory and used approximations are describing the pump-probe experiment with a quite reliable accuracy.

The good agreement of simulation and measurement observable in Fig. 6.33 at low initial temperature values T_0 is very surprising, considering the discussed assumptions for the Fourier heat law in Section 4. As discussed in Section 4 the energy transport caused by phonons inside a diamond crystal is characterized by a group velocity (Eq. 4.18) which is frequency dependent and is related to the dispersion relation (Fig. 4.3). For the derivation of the thermal conductivity a static situation and local thermal equilibrium has been assumed (Eq. 4.49). To define a meaningful local thermal equilibrium phonon scattering has to take place. In this context considering a situation where the scales of interests are much larger than the mean free path, the Fourier law might be assessed as a valid assumption and the FEM simulations which are using these assumptions may be expected to predict reliable results.

The penetration depth $\zeta \approx 5 \mu\text{m}$ which has been considered in the pump-probe experiment may be seen as such a scale of interest for a local thermodynamic equilibrium. At a temperature of $T_0 = 300 \text{ K}$ the mean free path is about $0.4 \mu\text{m}$ (see Fig 4.7a), which may be considered to be sufficient to resolve the dimensions of the penetration depth. However, it should be reminded that the mean free path is just a mean value (Eq. 4.51), thus the length scales on which particular phonons of various frequencies scatter may significantly deviate from this value. For an initial temperature of $T_0 = 260 \text{ K}$ the mean free path is already $0.7 \mu\text{m}$ (see Fig 4.7a) and the approximation of a local thermodynamic equilibrium may become questionable. At temperature values smaller than $T_0 = 160 \text{ K}$ the mean free

path gets larger than $5\ \mu\text{m}$ (see Fig 4.7a), which gives a kind of contradiction to the underlying assumption of the Fourier heat law approximation. However, the initial temperature value is not the only temperature value which has to be discussed. Also the temperature rise caused by the absorbed and into heat converted energy is important. As discussed in Section 6.2.4 the temperature rise strongly depends on the initial temperature value, due to the temperature dependence of the heat capacity. The temperature rise predicted by the FEM simulation at position ($z = 0, \rho_r = 0$) is illustrated in Fig. 6.32a. Due to the highest value of the external heat source (Eq. 6.55) at this position the temperature at ($z = 0, \rho_r = 0$) represents a maximum value for the temperature rise inside the crystal. If thermalization takes place sufficiently fast the mean free path in this area may be significantly reduced compared to the surrounding material area (see Section 4, Fig. 4.7a).

However, considering that for an initial temperature of $T_0 = 60\ \text{K}$ the temperature rise value is about $\Delta T = 100\ \text{K}$ (Fig. 6.32a), the mean free path is still in the range of a few micrometer. Thus for this initial temperature values a significant deviation of experiment and simulation may be expected. Nevertheless, for the case which has been investigated in this work (Fig. 6.33) such a clear deviation seems to be not present.

Comparing the simulations and measured signals it is also interesting to observe the kinetic energy integrated over the crystal domain (Fig. 6.32b). It can be seen that the kinetic energy predicted by the FEM simulation decreases with lowering the temperature, which may be connected to a smaller heat bump effect at these temperatures caused by a higher diffusivity. An explanation of this effect may be given as mentioned in Section 6.2.4, by considering that the time scales which are needed for the heat bump to build up (see Fig. 6.14a) are shorter than the time scales for the temperature profile to reach a nearly equilibrium temperature. In this context the amplitude of the radial wave (Fig. 6.15) caused by the heat bump will also be smaller which may be connected to a lower kinetic energy inside the crystal.

The constraints for the cylindrical crystal are quite different compared to the measurement conditions for the pump-probe experiment. Nevertheless, some results comparing a simulation time span of a few microseconds with experimental data may be useful, as illustrated in Fig. 6.34a, where an initial temperature of $300\ \text{K}$ has been considered.

As discussed in Section 6.2.1 the characteristic dip in the development of the displacement can be connected to the time when the propagation of radial waves reaches the center of the crystal. This characteristic dip is visible in the measurement for the SC CVD diamond (Fig. 5.12, Section 5) at a time about $230\ \text{ns}$. However, considering the position of the pump laser on the crystal (Fig. 5.10a) there are side boundaries, which are partly just one millimeter away from the center of the crystal, thus the characteristic dip will occur later in the simulations compared to the pump-probe experimental data. This is also visible considering the comparisons of the experimental data with the simulation results illustrated³² in Fig 6.33 and Fig 6.34a.

³²The illustrated values are the averaged displacement calculated with Eq. 6.59

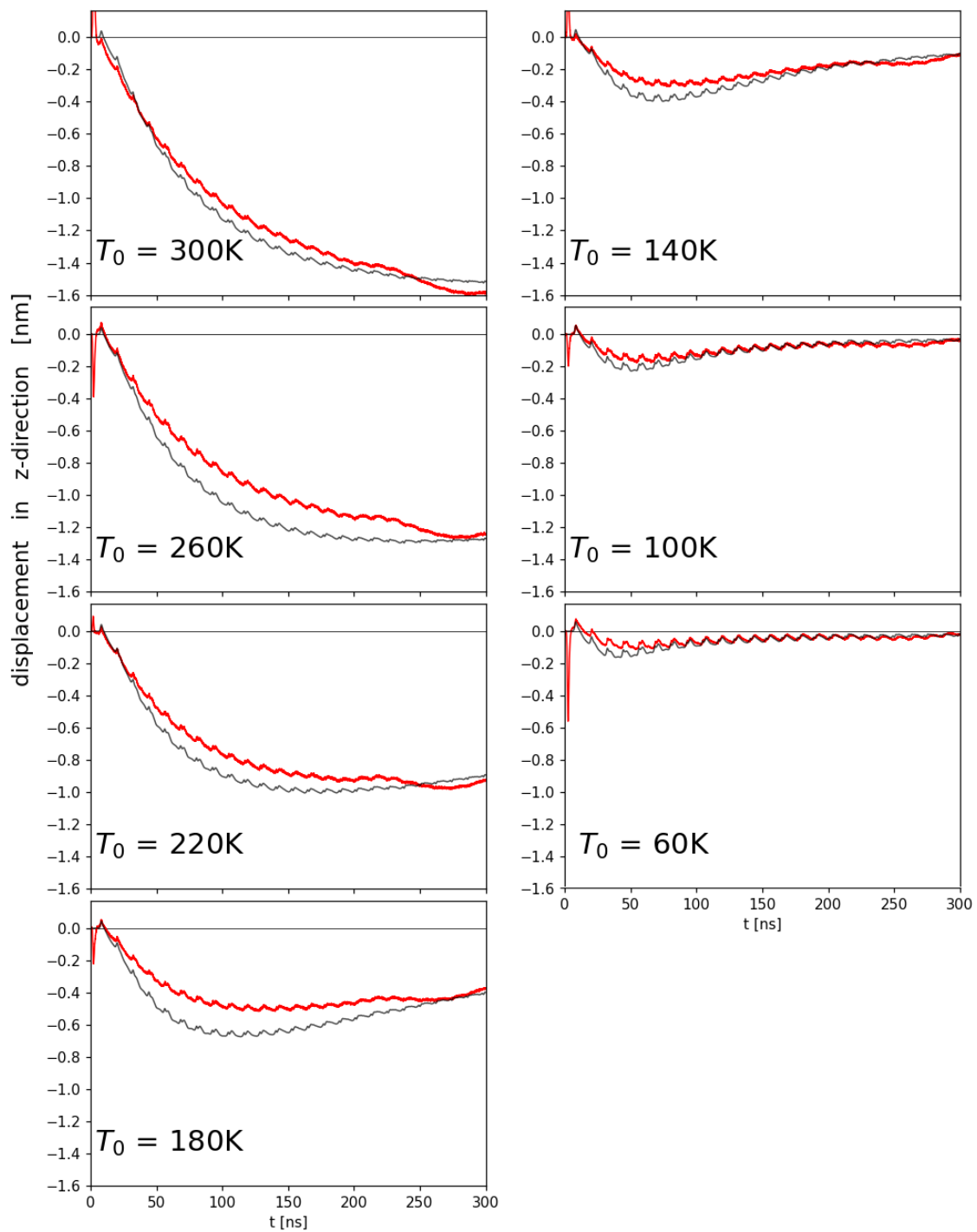


Figure 6.33.: Comparison of the axisymmetric FEM simulation represented by the black lines for a cylindrical crystal with $R_0 = 2000\ \mu\text{m}$ and $d = 108.72\ \mu\text{m}$ with the experimental data represented by the red lines (Fig. 5.12, Section 5).

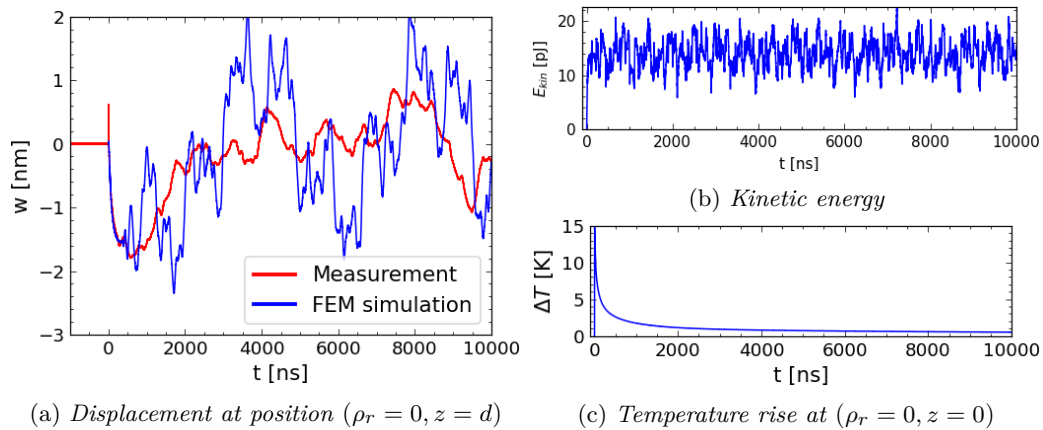


Figure 6.34.: (a) Displacement in z -direction at position $(\rho_r = 0, z = d)$ comparing the FEM simulation and measurements for the pump-probe experiment carried out for an initial temperature of $T_0 = 300$ K. (b) Kinetic energy integrated over the cylindrical crystal domain calculated with the FEM. (c) Temporal development of the temperature rise at $(\rho_r = 0, z = 0)$.

After this characteristic dip some oscillation can be observed for the experimental data as well as for the simulation. The maximum reached amplitude is similar in both cases. These oscillations may be connected to the propagation of radial waves (Fig. 6.15) which are reflected at the boundaries of the crystal. The maximum reached amplitude may be connected to the heat bump effect. As discussed in Section 6.2.1, Fig. 6.14b after the rise of the heat bump an oscillation can be observed which contains frequency components connected to the eigenfrequency values of the crystal (see Section 6.2.5, Fig. 6.28a). In Fig. 6.14b the oscillation takes place around the value of the heat bump. However, for the simulation and also for the measurement illustrated in Fig. 6.34a, the oscillation will take place around the zero position. The reason for the oscillation around the zero position is that a static heat bump exists only if a spatially varying constant temperature profile exists. This is not the case for the considered time span of the pump-probe simulation. Due to the thermal conductivity the spatial varying temperature profile reaches a nearly equilibrium temperature during the observed time span as illustrated in Fig. 6.34c.

Considering the calculated kinetic energy in Fig. 6.34b it can be seen that the kinetic energy in the start-up regime has a similar order of magnitude like the present magnitude after a few microseconds. For the simulation damping effects have been neglected and thus the mean kinetic energy which is predicted in Fig. 6.34b should not be expected to be reduced by considering larger time spans. The measurements presented in Fig. 5.13c are an indicator that such an assumption is indeed a realistic approximation for the time span in the range of 0.1 ms.

It should be mentioned that the experimental data given in Section 5, Fig. 5.14 may be compared with eigenfrequencies calculated from a three-dimensional FEM simulation. However, calculation and evaluation of such a simulation is a quite extensive topic, which will not be discussed in this work, but may be a topic for further research projects.

6.4. Simulations of the thermoelastic effects for a diamond Bragg reflector in a CBXFEL at the European XFEL

As mentioned in Section 1 this PhD project collaborates with the PhD project of P. Rauer. Parts of his thesis describe the conceptual design of an CBXFEL at the European XFEL [Rau21]. The simulation results of P. Rauer indicate that in saturation the heat load caused by the absorbed energy amount for each photon pulse can be approximated as an axisymmetric spatial distribution $\Phi_E(\rho_r, z)$ as illustrated in Fig. 6.35. The crystal thicknesses of the diamond Bragg reflectors which are planned to be used for the CBXFEL are $d = 150 \mu\text{m}$. Integrating $\Phi_E(\rho_r, z)$ over the crystal domain gives a pulse energy of about $E_{abs} = 45 \mu\text{J}$. The pulse duration of an X-ray pulse for the considered CBXFEL is only a few tens of femtoseconds. Investigating thermoelastic effects the thermalization time needed for the absorbed photon energy to be converted into heat energy in a diamond Bragg reflector with low defect concentration may be assumed to take place on the picosecond timescale³³. To carry out a simulation, a Gaussian temporal profile given by Eq. 6.38 with $t_p = 200 \text{ ps}$ has been considered in this work. The value for t_p in this case is not the pulse duration, but may be seen as an assumption for the thermalization time. Regarding one-dimensional displacement/strain waves it can be seen by considering the results of Section 6.2.2 Fig. 6.19 that for smaller values of t_p the amplitude of a traveling wave may be slightly higher, whereas for larger values the discontinuity, which would be present for $t_p = 0$, will be smeared out. However considering $0 < t_p < 1 \text{ ns}$ the strain and displacement values are roughly on the same order of magnitude. Therefore, the calculated solution using a value of $t_p = 200 \text{ ps}$ may be seen as a good assumption for a prediction of the strain and displacement values regarding thermoelastic effects, caused by the heat load of a saturated CBXFEL.

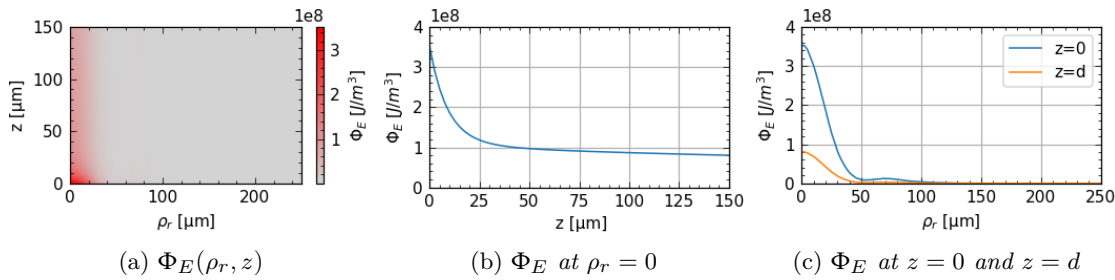


Figure 6.35.: (a) $\Phi_E(\rho_r, z)$ spatial distribution of the absorbed energy per unit volume per saturated pulse considering simulation result for a case with an initial crystal temperature of $T_0 = 77 \text{ K}$ [Rau21]. (b) values of $\Phi_E(\rho_r, z)$ in the center of the crystal at $\rho_r = 0$. (c) values of $\Phi_E(\rho_r, z)$ at the front side $z = 0$ and back side of the crystal $z = d = 150 \mu\text{m}$

The repetition rate considered in the simulations of P. Rauer is $f_R = 2.25 \text{ MHz}$. Thus, the diamond crystal is experiencing a periodic heat load, which is repeated every 440.44 ns and the absorbed energy per unit volume and per unit time which is assumed to be

³³For further discussion regarding this assumption see [Rau21].

completely converted into heat for a single pulse is given by:

$$Q_{CBXFEL}(\rho_r, z, t) = \mathfrak{T}(t)\Phi_E(\rho_r, z), \quad (6.60)$$

where $\mathfrak{T}(t)$ is a temporal Gaussian function (Eq. 6.44). For the simulation nearly the same temperature dependent material parameters have been considered, as mentioned in Section 6.3, however for the thermal conductivity the values calculated by P. Rauer for a 150 μm thick crystal have been considered (see Section 4, Fig. 4.6). For the simulation thermoelastic damping effects have been neglected and thus the solution of the temperature profile calculated by solving Eq. 3.74 could be calculated without considering the displacement field inside the crystal. The solution of the temperature profile could then be used to solve afterwards Eq. 3.70 (using the stress-strain³⁴ relation Eq. 3.68) for an axisymmetric problem. Investigating the heat load of several pulses the previous assumption that the crystal is thermal isolated is not applicable, because the equilibrium temperature in this case would increase after each absorbed pulse. The initial temperature considered by the simulation of P. Rauer is 77 K. To carry out a FEM simulation for a cylindrical crystal a radius $R_0 = 1000 \mu\text{m}$ and a thickness of $d = 150 \mu\text{m}$ is considered and the side boundaries of the crystal are assumed to have a fixed temperature of $T|_{S1_{\rho_r=R_0}} = 77 \text{K}$. Considering the temperature development under such condition it can be seen that the temporal temperature profile reaches after a setup time of a few pulses a periodic rise and fall profile from one pulse to another as shown in Fig. 6.36, where the temperature development at the position $(\rho_r = 0, z = 0)$ is illustrated.

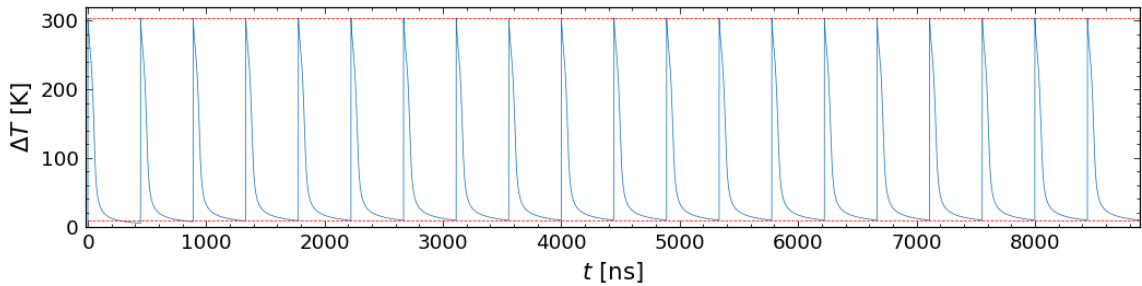


Figure 6.36.: *Temporal development of the temperature rise from an initial temperature $T_0 = 77 \text{K}$ at position $(\rho_0 = 0, z = 0)$. As indicated by the red dashed line the rise and fall of the temperature becomes periodically repeating after a setup time of a few pulses.*

However, the condition of a boundary with a fixed temperature corresponds to the assumption of an idealized heat transfer to the holder. Using Eq. 6.8 and considering a non zero heat transfer coefficient it can be investigated which conditions are necessary to avoid a temperature increase over several pulses. For a rough estimation of the relevance of heat transfer effects to the holder a condition may be considered where the complete back side of the crystal (at $z = d$) is connected to a heat bath with a temperature of 77 K. The area of the back side of the crystal is $A = 2\pi R_0^2 = 6.3 \text{mm}^2$. In Fig. 6.37 the simulation

³⁴Considering a Poisson's ratio of 0.076 and a Young's modulus of $E_{mean} = 1125 \text{GPa}$.

results for a heat transfer coefficient a_h of $100\,000\text{ W}/(\text{Km}^2)$ and $1\,000\,000\text{ W}/(\text{Km}^2)$ are illustrated. These temperature profiles are compared with a case of insulation boundaries and a case where a fixed temperature value is assumed at the side boundaries (Fig. 6.36). For better visualization only the temperature rise in the range of 0 K to 50 K is illustrated. It can be seen that for a heat transfer coefficient a_h of $100\,000\text{ W}/(\text{Km}^2)$ the temperature rise is nearly the same as if thermal insulating boundaries would be considered. Even for the quite high heat transfer coefficient a_h of $1\,000\,000\text{ W}/(\text{Km}^2)$ the increase of the temperature is still significantly higher than for a case where a fixed temperature at the side boundaries has been considered.

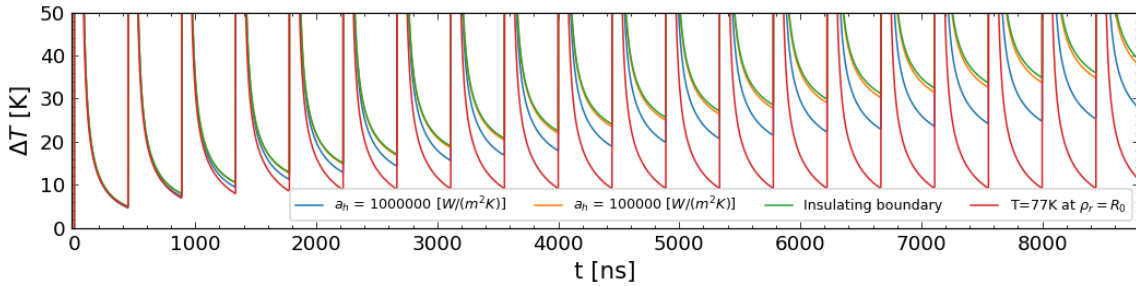


Figure 6.37.: Temperature rise at position ($\rho_0 = 0, z = 0$) for a periodic heat load considering different thermal boundary conditions.

For the thermal contact to the holder indium foil may be used for better thermal contact and the holder may be built of OFHC copper. The heat transfer coefficient a_h for such a condition can depend on temperature (of the holder) and the clamping contact. The heat transfer for such a condition has not been reported in the literature so far to the best knowledge of the author. However, the heat transfer of OFHC copper to OFHC copper is in the range of a few thousand $\text{W}/(\text{Km}^2)$ [MBUW12]. This leads to the conclusion that the heat load of a saturated CBXFEL pulse could be problematic if a diamond crystal of similar size would be used. However, this kind of problem may be solved by using a crystal with a sufficient larger volume.

To investigate the displacement field which is present after a time span of 444.44 ns, caused by a single saturated CBXFEL pulse, a FEM simulation using a triangular mesh with element size of $1\ \mu\text{m}$ in the range of $\rho_r = 100\ \mu\text{m}$ is used. In the range of $\rho_r = 100\ \mu\text{m}$ to $\rho_r = 1000\ \mu\text{m}$ element size of the mesh gradually increases to a value of $5\ \mu\text{m}$.

In contrast to the temperature rise discussed in Section 6.3, Fig. 6.32a, the predicted temperature rise illustrated in Fig. 6.36 is much higher. It should be noted that the absorbed energy used for the pump-probe experiment (Section 6.3) is similar to the absorbed energy of a saturated XFEL pulse. The difference in the temperature rise is caused by a different spatial distribution of the heat load profile given by the beam radius and penetration/extinction length. The penetration depth considered in the pump-probe experiment is $5\ \mu\text{m}$, thus the scales of interest considering Fig. 6.35 may be assumed to be significant larger than for the case described in Section 6.3. Under such condition the previous mentioned assessment that at low temperatures the mean free path is larger,

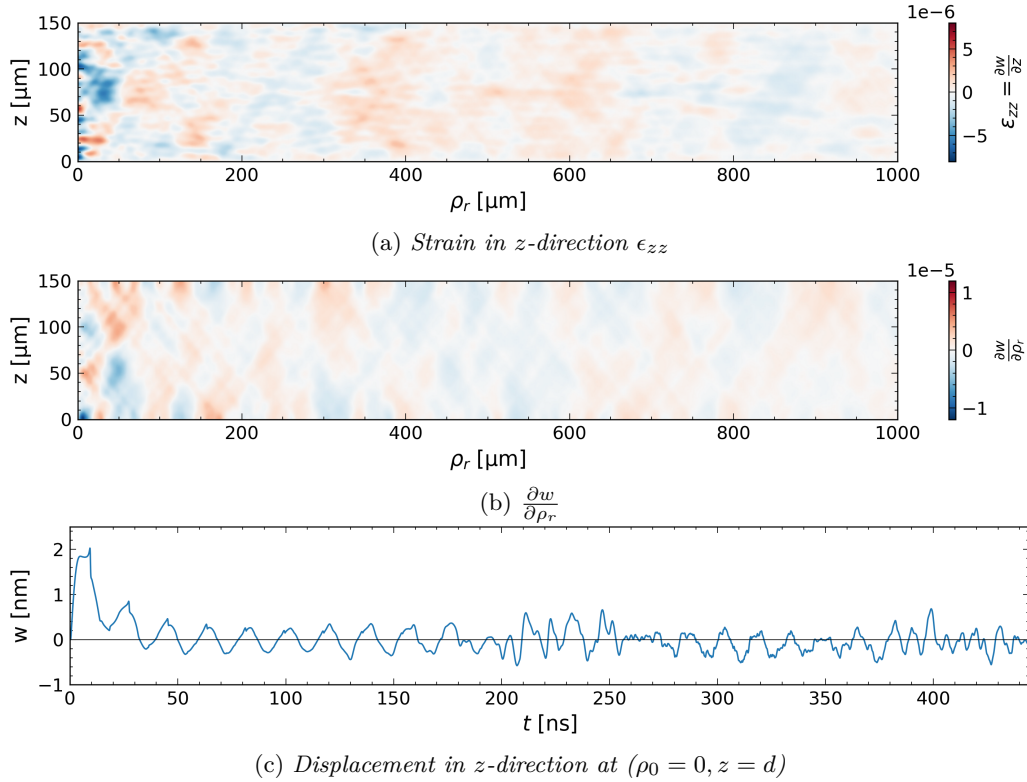


Figure 6.38.: *Axisymmetric FEM Simulation considering a heat load profile given by Fig. 6.35 with a repetition rate of $f_R = 2.25$ MHz and cylindrical geometry with radius $R_0 = 1000 \mu\text{m}$ and thickness $d = 150 \mu\text{m}$. (a) Strain in z -direction present at $t = 444.44$ ns directly before absorption of the next heat load pulse. (b) $\frac{\partial w}{\partial \rho_r}$ at $t = 444.44$ ns. (c) Displacement in z -direction at position $(\rho_0 = 0, z = d)$.*

everywhere inside the crystal, than the scales of interest would not hold. If thermalization after absorption occurs sufficiently fast phonon-phonon scattering could take place in the region $(\rho_r = 0, z = 0)$ and a local thermal equilibrium exists with temperatures near the values predicted by Fig. 6.36. The area, where a high energy density is present in Fig. 6.35 may be considered to be a kind of hot area where a quite short mean free path of a few hundred nanometers may be present shortly after absorption. However, the surrounding area has a temperature value of about $T_0 = 77$ K where the mean free path is in the range of a few tens of micrometers (see Fig 4.7a). Nevertheless, since already the result of the pump-probe experiment has shown quite good agreement with the FEM simulation, where such a hot zone was not present at low temperatures, using the theoretical framework presented in this work may give reliable result for the CBXFEL simulation.

The values of the strain in z -direction $\epsilon_{zz} = \frac{\partial w}{\partial z}$ and the spatial derivation of the displacement in z -direction with respect to the radial direction $\frac{\partial w}{\partial \rho_r}$ are illustrated in Fig. 6.38. These values, which can be calculated from the numerical solution of the displacement field, are of particular interest for the stability of a CBXFEL, as it will be discussed in the following part of this section. In Fig. 6.38 also the displacement at the position $(\rho_0 = 0, z = d)$ is illustrated for the first 444.44 ns. These illustrations may be useful for a comparison with the simulation of the previous sections. Comparing it to Fig. 6.33 it can

be seen that an overall rise of the displacement, observed for the pump-probe experiment, is in Fig. 6.38c not present and that the periodic fringes have a much higher amplitude. This observation can be referred to the difference of the heat load profiles.

Considering the simulation in Fig. 6.38 it should be noted that the initial conditions for the simulation is assumed to be an unstrained crystal. This is a quite unrealistic assumption, because it neglects the previously created strain fields, which will occur during the start up regime where the pulse energy increases over several pulses. However, these simulations are very useful for a first estimation of the relevance for the impact of thermoelastic effects on the stability criteria of an CBXFEL.

A detailed discussion about the underlying concepts of X-ray scattering is presented in the PhD thesis of P. Rauer [Rau21]. In the present work now only a short overview about this topic will be presented.

If an electromagnetic approximately plane wave has a wavelength, which is on the order of characteristic length scales of a single crystalline material, the plane wave will be diffracted at the crystal lattice. It can be derived that for each periodically repeating plane, which can be constructed from a given crystal structure, reciprocal lattice vectors (Eq. 4.4) can be obtained which are perpendicular to those lattice planes. For the shortest of those reciprocal lattice vectors the following relation can be obtained [GM18, p. 62]:

$$|\mathbf{G}_{min}| = \frac{2\pi}{d_L}, \quad (6.61)$$

where d_L is the distance period considering repeating planes of the crystal structure. In this case (h, k, l) of the lattice vector $\mathbf{G}_{min} = h\mathbf{b}_1 + k\mathbf{b}_2 + l\mathbf{b}_3$ gives the values of the so called Miller indices, which define the considered lattice planes. The Laue equation relates an incoming plane wave vector \mathbf{k} to the diffracted outgoing wave vectors \mathbf{k}' under consideration of a given three-dimensional crystal structure by [GM18, p. 62]

$$\mathbf{k}' - \mathbf{k} = \mathbf{G}, \quad (6.62)$$

which causes that a given set of reciprocal lattice vectors determines the possible diffraction conditions. For a elastic scattering $|\mathbf{k}| = |\mathbf{k}'|$ the Laue equation yield:

$$|\mathbf{G}| = 2k \sin(\Theta_B) \quad (6.63)$$

Using Eq. 6.61 an arbitrary reciprocal lattice vector may be expressed by n multiples of $|\mathbf{G}_{min}|$:

$$|\mathbf{G}| = n|\mathbf{G}_{min}| = n \frac{2\pi}{d_L} \quad (6.64)$$

Considering the connection of the magnitude of wave vector and wavelength $k = 2\pi/\lambda$ yields by inserting Eq. 6.64 into Eq. 6.63 Bragg's law:

$$n\lambda = 2d_L \sin(\Theta_B), \text{ where } n = 1, 2, 3... \quad (6.65)$$

For a crystal with a cubic lattice structure the lattice spacing is given by

$$d_L = \frac{a}{\sqrt{h^2 + k^2 + l^2}}, \quad (6.66)$$

where h , k and l are the Miller indices. Considering the orientation of the crystal lattice to the coordinate system (see for example Fig. 3.3) and considering orientation of the incoming plane waves vector \mathbf{k} the Ewald sphere may be used to check if a reciprocal lattice vector fulfills the Laue equation Eq. 6.62. For further information about the Ewald sphere see [GM18, p. 69]. For a suitable alignment of the crystal lattice relative to the incoming wave vector backscattering can be realized. In this context backscattering means the wave vector of the reflected beam points in the opposite direction referred to the incoming wave vector. Considering a diamond crystal (Fig. 4.1a) oriented for backscattering with the miller indices $(3, 3, 3)$ gives with Eq. 6.66 a value for d_L , which can be inserted into Eq. 6.65 to calculate³⁵ the wavelength $\lambda = 1.373 \text{ \AA}$ or a photon energy of $E = 9030 \text{ eV}$ (Eq. 2.65) of for a backscattering angle $\Theta_B = 90^\circ$.

The discussed theory of X-ray reflection so far predicts a discrete condition (Eq. 6.62). However, taking into account the density distribution of the atoms in the lattice and the refraction of the X-ray radiation inside the crystal, a tolerance for reflection condition may be visualized by a reflectance curve for the Bragg angle Θ_B or the connected phonon energy (Eq. 2.65) which are related by Eq. 6.65. If the crystal geometry and susceptibility values are known, the dynamical diffraction theory can be used to calculate the reflectance R . However, not all reciprocal lattice vectors give a non-zero reflectance for a single crystalline diamond (forbidden reflexes). Further information on the underlying assumptions of the dynamical diffraction theory can be found in the PhD thesis of P. Rauer [Rau21].

Considering an incoming wave vector with fixed orientation, but variable photon energy the reflectance curves illustrated in Fig. 6.39a can be calculated, for a crystal aligned for backscattering of the $(3,3,3)$ reflection. The value E_c is the central photon energy value of the reflection curve, which is given by the lattices constant at a temperature of 77 K and the Laue equation (Eq. 6.62). In Fig. 6.39b the reflection curve as a function of the Bragg angle is illustrated, the angle $\Theta_{B,c}$ is the central Bragg angle present at a temperature of 77 K. However, since the lattice constant of diamond is temperature dependent, a homogeneous temperature change of the crystal causes a change of the lattice constant (Eq. 4.33) and therefore changes the lattice spacing (Eq. 6.66) and the reflection conditions (Eq. 6.62), which causes a shift of the reflectance curve, as illustrated in Fig. 6.39. It should be mentioned that for the considered case of perfect aligned backscattering multiply reflectance condition would be satisfied, however tilting the crystal slightly to a non-exact backscattering condition it can be achieved that the $(3,3,3)$ reflection is the only relevant reflection the for backscattering condition. The reflectance curves in this case are nearly the same as for a exact backscattering condition. Under these assumptions the reflection

³⁵The value of the lattice constant is given by $a = 3.56690(8) \text{ \AA}$ (see Section 4)

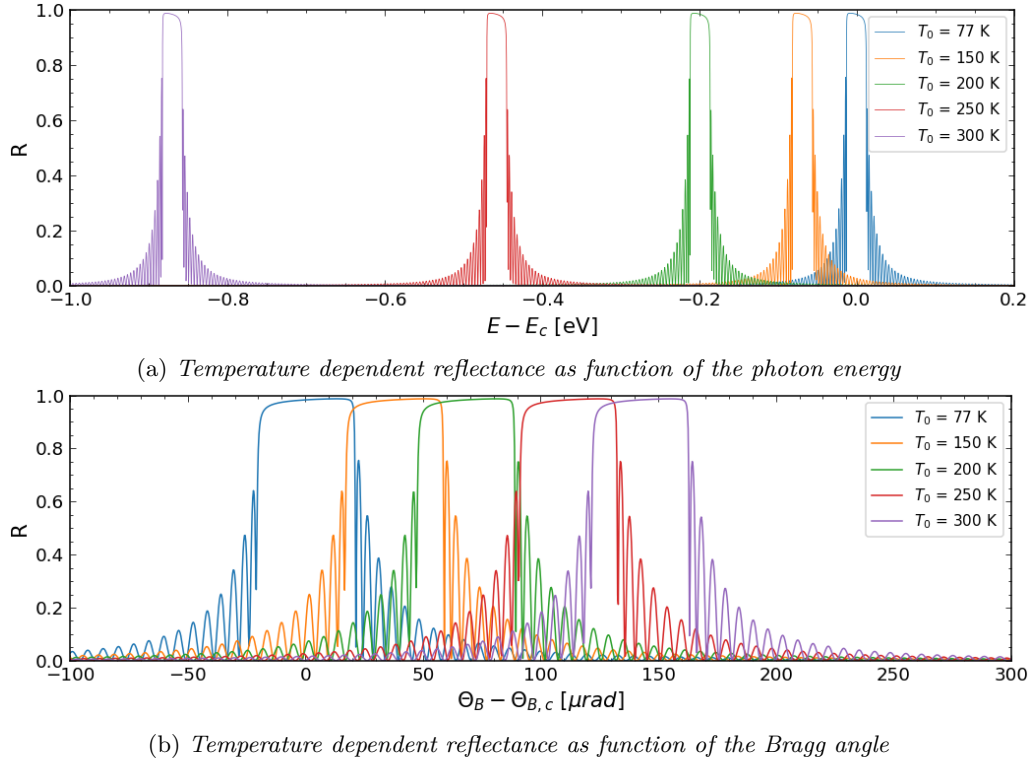


Figure 6.39.: Reflection curve of the (3,3,3) reflex for backscattering (a) as a function of the center photon energy at a crystal temperature of 77 K (b) as a function of the center Bragg angle (90°) at a crystal temperature of 77 K. Calculations for the reflections intensity using dynamical diffraction theory have been carried out by P. Rauer [Rau21]

curves illustrated in Fig. 6.39 can be calculated using the dynamical diffraction theory. Further information about the calculation can be found in the thesis of P. Rauer [Rau21].

Even if the temperature is constant and the crystal is unstrained a rotation of the crystal can change the reflection condition. The reflectance curve illustrated in Fig. 6.39b shows that in a range of about a few μrad around the central value the reflectance is still near the peak value. This range is larger than the angular stability criteria for the CBXFEL to ensure a stable round trip path for the photons inside the cavity. Thus, the angular stability may be investigated by considering simple concepts known from geometrical optics in this case.

The displacement field which is present after 444.44 ns gives the reflection condition for the next X-ray pulses. The angular stability regarding thermoelastic effects can be investigated by using the solution of the FEM simulation (Fig. 6.38). For the axisymmetric case the variation in ρ_r -direction of the displacement in z -direction w may be associated with a radial angular displacement.

$$\tilde{\alpha}_a = \frac{\partial w}{\partial \rho_r}. \quad (6.67)$$

Assuming that the value $\tilde{\alpha}_a$ is constant in the crystal thickness direction (z -direction)

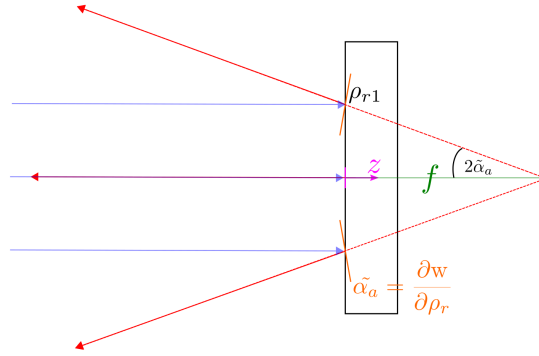


Figure 6.40.: Connection of radial angular displacement with focal length. Illustrated for an arbitrary point ρ_{r1} in radial direction.

this radial angular displacement may be associated with an focal length as illustrated in Fig. 6.40. However, the focal length in this case has not to be a constant value, but can depend on the radial coordinate ρ_r . Considering the sign convention used for the crystal coordinate system³⁶ and the sign convention that converging is denoted by a positive focal length a kind of focal length is

$$f(\rho_r) = -\frac{\rho_r}{2\tilde{\alpha}_a(\rho_r)}, \quad (6.68)$$

where the small angle approximation $\tan(2\tilde{\alpha}_a) \approx 2\tilde{\alpha}_a$ has been used. Considering that the mean extinction length for the X-rays for the planned CBXFEL is in the range of 20 μm to 40 μm and the beam radius is about 50 μm the region of interest for the radial angular displacement may be visualized by a zoom of Fig 6.38b as illustrated in Fig. 6.41a. For the illustration given by Fig. 6.41a it can be seen that the assumption that the relation $\tilde{\alpha}_a = \frac{\partial w}{\partial \rho_r}$ is constant in z -direction is not true for this case. However, to get a rough estimation for the effect of the angular misalignment which is present by this displacement field, an average value in z -direction as a function of ρ_r which is weighted by the mean extinction length $\langle l_{ext} \rangle$ may be calculated by

$$\langle \tilde{\alpha}_a \rangle(\rho_r) = \frac{\int \tilde{\alpha}_a(z, \rho_r) \exp(z/\langle l_{ext} \rangle) dz}{\int \exp(z/\langle l_{ext} \rangle) dz} \quad (6.69)$$

Using a mean extinction length $\langle l_{ext} \rangle = 30 \mu\text{m}$ the calculation of Eq. 6.69 is carried out by approximating the integral by a summation, using solution of the FEM simulation. This leads to the results shown in Fig. 6.41b, where the corresponding mean focal length for the mean angular displacement has been calculated by Eq. 6.68. These results show that the predicted angular displacement caused by thermoelastic effects is very problematic for a CBXFEL, which has a cavity with length dimension of tens of meters [Rau21].

Using the calculated strain field in z -direction (Fig. 6.38a) a distorted reflection curve

³⁶At the front surface z is zero and positive values are define in the direction as illustrated in Fig. 6.40.

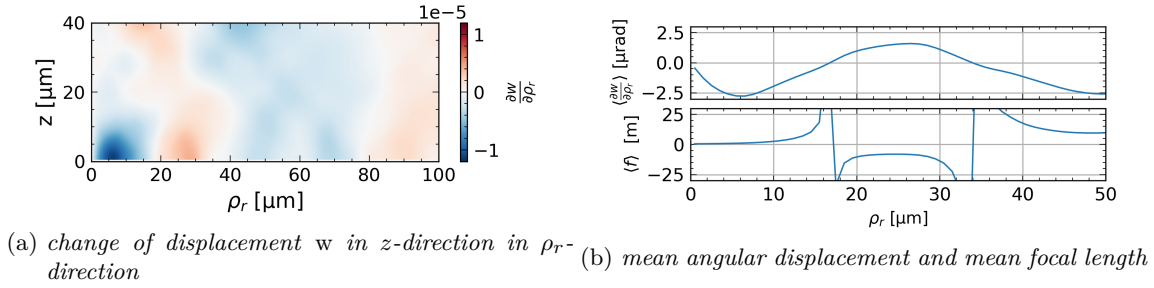


Figure 6.41.: Investigation of thermoelastic effects on the angular stability. (a) $\frac{\partial w}{\partial \rho_r}$ at $t = 444.44$ ns in the region of interest considering X-ray reflection of a CBXFEL. (b) mean angular displacement and mean focal length calculated with Eq. 6.68 and Eq. 6.69.

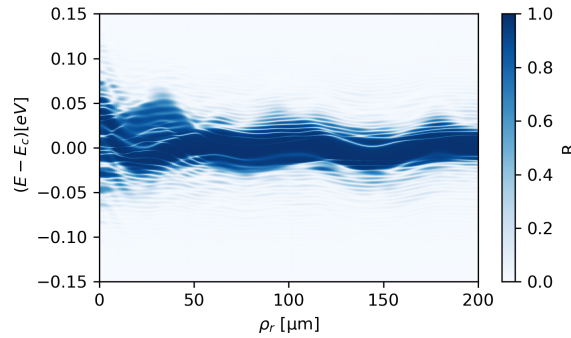


Figure 6.42.: Distortion of the reflection curve as a function of the radial direction, considering the strain in z -direction given by Fig. 6.38a

which is a function of the radial position can be calculated as illustrated in Fig. 6.42. Further information about the calculation for Fig. 6.42 can be found in the PhD thesis of P. Rauer [Rau21]. These calculations show that due to thermoelastic effects the bandwidth will be much wider compared to an unstrained crystal (blue line in Fig. 6.39a).

The results represented by Fig. 6.41b and Fig. 6.42 are both strong indicators that a stable operation of a saturated CBXFEL is not possible considering the heat load given by Fig. 6.35, if the underlying assumption for the thermoelastic simulations are correct. However, this does not mean that the CBXFEL planned to be built at the European XFEL will not work at all. Especially in the startup range the pulse energies inside the cavity are much smaller and the maximum temperature rise predicted by simulations carried out by P. Rauer [Rau21] are much smaller than 100 K. Under such conditions thermoelastic heat load effects may become less important.

Also it should be noted that if the gain of the CBXFEL could be reduced the heat load may be reduced to an amount where a stable operating CBXFEL is possible and thermoelastic effects do not affect the reflection conditions from one pulse to another.

7. Discussion and Outlook

One main question regarding this work is: Do dynamical thermoelastic effects have an impact on the stability of a CBXFEL? To answer this question two different effects should be investigated. First, which strain values inside the extinction length are present when an X-ray pulse is reflected? Second, to which degree is the crystal tilted (angular displacement)? These questions are essential for a stable operating CBXFEL.

For a CBXFEL it is desired that the reflection of the X-rays should take place in a narrow energy bandwidth. The presence of strain inside the extinction length may limit the bandwidth of the reflection curve (Fig. 6.42) and/or shift the central photon energy of the Darwin width (Fig. 6.39a). For a cavity with length scales of a few tens of meters, for a round trip, the angular stability of the Bragg reflector should not exceed the amount of about 100 nrad. For a larger angular displacements a stable path for a seeding photon pulse inside the cavity may not be fulfilled [Rau21]. Thermoelastic effects which may have an impact on this stability criteria have been introduced in the previous sections and will now be summarized and further discussed.

The angular stability for thermoelastically deformed Bragg reflectors may also be connected to the heat bump effect, which has been discussed in Section 6.2.1. In Fig. 6.12 various combinations of different parameters are illustrated, and show that the heat bump shape strongly depends on the particular crystal thickness, penetration depth and the beam radius. The considered shapes in Fig. 6.12 result from a quasi static simulation. For a dynamic deformation the heat bump needs a finite time to develop as discussed in Section 6.2.1. For a diamond Bragg reflector this time span can range over a few hundreds of nanoseconds, as shown by the example in Fig. 6.14b. It should be noted that for the different shapes of the heat bumps presented in Fig. 6.12 for all cases the same maximum temperature value has been considered. However, for most applications not the temperature rise may be seen as a fixed parameter, but the pulse energy. With optical elements (like lenses) the beam radius may be aligned to a desired value. As discussed in Section 6.1 a smaller beam radius will cause a higher energy density and therefore can cause a higher temperature rise (Eq. 6.16) and may also cause that more of the absorbed pulse energy will be converted into elastic energy (Eq. 6.33). Also, it should be noted that due to the small temperature rise considered for the calculations of Fig. 6.12 the material parameters may be assumed to be temperature independent. However, for a constant pulses energy decreasing the spot size would results in a significantly higher temperature rise compared to larger spot sizes. Therefore, in this case the temperature dependent material parameters have to be considered.

If heat conduction is taken into account it has to be considered on which timescales an initially introduced temperature profile will be converted by a diffusion process into a nearly equilibrium temperature rise (see Section 6.2.4). The existence of a temperature difference is important because the rise of the displacement, which can be connected to the heat bump effect, is only present for a non-uniform temperature profile. Thus, if the time scales on which a temperature profile reaches a nearly uniform temperature rise is shorter than the timescale which is needed for the heat bump to develop, the effect of the displacement rise will be reduced. Considering Fig. 6.23c and Fig. 6.23d it can be seen that, for the case of an initial temperature of 50 K, a nearly uniform temperature is reached after a few tens of nanoseconds. This fast decay of the temperature rise can be referred to the very high diffusivity¹ (Fig. 6.22a) at low temperatures for a diamond crystal. However, for an initial temperature of 300 K there is after 100 ns still a significant temperature difference, due to a lower diffusivity compared to an initial temperature of 50 K. Nevertheless, even at $T_0 = 300$ K the diffusivity of diamond is quite high, so that the static heat bump which would occur if heat conduction would be neglected will never be reached. This situation might change if diffusivity would be much lower. Such a condition might exist if the initial temperature is much higher than room temperature (see Fig. 6.22a) or other Bragg reflector materials with significantly lower diffusivity than diamond would be considered.

Considering a heat load profile with a spatial Gaussian distribution placed on a thin crystal sufficiently far away from the side boundaries of the crystal, the development of the displacement in the center region of the Gaussian profile in the setup range (here about the first 200 ns) is nearly independent of the exact lateral crystal geometry. This can be concluded from the discussion in Section 6.2.1 and the comparison of the measurements and simulations shown in Fig. 6.33 (at $T_0 = 300$ K). However, this situation changes when wave reflections from the side boundary have to be taken into account. In this context, it should be mentioned that the heat bump effect causing the radial wave propagation might also depend significantly on the particular three-dimensional structure of the crystal and the kind of boundary constraints. This effect has not been discussed in detail in this work. However, from the comparison of the pump-probe experiment with the simulation (Fig. 6.34) it can be seen that displacement development in the range of a few microseconds are on a similar order of magnitude. The temporal development of the displacement in Fig. 6.34 may be referred to the propagation and reflection of radial waves (Fig. 6.15), caused by the temporal development of the heat bump. The resulting displacement field caused by the reflecting radial waves seems to have in this case a similar order of magnitude, although the considered geometry and the kinds of constraints are quite different for the measurement and the simulation. However, it should be pointed out that this observation of a similar displacement magnitude does not exclude that a strong deviation might exist

¹The calculated diffusivity includes the value for the thermal conductivity, which is connected to the assumptions of the Fourier law. The systematic error which may be introduced by this assumption for the low temperature range is discussed in the following parts of this section.

for other kinds of crystal geometries.

The same theoretical framework which has been used to simulated the pump-probe experiment has also been used to simulate heat load effects for a saturated CBXFEL. Regarding the angular displacement, which may be connected to the value of $\frac{\partial w}{\partial \rho_r}$ illustrated in Fig. 6.41, it can be seen that the value of the created angular displacement by a single saturated pulse may already exceed the stability criteria for a CBXFEL. Also the distortion of the reflection curve is clearly noticeable in Fig. 6.42. However, it should be noted that the simulation carried out may include significant systematic errors due to the chosen theoretical framework of this work. The good agreement of the pump-probe experiment with the simulation presented in this work indicate that the chosen theoretical framework may be a good choice. However, to exclude that this good agreement is not only a coincident, due to the considered parameters chosen for the experiment, additional measurements have to confirm or falsified that this framework is really applicable for low initial temperatures for various parameters. Changing the pump laser spot size to create various heat load profiles could be realized quite easily in the existing experimental setup (Fig: 5.5) and could be the next step for upcoming projects to make progress in this direction.

The approximation to consider the elastic properties of diamond as isotropic, with a Poisson's ratio of zero as discussed in Section 4, seems to be a good choice for the qualitative investigation of the three-dimensional wave propagation (Fig. 6.30). This is an important result for the needs of this work, because it enables to connect the discussed effects in Section 6 and corresponding features in the temporal development of the displacement to the observed experimental data (Section 5). It should be noted that the verification of these approximations were not obvious, because the mean value of the Poisson's ratio of diamond is still 0.07. The calculated values of the bulk modules (Section 4) under different approximations show that neglecting the Poisson's ratio of diamond can have a significant impact on the elastic properties of the material. This also should be kept in mind when using this assumption for other Bragg reflector materials which might have a much larger Poisson's ratio. The introduced systematic error could have a significant impact on the kind of wave propagation in this case. The good agreement of the approximation of diamond to be elastic isotropic may be connected to the small variation of the Young' modulus with orientation (see Section 4, Fig. 4.2). However, also in this case it should be noted that Bragg reflectors made of other materials may not be suitable for this approximation. In other words, using the isotropic approximation it should always be noted that even for single crystalline materials with cubic lattice structure the elastic properties can show significant dependence on the orientation (see Appendix A.3).

For a thermoelastic simulation of a crystal which experiences a pulsed heat load, the temperature rise profile and the dynamic displacement field are characterized by a quite different development. This is, because the development of the temperature profile may be described by a diffusion PDE (Eq. 6.11), and the (Eq. 3.63) development of the dynamic

displacement field may be defined by a wave equation type PDE (Eq. 6.9 and Eq. 3.68).

If a crystal with insulating boundaries is considered, more absorbed energy means more energy inside the crystal. After heat dissipation due to thermal conductivity, taking place for a sufficiently long time span, there will be an equilibrium temperature rise of the crystal. This temperature rise will increase for every pulse, so far the heat capacity has a positive value. After the absorption of several pulses this might lead to a thermal energy value which eventually might cause a destruction of the crystal structure. However, of course a pulsed heat load with a constant repetition rate does not always cause a destruction of the crystal. If parts of the crystal boundary are not isolating, but allow energy transfer to a heat bath², via heat flux at the boundaries, and if heat conduction is sufficiently high, the temperature rise of the crystal due to a pulsed heat load results after some startup time in a periodic temperature profile. Such a case is illustrated in Fig. 6.36.

For a wave equation (PDE), if no damping effects are considered, once created displacement waves will be reflected at the boundaries and could exist theoretically forever. However, for a wave propagating in a real crystal various kinds of damping effects [MBUW12] exist such that the kinetic energy of the displacement wave will finally be converted into thermal energy. For the pump-probe experiment (Section 5) the repetition rate of the pump laser was 20 Hz, which means that the time span between two consecutive pulses is 50 ms. Considering that the displacement directly before the arrival of a new pulse which has been measured (Fig. 5.13) is nearly zero may be seen as a strong indicator that the displacement wave created by the previous laser pulse is damped to a value which does not affect the displacement wave of the following pulse. The measurement for time scales of 100 μ s (Fig. 5.13) shows that after this time span the amplitude still has an order of magnitude similar to the displacement reached in the start up range³. For the FEM simulation presented in Section 6 damping effects could be neglected. The good agreement between the measurements and the simulation may be seen as a verification for the assumption that on timescales of a few hundred nanoseconds damping effect may be neglected. Noting that the repetition rate of modern XFEL facilities is in the megahertz range which corresponds to a time spacing of a few hundred nanoseconds between one X-ray pulse to the following one, it is clear that the displacement wave created by the previous pulse can affect the displacement wave created by the following pulse. It should be mentioned that a pump laser with shorter pulse duration may introduce a strain/displacement wave with higher frequency components. The damping of high-frequency components has not been discussed in this work. However, this aspect has been investigated in the PhD thesis of C. Maag [Maa18], where frequency components of a one-dimensional strain wave (Eq. 6.21) and their damping coefficients due to phonon-phonon scattering have been discussed. Considering a frequency spectrum of such a one-dimensional strain pulse⁴ the

²Which may be given for example by a crystal holder with nearly constant temperature.

³The start up range in this context denotes the first hundreds of nanoseconds after the absorption of the pump laser pulse.

⁴The penetration depth in the considered case by C. Maag [Maa18] is 20 μ m.

highest amplitude is centered around frequency components of 140 MHz, and frequencies higher than 1 GHz have a quite small amplitude compared to the peak value. The acoustic attenuation coefficient for frequencies about 1 GHz is smaller than 0.1 cm^{-1} and for lower frequencies it is even much smaller [Maa18]. Thus, considering a time span of $1 \mu\text{s}$ and the speed of sound (Eq. 6.57), for a diamond crystal, a wave can travel a distance of about 1.8 cm. Therefore, even quite high frequency components experience only a small damping effect. For lower frequency components the damping effect is even smaller and, as the measurements of this work have shown, the time for a displacement wave to be damped might exceed the millisecond range (see Fig. 5.13). Therefore, regarding a repetition rate in the MHz range, thermoelastic wave effects may stack up and could become problematic.

In this work a Michelson interferometer has been used to investigate the thermoelastic effects in a pump-probe experiment. The advantage of this method is that a direct measurement of the displacement is possible. Since this is the variable which can be calculated by the thermoelastic FEM simulation presented in this work, the measured experimental data are optimal to benchmark simulation results. However, an disadvantage of this method is that the alignment is quite challenging, because several different optical and technique components need accurate alignment (see Section 5). For an in-house experimental setup this disadvantages are not so problematic, but using this setup at an XFEL beam line, where alignment has to be carried out remotely could be quite challenging to organize.

A quite simple experimental method is the measurement of the reflectance change. However, as shown by the measurements of this work the interpretation, in terms of thermoelastic effects, of this measured signals can be challenging. Actually the change of the reflectance shown in Fig. 5.11 and a related refractive index change seems to be not directly correlated to the change of the temperature or the displacement. This statement will now be further discussed.

It should be noted that the probe beam was measuring the signal at the opposite side regarding to the surface where the pump beam is penetrating into the crystal. Due to the penetration depth of $5 \mu\text{m}$ the initial temperature rise at the back side of a crystal with thickness $d = 100 \mu\text{m}$ is quite small. To give an estimation for this effect, an initial temperature of $T_0 = 300 \text{ K}$, the material properties of Table 6.1 and the experimental pump laser parameters of Section 5 may be considered. Under these assumptions a temperature rise of $\Delta T(0, d) = 5.5 \times 10^{-8} \text{ K}$ can be calculated⁵ (Eq. 6.16). Assuming isolated boundaries the equilibrium temperature rise which would take place after diffusion in this case gives $\Delta T_{eq} = 0.01 \text{ K}$ (Eq. 6.49). Noting that the initial temperature rise at position ($z = 0, \rho_r = d$) is smaller than the equilibrium temperature rise, causes, for time spans where a temperature change due to heat transfer to the holder can be neglected, a monotonic increase of the temperature rise. However, a clear peak with a width similar to the temporal laser pulse shape (Fig. 5.3) is measured in the range of the first few nanoseconds

⁵Actually due to the finite pulse duration of the pump laser the temperature rise will be even smaller.

of the photon-material interaction (Fig. 5.11). To reach a nearly equilibrium temperature rise, at an initial temperature $T_0 = 300$ K, a time much longer than a few nanoseconds is necessary (Fig. 6.23d) and the heat transfer to the holder might take place on even much longer time scales (see Fig. 6.37). Thus considering a crystal with a thermal insulating boundary at the position where the probe beam is reflected and contact to a cooled holder near the side boundaries should cause a monotonic increase of the temperature at position ($z = 0, \rho_r = d$) for a time span much longer than a few nanoseconds, followed⁶ by a gradual decrease of the temperature rise back to the initial temperature. Therefore, the measured signal which possesses a rise and fall time in the nanosecond range cannot be explained with the results of the simulated temperature profile investigated in this work. This is, because as given by Fig. 4.8 and Eq. 2.56, a monotonic increase of the temperature should cause a monotonically increasing reflectance signal.

The relation of the displacement or strain to a refractive index change has not been investigated in this work. However, considering the solution of the thermoelastic interaction it seems reasonable to conclude that neither the displacement nor related quantities can explain the observed peak of the reflectance signal in the first few nanoseconds. This is, because for a penetration depth of $5 \mu\text{m}$ the value of the displacement and the strain in the first nanoseconds is nearly zero (Fig. 6.4) at position ($z = 0, \rho_r = d$) and the wave needs a time span of a few nanoseconds to reach the back side of the crystal. However, the observed oscillations in Fig. 5.11 might be related to the propagation and reflection of thermoelastic waves.

In addition, as mentioned in Section 5 the measured reflectance change strongly depends on the initial temperature and the exact position of the probe beam relative to the center of the pump beam. Also, the offset signal which is following the peak of the reflectance signal (Fig. 5.11) and the connected sign change seems not to have a direct simple relation to the temperature or displacement field. Unfortunately, the origin of this reflectance change could not be explained in context of this work. Additional measurements to investigate this effect in detail might be an interesting topic for an upcoming research project.

The temperature rise in this work was calculated under the assumption that a local thermodynamic equilibrium exists for all time steps taken by the time dependent solver of the FEM simulation. However, the discussion in Section 4 shows that this assumption might be critical considering heat transfer at low temperatures. The partly ballistic heat transfer may be taken into account by the Cattaneo equation, as already introduced in the PhD thesis of C. Maag [Maa18], without considering thermoelastic effects. A detailed investigation, including the comparison of experimental data with simulation data under various conditions for a three-dimensional axisymmetric case, may be a very interesting topic for a further PhD project.

Another interesting question which could not be investigated experimentally in this

⁶The exact time span for this process will depend on the heat transfer coefficient to the holder as well as the position of the contact area of the crystal to the holder.

work is, what are the conditions present for a thermoelastic problem at temperatures lower than 60 K. The lowest temperature which can be achieved with the cryogenic cooler of the existing experimental setup is about 60 K (see Section 5), however this cooler could be replaced by a different cooling system to reach lower temperatures.

The simulation for the CBXFEL (Section 6.4) is a quite artificial case, because due to thermoelastic effects the predicted saturation heat load (Fig. 6.35a), which has been calculated by neglecting thermoelastic effects may never be reached. Nevertheless, the simulation presented in Section 6.4 is an important result because it predicts that thermoelastic effects can have a significant impact on the stability of a CBXFEL. It should be noted that this prediction was not obvious, before the investigations carried out in this work. However, in this context of course the question arises: What would be a condition for a stable working CBXFEL, considering thermoelastic effects? This question could not be completely answered in this work. However, the investigations of this work are very useful to estimate which kind of thermoelastic effects may be important for the stability of a CBXFEL. Considering the first pulses in the start up range of a CBXFEL a heat load much smaller than a few microjoule per pulse will be absorbed by the crystal [Rau21]. Therefore, the heat load effects and the connected wave propagation may be such small that it can be neglected regarding the stability of a CBXFEL. After the round trip of a few pulses the absorbed energy will increase and thermoelastic waves may have an noticeable effect on the stability. However, the simulation of the described startup range considering thermoelastic effects may not be performed correctly within the theoretic framework presented in this work, because only a diffusive kind of heat transfer has been considered (Section 3). The development of a new theoretical framework including partly ballistic heat transfer may be a very interesting topic for further research projects. In this context also the accumulation of thermoelastic waves created by a periodic heat load may be investigated. However, it should be noted that this topic is a quite challenging task, because possible excitation of eigenfrequencies (Section 6.2.5) and accumulation of strain/displacement fields will depend on the three-dimensional geometry and clamping condition of the crystal, as well as on the shape of the heat load profile, which, considering a CBXFEL, can also change its shape during the first pulses [Rau21]. Considering a three-dimensional geometry the axisymmetric assumptions (Section 3.5) used in this work may be not applicable anymore and computationally more time demanding simulations of a three-dimensional structure have to be considered.

8. Conclusion

In this work the thermoelastic effects introduced by the absorption of pulsed powerful electromagnetic radiation have been investigated, to predict if such effects can be problematic for the stability of Bragg reflectors used in fourth generation XFEL facilities. In this context the question arises: Do thermoelastic effects have an impact on the stability of a Bragg reflector regarding a specified tolerance for strain and angular displacement?

The answer to this question has been worked out in the previous sections, by theoretical and experimental investigations of a thin crystal diamond Bragg reflector under pulsed heat load. The dimensions of the investigated crystal are a few tens of micrometers in thickness and lateral size of a few millimeters.

A surprising result of this work is the conclusion that the time scales on which a displacement/strain wave is damped seems not to be an important issue for a periodic heat load with a MHz repetition rate, if a single crystalline diamond with low defect concentration is considered. The measurement results as well as the simulations carried out in this work have shown that the time scales on which strain waves in a diamond crystal are damped might extend to the millisecond range. The displacement waves regarding the pump-probe experiment presented in this work seem to experience a damping which can be neglected considering the time span of a few hundred nanoseconds. This time scale is in the range of the repetition rate of fourth generation XFELs. Therefore the important question considering a thin crystal is not how the displacement/strain waves are damped, but rather how they interact with the following created displacement waves and on which order of magnitude the accumulated displacement/strain amplitude will be.

To simulate the thermoelastic interaction of a powerful electromagnetic wave with a Bragg reflector, for the pump-probe experiment presented in this work, the assumption of a local thermodynamic equilibrium and heat transfer based on the Fourier law seems to be a quite accurate assumption. This result is quite surprising for lower temperatures, where the assumptions for the Fourier law may not be fulfilled due to the quite large mean free path of phonons.

The heat load of the CBXFEL could be reduced by changing the design parameters, which have been considered in this work. Under such circumstance the thermoelastic effects caused by the heat load might be secondary. However, it should be noted that also in this case the displacement created by several absorbed pulses could stack up to a critical amount for particular combinations of crystal geometries, heat load profiles and clamping conditions. Therefore a detailed theoretical and experimental investigation of the interaction of thermoelastic waves created by a pulsed heat load with megahertz repetition

rate seems to be an important and interesting topic for upcoming research projects.

A. Appendix

A.1. Cartesian coordinates and Cylindrical coordinates

In this work the propagation of electromagnetic waves and thermoelastic deformations in a three-dimensional Euclidean space are investigated by using Cartesian coordinates (x, y, z) and cylindrical coordinates (ρ_r, θ, z) , which are defined for $0 \leq \rho_r < \infty$, $-\pi < \theta \leq \pi$ and $-\infty < z < \infty$. The relation to Cartesian coordinates is

$$\begin{aligned} x &= \rho_r \cos \theta, & \rho_r &= \sqrt{x^2 + y^2}, \\ y &= \rho_r \sin \theta, & \theta &= \text{atan2}(y, x), \\ z &= z, & z &= z. \end{aligned}$$

and the relation of the unit vectors are

$$\begin{aligned} \hat{\rho}_r &= \cos \theta \hat{\mathbf{x}} + \sin \theta \hat{\mathbf{y}}, & \hat{\mathbf{x}} &= \cos \theta \hat{\rho}_r - \sin \theta \hat{\theta}, \\ \hat{\theta} &= -\sin \theta \hat{\mathbf{x}} + \cos \theta \hat{\mathbf{y}}, & \hat{\mathbf{y}} &= \sin \theta \hat{\rho}_r + \cos \theta \hat{\theta}, \\ \hat{\mathbf{z}} &= \hat{\mathbf{z}}, & \hat{\mathbf{z}} &= \hat{\mathbf{z}}. \end{aligned}$$

Considering a point in cylindrical coordinates (ρ_r, θ, z) the position is given by \mathbf{r} .

$$\mathbf{r} = \rho_r \hat{\rho}_r + z \hat{\mathbf{z}} \quad (\text{A.1})$$

It should be noted that the basis vectors $\hat{\rho}_r$ in this case is depending on the value of θ .

The del operator in Cartesian coordinates is given by

$$\nabla = \frac{\partial}{\partial x} \hat{\mathbf{x}} + \frac{\partial}{\partial y} \hat{\mathbf{y}} + \frac{\partial}{\partial z} \hat{\mathbf{z}}. \quad (\text{A.2})$$

Since the unit vectors in cylindrical coordinates are depended on the position the del operator is also different in this case and it can be derived that it is given by [Mal69, p. 667]:

$$\nabla = \frac{\partial}{\partial \rho_r} \hat{\rho}_r + \frac{1}{\rho_r} \frac{\partial}{\partial \theta} \hat{\theta} + \frac{\partial}{\partial z} \hat{\mathbf{z}} \quad (\text{A.3})$$

Considering the gradient of a scalar field \tilde{f} in Cartesian coordinates gives:

$$\nabla \tilde{f} = \frac{\partial \tilde{f}}{\partial x} \hat{\mathbf{x}} + \frac{\partial \tilde{f}}{\partial y} \hat{\mathbf{y}} + \frac{\partial \tilde{f}}{\partial z} \hat{\mathbf{z}} = \tilde{f}_{,i}. \quad (\text{A.4})$$

The notation $(\dots)_i$ denotes here the partial derivative with respect to the three coordinates x_i , which means for Cartesian coordinates $x_1 = x$, $x_2 = y$ and $x_3 = z$.

Considering the gradient of a scalar field \tilde{f} in cylindrical coordinates yields [Mal69, p. 667]:

$$\nabla \tilde{f} = \frac{\partial \tilde{f}}{\partial \rho_r} \hat{\rho}_r + \frac{1}{\rho_r} \frac{\partial \tilde{f}}{\partial \theta} \hat{\theta} + \frac{\partial \tilde{f}}{\partial z} \hat{z} \quad (\text{A.5})$$

Considering the divergence in Cartesian coordinates of a vector field $\tilde{\mathbf{v}} = \tilde{v}_x \hat{\mathbf{x}} + \tilde{v}_y \hat{\mathbf{y}} + \tilde{v}_z \hat{\mathbf{z}}$ (where i ranges over x, y, z) gives:

$$\nabla \cdot \tilde{\mathbf{v}} = \frac{\partial \tilde{v}_x}{\partial x} + \frac{\partial \tilde{v}_y}{\partial y} + \frac{\partial \tilde{v}_z}{\partial z} = \tilde{v}_{i,i} = \frac{\partial \tilde{v}_i}{\partial x_i}. \quad (\text{A.6})$$

The notation $(\dots)_i$ denotes here the partial derivative with respect to the three coordinates x_i , which means for Cartesian coordinates $x_1 = x$, $x_2 = y$ and $x_3 = z$.

Considering cylindrical coordinates the divergence of a vector field $\tilde{\mathbf{v}} = \tilde{v}_{\rho_r} \hat{\rho}_r + \tilde{v}_{\theta} \hat{\theta} + \tilde{v}_z \hat{z}$ using index notation \tilde{v}_i (where i ranges over ρ_r, θ, z) gives [Mal69, p. 667]:

$$\nabla \cdot \tilde{\mathbf{v}} = \frac{1}{\rho_r} \frac{\partial(\rho_r \tilde{v}_{\rho_r})}{\partial \rho_r} + \frac{1}{\rho_r} \frac{\partial \tilde{v}_{\theta}}{\partial \theta} + \frac{\partial \tilde{v}_z}{\partial z}. \quad (\text{A.7})$$

Another possible operation of the del operator on a vector field is $\tilde{\mathbf{v}} \nabla$ which yields in Cartesian coordinates:

$$\tilde{\mathbf{v}} \nabla = \begin{bmatrix} \frac{\partial \tilde{v}_x}{\partial x} & \frac{\partial \tilde{v}_x}{\partial y} & \frac{\partial \tilde{v}_x}{\partial z} \\ \frac{\partial \tilde{v}_y}{\partial x} & \frac{\partial \tilde{v}_y}{\partial y} & \frac{\partial \tilde{v}_y}{\partial z} \\ \frac{\partial \tilde{v}_z}{\partial x} & \frac{\partial \tilde{v}_z}{\partial y} & \frac{\partial \tilde{v}_z}{\partial z} \end{bmatrix}. \quad (\text{A.8})$$

In cylindrical coordinates this expression gives [Mal69, p. 667]

$$\tilde{\mathbf{v}} \nabla = \begin{bmatrix} \frac{\partial \tilde{v}_{\rho_r}}{\partial \rho_r} & \frac{1}{\rho_r} \frac{\partial \tilde{v}_{\rho_r}}{\partial \theta} - \frac{\tilde{v}_{\theta}}{\rho_r} & \frac{\partial \tilde{v}_{\rho_r}}{\partial z} \\ \frac{\partial \tilde{v}_{\theta}}{\partial \rho_r} & \frac{1}{\rho_r} \frac{\partial \tilde{v}_{\theta}}{\partial \theta} + \frac{\tilde{v}_{\rho_r}}{\rho_r} & \frac{\partial \tilde{v}_{\theta}}{\partial z} \\ \frac{\partial \tilde{v}_z}{\partial \rho_r} & \frac{1}{\rho_r} \frac{\partial \tilde{v}_z}{\partial \theta} & \frac{\partial \tilde{v}_z}{\partial z} \end{bmatrix}. \quad (\text{A.9})$$

For both equations Eq. A.8 and Eq. A.9 the relation $(\tilde{\mathbf{v}} \nabla)^T = \nabla \tilde{\mathbf{v}}$ can be used.

Considering a symmetric second order tensor (which is considered to be time and position dependent and may be thus considered to be a tensor field) which may be written for Cartesian coordinates as:

$$\tilde{\mathbf{T}} = \begin{bmatrix} \tilde{T}_{xx} & \tilde{T}_{xy} & \tilde{T}_{xz} \\ \tilde{T}_{yx} & \tilde{T}_{yy} & \tilde{T}_{yz} \\ \tilde{T}_{zx} & \tilde{T}_{yz} & \tilde{T}_{zz} \end{bmatrix} = T_{ij}. \quad (\text{A.10})$$

The del operation on a tensor field on this tensor field gives:

$$\begin{aligned} \nabla \cdot \tilde{\mathbf{T}} &= \tag{A.11} \\ \left(\frac{\partial \tilde{T}_{xx}}{\partial x} + \frac{\partial \tilde{T}_{yx}}{\partial y} + \frac{\partial \tilde{T}_{zx}}{\partial z} \right) \hat{\mathbf{x}} + \left(\frac{\partial \tilde{T}_{xy}}{\partial x} + \frac{\partial \tilde{T}_{yy}}{\partial y} + \frac{\partial \tilde{T}_{yz}}{\partial z} \right) \hat{\mathbf{y}} + \left(\frac{\partial \tilde{T}_{xz}}{\partial x} + \frac{\partial \tilde{T}_{yz}}{\partial y} + \frac{\partial \tilde{T}_{zz}}{\partial z} \right) \hat{\mathbf{z}} \\ &= \tilde{T}_{ij,j} = \frac{\partial \tilde{T}_{ij}}{\partial x_j} \end{aligned}$$

where $(\dots), j$ denotes the partial derivative with respect to the three coordinates x_j , which means for Cartesian coordinates $x_1 = x$, $x_2 = y$ and $x_3 = z$.

Considering cylindrical coordinates an a tensor field with second order tensors:

$$\tilde{\mathbf{T}} = \begin{bmatrix} \tilde{T}_{\rho_r \rho_r} & \tilde{T}_{\rho_r \theta} & \tilde{T}_{\rho_r z} \\ \tilde{T}_{\theta \rho_r} & \tilde{T}_{\theta \theta} & \tilde{T}_{\theta z} \\ \tilde{T}_{z \rho_r} & \tilde{T}_{\theta z} & \tilde{T}_{zz} \end{bmatrix} = T_{ij}. \tag{A.12}$$

the del operation gives in this case [Mal69, p. 667]:

$$\begin{aligned} \nabla \cdot \tilde{\mathbf{T}} &= \left(\frac{\partial \tilde{T}_{\rho_r \rho_r}}{\partial \rho_r} + \frac{1}{\rho_r} \frac{\partial \tilde{T}_{\theta \rho_r}}{\partial \theta} + \frac{\partial \tilde{T}_{z \rho_r}}{\partial z} + \frac{1}{\rho_r} (\tilde{T}_{\rho_r \rho_r} - \tilde{T}_{\theta \theta}) \right) \hat{\boldsymbol{\rho}}_r \tag{A.13} \\ &+ \left(\frac{\partial \tilde{T}_{\rho_r \theta}}{\partial \rho_r} + \frac{1}{\rho_r} \frac{\partial \tilde{T}_{\theta \theta}}{\partial \theta} + \frac{\partial \tilde{T}_{z \theta}}{\partial z} + \frac{1}{\rho_r} (\tilde{T}_{\rho_r \theta} + \tilde{T}_{\theta \rho_r}) \right) \hat{\boldsymbol{\theta}} \\ &+ \left(\frac{\partial \tilde{T}_{\rho_r z}}{\partial \rho_r} + \frac{1}{\rho_r} \frac{\partial \tilde{T}_{\theta z}}{\partial \theta} + \frac{\partial \tilde{T}_{zz}}{\partial z} + \frac{\tilde{T}_{\rho_r z}}{\rho_r} \right) \hat{\mathbf{z}} \end{aligned}$$

A.2. Equation of motion

Here the derivation of the equation of motion is presented in Cartesian coordinates. We consider a body acted upon by an arbitrary traction surface force \mathbf{t}^n and a body force \mathbf{F} per unit volume and assume that the body occupies the volume V , bounded by an exterior surface A at a time t . The resulting force \mathbf{F}^{tot} acting on the body is [HEG09, p. 4]:

$$F_i^{tot} = \int_A t_i^n dA + \int_V F_i dV \tag{A.14}$$

Inserting Eq. 3.5 and using Gauss theorem to transform the surface integral of the traction forces to the volume integral ($\int_A \sigma_{ji} n_j dA = \int_V \sigma_{ij,j} dV$) gives:

$$F_i^{tot} = \int_V (\sigma_{ji,j} + F_i) dV \tag{A.15}$$

Defining the linear momentum by $p_i = \int_V \rho \dot{u}_i dV$, where ρ is the mass density and using Newton's law of motion $\mathbf{F}^{tot} = \dot{\mathbf{p}}$ Eq.A.15 becomes:

$$\int_V \rho \ddot{u}_i dV = \int_V (\sigma_{ji,j} + F_i) dV \quad (\text{A.16})$$

Since the volume V is arbitrary, Eq. A.16 reduces to the equation of motion:

$$\sigma_{ij,j} + F_i = \rho \ddot{u}_i \quad (\text{A.17})$$

A.3. Anisotropic elasticity of cubic crystal

In case of cubic symmetry it is also possible to give the elastic properties in terms of orthotropic¹ material constants and connect the matrix elements to the engineering quantities of Young's modulus E , Poisson's ratio ν , and the shear modulus μ in the axes of interest (x, y, z) [Bow09, p. 87][N⁺85, p. 106][HMK]:

$$\mathbf{C} = \begin{bmatrix} \frac{1-\nu_{yz}\nu_{zy}}{E_y E_z \varpi} & \frac{\nu_{yx}+\nu_{yz}\nu_{zy}}{E_y E_z \varpi} & \frac{\nu_{zx}+\nu_{yz}\nu_{zy}}{E_y E_z \varpi} & 0 & 0 & 0 \\ \frac{\nu_{xy}+\nu_{xz}\nu_{zy}}{E_x E_z \varpi} & \frac{1-\nu_{zx}\nu_{xz}}{E_x E_z \varpi} & \frac{\nu_{zy}+\nu_{zx}\nu_{xy}}{E_x E_z \varpi} & 0 & 0 & 0 \\ \frac{\nu_{xz}+\nu_{xy}\nu_{yz}}{E_x E_y \varpi} & \frac{\nu_{yz}+\nu_{xz}\nu_{yx}}{E_x E_y \varpi} & \frac{1-\nu_{xy}\nu_{yx}}{E_x E_y \varpi} & 0 & 0 & 0 \\ 0 & 0 & 0 & \mu_{yz} & 0 & 0 \\ 0 & 0 & 0 & 0 & \mu_{zx} & 0 \\ 0 & 0 & 0 & 0 & 0 & \mu_{xy} \end{bmatrix} \quad (\text{A.18})$$

$$\mathbf{S} = \begin{bmatrix} \frac{1}{E_x} & -\frac{\nu_{yx}}{E_y} & -\frac{\nu_{zx}}{E_z} & 0 & 0 & 0 \\ -\frac{\nu_{yx}}{E_x} & \frac{1}{E_y} & -\frac{\nu_{zy}}{E_z} & 0 & 0 & 0 \\ -\frac{\nu_{xz}}{E_x} & -\frac{\nu_{yz}}{E_y} & \frac{1}{E_z} & 0 & 0 & 0 \\ 0 & 0 & 0 & \frac{1}{\mu_{yz}} & 0 & 0 \\ 0 & 0 & 0 & 0 & \frac{1}{\mu_{zx}} & 0 \\ 0 & 0 & 0 & 0 & 0 & \frac{1}{\mu_{xy}} \end{bmatrix}$$

where $\varpi = \frac{1 - \nu_{xy}\nu_{yx} - \nu_{yz}\nu_{zy} - \nu_{zx}\nu_{xz} - 2\nu_{xy}\nu_{yz}\nu_{zx}}{E_x E_y E_z}$

Here, the generalized Poisson's ratios are not symmetric but instead satisfy²: $\nu_{ij}/E_i = \nu_{ji}/E_j$. This ensures that the stiffness matrix is symmetric. The relation between the matrix ele-

¹material has three mutually perpendicular symmetry planes

²No sums convention is used in this case

ments of Eq. A.18 and Eq. 3.9 is:

$$\begin{aligned}
E_x &= (c_{11}c_{22}c_{33} + 2c_{23}c_{12}c_{13} - c_{11}c_{23}^2 - c_{22}c_{13}^2 - c_{33}c_{12}^2)/(c_{22}c_{33} - c_{23}^2) & (A.19) \\
E_y &= (c_{11}c_{22}c_{33} + 2c_{23}c_{12}c_{13} - c_{11}c_{23}^2 - c_{22}c_{13}^2 - c_{33}c_{12}^2)/(c_{11}c_{33} - c_{13}^2) \\
E_z &= (c_{11}c_{22}c_{33} + 2c_{23}c_{12}c_{13} - c_{11}c_{23}^2 - c_{22}c_{13}^2 - c_{33}c_{12}^2)/(c_{11}c_{22} - c_{12}^2) \\
\nu_{yx} &= (c_{12}c_{33} - c_{13}c_{23})/(c_{11}c_{33} - c_{13}^2), & \nu_{xy} &= (c_{12}c_{33} - c_{13}c_{23})/(c_{22}c_{33} - c_{23}^2) \\
\nu_{zx} &= (c_{13}c_{22} - c_{12}c_{23})/(c_{11}c_{22} - c_{12}^2), & \nu_{xz} &= (c_{22}c_{13} - c_{12}c_{23})/(c_{22}c_{33} - c_{23}^2) \\
\nu_{yz} &= (c_{11}c_{23} - c_{12}c_{13})/(c_{11}c_{33} - c_{13}^2), & \nu_{zy} &= (c_{11}c_{23} - c_{12}c_{13})/(c_{11}c_{22} - c_{12}^2) \\
\mu_{yz} &= c_{44} & \mu_{xz} &= c_{55} & \mu_{xy} &= c_{66}.
\end{aligned}$$

For the special case where the basis vectors are perpendicular to the symmetry planes for a cubic crystal like illustrated in Fig. 3.3 Eq. A.19 reduces to

$$\begin{aligned}
E_x &= E_y = E_z = E = (c_{11}^2 + c_{12}c_{11} - 2c_{12}^2)/(c_{11} + c_{12}) & (A.20) \\
\nu_{yx} &= \nu_{xy} = \nu_{zx} = \nu_{xz} = \nu_{yz} = \nu_{zy} = \nu = \frac{c_{12}}{c_{11} + c_{12}} \\
\mu_{yz} &= \mu_{xz} = \mu_{xy} = \mu = c_{44}
\end{aligned}$$

To carry out a rotating of the crystal system relative to the coordinate system and to calculate the material properties in the new orientation a transformation can be carried out [Tin96]. To plot these orientation dependent properties the following Python script may be used (here only the calculation for the Young's modulus is shown, but the calculation for the shear modulus and the Poisson's ration can be calculated with the same rotation transformation):

```

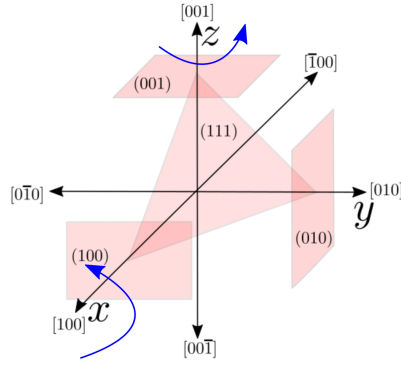
1 import numpy as np
2 from numpy import sin
3 from numpy import cos
4 import matplotlib.pyplot as plt
5 C_matrix = np.array([[1079., 124., 124., 0., 0., 0.],
6 [ 124., 1079., 124., 0., 0., 0.],
7 [ 124., 124., 1079., 0., 0., 0.],
8 [ 0., 0., 0., 578., 0., 0.],
9 [ 0., 0., 0., 0., 578., 0.],
10 [ 0., 0., 0., 0., 0., 578.]])
11 def Rot(a,b,matrix):
12 Rot_z = np.array([[cos(a)**2, sin(a)**2, 0., 0., 0., 2*sin(a)*cos(a)],
13 [sin(a)**2, cos(a)**2, 0., 0., 0., -2*sin(a)*cos(a)],
14 [0., 0., 1, 0., 0., 0.],
15 [0., 0., 0., cos(a), sin(a), 0.],
16 [0., 0., 0., -sin(a), cos(a), 0.],
17 [-sin(a)*cos(a), sin(a)*cos(a), 0., 0., 0., cos(a)**2-sin(a)**2]])
18 Rot_x = np.array([[1., 0., 0., 0., 0., 0.],
19 [0., cos(b)**2, sin(b)**2, -2*sin(b)*cos(b), 0., 0.],
20 [0., sin(b)**2, cos(b)**2, 2*sin(b)*cos(b), 0., 0.],
21 [0., sin(b)*cos(b), -sin(b)*cos(b), cos(b)**2-sin(b)**2, 0., 0.],
22 [0., 0., 0., 0., cos(b), sin(b)],
23 [0., 0., 0., 0., -sin(b), cos(b)]])
24 C_matrix_Rot_x= np.matmul(Rot_x,np.matmul(matrix ,Rot_x.transpose()))
25 C_matrix_new_correct = np.matmul(Rot_z,np.matmul(C_matrix_Rot_x,Rot_z.transpose()))
26 return C_matrix_new_correct
27 def E_x(matrix):
28 E_x = (matrix[0,0]*matrix[1,1]*matrix[2,2]+2*matrix[1,2]*matrix[0,1]*matrix[0,2] -
29 matrix[0,0]*matrix[1,2]**2-matrix[1,1]*matrix[0,2]**2 -
30 matrix[2,2]*matrix[0,1]**2)/(matrix[1,1]*matrix[2,2]-matrix[1,2]**2)
31 return E_x
32 def E_y(matrix):

```

```

33 E_y = (matrix[0,0]*matrix[1,1]*matrix[2,2] + 2*matrix[1,2]*matrix[0,1]*matrix[0,2] -
34 matrix[0,0]*matrix[1,2]**2 - matrix[1,1]*matrix[0,2]**2 -
35 matrix[2,2]*matrix[0,1]**2)/(matrix[0,0]*matrix[2,2] - matrix[0,2]**2)
36 return E_y
37 def E_z(matrix):
38 E_z = (matrix[0,0]*matrix[1,1]*matrix[2,2] + 2*matrix[1,2]*matrix[0,1]*matrix[0,2] -
39 matrix[0,0]*matrix[1,2]**2 - matrix[1,1]*matrix[0,2]**2 -
40 matrix[2,2]*matrix[0,1]**2)/(matrix[0,0]*matrix[1,1] - matrix[0,1]**2)
41 return E_z
42 fig = plt.figure();ax = plt.subplot(111, projection='polar')
43 gamma_r = np.linspace(0, 2*np.pi, 100);phi_r = np.linspace(0, 2*np.pi, 100)
44 intensity =0.06
45 all_values=np.array([])
46 for i in gamma_r:
47 ax.plot(phi_r, E_x(Rot(phi_r,i,C_matrix)), color='r',alpha=intensity)
48 all_values=np.append(all_values,E_x(Rot(phi_r,i,C_matrix)))
49 for i in gamma_r:
50 ax.plot(phi_r, E_y(Rot(phi_r,i,C_matrix)), color='b',alpha=intensity)
51 all_values=np.append(all_values,E_y(Rot(phi_r,i,C_matrix)))
52 for i in gamma_r:
53 ax.plot(phi_r, E_z(Rot(phi_r,i,C_matrix)), color='g',alpha=intensity)
54 all_values=np.append(all_values,E_z(Rot(phi_r,i,C_matrix)))
55 plt.show()

```



(a) Coordinate system rotation

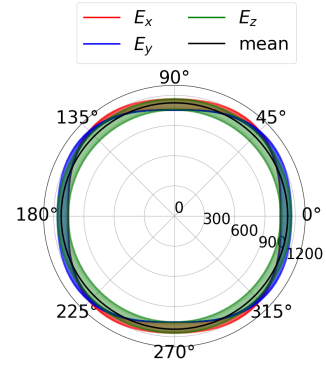
(b) Young's modulus E [GPa]

Figure A.1.: Illustration of the elastic properties of SC diamond in various orientations calculated with the Python script introduced in this section. In (a) rotation to calculate plot is illustrated. The first step is to plot the value by step wise rotating the coordinate system 2π around the z axis. The next step is rotating around the fixed x axis only a small step ($\pi/50$) and then again plot a rotation of 2π around the new z' axis. Repeating this process illustrates various possible orientations of the crystal. It should be notice that the lines are plotted slightly transparent so that darker colors represent more frequently occurring values. (b) Calculated values of the Young's modulus for various orientations $E_{mean}=1125$ GPa, $E_{min}=1053$ GPa, $E_{max}=1207$ GPa

Comparing the compliance matrix \mathbf{S} for an orthotropic matrix Eq. A.18 and isotropic material Eq. 3.13, certain similarity are visible. Indeed, for the cubic material it can be seen by using Eq. A.20 that the matrix elements are identical to the constitutive law for an isotropic solid if $\frac{2\mu(1+\nu)}{E} = \frac{2c_{44}}{c_{11}-c_{12}}$. In this in this context

$$A_{iso} = \frac{2c_{44}}{c_{11} - c_{12}} \quad (\text{A.21})$$

may be used as a measure for the anisotropy for a cubic material, which is $A_{iso} = 1$ for the isotropic case.

A.4. Input file for ab initio calculation

For the ab initio calculations the following input file for the exciting code (version nitrogen) has been used. Further information can be found under <http://exciting-code.org> and <http://exciting-code.org/nitrogen-phonon-properties-diamond>.

```

1 <input>
2 <title>Diamond: PhononDOS</title>
3 <structure speciespath="/home/user/tutorials/exciting/species">
4 <crystal scale="6.7468">
5 <basevect>0.5 0.5 0.0</basevect>
6 <basevect>0.5 0.0 0.5</basevect>
7 <basevect>0.0 0.5 0.5</basevect>
8 </crystal>
9 <species speciesfile="C.xml" rmt="1.25">
10 <atom coord="0.00 0.00 0.00" />
11 <atom coord="0.25 0.25 0.25" />
12 </species>
13 </structure>
14 <groundstate
15 ngridk="8 8 8"
16 rgkmax="7.0"
17 xctype="GGA_PBE"/>
18 <phonons
19 ngridq="4 4 4">
20 <phonondos
21 ngrdos="100"
22 nwdos="500"
23 ntemp="200"
24 nsmdos="2"/>
25 <qpointset>
26 <qpoint> 0.0 0.0 0.0 </qpoint>
27 <qpoint> 0.5 0.5 0.0 </qpoint>
28 <qpoint> 0.5 0.5 0.5 </qpoint>
29 </qpointset>
30 <phonondisplot>
31 <plot1d>
32 <path steps="300">
33 <point coord="0.000000 0.000000 0.000000" label="Gamma"/>
34 <point coord="0.500000 0.000000 0.500000" label="X"/>
35 <point coord="0.500000 0.250000 0.750000" label="W"/>
36 <point coord="0.375000 0.375000 0.750000" label="K"/>
37 <point coord="0.000000 0.000000 0.000000" label="Gamma"/>
38 <point coord="0.500000 0.500000 0.500000" label="L"/>
39 <point coord="0.625000 0.250000 0.625000" label="U"/>
40 <point coord="0.500000 0.250000 0.750000" label="W"/>
41 <point coord="0.500000 0.500000 0.500000" label="L"/>
42 <point coord="0.375000 0.375000 0.750000" label="K"/>
43 </path>
44 </plot1d>
45 </phonondisplot>
46 </phonons>
47 </input>

```

A.5. Temperature dependent thermal expansion coefficient

In Eq. 3.41 it is stated that a change of temperature causes a thermal strain, which is related to the stress by the elastic stiffness tensor:

$$\sigma_{ij} = C_{ijkl}[\epsilon_{kl} - \epsilon_{kl}^{th}] \quad (\text{A.22})$$

The thermal expansion presented in Eq. 4.32 may be interpreted as a tangent thermal

expansion coefficient $\alpha_t(T)$ which describes a infinitesimal length change dL by:

$$\frac{dL}{L} = \alpha_t(T)dT, \quad (\text{A.23})$$

where L is the current length under consideration of the absolute temperature. This infinitesimal length change may be connected to a change of the thermal stain by $d\epsilon_{kl}^{th}(T) = \frac{dL}{L_0}$. However, considering a finite temperature rise ΔT referred to a initial temperature T_0 an integration has to be carried out to calculate the thermal strain:

$$\epsilon_{kl}^{th} = \int_{T_0}^{T_0+\Delta T} \alpha_t(T)dT, \quad (\text{A.24})$$

Also, it should be noted that Eq. A.24 is connected to the assumption, that the initial thermal strain is assumed to be zero.

Considering a finite temperature change also a secant thermal coefficient may be used which may be expressed by

$$\frac{\Delta L}{L_0} = \alpha_s(T, T_0)\Delta T, \quad (\text{A.25})$$

where L_0 is the initial length. To calculate the secant thermal coefficient from the values of the tangent thermal expansion coefficient Eq. A.23 can be integrated yielding:

$$\ln(L_0 + \Delta L) - \ln(L_0) = \ln\left(1 + \frac{\Delta L}{L_0}\right) = \int_{T_0}^{T_0+\Delta T} \alpha_t(T)dT, \quad (\text{A.26})$$

which can be rearrange to

$$\frac{\Delta L}{L_0} = \exp\left(\int_{T_0}^{T_0+\Delta T} \alpha_t(T)dT\right) - 1 \quad (\text{A.27})$$

Since the integral calculation in Eq. A.27 gives small values, due to small values of the tangent thermal coefficient (Fig. 4.5) and by considering that the maximum temperature rise considered in this work is about hundred Kelvin, the approximation

$$\exp\left(\int_{T_0}^{T_0+\Delta T} \alpha_t(T)dT\right) - 1 \approx \int_{T_0}^{T_0+\Delta T} \alpha_t(T)dT \quad (\text{A.28})$$

may be used to calculate the secant thermal expansion coefficient (Eq. A.25):

$$\alpha_s(T, T_0) = \frac{\int_{T_0}^T \alpha_t(T')dT'}{T - T_0}, \text{ where } T = T_0 + \Delta T \quad (\text{A.29})$$

Considering L'Hospital's rule for Eq. A.29 it can be derived that at $T = T_0 \rightarrow \alpha_s(T_0, T_0) = \alpha_t(T_0)$. In Fig. A.2 an illustration of the functions used in this work for the secant thermal expansion coefficient is given.

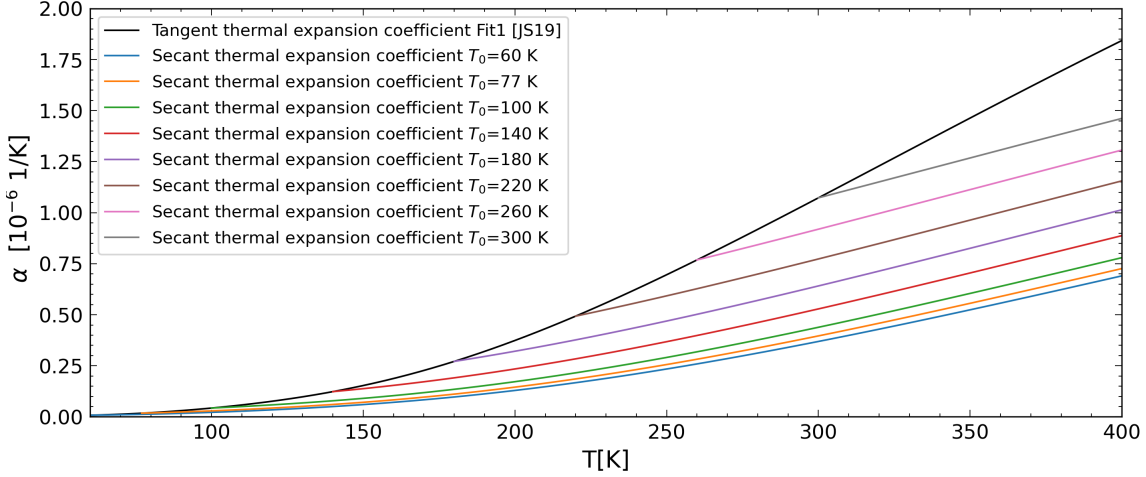


Figure A.2.: Secant thermal expansion coefficient as a function of temperature T and particular initial temperature values T_0 .

Inserting Eq. A.29 into Eq. A.24 gives

$$\epsilon_{kl}^{th} = \alpha_s(T, T_0)\Delta T, \quad (\text{A.30})$$

A.6. Finite element method (FEM)

To understand the underlying concept of the FEM a one-dimensional example is presented in this section. The chosen methods for the approximation by shape functions and numerical integration are the ones also used in the software COMSOL Multiphysics® and similar concepts can be used to derive a FEM code for a three-dimensional or two-dimensional axisymmetric formulation. The concepts used in this section are based on the FEM codes presented by [Bow09, Chapter 8] and [Bal89]. It should be mentioned that in the presented code in the following section only the displacement is calculated. However, a similar FEM code can also be used to solve the temperature and displacement simultaneously, for further information about this topic see [Bal89].

One-dimensional example of solving thermoelastic problems with FEM In this example the same one-dimensional problem that was formulated by Eq. 6.21 is discussed, considering to a homogeneous temperature rise ΔT . The strong form PDE of this equation is:

$$\sigma_{zz} = E \frac{\partial w(z, t)}{\partial z} - \alpha E \Delta T, \quad \text{boundary conditions } \sigma_{zz}|_{z=0} = 0, \sigma_{zz}|_{z=d} = 0 \quad (\text{A.31})$$

$$\rho \frac{\partial^2 w(z, t)}{\partial t^2} = \frac{\partial \sigma_{zz}}{\partial z}.$$

The weighted residual method prescribes that the weighted integral value of this residual

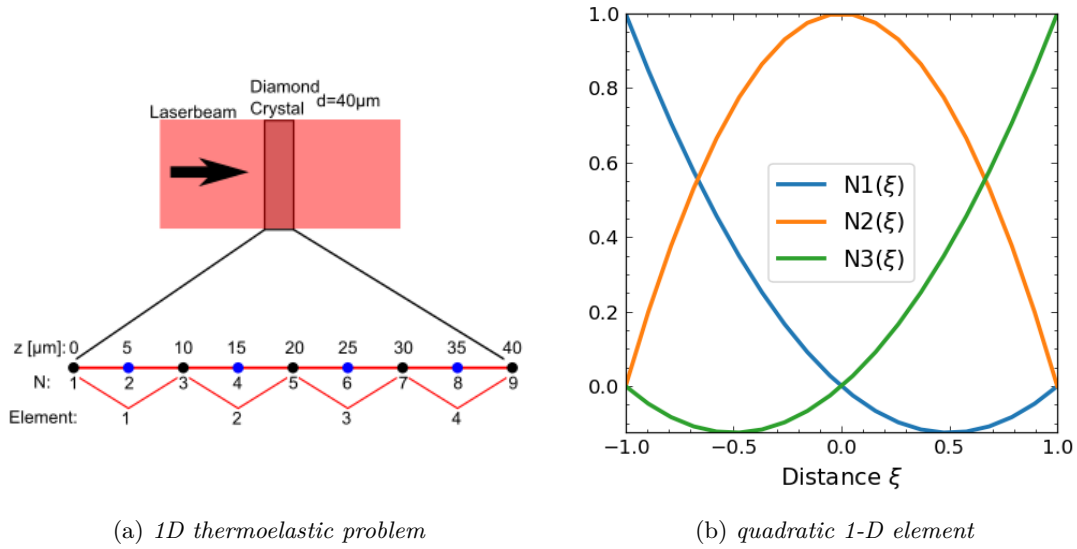


Figure A.3.: (a) sketch of the 1D thermoelastic problem with $\Delta T = \text{constant}$ (b) Illustration of shape functions of a quadratic 1-D element calculated with Eq. A.43

should be zero:

$$\int_0^d S_w(z, t) \left[\frac{\partial}{\partial z} \sigma_{zz} - \rho \frac{\partial^2 w(z, t)}{\partial t^2} \right] dz = 0 \quad (\text{A.32})$$

$$\int_0^d S_w(z, t) \left[\frac{\partial}{\partial z} \left(E \frac{\partial w(z, t)}{\partial z} - \alpha E \Delta T \right) - \rho \frac{\partial^2 w(z, t)}{\partial t^2} \right] dz = 0, \quad (\text{A.33})$$

where S_w denotes the weighted functions and the equation inside the square brackets is called the Residual.

Using integration by parts³ we can write

$$\begin{aligned} \int_0^d S_w(z, t) \frac{\partial}{\partial z} \sigma_{zz} dz &= \int_0^d S_w(z, t) \frac{\partial}{\partial z} \left(E \frac{\partial w(z, t)}{\partial z} - \alpha E \Delta T \right) dz \\ &= - \int_0^d \left(E \frac{S_w(z, t)}{\partial z} \frac{\partial w(z, t)}{\partial z} - \frac{S_w(z, t)}{\partial z} \alpha E \Delta T \right) dz + S_w(z, t) \sigma_{zz} |_{z=d} - S_w(z, t) \sigma_{zz} |_{z=0}, \end{aligned} \quad (\text{A.34})$$

Considering the strong form Eq. A.31 it can be seen that the boundary conditions are fulfilled by setting the last two terms in Eq. A.32 to zero. These kind of boundary conditions in context of the FEM are also called natural or Neumann boundary conditions. Inserting Eq. A.34 into Eq. A.32 yields the so called weak form. And integrating term by term it

³For a three-dimensional problem the Gauss Theorem can be used in this context.

can be obtained:

$$\int_0^d E \frac{\partial w(z,t)}{\partial z} \frac{\partial S_w(z,t)}{\partial z} dz - \int_0^d E \alpha \Delta T \frac{\partial S_w(z,t)}{\partial z} dz + \int_0^d \rho \frac{d^2 w(z,t)}{dt^2} S_w(z,t) dz = 0. \quad (\text{A.35})$$

To solve Eq. A.35, the displacement can be discretized, which means that the displacement is calculated at a set of n discrete points called nodes. These nodes are special points z_a denoting the position of the unknown displacement w_a at this position. For example the displacement w_5 at node five in Fig. A.3a has the coordinate $z_5 = 20 \mu\text{m}$. The index a is covering all nodes of the domain from 1 to n (in the illustration of Fig. A.3a the total number of nodes is $n=9$). The displacement field at an arbitrary point within the crystal will be specified by interpolating between these nodal values:

$$w(z,t) = \sum_{a=1}^n N_a(z) w_a(t) \quad (\text{A.36})$$

Here z denotes the coordinates of an arbitrary point in the crystal. The interpolation functions $N_a(z)$ are functions of position only, which must have the property that:

$$w_i(z,t) = \sum_{a=1}^n N_a(z_i) w_a(t) \quad (\text{A.37})$$

Here i is an index that covers all nodes from 1 to n and a common approach for a FEM is to choose:

$$N_a(z_i) = \begin{cases} 1, & a = i \\ 0, & a \neq i \end{cases} \quad (\text{A.38})$$

Choosing for the weighted functions the same interpolation scheme like for the displacement is known as the Galerkin's method:

$$S_w(z,t) = \sum_{a=1}^n N_a(z) S_{w_a}(t) \quad (\text{A.39})$$

Inserting the interpolations Eq. A.36 and Eq. A.39 into the weak form Eq. A.35 gives the equation:

$$\sum_{a=1}^n \sum_{b=1}^n \left(\int_0^d E \frac{\partial N_b(z)}{\partial z} w_b \frac{\partial N_a(z)}{\partial z} S_{w_a} dz + \int_0^d \rho N_b(z) N_a(z) \ddot{w}_b S_{w_a} dz \right) - \sum_{a=1}^n \int_0^d E \alpha \Delta T \frac{\partial N_a(z)}{\partial z} S_{w_a} dz = 0,$$

which may be written in the following matrix form:

$$(K_{ab}w_b + M_{ab}\ddot{w}_b - F_a)S_{w_a} = 0 \quad (\text{A.40})$$

$$K_{ab} = \int_0^d E \frac{\partial N_a(z)}{\partial z} \frac{\partial N_b(z)}{\partial z} dz$$

$$M_{ab} = \int_0^d \rho N_a(z) N_b(z) dz$$

$$F_a = \int_0^d E \alpha \Delta T \frac{\partial N_a(z)}{\partial z} dz$$

It should be mentioned that the boundary condition in this particular example is that the traction is zero at $z = 0$ and $z = d$ for a none zero value there would be an additional contribution to the last equation in Eq. A.40 at the first and last node. Non trivial solutions to Eq. A.40 are found by solving

$$K_{ab}w_b + M_{ab}\ddot{w}_b - F_a = 0. \quad (\text{A.41})$$

Here K_{ab} is the so called stiffness matrix, F_{ab} called the force vector and M_{ab} the mass matrix. Writing out the matrices gives:

$$K_{ab} = E \begin{bmatrix} \int_0^d \frac{\partial N_1(z)}{\partial z} \frac{\partial N_1(z)}{\partial z} dz & \int_0^d \frac{\partial N_1(z)}{\partial z} \frac{\partial N_2(z)}{\partial z} dz & \dots & \int_0^d \frac{\partial N_1(z)}{\partial z} \frac{\partial N_n(z)}{\partial z} dz \\ \int_0^d \frac{\partial N_2(z)}{\partial z} \frac{\partial N_1(z)}{\partial z} dz & \int_0^d \frac{\partial N_2(z)}{\partial z} \frac{\partial N_2(z)}{\partial z} dz & \dots & \int_0^d \frac{\partial N_2(z)}{\partial z} \frac{\partial N_n(z)}{\partial z} dz \\ \vdots & \vdots & & \vdots \\ \int_0^d \frac{\partial N_n(z)}{\partial z} \frac{\partial N_2(z)}{\partial z} dz & \int_0^d \frac{\partial N_n(z)}{\partial z} \frac{\partial N_1(z)}{\partial z} dz & \dots & \int_0^d \frac{\partial N_n(z)}{\partial z} \frac{\partial N_n(z)}{\partial z} dz \end{bmatrix} \quad (\text{A.42a})$$

$$M_{ab} = \rho \begin{bmatrix} \int_0^d N_1(z) N_1(z) dz & \int_0^d N_1(z) N_2(z) dz & \dots & \int_0^d N_1(z) N_n(z) dz \\ \int_0^d N_2(z) N_1(z) dz & \int_0^d N_2(z) N_2(z) dz & \dots & \int_0^d N_2(z) N_n(z) dz \\ \vdots & \vdots & & \vdots \\ \int_0^d N_n(z) N_2(z) dz & \int_0^d N_n(z) N_1(z) dz & \dots & \int_0^d N_n(z) N_n(z) dz \end{bmatrix} \quad (\text{A.42b})$$

$$F_a = E \alpha \Delta T \begin{bmatrix} \int_0^d \frac{\partial N_1(z)}{\partial z} dz \\ \vdots \\ \int_0^d \frac{\partial N_n(z)}{\partial z} dz \end{bmatrix} \quad (\text{A.42c})$$

The stiffness matrix and the mass matrix are $n \times n$ matrices and the force vector has n components, where n is the total number of nodes. To interpolate and integrate Eq. A.40 various different methods can be used. However, it turns out to be particularly convenient to use a piecewise-Lagrangian interpolation scheme and to evaluate the integrals numerically using a Gaussian quadrature scheme. Considering a generic quadratic 1-D element that lies in the region $-1 < \xi < 1$, as illustrated in Fig. A.3b the corresponding

piecewise-Lagrangian interpolation scheme is given by the following shape functions:

$$N_1(\xi) = -0.5\xi(1 - \xi), N_2(\xi) = (1 - \xi)(1 + \xi), N_3(\xi) = 0.5\xi(1 + \xi). \quad (\text{A.43})$$

The displacements w within the element are then interpolated as

$$w(\xi) = \sum_{a_e=1}^{n_e} N_{a_e}(\xi) w_{a_e} \quad (\text{A.44})$$

where n_e denotes the number of nodes on the element and w_{a_e} denotes the value of the displacement at each node. The actual nodal coordinates do not lie necessarily at -1 , $+1$ and 0 , but the function can be mapped to the region of interest by setting

$$z(\xi) = \sum_{a_e=1}^{n_e} N_{a_e}(\xi) z_{a_e}. \quad (\text{A.45})$$

By substituting Eq. A.43 into Eq. A.45 it can be found that an uniform spacing ($z_2 = (z_1 + z_3)/2$) of the nodes gives a linear mapping:

$$z_e(\xi) = \frac{h_e}{2}\xi + \frac{z_1 + z_3}{2}, \quad \xi(z) = \left(z - \frac{z_1 + z_3}{2} \right) \frac{2}{h_e}, \quad (\text{A.46})$$

where $h_e = z_3 - z_1$ is the length of the element. Elements that interpolate displacements and position using the same shape functions are called isoparametric elements. The Jacobian $J = \left| \frac{\partial z}{\partial \xi} \right|$ associated with the mapping in this case may be computed as:

$$\frac{\partial z}{\partial \xi} = \frac{\partial}{\partial \xi} \sum_{a_e=1}^{n_e} N_{a_e}(\xi) z_{a_e} = \sum_{a_e=1}^{n_e} \frac{\partial N_{a_e}(\xi)}{\partial \xi} z_{a_e} \quad (\text{A.47})$$

The mapping also can be used to calculate the shape function derivatives:

$$\frac{\partial N_{a_e}(z)}{\partial z} = \frac{\partial N_{a_e}(\xi)}{\partial \xi} \frac{\partial \xi}{\partial z} = \frac{\partial N_{a_e}(\xi)}{\partial \xi} \left(\frac{\partial z}{\partial \xi} \right)^{-1} \quad (\text{A.48})$$

To evaluate the integrals numerically a Gaussian quadrature scheme can be used:

$$\int_{-1}^1 g(\xi) \approx \sum_{I=1}^M w_I g(\xi_I) \quad (\text{A.49})$$

Where ξ_I denotes set of integration points in the region $[-1, 1]$, and w_I is a set of integration weights, which are chosen so as to make the approximation as accurate as possible.

The values for $M = 1, 2$ and 3 are:

$$M = 1 : \xi_1 = 0, w_1 = 2 \quad (A.50)$$

$$M = 2 : \xi_1 = -\sqrt{\frac{1}{3}}, w_1 = 1 \quad \xi_2 = \sqrt{\frac{1}{3}}, w_2 = 1 \quad (A.51)$$

$$M = 3 : \xi_1 = -\sqrt{\frac{3}{5}}, w_1 = \sqrt{\frac{5}{9}} \quad \xi_2 = 0, w_2 = \sqrt{\frac{8}{9}} \quad \xi_3 = \sqrt{\frac{3}{5}}, w_3 = \sqrt{\frac{5}{9}} \quad (A.52)$$

$$(A.53)$$

As illustrated in Fig. A.3a the domain can be sub-divided into a series of elements. The quadratic 1-D element is bounded by two nodal points (black dots), and also contains one interior node (blue dots). The chosen interpolation scheme causes that the integral over the l_{th} element depends only on the shape functions associated with the nodes on the l_{th} element, the corresponding element matrix depends on the geometry, and material properties, which in this example are constant values. To derive the matrices of Eq. A.41 all elements matrices have to be assembled into a global matrix. For assembling the global matrices notice that for the first element matrix the connection between global and element coordinates are $z_1 = z_{1e1}$ and $z_2 = z_{2e1}$ and $z_3 = z_{3e1}$. For the second element $z_3 = z_{1e2}$ and $z_4 = z_{2e2}$ and $z_5 = z_{3e2}$ and so on up to the l_{th} element.

Considering Eq. A.42a the element matrices for the first element are:

$$k_{a_{e1}b_{e1}} = E \begin{bmatrix} \int_{z_{1e1}}^{z_{3e1}} \frac{\partial N_1(z)}{\partial z} \frac{\partial N_1(z)}{\partial z} dz & \int_{z_{1e1}}^{z_{3e1}} \frac{\partial N_1(z)}{\partial z} \frac{\partial N_2(z)}{\partial z} dz & \int_{z_{1e1}}^{z_{3e1}} \frac{\partial N_1(z)}{\partial z} \frac{\partial N_3(z)}{\partial z} dz \\ \int_{z_{1e1}}^{z_{3e1}} \frac{\partial N_2(z)}{\partial z} \frac{\partial N_1(z)}{\partial z} dz & \int_{z_{1e1}}^{z_{3e1}} \frac{\partial N_2(z)}{\partial z} \frac{\partial N_2(z)}{\partial z} dz & \int_{z_{1e1}}^{z_{3e1}} \frac{\partial N_2(z)}{\partial z} \frac{\partial N_3(z)}{\partial z} dz \\ \int_{z_{1e1}}^{z_{3e1}} \frac{\partial N_3(z)}{\partial z} \frac{\partial N_1(z)}{\partial z} dz & \int_{z_{1e1}}^{z_{3e1}} \frac{\partial N_3(z)}{\partial z} \frac{\partial N_2(z)}{\partial z} dz & \int_{z_{1e1}}^{z_{3e1}} \frac{\partial N_3(z)}{\partial z} \frac{\partial N_3(z)}{\partial z} dz \end{bmatrix} \quad (A.54a)$$

$$m_{a_{e1}b_{e1}} = \rho \begin{bmatrix} \int_{z_{1e1}}^{z_{3e1}} N_1(z)N_1(z)dz & \int_{z_{1e1}}^{z_{3e1}} N_1(z)N_2(z)dz & \int_{z_{1e1}}^{z_{3e1}} N_1(z)N_3(z)dz \\ \int_{z_{1e1}}^{z_{3e1}} N_2(z)N_1(z)dz & \int_{z_{1e1}}^{z_{3e1}} N_2(z)N_2(z)dz & \int_{z_{1e1}}^{z_{3e1}} N_2(z)N_3(z)dz \\ \int_{z_{1e1}}^{z_{3e1}} N_3(z)N_1(z)dz & \int_{z_{1e1}}^{z_{3e1}} N_3(z)N_2(z)dz & \int_{z_{1e1}}^{z_{3e1}} N_3(z)N_3(z)dz \end{bmatrix} \quad (A.54b)$$

$$f_{a_{e1}} = E\alpha\Delta T \begin{bmatrix} \int_{z_{1e1}}^{z_{3e1}} \frac{\partial N_1(z)}{\partial z} dz \\ \int_{z_{1e1}}^{z_{3e1}} \frac{\partial N_2(z)}{\partial z} dz \\ \int_{z_{1e1}}^{z_{3e1}} \frac{\partial N_3(z)}{\partial z} dz \end{bmatrix} \quad (A.54c)$$

Using the piecewise-Lagrangian interpolation scheme and Gaussian quadrature as previously described, the calculation of the values can be carried out. To clarify the calculation process of the components, an example is carried out by calculating the first component of Eq. A.54a and Eq. A.54b. All other components can be carried out in a similar way.

$$k_{1e11e1} = \int_{z_{1e1}}^{z_{3e1}} \frac{\partial N_1(z)}{\partial z} \frac{\partial N_1(z)}{\partial z} dz = \int_{-1}^1 \frac{\partial N_1(z)}{\partial z} \frac{\partial N_1(z)}{\partial z} J d\xi \quad (A.55)$$

Using Eq. A.47 and Eq. A.48 to calculate the Jacobian and the derivatives of the shape function gives:

$$J = \left| \frac{\partial z}{\partial \xi} \right| = |(\xi - 0.5)z_{1e} - 2\xi z_{2e} + (\xi + 0.5)z_{3e}| \quad (\text{A.56a})$$

$$\frac{\partial \xi}{\partial z} = 1/((\xi - 0.5)z_{1e} - 2\xi z_{2e} + (\xi + 0.5)z_{3e}) \quad (\text{A.56b})$$

$$\frac{\partial N_{1e}(z)}{\partial z} = (\xi - 0.5) \frac{\partial \xi}{\partial z} \quad (\text{A.56c})$$

Using Gaussian quadrature Eq. A.49 and two integration point gives:

$$k_{1e11e1} = \int_{-1}^1 \frac{\partial N_1(z)}{\partial z} \frac{\partial N_1(z)}{\partial z} J d\xi =$$

$$\sum_{I=1}^2 w_I \left(\frac{\xi_I - 0.5}{(\xi_I - 0.5)z_{1e} - 2\xi_I z_{2e} + (\xi_I + 0.5)z_{3e}} \right)^2 |(\xi_I - 0.5)z_{1e} - 2\xi_I z_{2e} + (\xi_I + 0.5)z_{3e}|$$

Calculating the element mass matrix leads to

$$m_{1e11e1} = \int_{z_{1e1}}^{z_{3e1}} N_1(z) N_1(z) dz = \rho \int_{-1}^1 N_1(\xi) N_1(\xi) J d\xi = \quad (\text{A.57})$$

$$\sum_{I=1}^3 w_I (0.5\xi^2 - 0.5\xi)^2 |(\xi_I - 0.5)z_{1e} - 2\xi_I z_{2e} + (\xi_I + 0.5)z_{3e}|.$$

Substitution Eq. A.46 in Eq. A.56 gives

$$J = \frac{h_e}{2} \quad (\text{A.58})$$

$$\frac{\partial \xi}{\partial z} = \frac{2}{h_e}, \text{ with } h_e = z_3 - z_1, \quad z_3 > z_1. \quad (\text{A.59})$$

and Eq. A.54 becomes:

$$k_{a_e1b_e1} = \frac{E}{3h_e} \begin{bmatrix} 7 & -8 & 1 \\ -8 & 16 & -8 \\ 1 & -8 & 7 \end{bmatrix} \quad (\text{A.60a})$$

$$m_{a_e1b_e1} = \frac{\rho h_e}{30} \begin{bmatrix} 4 & 2 & -1 \\ 2 & 16 & 2 \\ -1 & 2 & 4 \end{bmatrix} \quad (\text{A.60b})$$

$$f_{a_e1} = E\alpha\Delta T \begin{bmatrix} -1 \\ 0 \\ 1 \end{bmatrix} \quad (\text{A.60c})$$

Time integration The Newmark method may be used for the time integration [Bow09, p. 493]. In this example it is assumed that the crystal at a time $t = 0$ has the initial conditions $w(z, 0) = 0$ and $\dot{w}(0) = 0$. The first step is to calculate the acceleration $\ddot{w}(t)$ at $t = 0$ by rearranging Eq. A.41:

$$M_{ab}\ddot{w}(0) = -K_{ab}w(0) + F_a \quad (\text{A.61})$$

The acceleration $\ddot{w}(t + \Delta t)$ for a time step Δt after $t=0$ can be calculated by:

$$\left(M_{ab} + \frac{\beta_2 \Delta t^2}{2} K_{ab} \right) \ddot{w}(t + \Delta t) = -K_{ab} \left(w(t) + \Delta t \dot{w}(t) + \frac{\Delta t^2}{2} (1 - \beta_2) \ddot{w}(t) \right) + F(t + \Delta t) \quad (\text{A.62})$$

with these two acceleration values the displacement and velocity at the time Δt can be calculated:

$$w(t + \Delta t) \approx w(t) + \Delta t \dot{w}(t) + \frac{\Delta t^2}{2} [(1 - \beta_2) \ddot{w}(t) + \beta_2 \ddot{w}(t + \Delta t)] \quad (\text{A.63a})$$

$$\dot{w}(t + \Delta t) \approx \dot{w}(t) + \Delta t [(1 - \beta_1) \ddot{w}(t) + \beta_1 \ddot{w}(t + \Delta t)] \quad (\text{A.63b})$$

Using the values of $w(t + \Delta t)$ and $\dot{w}(t + \Delta t)$ in Eq. A.61 the successive time steps can be computed.

The value of β_1 and β_2 are two adjustable parameters that determine the behavior of the time integration. If $\beta_1 = \beta_2 = 0$ the integration scheme is called explicit. In this case the calculation of Eq. A.62 can be skipped. On the other hand, if $\beta_1 = \beta_2 = 1$, the acceleration is estimated only from its value at time $t + \Delta t$. This is known as a fully implicit time integration.

Mesh and time stepping parameters for FEM simulation The one-dimensional model described in Eq. 6.21 can be solved analytically. The analytic solution can be used to compare the results calculated with a self written FEM code based on the theory described in this section. The plot in Fig. A.4 compares the FEM simulation with the analytical solution for a $d = 100 \mu\text{m}$ thick diamond crystal at a time $t = 13 \text{ ns}$. For the simulations the material parameters of Table 6.1 and an initial temperature rise of $\Delta T = 1 \text{ K}$ have been considered. A uniform mesh size of $h_m = 1 \mu\text{m}$ between neighboring nodes and an implicit time integration with $\beta_1 = \beta_2 = 0.5$ has been used.

Temperature dependent material constants For the presented FEM code an linear equation system has to be solved for each time step considered in the simulation and the material parameters in this context are parts of characteristic matrices like the stiffness matrix for example the (Eq. A.42c) by updating the material constants inside these matrices during the calculation the temperature dependence of the material parameter can be taken into account.

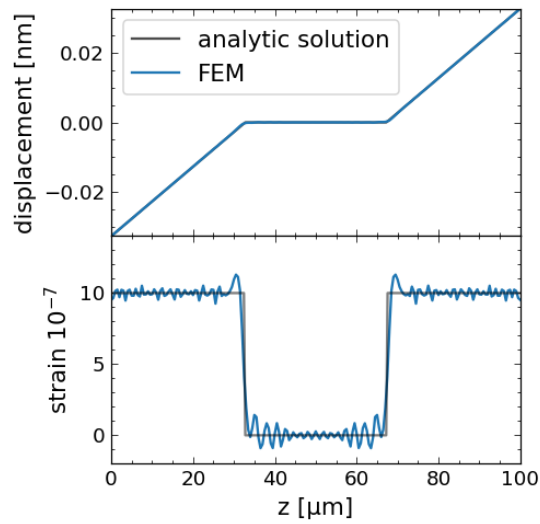


Figure A.4.: *Displacement and strain for a 100 μm thick diamond crystal calculated with a FEM simulation for an instantaneously temperature rise $\Delta T = 1 \text{ K}$ at a time $t = 13 \text{ ns}$ with uniform mesh size of $1 \mu\text{m}$ between neighboring nodes and uniform time stepping of $\Delta t = 10 \text{ ps}$.*

Bibliography

- [AB13] ALLMEN, Martin v. ; BLATTER, Andreas: *Laser-beam interactions with materials: physical principles and applications*. Bd. 2. Springer Science & Business Media, 2013
- [ABB⁺12] AMANN, J ; BERG, W ; BLANK, V ; DECKER, F-J ; DING, Y ; EMMA, P ; FENG, Y ; FRISCH, J ; FRITZ, D ; HASTINGS, J u. a.: Demonstration of self-seeding in a hard-X-ray free-electron laser. In: *Nature photonics* 6 (2012), Nr. 10, S. 693–698
- [ASL⁺09] ARAÚJO, Marcos A. ; SILVA, Rubens ; LIMA, Emerson de ; PEREIRA, Daniel P. ; OLIVEIRA, Paulo C.: Measurement of Gaussian laser beam radius using the knife-edge technique: improvement on data analysis. In: *Applied optics* 48 (2009), Nr. 2, S. 393–396
- [Bal89] BALLA, M: FORMULATION OF COUPLED PROBLEMS OF THERMOELASTICITY BY FINITE ELKMENTS. In: *Periodica Polytechnica Mechanical Engineering* 33 (1989), Nr. 1-2, S. 59–70
- [Bow09] BOWER, Allan F.: *Applied mechanics of solids*. CRC press, 2009
- [BTM⁺18] BAHNS, I ; THIESSEN, P ; MAAG, C ; ROSSBACH, J ; ZEMELLA, J ; SLEZIONA, Germany V. ; SINN, H: THERMAL AND MECHANICAL STABILITY OF BRAGG REFLECTORS UNDER PULSED XFEL-RADIATION. (2018)
- [BZKW03] BRAIG, Christoph ; ZARDA, Patrick ; KURTSIEFER, Christian ; WEINFURTER, Harald: Experimental demonstration of complementarity with single photons. In: *Applied Physics B* 76 (2003), Nr. 2, S. 113–116
- [CL05] CLERC, Daryl G. ; LEDBETTER, Hassel: Second-order and third-order elastic properties of diamond: An ab initio study. In: *Journal of Physics and Chemistry of Solids* 66 (2005), Nr. 10, S. 1589–1597
- [DAA⁺20] DECKING, W ; ABEGHYAN, S ; ABRAMIAN, P ; ABRAMSKY, A ; AGUIRRE, A ; ALBRECHT, C ; ALOU, P ; ALTARELLI, M ; ALTMANN, P ; AMYAN, K u. a.: A MHz-repetition-rate hard X-ray free-electron laser driven by a superconducting linear accelerator. In: *Nature Photonics* 14 (2020), Nr. 6, S. 391–397
-

-
- [DE72] DAVIES, G ; EVANS, Trevor: Graphitization of diamond at zero pressure and at a high pressure. In: *Proceedings of the Royal Society of London. A. Mathematical and Physical Sciences* 328 (1972), Nr. 1574, S. 413–427
- [DeS53] DESORBO, Warren: Specific heat of diamond at low temperatures. In: *The Journal of Chemical Physics* 21 (1953), Nr. 5, S. 876–880
- [FW01] FENG, Simin ; WINFUL, Herbert G.: Physical origin of the Gouy phase shift. In: *Optics letters* 26 (2001), Nr. 8, S. 485–487
- [GKM⁺14] GULANS, Andris ; KONTUR, Stefan ; MEISENBICHLER, Christian ; NABOK, Dmitrii ; PAVONE, Pasquale ; RIGAMONTI, Santiago ; SAGMEISTER, Stephan ; WERNER, Ute ; DRAXL, Claudia: Exciting: a full-potential all-electron package implementing density-functional theory and many-body perturbation theory. In: *Journal of Physics: Condensed Matter* 26 (2014), Nr. 36, S. 363202
- [GM18] GROSS, Rudolf ; MARX, Achim: *Festkörperphysik*. Walter de Gruyter GmbH & Co KG, 2018
- [Har18] HARRIS, Peter J.: Transmission electron microscopy of carbon: a brief history. In: *C—Journal of Carbon Research* 4 (2018), Nr. 1, S. 4
- [Hec16] HECHT, Eugene: *Optics*. Pearson, 2016
- [HEG09] HETNARSKI, Richard B. ; ESLAMI, M R. ; GLADWELL, GML: *Thermal stresses: advanced theory and applications*. Bd. 158. Springer, 2009
- [Hes12] HESS, Peter: The mechanical properties of various chemical vapor deposition diamond structures compared to the ideal single crystal. In: *Journal of Applied Physics* 111 (2012), Nr. 5, S. 3
- [HNK] HOPCROFT, Matthew A. ; NIX, William D. ; KENNY, Thomas W.: What is the Young’s Modulus of Silicon?,”. In: *J. Microelectromechanical Systems* 19
- [Höl15] HÖLZER, Martin: Lattice dynamics from first principles. (2015)
- [HY07] HOLT, David B. ; YACOBI, Ben G.: *Extended defects in semiconductors: electronic properties, device effects and structures*. Cambridge University Press, 2007
- [HY12] HASHIGUCHI, Koichi ; YAMAKAWA, Yuki: *Introduction to finite strain theory for continuum elasto-plasticity*. John Wiley & Sons, 2012
- [JC72] JOHNSON, Peter B. ; CHRISTY, R-WJPrB: Optical constants of the noble metals. In: *Physical review B* 6 (1972), Nr. 12, S. 4370
- [JOP⁺] JONES, Eric ; OLIPHANT, Travis ; PETERSON, Pearu u. a.: *SciPy: Open source scientific tools for Python*. <http://www.scipy.org/>. Version: 2001–
-

-
- [JS19] JACOBSON, P ; STOUPIN, S: Thermal expansion coefficient of diamond in a wide temperature range. In: *Diamond and Related Materials* 97 (2019), S. 107469
- [KC93] KLEIN, Claude A. ; CARDINALE, Gregory F.: Young's modulus and Poisson's ratio of CVD diamond. In: *Diamond and Related Materials* 2 (1993), Nr. 5-7, S. 918–923
- [KSR08] KIM, Kwang-Je ; SHVYD'KO, Yuri ; REICHE, Sven: A proposal for an x-ray free-electron laser oscillator with an energy-recovery linac. In: *Physical review letters* 100 (2008), Nr. 24, S. 244802
- [Lau57] LAUE, Max von: "*Clausius, Rudolf*" in: *Neue Deutsche Biographie* 3. <https://www.deutsche-biographie.de/pnd116540486.html#ndbcontent>. Version: 1957
- [LD18] LI, Kai ; DENG, Haixiao: Systematic design and three-dimensional simulation of x-ray FEL oscillator for shanghai coherent light facility. In: *Nuclear Instruments and Methods in Physics Research Section A: Accelerators, Spectrometers, Detectors and Associated Equipment* 895 (2018), S. 40–47
- [LKSF11] LINDBERG, RR ; KIM, K-J ; SHVYD'KO, Yu ; FAWLEY, WM: Performance of the x-ray free-electron laser oscillator with crystal cavity. In: *Physical Review Special Topics-Accelerators and Beams* 14 (2011), Nr. 1, S. 010701
- [Maa18] MAAG, Christoph: *Influence of pulsed heat load on the performance of diamond bragg mirrors for an xfel-oscillator*, Staats-und Universitätsbibliothek Hamburg Carl von Ossietzky, Diss., 2018
- [Mal69] MALVERN, Lawrence E.: *Introduction to the Mechanics of a Continuous Medium*. 1969 (Monograph)
- [MBUW12] MYKHAYLYK, VB ; BURT, M ; URSACHI, C ; WAGNER, A: Thermal contact conductance of demountable in vacuum copper-copper joint between 14 and 100 K. In: *Review of Scientific Instruments* 83 (2012), Nr. 3, S. 034902
- [Mes10] MESCHÉDE, Dieter: *Gerthsen physik*. 24. Springer-Verlag, 2010
- [MM16] MALHOTRA, Abhinav ; MALDOVAN, Martin: Impact of phonon surface scattering on thermal energy distribution of Si and SiGe nanowires. In: *Scientific reports* 6 (2016), Nr. 1, S. 1–13
- [Mur13] MURA, Toshio: *Micromechanics of defects in solids*. Springer Science & Business Media, 2013
- [N⁺85] NYE, John F. u. a.: *Physical properties of crystals: their representation by tensors and matrices*. Oxford university press, 1985
-

- [Now13] NOWACKI, Witold: *Thermoelasticity*. Elsevier, 2013
- [Par77] PARSONS, BJ: Spectroscopic mode Grüneisen parameters for diamond. In: *Proceedings of the Royal Society of London. A. Mathematical and Physical Sciences* 352 (1977), Nr. 1670, S. 397–417
- [PK13] PAN, Lawrence S. ; KANIA, Don R.: *Diamond: electronic properties and applications*. Springer Science & Business Media, 2013
- [PT64] PHILLIP, HR ; TAFT, EA: Kramers-Kronig analysis of reflectance data for diamond. In: *Physical Review* 136 (1964), Nr. 5A, S. A1445
- [Ram47] RAMACHANDRAN, GN: Thermo-optic behaviour of solids. In: *Proceedings of the Indian Academy of Sciences-Section A* Bd. 25 Springer, 1947, S. 481
- [Rau21] RAUER, Patrick: *Feasibility of a Cavity-Based X-Ray Free-Electron-Laser at the European XFEL*, Universität Hamburg, Diss., probably 2021
- [Ree75] REEBER, ROBERT R.: Thermal expansion of some group IV elements and ZnS. In: *physica status solidi (a)* 32 (1975), Nr. 1, S. 321–331
- [RLB19] RITZ, Ethan T. ; LI, Sabrina J. ; BENEDEK, Nicole A.: Thermal expansion in insulating solids from first principles. In: *Journal of Applied Physics* 126 (2019), Nr. 17, S. 171102
- [RPJG⁺99] ROSE-PETRUCK, Christoph ; JIMENEZ, Ralph ; GUO, Ting ; CAVALLERI, Andrea ; SIDERS, Craig W. ; RKSI, Ferenc ; SQUIER, Jeff A. ; WALKER, Barry C. ; WILSON, Kent R. ; BARTY, Christopher P.: Picosecond–milliångström lattice dynamics measured by ultrafast X-ray diffraction. In: *Nature* 398 (1999), Nr. 6725, S. 310
- [Sad09] SADD, Martin H.: *Elasticity: theory, applications, and numerics*. Academic Press, 2009
- [SBC⁺19] SAMOYLOVA, Liubov ; BOESENBERG, Ulrike ; CHUMAKOV, Aleksandr ; KAGANER, Vladimir ; PETROV, Ilia ; ROTH, Thomas ; RÜFFER, Rudolf ; SINN, Harald ; TERYTYEV, Sergey ; MADSEN, Anders: Diffraction properties of a strongly bent diamond crystal used as a dispersive spectrometer for XFEL pulses. In: *Journal of synchrotron radiation* 26 (2019), Nr. 4, S. 1069–1072
- [SBT17] SHVYD'KO, Yuri ; BLANK, Vladimir ; TERYTYEV, Sergey: Diamond X-ray optics: transparent, resilient, high-resolution, and wavefront preserving. In: *MRS Bulletin* 42 (2017), Nr. 06
- [SC10] SETYAWAN, Wahyu ; CURTAROLO, Stefano: High-throughput electronic band structure calculations: Challenges and tools. In: *Computational materials science* 49 (2010), Nr. 2, S. 299–312
-

-
- [Sch10] SCHAAF, Peter: *Laser processing of materials: fundamentals, applications and developments*. Bd. 139. Springer Science & Business Media, 2010
- [SMW⁺12] STOUPIN, S ; MARCH, AM ; WEN, H ; WALKO, DA ; LI, Y ; DUFRESNE, EM ; STEPANOV, SA ; KIM, K-J ; SHVYD'KO, Yu V. ; BLANK, VD u. a.: Direct observation of dynamics of thermal expansion using pump-probe high-energy-resolution x-ray diffraction. In: *Physical Review B* 86 (2012), Nr. 5, S. 054301
- [SS10] STOUPIN, Stanislav ; SHVYD'KO, Yuri V.: Thermal expansion of diamond at low temperatures. In: *Physical review letters* 104 (2010), Nr. 8, S. 085901
- [ST19] SALEH, Bahaa E. ; TEICH, Malvin C.: *Fundamentals of photonics*. John Wiley & Sons, 2019
- [SWM⁺12] SHAO, Tianjiao ; WEN, Bin ; MELNIK, Roderick ; YAO, Shan ; KAWAZOE, Yoshiyuki ; TIAN, Yongjun: Temperature dependent elastic constants for crystals with arbitrary symmetry: Combined first principles and continuum elasticity theory. In: *Journal of Applied Physics* 111 (2012), Nr. 8, S. 083525
- [SZG⁺20] SOBOLEV, Egor ; ZOLOTAREV, Sergei ; GIEWEKEMEYER, Klaus ; BIELECKI, Johan ; OKAMOTO, Kenta ; REDDY, Hemanth K. ; ANDREASSON, Jakob ; AYYER, Kartik ; BARAK, Imrich ; BARI, Sadia u. a.: Megahertz single-particle imaging at the European XFEL. In: *Communications Physics* 3 (2020), Nr. 1, S. 1–11
- [Tak79] TAKEUTI, Y: Foundations for coupled thermoelasticity. In: *Journal of Thermal Stresses* 2 (1979), Nr. 3-4, S. 323–339
- [TGMT86] THOMSEN, C ; GRAHN, Holger T. ; MARIS, Humphrey J. ; TAUC, Jan: Surface generation and detection of phonons by picosecond light pulses. In: *Physical Review B* 34 (1986), Nr. 6, S. 4129
- [Tin96] TING, Thomas Chi-tsai: *Anisotropic elasticity: theory and applications*. Oxford University Press on Demand, 1996 (45)
- [VT98] VARGA, P ; TÖRÖK, P: The Gaussian wave solution of Maxwell's equations and the validity of scalar wave approximation. In: *Optics communications* 152 (1998), Nr. 1-3, S. 108–118
- [WKT⁺93] WEI, Lanhua ; KUO, PK ; THOMAS, RL ; ANTHONY, TR ; BANHOLZER, WF: Thermal conductivity of isotopically modified single crystal diamond. In: *Physical review letters* 70 (1993), Nr. 24, S. 3764
- [WW17] WALLANDER, Harald ; WALLENTIN, Jesper: Simulated sample heating from a nanofocused X-ray beam. In: *Journal of synchrotron radiation* 24 (2017), Nr. 5, S. 925–933
-

- [WYDC67] WARREN, JL ; YARNELL, JL ; DOLLING, G ; COWLEY, RA: Lattice dynamics of diamond. In: *Physical Review* 158 (1967), Nr. 3, S. 805
- [XWCH91] XU, CH ; WANG, CZ ; CHAN, Che T. ; HO, KM: Theory of the thermal expansion of Si and diamond. In: *Physical review B* 43 (1991), Nr. 6, S. 5024
- [YWW18] YANG, Bo ; WANG, Songwei ; WU, Juhao: Transient thermal stress wave and vibrational analyses of a thin diamond crystal for X-ray free-electron lasers under high-repetition-rate operation. In: *Journal of synchrotron radiation* 25 (2018), Nr. 1, S. 166–176
- [Zem13] ZEMELLA, Johann Christian U.: *Untersuchungen zu einem Freie-Elektronen-Laser-Oszillator im Röntgen-Wellenlängenbereich für den European XFEL*, DESY, Diss., 2013
-

Acknowledgment

I would like to thank my supervisors Prof. Dr. Jörg Rossbach, Dr. Harald Sinn, Prof. Dr. Wolfgang Hillert and Maurizio Vannoni for their support during this thesis and for their doors which were always open for helpful discussions when I needed them.

Also I want to give a special thanks to my co-worker Patrick Rauer, for countless hours of constructive discussions about our collaborating PhD projects.

I want to thank Dr. Christoph Maag and Dr. Johann Zemella for helpful discussions about their PhD projects and for giving me an introduction to the laser lab and the existing experimental setup.

I want to thank Max Trunk and Stefan Holm for their support regarding the cleaning and improvements of the vacuum chamber system.

For their support regarding the motor control positioning system I want to thank Marcus Fleck and Johannes Gebauer.

Also I would like to thank Dr. Sebastian Steinlechner for discussions about the experimental components which can be used to build up a stable working interferometer. Dr. Christian Henkel and Dr. Christoph Lechner I want to thank for shareing the oscilloscope with me and for helpful technical discussions about this device.

I am very thankful that I could share my office with Philipp Amstutz, Dr. Thorsten Hellert, Dr. Christian Henkel, Max Kellermeier, Dr. Willi Kuroopka, Vivien Sleziona and Patrick Rauer. It was always a great pleasure to be with you at this place!

A special thanks goes to my small beloved family Eva Witzler and Theodor Bahns for their support and patience during this difficult time especially when it comes to writing the thesis. Also, I want to thank my parents Dr. Ernst Bahns and Sieglinde Bahns for their support during this thesis.

Eidesstattliche Versicherung

Hiermit versichere ich an Eides statt, dass ich die vorliegende Arbeit selbstständig und ohne fremde Hilfe angefertigt und mich anderer als der im beigefügten Verzeichnis angegebenen Hilfsmittel nicht bedient habe. Alle Stellen, die wörtlich oder sinngemäß aus Veröffentlichungen entnommen wurden, sind als solche kenntlich gemacht. Ich versichere weiterhin, dass ich die Arbeit vorher nicht in einem anderen Prüfungsverfahren eingereicht habe und die eingereichte schriftliche Fassung der auf dem elektronischen Speichermedium entspricht.

Ich bin mit einer Einstellung in den Bestand der Bibliothek des Fachbereiches einverstanden.

Hamburg, den _____ Unterschrift: _____